Yurii Galushkin

Non-standard Problems in Basin Modelling

Springer

Non-standard Problems in Basin Modelling

Yurii Galushkin

Non-standard Problems in Basin Modelling

Springer

Yurii Galushkin
Earth Science Museum
Lomonosov Moscow State University
Moscow
Russia

ISBN 978-3-319-33881-1 ISBN 978-3-319-33882-8 (eBook)
DOI 10.1007/978-3-319-33882-8

Library of Congress Control Number: 2016938401

Printed on acid-free paper

This Springer imprint is published by Springer Nature
The registered company is Springer International Publishing AG Switzerland

Contents

Introduction

In the book, the GALO system for basin modeling is applied to the analysis of some nonstandard problems of geology. Chapter 1 considers the problem of reflection of tectonic and thermal history of the basin lithosphere in variations of the basin tectonic subsidence. The GALO system provides an ability to calculate the amplitude of the basin tectonic subsidence in two ways: standard—by removal of the water and sediment load from the basement surface, and other—by computing variations in density distribution of the basement rocks with depth and time. Comparison of the amplitudes calculated by above two methods gives a possibility to estimate the amplitude and the duration of the thermal and stretching events of the basin lithosphere. Chapter 1 considers the basic principles underlying the tectonic method and analyzes an application of the method to concrete sedimentary section of the Yasnoe field in the West Siberian Basin. The analysis of tectonic subsidence used in our modeling suggests local-isostasy response of the lithosphere on load. The state of isostasy closely linked to the strength of the lithosphere and therefore, in the last section of Chap. 1 the relationship between isostasy of the basin and the strength of its lithosphere is discussed.

In Chap. 2, the method discussed in previous chapter is applied to analysis of thermal and maturation evolution of sedimentary basins in passive continental margin of India in the Bay of Bengal. The difference in the crust thinning, thermal and maturation histories of the main sedimentary formations in sedimentary sections of shallow- and deep-water offshore are discussed here. In Chap. 3, the GALO basin modeling system is applied to reconstruct numerically burial, thermal and maturation histories of the East Barents Basin on the example of two areas (the Admiralteyskaya and Arctic areas). Tectonic history of the basin includes the continental rifting in the Devonian and considerable thinning of the crust in the Permian and Triassic, associated with intensive sedimentation. It will be shown that sufficient part of the Permian–Triassic deposits in center of the South Barents depression occurs within the gas generation zone. Chapter 4 considers the reconstructions of burial, thermal and maturation histories sedimentary sections along the profile from the Cyrenaica Platform on the eastern coast of the Sirte Basin to the Hun Graben on the western border of the Sirte paleoift. The analysis of the

variations in the basin tectonic subsidence suggests that two intervals of significant extension of the lithosphere in the Upper Cretaceous and Paleocene are common for all areas within the basin. This analysis will show that the total amplitude of the crustal extension attains 1.5 in the central part of the Sirte Basin (the Ajdabiya and Maradah troughs and Zelten and Dahra platforms). It is equal to 1.3 in the Hameimat and Zallah troughs, and minimal (1.11–1.17) in the periphery of the basin (within the Hun Graben and Cyrenaica Platform). The last chapter of the Part I in the book demonstrates application of tectonic block of the GALO system to reconstruct the burial, thermal and catagenesis histories of sedimentary sections in the Kaigan–Vasyukan sector of the Sakhalin-5 area in the northeastern shelf of Sakhalin. The considered area of the shelf locates within the Okhotsk block margin near to the East Sakhalin accretion complex in the region subjected by active fault tectonics. Consequently, two versions of the basin's development are analyzed in this chapter: the first with the local-isostasy response of the basin's lithosphere during the basin's entire history and the second with the isostatic behavior of the lithosphere beginning from the time of the Kuril Island Arc's formation (about 34 Ma BP). The computations demonstrate a weak dependency of the lithosphere thermal regime and organic matter maturation in the Cenozoic on the choice of the variants of the basin evolution. Rather high sedimentation rate during the last 10 My together with thermal activation of the basin lithosphere, assumed by tectonic analysis of the basin, are responsible for the striking nonsteady thermal regime of the region. The modeling suggests that the rocks of the upper half of the Late Cretaceous formation; the Eocene, Machigar, and Daekhurin formations; and the lower half of the Uinin complex could generate oil up to the present time.

In Part II of the book, the problem of formation of the temperature and maturity aureoles in the vicinity of intrusions and subtrappean sedimentary complexes is considered. The GALO system and some modifications of its programs make it possible to consider the formation of these aureoles in time and to establish a link between the duration of formation of the trap complex and the size of their maturity aureole. Chapter 6 of Part II is devoted to the study of thermal effect of numerous dolerite intrusions of the Lower Triassic age presented widely in sedimentary basins of the East Siberia platform. The modeling of thermal regime and maturation history of sedimentary basin of the Siberian Platform is conducted on the examples of two sedimentary sections: the Kuyumba-12 well in the Kamo swell containing six sills in sedimentary section and the Kiramkinskaya-1 well of the Kureika Basin with eight intrusive bodies of the Lower Triassic age in sedimentary cover. The modeling in the framework of a model of instantaneous intrusions demonstrates that the thermal influence of the intrusive complex on the maturation history of the basin rocks can be both significant and negligible depending on the size of the intrusion and the distance of the host rocks to the surface of the intrusive body. In Chap. 7, it is shown that a size of maturity aureoles of the single intrusions and trap complex decreases considerably with increase of duration of formation of these complexes. The modeling demonstrates that a maturation level of organic matter in sedimentary rocks under trap and within the host rocks of single intrusions can be rather moderate if the time

span of formation of these structures was enough long. Comparison of computed and measured values of vitrinite reflectance within the thermal aureole of some well-dated intrusions shows that traditional calculations in the frame of the model of instantaneous intrusion considerably over-estimate temperatures and maturation of organic matter in the host rocks. In Chap. 8, the modified GALO program package for basin modeling is used to calculate the temperature and vitrinite reflectance distributions with depth at any time before, during and after the Deccan Trap formation. We consider five specific profiles crossing the Saurashtra and Kutch regions in northwestern India, central part of the Deccan Plateau and western passive margin of India near the Mumbai offshore. The modeling demonstrates that the maturity level *of organic matter in the rocks at the distance of* 100–200 m below the base of the trap complex can be rather moderate *even for the traps of thickness 1 km or more*, if the trap was formed over fairly a long time.

The last part of the book deals with the application of the GALO system for basin modeling and some its modifications to paleoclimatic studies in sedimentary basins, namely, to the formation of temperature and heat flow distributions with depth during sharp fluctuations of climate in the Quaternary with the repeated formation and degradation of permafrost zones in sedimentary rocks. Chapter 9 shows that the GALO system has a distinct advantage in application to such problems compared to the one- or two-layer models in the literature. It is associated primarily with possibility to take into account the changes in the composition and moisture of sedimentary rocks with depth that has significant effect on formation and degradation of permafrost zones. In Chap. 10, the algorithms considered in previous chapter are examined on a number of actual sedimentary sections of the Eastern Barents Sea, West Siberian basins, the Kuyumbinskaya area of the Siberian Platform, and the northeastern shelf of Sakhalin.

In general, the modeling examples presented in three parts of the book confirm an expedience of using of the GALO system for basin modeling in the analysis of some nonstandard problems in geology of the oil- and gas-bearing provinces discussed in the book.

I hope that this book will be useful for students and professionals interested in numerical modeling of thermal evolution of sedimentary basins, for the petroleum geologists involved in the oil and gas exploration in the trap provinces of the world and for students and geologists dealing with thermal field of sedimentary blanket in the permafrost and degraded permafrost areas.

Yurii Galushkin

Part I
Isostatic Control of Basin Subsidence in Response to Extension and Thermal Activation of the Lithosphere

Chapter 1
Amplitude and Duration of Thermal and Tectonic Activation of Basins—An Assessment in the GALO System

Abstract This chapter considers the problem of reflection of tectonic and thermal history of the basin lithosphere in variations in the basin tectonic subsidence. The GALO system provides an ability to calculate the amplitude of the basin tectonic subsidence in two ways: standard—by removal of the water and sediment load from the basement surface, and other nonstandard—by computing variations in density distribution of the basement rocks with depth and time. Comparison between the amplitudes calculated by the above two methods gives a possibility to estimate the amplitude and duration of the thermal and stretching events in the basin lithosphere. The method is applied in next chapters to the basins with different amplitudes of lithosphere stretching including both continental rift basins and basins of continental passive margins. In last section, the relationship between isostasy of the basin and the strength of its lithosphere is discussed.

Keywords Tectonic subsidence · Lithosphere extension · Thermal activation · Basin modeling · Lithosphere rheology

1.1 The Principles of the Numerical Reconstruction of the Thermal History of the Basin

The principles and algorithms of reconstructing the thermal history of the basin are described in detail in paper [1]. That is why only the key points of the modeling and some problems that were not addressed in [1] will be discussed in this section.

1.1.1 Equation and Physical Attributes of Sedimentary Rocks

The input parameters for the model include the present-day sedimentary cross-section, estimations of the amplitude and rate of erosion, lithological composition and

Y. Galushkin, *Non-standard Problems in Basin Modelling*,
DOI 10.1007/978-3-319-33882-8_1

petrophysical characteristics of rocks, structure of the lithosphere (basement) and its rock parameters, paleotemperature markers (vitrinite reflectance), paleoclimate, sea paleodepths, present-day surface heat flow, measurements of rock temperatures and vitrinite reflectance and information on paleo- and present-day tectonic setting of basin development. The temperature distribution in the rocks is obtained by solving the one-dimensional (plane) non-steady heat transfer equation [2]:

$$\frac{\partial[C_V(Z,t)\cdot T(Z,t)]}{\partial t}+\frac{\partial[C_{VW}(Z,t)\cdot V(Z,t)\cdot T(Z,t)]}{\partial Z} = \frac{\partial[K(Z,t)\cdot\frac{\partial T(Z,t)}{\partial Z}]}{\partial Z}+A(Z,t) \tag{1.1}$$

here T temperature, K heat conductivity, Cv = ρCp and Cp are heat capacity per volume and mass units, ρ density, A heat generation per volume unit, Z depth and t time. Equation (1.1) is solved in the frame related with the basement and the domain in which the temperature distribution is found increases during sedimentation and decreases during erosion. Therefore, the convection member in this equation is associated only with the vertical movement of groundwater, but not with the movement of the sedimentary rocks. If the rate of groundwater is small or information about these rates is limited, we do not consider convective term in the Eq. (1.1). Thus, the modeling simulates a formation of sedimentary section in nature when the domain of temperature calculation is accreted from above by thin layer, dz, of unconsolidated sediment deposited during time interval dt during sedimentation or decreased by dz during erosion. The thicknesses of each elementary sedimentary layer dz_k under upper layer dz decrease due the compaction caused by load of dz according to the porosity-depth relationship [1, 3]. The grid points within the computation domain then move to new positions, which are determined by the deposition of layer dz, as well as by subsequent compaction of the column. Temperatures, obtained in the previous time step, are assigned to these moved grid points. The first grid point (n = 1) has the temperature determined by paleo-climate conditions at the basin surface during time interval dt. The temperature distribution, obtained in this way, is the one used to solve the Eq. (1.1) in the next time-step.

The thermophysical parameters of sedimentary rocks in Eq. (1.1) are functions of porosity and temperature. Density (ρ), volume heat capacity (Cv), thermal conductivity (K), and heat generation (A) are specified by the values for the mineral matrix (ρ_m, Cvm, Km, Am) and for water (ρw, Cvw, Kw) and by rock porosity φ [1, 4–8]. The thermal conductivity of the mineral matrix decreases with temperature increase and the water heat conductivity also depends on temperature [1, 7]. The world-average values of Km, Cvm, ρ_m, Am and Al (temperature coefficient in matrix heat conductivity) as well as values of the porosity parameters φ and B in expression $\varphi(z) = \varphi o \cdot exp(-z/B)$ for the main lithological units are taken from the papers [4–10] and shown in [1]. These parameters are used to compute

corresponding petrophysical coefficients for arbitrary mixture of the rocks [1, 7]. The calculations show that the thermal conductivity of sedimentary rocks can increase by a factor of 2–2.5 during their burial history.

1.1.2 The Basement of the Basin

In our modeling the domain for temperature calculation includes in addition to sedimentary blanket the basement to a depth of 100–200 km.

In most variants of modeling, the basement of the sedimentary basin during initial stage of its evolution is presented by continental lithosphere, the parameters of which differ slightly for different basins. Table 1.1 presents an example of such a standard model of the continental lithosphere, often used in modeling. A contribution of consolidated continental crust to surface heat flow is about 15–25 mW/m^2 resulting from radioactive decay mainly in the crust [11]. Heat conductivity and heat capacity of the mantle rocks in our modeling depend on temperature and are computed with consideration of recent studies of these parameters in the papers [12, 13]. The theoretical and experimental estimates of the thermal conductivity of the mantle rocks in [12] shown that the contribution of photon conductivity (radiation component of thermal conductivity) to this value increases with the temperature much slower than it was assumed in the previous studies [14]. The results of [12, 13] suggested a simple formula to describe the temperature dependence of thermal conductivity of the mantle rocks:

$$k_H(T) = \frac{b}{1 + c \cdot T} + \sum_0^3 d_m \cdot (T + 273)^m \tag{1.2}$$

that was used in our modeling. This formula closely fits the empirical data on thermal conductivity of the mantle if the thermal conductivity is expressed in W/m K and temperature T in °C; $b = 5.3, c = 0.0015, d_0 = 1.753 \times 10^{-2}, d_1 = -1.0365 \times 10^{-4}$, $d_2 = 2.245 \times 10^{-7}$, and $d_3 = -3.4071 \times 10^{-11}$. The new formula for calculating the

Table 1.1 Structure of the continental lithosphere and thermophysical parameters of the rocks [11]

Layer	Granitic		"Basaltic"	Mantle
Depth of the layer base	5.0	15.0	35.0	>35
Density (kg/m^3)	2750	2750	2900	3300
Heat conductivity (W/m °K)	2.72	2.72	1.88	K = f(T)*
Radiogenic heat production ($\mu W/m^3$)	1.26	0.71	0.21	0.0042

Remark Dependence heat conductivity K on temperature T in the mantle (function K = f(T) is determined according to [12, 13])

thermal capacity of the mantle rocks as a function of temperature, which is used in our modeling system, is based on the data in papers [12, 13]:

$$\begin{aligned} Cp &= 235.25 - 1825.0/sqrt(T^{\circ}K) - 24.53 \times 10^7/T^3\ (\mathrm{J/mol}^{\circ}\mathrm{K}) \\ &= 1618.27 - 12538.9/SQRT(T^{\circ}K) - 173.7 \times 10^7/T\ (^{\circ}\mathrm{K})^3 (\mathrm{J/kg}^{\circ}\mathrm{K}) \end{aligned} \tag{1.3}$$

This formula predicts Cp to grow approximately by a factor of 1.6 with the temperature increasing from 25 to 1300 °C, which agrees with the experimental data for an olivine mantle composed of 89 % forsterite and 11 % fayalite [15–17].

1.1.3 The Base of the Lithosphere and Latent Heat Effect

The thickness of the lithosphere is an important parameter of sedimentary basin. It determines his rheological behavior and is significant in the analysis of the tectonic history of the basin. In this section, we will focus on the definition of this concept. In geophysical literature, prevails the thermal definition of the thickness, when the base of the lithosphere (or roof of the asthenosphere) is determined by the intersection of the current temperature distribution in the lithosphere T(z, t) with the temperature curve Ts(z) of start of melting of the mantle rock, called the solidus curve. It is known that this definition is ambiguous because solidus of the mantle rock depends strongly on the volatile content in the rock (see below). In the general case, solidus temperature T_s changes with depth in the mantle. So, for peridotite with 0.2 % H_2O the solidus as a function of pressure is (line 7 in Fig. 1.1; [18]):

$$\begin{aligned} T_s &= 1.03 + 0.00391 \cdot P \quad (0 \le P \le 12.8) \\ T_s &= 1.236 - 0.0122 \cdot P \quad (12.8 \le P \le 20.16) \\ T_s &= 0.742 + 0.0122 \cdot P \quad (P \le 20.16) \end{aligned} \tag{1.4}$$

here, solidus *Ts* in 1000 °C and pressure *P* in Kbar. The solidus (1.4) is close to the solidus of lerzolite with the volatile content less than 0.5 % H_2O in [19]. The solidus T_s relates to the liquidus T_1 by relationship: $T_l = T_s$ + 450–600 °C for the mantle rocks and $T_l = T_s$ + 75–100 °C for the basalt [20]. The solidus (1.4) is used for determination of the lithosphere thickness in many numerical reconstructions, presented in the book.

These determinations of the lithosphere thickness are often approximate, since the compositions of mantle rocks vary in different basins. For example, experiments show that melting of the mantle rocks with small content of volatiles (dry melting conditions) more typical for oceanic mantle rocks than the wet conditions. This is due to the fact that the solubility of water in basalt at pressure P = 0.3 GPa (≈9.3 km) is almost 2500 times greater than in the olivine, that is, even a small proportion of the melt can significantly dry up the mantle. The study of variations in water content in olivine with depth under Mid-Oceanic Ridges (MOR) shows that

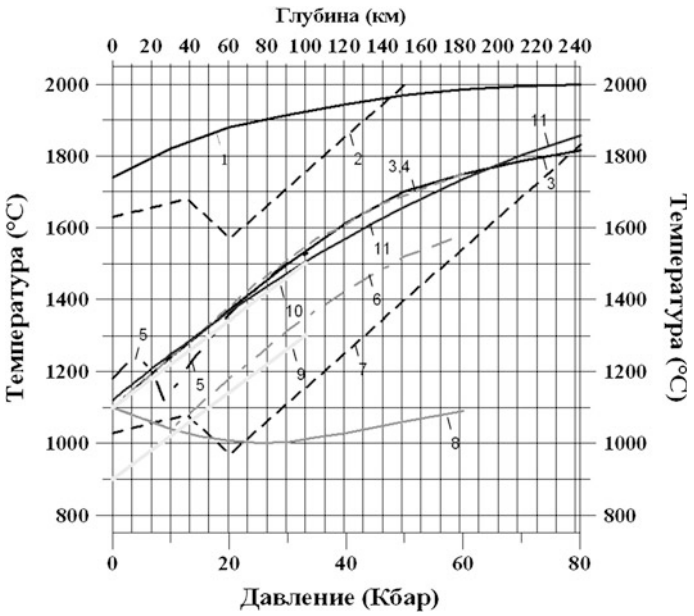

Fig. 1.1 Solidus, Ts, (lines *3–11*) and liquidus, Tl, (lines *1*, *2*) of the mantle rocks of different composition and with different volatile content. *1* and *3* liquidus and solidus of dry garnet peridotite [21]; *2* and *7* liquidus and solidus of peridotite with 0.2 % H_2O (Eq. 1.4 [18]); *4* solidus of dry olivine [22]; *6* solidus of olivine with 810 $H/10^6Si$ = 0.00547 % (wt H_2O)—typical volatile content in the mantle rocks at the depth 90–120 km, generating basalt under axial zones of MOR [23]; *8* solidus of wet olivine [22]; *5* solidus of peridotite in oceanic lithosphere [23]; *9* and *10* solidus of wet and dry peridotite [24]; *11* solidus of normal dry peridotite [25]

the composition of mantle rocks under MOR at the depth from 0 to 60 km is assumed to be similar to dry peridotite, whereas at start of olivine melting (depth of about 120 km) the water content in peridotite can be equaled to 54.7 ppm H_2O [23]. The diversity of the solidus and liquidus of the mantle rocks that are considered in the literature is presented in Fig. 1.1. This figure shows the closeness of all curves of solidus for dry mantle rocks (lines 3, 4, 10 and 11) and significant dependence of solidus curves on volatile content in the rocks (compare lines 4, 6 with 8 and 9 with 10). In the region with higher content of volatiles, solidus is considerably lower (for example, the Saharan Basins [1]) and the use of a solidus curve 7 on Fig. 1.1 here is justified. Such situation is typical for many other regions of continental rifting. For normal dry peridotite, Hirschmann [25] suggests to use in determination of the base of the continental lithosphere at pressures $0 < P < 10$ GPa ($0 < z < 330$ km) the solidus:

$$Ts(P) = 1120.661 + 132.899P - 5.104\,P^2 \tag{1.5}$$

here pressure P is in GPa and temperature T is in °C. This curve Ts is close to the solidus of the line 3 in Fig. 1.1 for garnet peridotite [21] and to other lines of dry solidus in Fig. 1.1. The data of experimental studies of melting of the mantle rocks in the oceanic lithosphere favor the solidus of the line 5 in Fig. 1.1 from the paper [21].

Especially important is the fact that the experimental research of the melting of the mantle rocks shows clearly that the percentage of melting of mantle rocks significantly nonlinearly depends on temperature. Even in rocks with a significant water content and at temperatures appreciably greater than Ts, the melt fraction will not exceed 2–3 % until the temperature is reached the dry solidus of the mantle rocks [23]. In whole, extraction and consumption of the melting latent heat must slow down the processes of cooling and heating of the basin lithosphere in the stages of its thermal relaxation or reactivation.

In our modeling, the domain for temperature calculation includes the lithosphere together with the upper asthenosphere, which contains a partly melted peridotite. As shown above, the melt fraction of the mantle material in the asthenosphere at depths of 100–150 km usually does not exceed 2–3 %. Therefore, the contribution of release or consumption of the melting latent heat in the mantle rocks of the asthenosphere into the heat balance must be small in contrast to the situation with intrusions and traps dealt with in part 2 of the book. The thermal contribution of the latent heat is computed in our modeling by the usual enthalpy approach [1–3], when effective rock heat capacity Cp in the first member of the Eq. (1.1) increases within the temperature interval $Ts < T < Tl$:

$$Cp' = Cp + L \times (dX/dT) \tag{1.6}$$

where X is the melt fraction of the mantle rock, L latent heat of fusion, T_s and T_l are solidus and liquidus of the rock. If the melt fraction increases linearly

$$X = (T - T_s)/(Tl - Ts) \quad at \quad Ts < T < Tl \tag{1.7}$$

effective heat capacity is [2]:

$$Cp' = Cp + \frac{L}{Tl - Ts} \tag{1.8}$$

For peridotite, latent heat of fusion $L = (3.8–4.2) \times 10^5$ J/kg, Cp $\approx 1.05 \times 10^3$ J/kg °K, $Tl - Ts \approx$ 450–600 °C [20]. Therefore, Cp' can exceed Cp almost twice within the temperature interval $Ts < T < Tl$ and even more for the basalt, for which $Tl - Ts \approx$ 75–100 °C. However, as noted above, the thermal effect for peridotite is decrease considerable due to low degree of melting.

1.1.4 Boundary and Initial Conditions

The upper boundary condition for solution of Eq. (1.1) corresponds to the temperature at the basin surface ($z = 0$) at given time, t. This value, specified as the mean-annual temperature, is derived from paleoclimate data. The second boundary condition for the Eq. (1.1) corresponds in our modeling to steady temperature TM maintained during the whole time of the basin evolution at lower boundary of the domain, ZM. The depth ZM is specified at the initial modelling stage by the intersection of the geotherm $Tmin(z)$ with the solidus curve for peridotite $Ts(z)$ [1, 3]. In turn, the temperature distribution $Tmin(z)$ is computed as the steady-state geotherm in the initial basement corresponding to lowest value of surface heat flow $Q = Q_{min}$ in the basin history. The calculation is carried out using the solution of the stationary version of Eq. (1.1):

$$T(Z,Q) = To + \int_0^Z \left[\frac{Q - \int_0^{Z'} A(Z'') \cdot dZ''}{K(Z')}\right] \cdot dZ' \tag{1.9}$$

here, Q is the heat flow through the basin surface, To is the temperature on the basin surface in the considered stage of the basin evolution, $K(Z)$ is the thermal conductivity of the basement rocks, $A(Z)$ is the heat generation per unit volume in these rocks and Z-depth. It is sometimes useful to use a variant of the solution (1.9) for layered-homogeneous medium similar to Table 1.1, when $A(z) = A_i$, $K(z) = K_i$ within the i-th layer $z_{i-1} \le z \le z_i$ [20]:

$$\begin{aligned} T(z) &= T_{i-1} + \tfrac{1}{K_1} \cdot \left[Q_{i-1} \cdot (z - z_{i-1}) - \tfrac{A_i \cdot (z - z_{i-1})^2}{2}\right] \\ Q(z) &= K_i \cdot \tfrac{dT}{dz} = Q_{i-1} - A_i \cdot (z - z_{i-1}) \end{aligned} \quad \text{for } z_{i-1} \le z \le z_i \tag{1.10}$$

In Eq. (1.10) $Q_i = Q(z = z_i)$ heat flow in the base of the i-th layer; Q_0 heat flow through the basement surface ($z = z_0$); $i = 1, 2, \ldots, n$; n number of the layers.

As mentioned above, after calculation of $Tmin(z)$, the depth ZM is determined by the intersection of the geotherm $Tmin(z)$ with the solidus curve for peridotite $Ts(z)$. If intersection of $Tmin(z)$ and $Ts(z)$ doesn't occur, then ZM is assumed to be 200 km. The temperature at the lower boundary is specified as $TM = Tmin(ZM)$. For many basins the coldest geotherm $Tmin(Z)$ corresponds to the present state of the basin lithosphere. But this is not always the case. During the basin evolution the depth to the lower boundary ZM can increase from the initial value by the thickness of the sedimentary cover. The steady state temperature, $T = TM$ is maintained at the boundary ZM. For physical reasons, the steady state temperature at the lower boundary of the modeled region is preferred over a fixed steady heat flow [1, 3, 26, 27]. In fact, heat flow through the MOHO or deeper horizons can change more than an order of magnitude during cooling of the lithosphere from initial rift stage, whereas changes in temperature at sufficiently deep levels will be less significant.

The solution of Eq. (1.1) requires one more condition—the initial. The initial temperature profile is determined by solution of steady-state variant of the Eq. (1.1) for surface heat flow *Qo* and surface temperature *To* typical for the early evolution of the basin ($t = 0$). It is assumed in construction of initial temperature distribution that the temperatures at the depth from the base of the lithosphere (*Zlit*) to the low boundary *ZM* increase linearly from the temperature *Tlit* at the base of lithosphere to the temperature *TM* at the lower boundary *ZM*. Initial heat flow, *Qo*, is estimated from the present-day values of surface heat flow in the regions with tectonic setting similar to that expected for the time of the basin initiation. Estimations of the initial heat flow can be adjusted by analysis of variations in tectonic subsidence of the basement (see below).

1.1.5 Numerical Solution of the Equation

Equation (1.1), together with its boundary and initial conditions, are solved by the implicit finite-difference scheme [1, 3, 28]. This scheme closely resembles that of [29] but is modified to include the variable values of the thermophysical parameters and variable steps *dz* and *dt*: For constant thermophysical parameters and absence of convective members in Eq. (1.1), the implicit finite-difference schema is unconditionally stable. But the above parameters depend on porosity, temperature, depth and time. Therefore, in a real situation it is impossible to estimate analytically a stability of the scheme. It can be made only empirically by comparison of solutions obtained for different time and space steps (*dt* and *dz*). The validity of the finite-difference scheme was checked also against the analytical solution for temperature distribution $T(z, t)$ and heat flow $Q(t)$ from [2]. The following variants were considered: (a) a steady-rate deposition of homogeneous sediments on the basement with similar thermal characteristics; (b) an erosion of a homogeneous half-space; (c) a cooling of the half-space with homogeneous initial temperature $T = Ts$; (d) a temperature distribution within homogeneous half-space with periodically variable surface temperature. In addition a comparison of our numerical results with temperature and heat flow data computed by semi-analytical methods was carried out for homogeneous sediments deposited on homogeneous basement with thermophysical characteristics different from those of the sedimentary cover rocks [1]. In all the considered variants, an appropriate choice of *dz* and *dt* steps has allowed us to achieve a coincidence of computed and analytical temperature distributions and surface heat flows with an accuracy up to 0.1 %. The analysis has shown that a special care is necessary in erosion estimations to avoid too great steps in *dz* and *dt* [1, 3, 27]. The correct numerical simulation of natural sedimentation and erosion processes requires sufficient small the time- and space-steps. In our calculations the total number of time steps range from 1000 to 4000. Space steps, dz_k, change linearly within each lithological unit and as a continual peace-linear function

of depth for the whole column, including the sedimentary cover and the basement. The steps can change from 1 to 4 m at the surface of computing domain up to 1–3 km at the bottom of the basement, at depth z = 100–200 km.

1.2 Tectonic Subsidence in Burial History of Sedimentary Basin—Algorithm of Calculation

As it is known, the tectonic subsidence of the basin referred to that part of the basement surface subsidence, which remains after removing from this surface the load of water and sediments [30, 31]. This assumes local isostatic response of the lithosphere to the load. As noted above, the GALO system for basin modeling considers heat transfer in the domain included sedimentary cover of the basin, the underlying lithosphere and the asthenosphere up to the depths of 100–200 km. The great depth of the lower boundary of the domain takes an opportunity to use calculated variations in the basin tectonic subsidence for an assessment of duration and amplitude of tectonic and thermal events in the basin lithosphere. For this purpose in the GALO system, the tectonic subsidence of the basin are calculated by two methods [1, 27, 32].

1.2.1 The First Method of Tectonic Subsidence Calculation

The first method calculates the response of the lithosphere to the removal of the water and sediments load on the basement surface (the common back-stripping procedure). Equality of the weight of AA-column to the weight of A1A1-column on Fig. 1.2 leads to an expression for tectonic subsidence *ZTs* determined as the position of the basement surface after removing the water and sediment load:

$$ZTs(t) - ZTs(0) = \frac{\rho_a - \rho_s}{\rho_a} \cdot S(t) + \frac{\rho_a - \rho_w}{\rho_a} \cdot [Z_w(t) - Z_w(0)] \tag{1.11}$$

In Eq. (1.11), t is time, $t = 0$ is the time of the basin initiation, $Zw(t)$ is the paleodepth of water column at the time t, $ZTs(t)$ is the tectonic subsidence amplitude, $S(t)$ is the total thickness of sedimentary cover ($S(0) = 0$), ρ_a and ρ_w are the asthenosphere and water densities, $\rho_s(t)$ is the average density in the sedimentary column:

$$\rho_s(t) = \frac{\int_0^{S(t)} \rho_s(z,t) \cdot dz}{S(t)} \tag{1.12}$$

The porosity $\phi(z, t)$ and density $\rho_s(z, t) = \rho_m(z, t) \cdot [1 - \phi(z, t)] + \rho_w \cdot \phi(z, t)]$ of the rocks within the sedimentary column and the weight of the column are

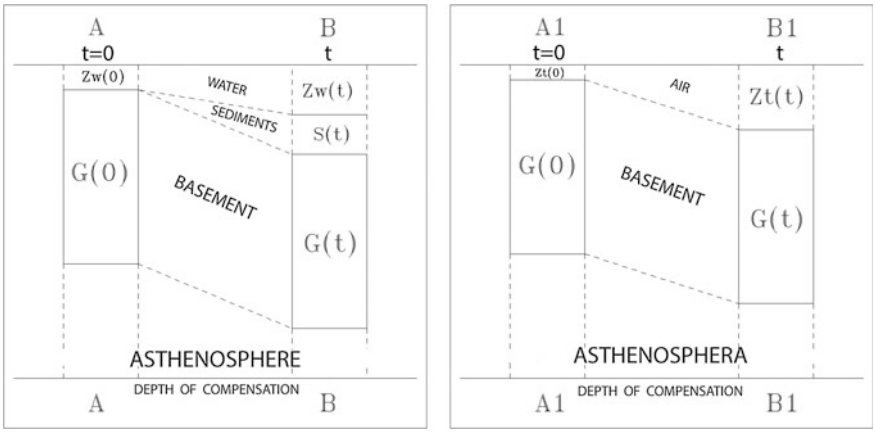

Fig. 1.2 Variations of tectonic subsidence of the basement during the basin evolution (general scheme; [1, 27, 32])

calculated in order to determine the mean density $\rho_s(t)$ according to (1.12) at each time step of the basin evolution. Matrix density ρ_m is determined by lithological composition of sedimentary rock and its temperature and therefore depends on the depth z and time t. Thus, the tectonic subsidence of the basin is controlled by the changes in the mass (weight) of the sedimentary column and by the variations in the paleo-depth of the sea relative to the corresponding values at the time of basin nucleation ($t = 0$).

Interestingly, fluctuations in the global sea level (eustatic sea level changes) are not included in Eq. (1.11) in an explicit form, i.e. as a separate member. These fluctuations are involved implicitly in variations in the sea paleodepth $[Z_w(t) - Z_w(0)]$, where $t = 0$ is the time of the basin initiation. Although some of tectonic studies of passive margins consider the eustatic sea level changes separately [30, 31], we prefer to use the form (1.11). The main reason is the large uncertainty in the estimates of the amplitudes of eustatic changes. Believe that these fluctuations could be caused by widespread melting of glaciers, global changes in location of Mid Oceanic Ridges, draining or filling large water basins due to regional or local movements of the slabs [33]. The Vail's curve of the eustatic sea level changes [34] suggests that the level of global ocean in the Cretaceous exceeds the modern one by 350 m. This curve has been criticized in several works [35–38]. Estimation the global sea level by three different eustatic curves taken in the literature, results in difference in the level of 100–250 m [37]. Application of the eustatic curves [34, 38] to sedimentary basins of the continental margin of South Australia [39] obscure the effect of tectonic events on formation of the sedimentary layers. Artyushkov et al. [40–42] shown that a great part of fast changes in paleo-sea depth in continental basins which were explained early by eustatic changes can be caused by relatively fast vertical tectonic movements with amplitude 20–100 m. As a result, we use Eq. (3.11) and do not consider the member with changes of eustatic sea level separately.

1.2.2 Calculation of Tectonic Subsidence by Second Method

In the second method, the tectonic subsidence of the basin is derived from the time variations in the depth distribution of the density of the basement rocks [1, 3, 26, 27, 32]. The equality of the weight of A1A1-column to the weight of B1B1-column on Fig. 1.1 leads to other expression for tectonic subsidence, *ZTb* [1, 3, 27]:

$$ZT_b(t) - ZT_b(0) = \frac{G(t) - G(0)}{\rho_a \cdot g}. \tag{1.13}$$

Here g is the gravity acceleration, G is the weight of the basement column of fixed high *lo* (Fig. 1.1):

$$G(t) = g \cdot \int_0^{lo} \rho_l(z,t) \cdot dz \tag{1.14}$$

The weight G is calculated at every time step. The rock density $\rho_l(Z, t)$ in the lithosphere underlying sedimentary blanket is a function of temperature $T(z, t)$ and pressure $P(z, t)$:

$$\rho_l(z,t) = \rho_0(z,t) \cdot [1 - \alpha \cdot T(z,t) + \beta \cdot P(z,t)] \tag{1.15}$$

where $\alpha = 3.2 \times 10^{-5}$ °C^{-1} is the thermal expansion coefficient, $\beta = 0.00079$ Kbar^{-1} is the isothermal compressibility of the rock, $\rho_o(z, t)$ is the density at the standard conditions (P = 1 atm and T = 20 °C). The Tables 1.2 and 1.3 illustrate a relative contribution of compressibility and thermal expansion to change in the mantle rock density. So, at P = 30 Kbar and T = 1000 °C $\Delta\rho = 0.078–0.106 = -0.028$ г/см^3, whereas at P = 50 Kbar (z = 154 km) and T = 1200 °C $\Delta\rho \approx 0$. Thus, the contribution of temperature to the mantle rock density will dominate at the depth z < 100 km and pressure contribution will dominate at depth z > 200 km. Our modeling take into consideration both effects.

Parameter ρ_0 reflects variations in the density of the basement rocks due to the changes in the rock types with depth (the transitions from granite to "basaltic" rocks

Table 1.2 Increase in density and variations in isothermal compressibility of the mantle rocks with pressure and depth [43]

P (Kbar)	1	10	20	30	40	50	60	70	80
Z (km)	3.1	31	62	93	124	154	185	216	247
β (Kbar^{-1})	7.9×10^{-4}	7.9×10^{-4}	7.8×10^{-4}	7.7×10^{-4}	7.6×10^{-4}	–	–	–	–
Δρ (g/cm^3)	0.0026	0.026	0.052	0.078	0.104	0.130	0.156	0.182	0.208

Remarks calculation of Δρ was carried out for steady temperature T = 20 °C and steady value of isothermal compressibility $\beta = \frac{1}{\rho_0} \cdot \frac{\partial \rho}{\partial P} = 0.00079$ Kbar^{-1}—typical value for olivine in the mantle; computations of depth (Z) assume steady pressure gradient dP/dz = 0.32 Kbar/km

Table 1.3 Decrease of the mantle rock density with temperature [43]

T (°C)	200	400	600	800	1000	1200	1400
$\Delta\rho$ (g/cm^3)	−0.021	−0.042	−0.063	−0.094	−0.106	−0.127	−0.148

Remarks calculation of $\Delta\rho$ was carried out for steady pressure P = 1 atm. and for the value of the thermal expansion coefficient $\alpha = \frac{1}{\rho_0} \cdot \frac{\partial \rho}{\partial T} = 3.2 \times 10^{-5}$ °C^{-1}—typical value for olivine in the mantle

in the crust, from the crust to the mantle, phase transitions in the mantle) and density redistribution with depth due to the extension of the basement [1, 3, 26, 27, 32]. The change in the depth of the spinel peridotite (ρ_0 = 3.30 g/cm^3) to the garnet_peridotite (ρ_0 = 3.38 g/cm^3) phase transition is described by expression [44, 45]:

$$\mathrm{P(Kbar)} = 0.000025 \cdot [\mathrm{T(^{\circ}C)} - 900]^2 + 15. \tag{1.16}$$

According to (1.16), this phase transition occurs at the depth from 24 to 70 km and can result in additional tectonic subsidence of the basement with an amplitude of a few hundreds of meters. The depth of the other phase transition (plagioclase peridotite (ρ_0 = 3.26 g/cm^3) to spinel peridotite (ρ_0 = 3.30 g/cm^3)) varies according to another law [45]:

$$\mathrm{P(Kbar)} = 0.00515 \cdot \mathrm{T(^{\circ}C)} + 3.92 \tag{1.17}$$

This transition occurs at more shallow depth from 12 to 32 km that often is within the continental crust. That is why this phase transition often does not contribute to tectonic subsidence of the basin under consideration [45, 46]. In the basins developed on the oceanic crust both phase transitions can contribute to the basin tectonic subsidence and this contribution can reach 800 m.

The bases of the AA, BB, A1A1, B1B1 columns on Fig. 1.1 locate at the isostasy depth (compensation depth in Fig. 1.1), *Zi*. In our model, this depth coincides with the lower boundary of the domain for temperature computation, *ZM*, which was determined above. The great depth of *ZM* and high rock temperatures assume rheologically weak rocks at this depth. Then, any small stress difference must be relaxed here and restore nearly steady pressure at the depth $z \approx Zi$. In the frame of the local isostatic approach, the Eqs. (1.11) and (1.13) describe the main processes, which can contribute to changes in amplitude of the tectonic subsidence. Then, the tectonic curve (1.11), computed by removing of the water and the sediment load from the basement surface and presented usually by solid line in the plot of tectonic subsidence, must coincide with the subsidence (1.13). The latter is determined by variations in density of the basement rocks with temperature and pressure. In the plot of the tectonic subsidence, it is presented usually by dashed line (line 3 in Fig. 1.3c). In next section, we will show how the comparison of these two curves of tectonic subsidence helps to assess the amplitude and duration of tectonic and thermal events in the basin lithosphere.

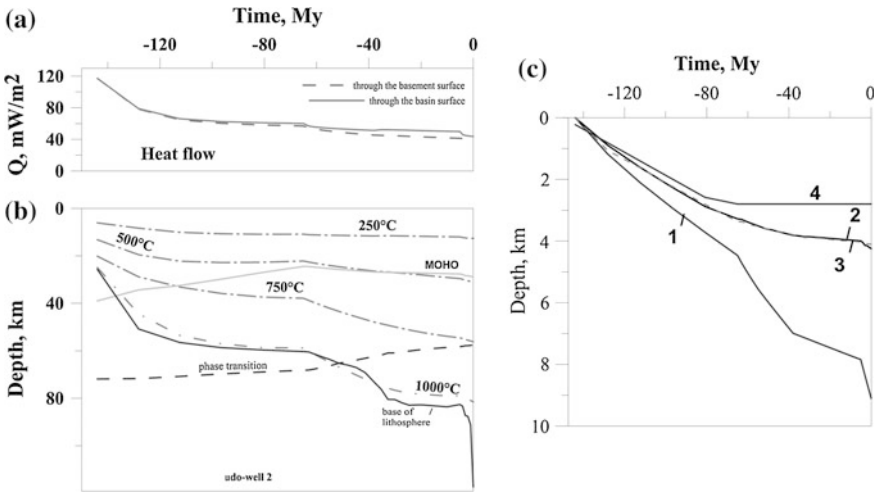

Fig. 1.3 Heat flow (**a**), thermal history of the lithosphere (**b**) and tectonic subsidence of the basin (**c**) in the burial history of deep shelf of the Krishna-Godavari Basins (location of reconstructed pseudo-well 2 and geological history of the region are discussed in the next chapter). (**a**) The heat flows through the sediment (*1*) and basement (*2*) surfaces; difference between the flows is mainly due to radiogenic heat generation in sediments. (**b**) *Long dashed* lines are isotherms. *The "moho"-line* is the base of the crust. *The "phase transition" line* is the location of the "spinel peridotite—garnet peridotite" compositional transition in the mantle (1.16). (**c**) Tectonic subsidence of the basement surface calculated in the local isostasy approach. *1* depth of the base of sedimentary cover (or the depth of the basement surface) computed by usual "backstripping" procedure; *2* (*upper solid line*) tectonic subsidence of the basin calculated by removing the sediment and water load from the basement surface (1.11); *3* (*upper dashed line*) tectonic subsidence calculated by consideration of time-variations in density profile in the basement (1.13); *4* paleo-sea depth

1.3 Numerical Simulation of Thermal Activation and Stretching of the Basin Lithosphere in the GALO System

Analysis of variations in amplitudes of the basin tectonic subsidence was first used to study the formation history and development of sedimentary basins of the North sea and some passive margins of the North Atlantic [30, 31, 47, 48]. It was used to study the basins with relatively simple tectonic history. These are the basins, the lithosphere which had cooled from hot initial rift stage to the modern cold state. In consequence, an analysis of the curves of tectonic subsidence was used repeatedly to prove a simple tectonic history of sedimentary basins in the passive margins of Australia, Africa, the basins of the North Sea and the South Caspian Sea and other areas [30, 31, 38, 47, 48]. However, numerous studies show that the evolution of most sedimentary basins is not described by a simple cooling of the lithosphere from its initial hot rift stage.

The deviations relate to the duration and repeatability of the rift stage of basin development. This stage is not instantaneous, as it should be in [30, 31, 47, 48], and it may be quite long. Changes in the stress fields of the region can disrupt the rifting in the beginning. But if the stretching of the lithosphere continues, the lithosphere rupture can be achieved as during 10 million years or faster (back-arc rifting in the Tyrrhenian and the Aegean sea, Panonian Basin, etc.) as during 20–70 million years, which is typical of most continental rifts [49, 50]. Another difference from the McKenzie model is the possibility of the recurrence of stretching periods. Indeed, the analysis of tectonic subsidence curves for about 2000 profiles in different sedimentary basins of the world showed that in the history of many basins the stages of the lithosphere stretching could be repeated not once (the East-Barents Sea Basin, the basins in the North Norwegian shelf and in the North sea, etc.; [51]). In such basins, the first tension event associated with the initial rifting, after the 40–100 million years could be followed by the additional lithosphere stretching (or erosion from the crust bottom) with moderate amplitudes 1.03–1.2 [50–52]. There are the basins in which the rifting was an intermediate stage of their development [53]. Then the rift grabens are superimposed on the sedimentary deposits of previous stages and buried under the sediments of the subsequent formations (the Upper Cretaceous—Miocene Graben of the Sirte Libyan Basin, the Jurassic-Lower Cretaceous depositions in the Central Viking Graben in the North Sea Basin, etc.; [51, 52]).

Consequently, the stages of stretching and thermal activation of the lithosphere could be repeated in the history of sedimentary basins and these events cannot be described within a simple model of the cooling of the lithosphere. We apply the analysis of the variation in the tectonic subsidence for the reconstruction of tectonic and thermal history of these basins. In particular we use this analysis to assess the amplitude and duration of periods of thermal and tectonic re-activation of the basin lithosphere. These estimates are based on calculating the variations of the amplitude of the basin tectonic subsidence by alternative methods described in Sect. 1.2.

In isostatic approach, cooling of the lithosphere leading to increase density of the mantle rock and its stretching with decrease of the crust thickness explain the subsidence of the basement surface. Another isostatic mechanism, explaining basement subsidence can be related to the phase transitions considered above including the compositional change of light basalt to heavy eclogue [40–42]. At the same time, thermal activation decreasing density of the lithosphere rock results in rising of the basement surface. The high relief near the Red Sea is the example of such thermal activation of the lithosphere near to rift, whereas the Afar region is the example of simultaneous action of stretching and thermal activation of the basement. Of course, in dynamically active regions (young mountain belts, accretion prisms) the basement sinking and rising can result from collision of the plate margins (the South-Caspian basin, the Alpine-Himalayan mountain belt). All these regions are essentially nonisostatic and are characterized by free air gravity anomalies exceeding 100 mgal. In such areas the dynamic correction to tectonic subsidence must be introduced.

Therefore in the case of a locally isostatic response of the lithosphere to the external (water and sedimentary cover) and internal (variations in the density distribution in the basement column) loads, the curves of tectonic subsidence calculated by the two methods (Sect. 1.2) and presented for example in Fig. 1.3c by solid (2) and dashed (3) lines should coincide. In other words, the tectonic curve, shown by the dashed line and controlled by the thermal and tectonic events in the underlying basement, should reproduce the observed variations in the tectonic subsidence shown by solid line and obtained from the curve of actual subsidence of the basin by the back-stripping procedure. The events of thermal activation or extension change distribution of density across the basement column and, as a result, modulate the depth of the dashed line of tectonic subsidence. Then, the time, amplitude, and duration of these events are selected to ensure the coincidence of the dashed and solid lines, provided the selected parameters described the proposed events in the basement are consistent with the geological and geophysical data on the structure and evolution of the region.

In the modeling, the thermal activation of the basin lithosphere are numerically reproduced by gradual uplift of the isotherm 1100 °C which in our model is associated with a thermal diapir roof. The time, depth and rate of the uplift of the isotherm are selected to ensure the minimum deviation of the dashed curve of tectonic subsidence from the observed variations in tectonic dip presented by solid line (see for example lines 2 and 3 in Fig. 1.3). The temperature distribution with depth in the interval 1100 °C $\leq T \leq TM$ is rewritten at each time step of the thermal activation on the temperature increasing linearly from $T = 1100$ °C at the roof of diaper to TM at the domain base ZM. The temperature gradient within the diapir (1100 °C < T < TM) is comparative with the adiabatic gradient in the mantle (0.5 °C per km [20]). For example, an analysis of tectonic subsidence of the Krishna-Godavari Basin in the region of pseudo-well 2 (see Chap. 2) suggests a very slow uplift of the 1100 °C isotherm (the top of the diapir) by about 260 m during 35 Ma. This slow uplift prevent cooling of the lithosphere in the time from 40 to 5 My, maintaining the depth of the basement surface at the same level (Fig. 1.3c). Then, the thermal activation accounts for the relatively slow subsidence of the basin in the Eocene—Miocene (Fig. 3.1c).

The lithospheric extension with the resultant (cumulative) amplitude β is numerically reproduced in the GALO modeling system by a series of n small successive intervals of adiabatic extension of the basement with amplitude $\Delta\beta i$. Therefore, the total amplitude of the extension is determined as the product of the small amplitudes $\Delta\beta i$: $\beta = \Delta\beta_1\Delta\beta_2 \ldots \Delta\beta i \ldots \Delta\beta n$. If the extension amplitude is 1.2 or lesser and the duration of the events ranged from a few to 20 Ma, the rate of the lithosphere extension is rather low ($V < 0.06$/year). Then, the result of the extension will be observable in the changes of the Moho depth and it will be almost invisible in the depths of the isotherm. Such low rates of deformation do not leave any noticeable footprints in the morphology of the basin surface. The listric faults expected in the models of continental rifting imply an almost instantaneous extension with amplitude $\beta = 1.8$–2 and higher. The estimates of the time, duration, and amplitude of the extension and thermal activation events in the basin lithosphere are

carried out successively, starting from the time of basin nucleation. The intervals of extension suggested by analysis of the tectonic subsidence of the basin explain the stages of relatively rapid subsidence of the basin. So, in the example of the Krishna-Godavari Basin in the region of pseudo-well 2 (see Chap. 2) this analysis assumes two periods of the lithosphere extension: the first lasted from 143 to 120 My with extension amplitude $\beta = 1.28$ and the second lasted from 110 to 65 My with greater total extension amplitude $\beta = 1.50$. According to our analysis, the initial period of basin development is characterized by cooling of the lithosphere from the initial rifting stage with surface heat flow about 120 mW/m^2 and moderate amplitude of the lithosphere stretching ($\beta = 1.28$). Stretching of the lithosphere in subsequent 45 My was more intense. It was provided by increase as in sedimentary load as in the depths of the sea (line 4 in Fig. 3.1c). The total amplitude of the lithosphere stretching in this example reached 1.92. As result of such stretching, the thickness of the consolidated crust has decreased from 40 to 21 km, and the depth of the MOHO boundary rose from a depth of 40 to 29 km (Fig. 1.3b). It is believed that the main part of the extension ensured by opening of the Bay of Bengal in the Lower and Upper Cretaceous (see Chap. 2).

1.4 Analysis of the Tectonic Subsidence in Application to Concrete Basin

It should be noted that analysis of tectonic subsidence does not allow to estimate the amplitudes of thermal and tectonic events in the lithosphere exactly. There are always uncertainties associated with errors in determining initial parameters of the modeling that have an impact on the simulation results. In this section, we will consider some of these problems on the example of sedimentary basin with moderate rates of sedimentation, namely the Yasnoe oil field, located in the area of the latitudinal Ob′ region in the West Siberia basin. Table 1.4 presentsthe main stages of the basin development, which include 10 stages of sedimentations, 1 stage of interruption (no sedimentation, no erosion) and 1 stage erosion of amplitude 150 m. The basin has started its development on standard continental lithosphere of Table 1.1 with initial heat flow 80 mW/m^2 (1.9 HFU), that corresponds to thermal conditions in the side of continental rift zone. This flow and type of the lithosphere determined the initial temperature profile in the basin basement (Sect. 1.1.4). The heat flow Qmin was equaled 52 mW/m^2 (1.25 HFU) in the modeling. It is close to the modern heat flow through the basement surface (Fig. 1.4a). Together with solidus (1.4) and basement structure of Table 1.1, this flow determines depth of the lower boundary of the domain for temperature computation, ZM, and temperature TM at this boundary, which in our case are equaled to 77 km and 1170 °C, correspondingly (Fig. 1.4b).

Table 1.4 Main stages of evolution of the West Siberia Basin and lithology of sedimentary layers in the Yasnoe area

N	NN	Z (km)	Time (My)		Lithology				
			t1	t2	shale	alevr.	sandst.	marle.	Corg
1	1	3.075	200	188	0.700	0.150	0.150	0.000	0.000
2	1	2.975	188	176	0.730	0.000	0.110	0.000	0.160
3	1	2.735	176	163	0.760	0.000	0.200	0.000	0.040
4	2	–	163	144	–	–	–	–	–
5	1	2.640	144	136	1.000	0.000	0.000	0.000	0.000
6	1	2.360	136	124.5	0.010	0.000	0.990	0.000	0.000
7	1	2.300	124.5	119	0.830	0.110	0.060	0.000	0.000
8	1	1.760	119	91	0.610	0.040	0.350	0.000	0.000
9	1	0.870	91	65	0.810	0.080	0.000	0.110	0.000
10	1	0.500	65	25	0.910	0.000	0.090	0.000	0.000
11	4	0.150	25	2	–	–	–	–	–
12	1	0.030	2	0	0.500	0.000	0.500	0.000	0.000

Remarks *N* number of stage of the basin evolution; *NN* type of evolution (*1* sedimentation, *2* interruption, *4* erosion); *Z* depth of base of the layer in the present-day section or erosion amplitude (in km); *t1* and *t2* times of initiation and finish of the stage (in My); in columns of "lithology" the relative fractions of every lithological unit in the rock of given layer are shown
Abbreviations: *alevr.* alevrolite; *sandst.* sandstone

Main result of modeling is shown in Fig. 1.5 where the burial, thermal and maturity histories of sedimentary section of the basin are presented. The reconstruction presented in this section are considered only as the model example designed to evaluate the impact of variations in our assumptions and selected parameters on the simulation results. Therefore, we do not consider here the basin history and are not analyzing the simulation results, as will be done in subsequent chapters. In this section, we are limited to analysis of the process simulation and the main factors affecting it.

The Figs. 1.6a–c present the main factors that are used to control the validity of the modeling results along with the modern sedimentary section of the basin. Figures 1.6a, b compare the measured and computed values T and %Ro. The lines 1 and 2 in Fig. 1.6c include an analysis of tectonic subsidence of the basin. This analysis suggests 3 periods of moderate thermal activation of the basin lithosphere and 3 periods of very moderate lithosphere extension (stretching) presented in Tables 1.5 and 1.6.

Figure 1.7a–g illustrate the using of tectonic analysis in the GALO system of basin modeling. These Figures demonstrate the ratio of the curves 1 and 2 in different situations when we include in succession in modeling procedure one by one the stages from Tables 1.5 and 1.6. Curves 1 are the same in all variants of Fig. 1.7, while the dotted curves 2 change from variant to variant. Figure 1.7a shows the ratio curves 1 and 2 of the tectonic basement subsidence for the case when we decline all stages of thermal activation and stretching of the lithosphere of

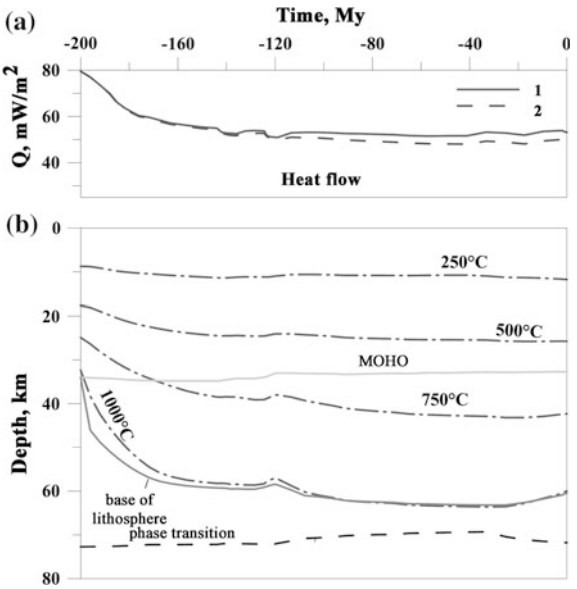

Fig. 1.4 Variations in heat flow (**a**) and thermal state of the lithosphere (**b**) reconstructed numerically in the GALO system for the Yasnoe area of the West Siberia Basin. **a** *1* and *2* the heat flows through the sediment and basement surfaces. **b** *Long dashed* lines are isotherms. *The "MOHO"-line* is the base of the crust. *The "phase transition" line* is the location of "spinel peridotite- garnet peridotite" compositional transition in the mantle (Eq. (1.16)). *Base of the lithosphere* depth of intersection of the current geotherm of the lithosphere with the solidus of peridotite with 0.2 % H_2O (Eq. (1.4))

the basin, presented in Tables 1.5 and 1.6. The dashed line 2 in this figure shows change in the basin tectonic subsidence in the stage of simple cooling of the lithosphere from the initial heat flow 80 mW/m^2 (1.9 HFU). Next Fig. 1.7b reflects the influence of the first thermal activation in Table 1.5 on tectonic curve 2. This activation slows down the cooling of the basin lithosphere in the time from 160 to 144 million years ago and thus explains the absence of subsidence of the tectonic curve 1 at this time. In Fig. 1.7c, action of the first activation from Table 1.6 is added to previous thermal action in Fig. 1.7b. This action is very moderate lithosphere stretching with amplitude 1.03. It help to explain local subsidence of the tectonic curve 1 in the time from 143 to 136 My ago, which cannot be explained by simple cooling of the lithosphere during this period. Figure 1.7d includes an action another local moderate thermal activation (second activation in Table 1.5). This activation explains the absence of subsidence of the tectonic curve 1 in the time-interval $-137 \leq t \leq -124$ My similarly to the first thermal activation in Fig. 1.7b. Next extension of the lithosphere of amplitude 1.06 (second stage in Table 1.6) explains sharp subsidence of the tectonic curve 1 in the time from 125 to 119 My ago (Fig. 1.7e). Figure 1.7f includes period of very slow extension of amplitude 1.045 in the time from 115 to 30 My ago (the third activation in Table 1.6). An influence of

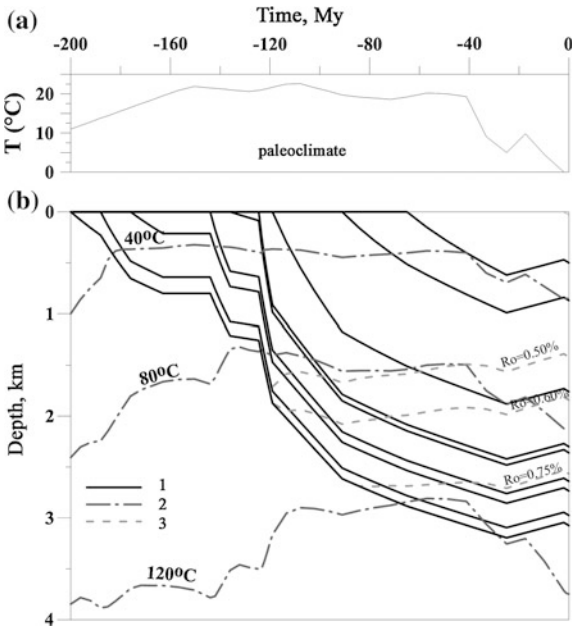

Fig. 1.5 Variations in mean-annual temperature at the basin surface (*upper figures*) and burial, thermal and maturation histories (*lower figures*) of sedimentary sections in the Yasnoe area of the West Siberia Basin. *1* The base of sedimentary layers; *2* isotherms; *3* isolines of vitrinite reflectance (%Ro)

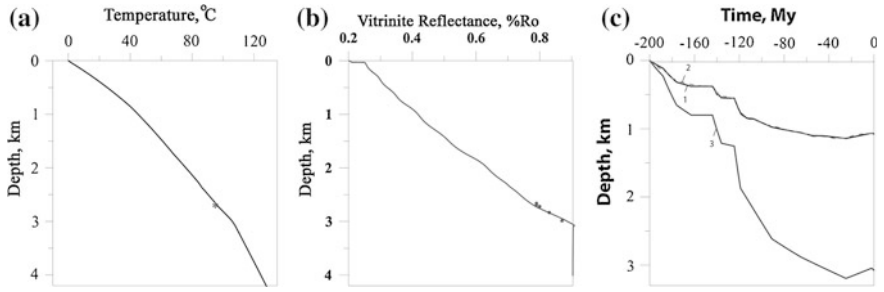

Fig. 1.6 The main controlling factors of the modeling of sedimentary section in the Yasnoe area of the West Siberia Basin. **a** Temperature distribution with depth calculated in present-day section of the basin (*solid line*) and the measured reservoir temperature (*symbol*). **b** Distribution of vitrinite reflectance (%Ro) with depth calculated in present-day section of the basin by the EASY-model (*solid line*) and the measured values of %Ro (*symbols*). **c** Tectonic subsidence of the basement surface calculated in the local isostasy approach. *1* (*upper solid line*) tectonic subsidence of the basin calculated by removing the sediment and water load from the basement surface (1.11); *2* (*upper dashed line*) tectonic subsidence calculated by consideration of time-variations in density profile in the basement (1.13); *3* depth of the base of sedimentary cover (or the depth of the basement surface) computed by usual "backstripping" procedure; the paleo-sea depth was estimated to be equal to zero

Table 1.5 The stages of thermal activation of the basin lithosphere suggested by analysis of variations in tectonic subsidence of the West Siberia Basin in the Yasnoe field

N	T1	T2	T3	Q1	Q2
	Million years			HFU	
1	165	160	144	1.3	1.3
2	137	125	124	1.30	1.30
3	30	25	0.20	1.25	1.30

Comments: N number of stage; $(-T1 \leq t \leq -T2)$—the time-interval during which the equivalent heat flow through the basement surface varies from the current heat flow in the basin lithosphere to Q1; $(-T2 \leq t \leq -T3)$—the time-interval during which the equivalent heat flow through the basement surface varies from Q1 to Q2. Increase of the heat flow from the current value to Q1 and then from Q1 to Q2 is simulated in the program by raising the isotherms of 1100 °C up to certain depths in the basement (see Sect. 1.3); 1 HFU = 41.868 mW/m^2

Table 1.6 The stages of extension of the basin lithosphere suggested by analysis of variations in tectonic subsidence of the West Siberia Basin in the Yasnoe field

N	T1	T2	β
	Million years		
1	143	136	1.030
2	125	119	1.060
3	115	30	1.045

Comments: N number of stage; $(-T1 \leq t \leq -T2)$—the time-interval of homogeneous extension of the basin basement, i.e. homogeneous extension of the depth-domain $ZS \leq z \leq ZM$ (see Sect. 1.3); β extension amplitude

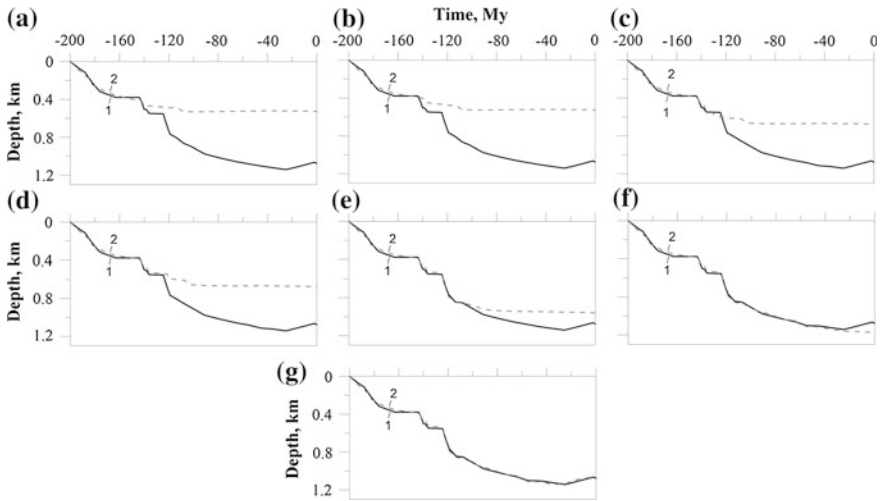

Fig. 1.7 Consistent application of analysis of variations in the basin tectonic subsidence to the definition of the local stages of the lithosphere thermal activation and its stretching in the Yasnoe area of the West Siberian basin (see text)

this extension on tectonic subsidence can be seen by comparison the tectonic curves 2 in Fig. 1.7e, f. Similarly, an action of the last thermal activation in Table 1.5 can be estimated from comparison of the curves 2 in Fig. 1.7f, g. The last activation explains the erosion at the time from 30 to 1.81 My ago which is typical for all northern half of the West Siberian Basin (Chap. 10). Figures 1.6c and 1.7g show the tectonic curve 2 that takes into account the effect of all six activations of the Tables 1.5 and 1.6. Recall that the assumption of local isostatic response of the basin lithosphere to the load was used in the calculation of the curves 1 and 2 in Fig. 1.7.

Figure 1.8 a–c present the main factors of control the validity of the modeling in other variant of basin modeling when minimal heat flow Qmin equaled 46 mW/m^2 (1.10 HFU) and initial heat flow is the same. New value of Qmin corresponds the thicker lithosphere. In this variant, temperature TM about of 1170 °C is maintained at the depth of 97 km. Analysis of the tectonic subsidence of the basin allows to choose the sequence of events of stretching and thermal activation of the lithosphere, which explains the variations in the depth of the tectonic curve 1. The new version of modeling preserves the first stage of lithosphere stretching, whereas amplitude of the stretching in the second stage of Table 1.6 is reduced to 1.04, and the third stage of the stretching is absent. As result, extension amplitude decreases from 1.14 in the first version of the simulation to 1.07 in the second. As for heat activation, the first two periods of Table 1.5 remain unchanged, while the parameters of the third period are replaced by T1 = 100 My, T2 = 25 My, T3 = 0.2 My and Q1 = 1.15 mW/m^2, Q2 = 1.23 mW/m^2. Therefore, the third activation of Table 1.5 in new variant is longer and more moderate than in the old one.

Examples of two variants of the simulation show that the definition of the stages of lithosphere activation with the use of a single analysis of the variations in the basin tectonic subsidence is conditional. Changing the initial parameters of the simulation (for example, the initial heat flow Q_0 and minimal heat flow Q_{min}), we can choose the appropriate sequence of events in the lithosphere that will corresponds to the same tectonic curve. The number of possible variants of the basin model will be considerably narrower, if we take into account measured values of temperature and vitrinite reflectance together with geological and geophysical

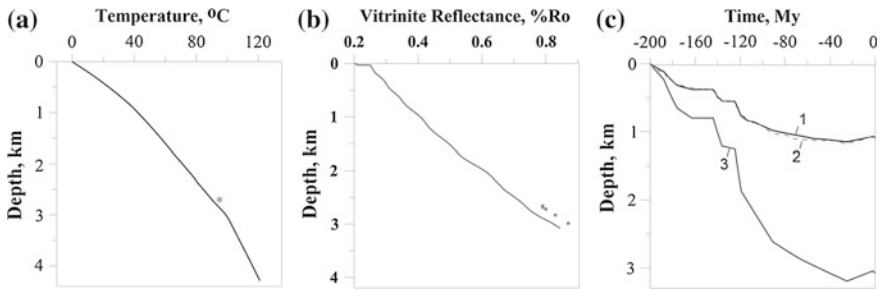

Fig. 1.8 The main controlling factors of the modeling of sedimentary section in the Yasnoe area of the West Siberia Basin in second variant of basin modeling (see text). Legent see in Fig. 1.6

information about the structure and development of the region. So, a comparison of Fig. 1.8a, b with Fig. 1.6a, b show that the first variant of basin modeling is preferred. The influence of possible changes of the temperature TM (the temperature maintained at the base of the domain of temperature computation) during evolution of the basin will be the subject of special studies in the future.

1.5 Isostatic Approach and Yield Strength of the Lithosphere

The analysis of tectonic subsidence, used in our modeling to estimate the duration and the amplitude of the thermal reactivation and stretching events occurring in the history of the basin lithosphere, suggests local isostasy of the considered areas (local-isostasy response of the lithosphere on load). The state of isostasy closely linked to the strength of the lithosphere, whereas the thickness of the lithosphere often means its thermal thickness. In this section, we examine the relationship of these parameters of the lithosphere in the light of the basin isostasy. Thermal thickness of the lithosphere is determined by intersection of the current geotherm of the lithosphere with the solidus of the mantle rock. At the same time, the solidus depends strongly on volatile content in the mantle rock (Fig. 1.1). The thermal thickness of the lithosphere determined by different solidus curves will also differ considerably. The lithosphere thickness in Figs. 1.3b and 1.4b uses solidus of peridotite with 0.2 % H_2O (Eq. (1.4) [18]). But the state of local isostasy is suggests sufficient rheological weakness of the basin lithosphere. It is known that in sedimentary basins this state is reached if the typical horizontal size of the sediment and water load exceeds considerably the thickness of the effective elastic lithosphere (EEL). Therefore, decrease of the thickness of EEL promotes the local isostasy. It was believed early that the lower boundary of EEL is enough deep, coinciding with isotherm of 600–750 °C [20]. Then, in the example shown in Fig. 1.9 for the West Baskirian Basins, the present-day thickness of EEL could amount to 120–150 km [3]. But such determination of the EET is valid partly for the oceanic lithosphere, but it is not valid for the continental lithosphere. Indeed, an analysis of variations in strength of the lithosphere rocks with depth suggests that even the relatively cold ancient continental lithosphere, an example of which is shown in Fig. 1.9, is considerably weaker than it was thought early [54–57].

Figure 1.9 demonstrate the change in yielding strength $\sigma_{xx} - \sigma_{zz}$ of rocks versus depth computed for the continental lithosphere of the West Bashkiria with relatively low present-day temperature regime of the lithosphere. Principles of calculation of these strengths are the following.

The depth intervals with a linear increase in yielding strength in Fig. 1.9 correspond to brittle deformation of rocks. The strength for brittle deformation in the continental lithosphere is taken from [58] using the Byerlee's law [59] for static friction and variation of rock density with depth from Table 1.1. Then, brittle

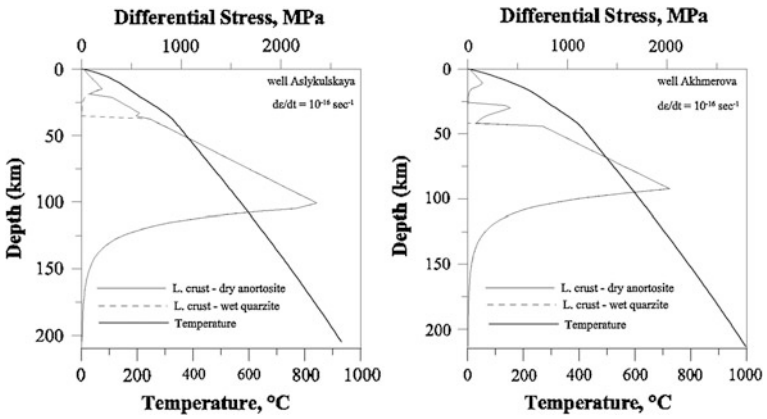

Fig. 1.9 Yielding strength $\sigma_{xx} - \sigma_{zz}$ of the lithosphere rocks versus depth z calculated from (1–5) for the present-day temperature distribution in the lithosphere of the West Bashkiria near the wells Aslykulskaya and Akhmerova for the strain rate $\dot{\varepsilon} = 10^{-16}1/\mathrm{s}$ and reology laws discussed in the text [3]

strength within the sedimentary layer of the continental crust with mean density $\rho \approx 2600$ kg/m^3 ($0 \leq z \leq S_{sed}$) must increase linearly with depth:

$$\sigma_{xx} - \sigma_{zz} = 120.0 \cdot z + 20 \tag{1.18}$$

Within the granitic layer with density $\rho \approx 2750$ kg/m^3 ($S_{sed} \leq z \leq S_{sed} + S_{gran}$) the strength rises by the law:

$$\sigma_{xx} - \sigma_{zz} = 12 \cdot S_{sed} + 12.8 \times (z - S_{sed}) + 20. \tag{1.19}$$

Within the "pseudo-basaltic" layer with $\rho \approx 2900$ kg/m^3 ($S_{sed} + S_{gran}. \leq z \leq S_{MOHO}$) the brittle strength changes with depth as:

$$\sigma_{xx} - \sigma_{zz} = 12 \cdot S_{sed} + 12.8 \cdot (S_{sed} + S_{gran}) + 23.2 \cdot (z - S_{sed} - S_{gran}) + 20 \tag{1.20}$$

and finally within the mantle ($z \geq S_{MOHO}$) with $\rho \approx 3300$ kg/m^3:

$$\sigma_{xx} - \sigma_{zz} = 12 \cdot S_{sed} + 12.8 \cdot (S_{sed} + S_{gran}) + 23.2 \cdot (S_{MOHO} - S_{sed} - S_{gran}) + 26.4 \cdot (z - S_{MOHO}) + 20. \tag{1.21}$$

In Eqs. (1.18)–(1.21), $\sigma_{xx} - \sigma_{zz}$ is the principal stress difference in Mpa, S_{sed}, S_{gran}, S_{MOHO} are the thickness of sedimentary blanket, upper crust (granite layer) and depth of lower boundary of the crust, correspondingly (in km), z is a depth

in km and 20 MPa is the assumed value of the rock strength at the surface [59]. The expressions (1.18)–(1.21) for brittle deformation assume that the pore pressure is hydrostatic within the upper continental crust and equal to zero within the lower crust and the mantle [60, 61].

The power-low [60, 62] describes the strength for ductile (creep) deformation in the crust and mantle:

$$\sigma_{xx} - \sigma_{zz} = (\dot{\varepsilon}/A)^{1/n} \cdot \exp[E/n \cdot R \cdot T] \tag{1.22}$$

where $\dot{\varepsilon}$ is the deformation rate in 1/s, $(\sigma_{xx} - \sigma_{zz})$ is in MPa, E is the activation energy for the ductile deformation in J/mol, R = 8.31441 J/mol °K is the universal gas constant, T is the absolute temperature, A is a material constant in $MPa^{-n}\ s^{-1}$ and n is dimensionless parameter. Values of parameters E, A and n depend on the mineral types. The rheology of wet quartz with parameters A = 0.00291 $MPa^{-n}\ s^{-1}$, E = 151 kJ/mol and n = 1.8 [63, 64] describes in our model a behavior of the continental upper crust. At the temperatures of 200–700 °C it is very close to the rheology of wet granite with the parameters A = 0.0002 $MPa^{-n}\ s^{-1}$, E = 137 kJ/mol and n = 1.9 [62, 64, 65]. The rheology of the lower continental crust is assumed to correspond to that of dry anortosite with the following parameters: $A = 3.27 \times 10^{-4}$ $MPa^{-n}\ s^{-1}$, E = 239 kJ/mol and n = 3.2 [64, 66–68]. At the temperatures T > 500 °C, this rheology is close to that of dry quartz [63] with parameters $A = 3.44 \times 10^{-6}$ $MPa^{-n}\ s^{-1}$, E = 184 kJ/mol and n = 2.8. Finally, the rheological behavior of the mantle material is described by the deformation law (1.22) with the parameters for dry dunite ($A = 2.88 \times 10^{4}$ $MPa^{-n}\ s^{-1}$, E = 535 kJ/mol and n = 3.6). They are taken from the papers [69, 70], in which temperature control of deformation experiments is, perhaps, the most reliable [64].

The distribution of the rock strength with depth is inferred then by choice of the minimal value among the stress differences, calculated by (1.18)–(1.22) for the given depth [64, 67]. Figure 1.9 demonstrates the calculated distribution of yielding strength with depth in the West Bashkirian region on an example of the present-day sections in two areas: Aslykulskaya and Akhmerova [3]. The calculations are carried out for the strain rate $\dot{\varepsilon} = 10^{-16} 1/s$, which is expected to be typical for stable continental areas [68] and characterizes greater part of the region history excluding perhaps the relative short times close to riftng or the stage of Urals Orogeny. For comparison, the profiles with wet quartzite rheology for all the continental crust considered in many papers [60, 62, 64, 71] are shown in these figures by dotted lines. Figure 1.9 shows considerable weakening of the mantle lithosphere at depths of below 90–110 km even for the low-temperature present-day regime of the West Bashkirian lithosphere. For the reology of wet quartzite for all the crust, ductile zone occupies all of the lower crust even in the western section of the region (Fig. 1.9). Stress-profiles in Fig. 1.9 demonstrate clearly considerable weakening of the crust due to deposition of thick sedimentary

cover (compare Fig. 1.9b and 1.9a). This effect is mainly due to an increase in rock temperature under the thick sedimentary cover. This fact explains to some extent a readiness of thick sedimentary basins to tectonic remobilization (the East Barents basin, West Siberia basin and others). At significant sediment deposition, ductile zone appears even at the base of the granite layer (Fig. 1.9b). In any case, the modeling results in Fig. 1.9 suggest that the rheological thickness of the lithosphere must be considerably lesser than its thermal thickness exceeding in the region 200 km. Reactivation of existing faults during restoration of isostasy state of the lithosphere increased the above difference [71]. Certainly, deviation from the local isostasy can arise during periods of regional compression. But their duration is rather short (10–15 My). After their completion, the state (at least) of regional isostasy will be restored. The relative low free-air gravity anomalies speak well also for the state close to isostatic equilibrium of the present-day lithosphere in the studied region [72]. Of course, the only tectonic analysis does not give the desirable assessment of amplitude and duration of the extension and heating events in the basin lithosphere. However, combination of the tectonic method with the control by temperatures measured in boreholes and by measured vitrinite reflectance decreases the uncertainties in modeling procedure and reduces the number of appropriate variants suggested by modeling for the basin evolution.

1.6 Conclusion

An analysis of variations in the basin tectonic subsidence calculated by removal of the water and sediment load from the basement surface, and by computing variations in density distribution of the basement rocks with depth and time provides an ability to estimate the amplitude and duration of the thermal and stretching events in the basin lithosphere. The method is applied in next chapters to the basins with different amplitudes of lithosphere stretching including both continental rift basins and basins of continental passive margins. Modeling the distribution of stress with depth in the lithosphere suggests a considerable weakening of the continental crust due to deposition of thick sedimentary cover. At significant sediment deposition, ductile zone appears even at the base of the granite layer. In any case, the modeling results suggest that the rheological thickness of the lithosphere is considerably lesser than its thermal thickness. Of course, the only tectonic analysis does not give the desirable assessment of amplitude and duration of the extension and heating events in the basin lithosphere. However, combination of the tectonic method with the control by temperatures measured in boreholes and by measured vitrinite reflectance decreases the uncertainties in modeling procedure and reduces the number of appropriate variants suggested by modeling for the basin evolution.

References

1. Makhous M, Galushkin Y (2005) Basin analysis and modeling of the burial, thermal and maturation histories in sedimentary basins. Editions TECHNIP, Paris
2. Carlslaw HS, Jaeger JC (1959) Conduction of heat in solids. Oxford University Press, New York
3. Galushkin YuI, Yakovlev GE (2004) Burial and thermal history of the West Bashkirian sedimentary basins. Tectonophysics 379:139–157
4. Deming D, Chapman DS (1989) Thermal histories and hydrocarbon generation: example from Utah-Wyoming thrust belt. AAPG Bull 73(12):1455–1471
5. Doligez B, Bessis F, Burrus J, Ungerer P, Chenet PY (1986) Integrated numerical simulation of the sedimentation heat transfer, hydrocarbon formation and fluid migration in a sedimentary basin. The THEMIS model. In: Burrus J (eds) Thermal modelling in sedimentary basins: Paris, pp 173–195
6. Ungerer P (1990) State of the art of research in kinetic modelling of oil formation and expulsion. Org Geochem 16(1–3):1–27
7. Ungerer P (1993) Modeling of petroleum generation and migration. In: Bordenave ML (ed) Applied petroleum geochemistry, Technip, Paris, pp 397–442
8. Welte DH, Horsfield B, Baker DR (eds) (1997) Petroleum and basin evolution. Springer
9. Nyblade AA, Suleiman IS, Roy RF, Pursell R, Suleiman AS, Doser DL, Keller GR (1996) Terrestrial heat flow in the Sirt Basin, Libya, and the pattern of heat flow across northern Africa. J Geophys Res 101(B8):17736–17746
10. Midttomme K, Roaldset E (1999) Thermal conductivity of sedimentary rocks: uncertainties in measurement and modeling. In: Aplin AC, Fleet AJ, Macquaker JHS (eds) Mud and mudstones: physical and fluid flow properties. Geolog. Soc. London. Special Publ., N. 158, pp 45–60
11. Baer AJ (1981) Geotherms evolution of the lithosphere and plate tectonics. Tectonophysics 72:203–227
12. Hofmeister A (1999) Mantle values of thermal conductivity geotherm from phonon lifetimes. Science 283:1699–1709
13. McKenzie D, Jackson J, Priestley K (2005) Thermal structure of oceanic and continental lithosphere. Earth Planet Sci Lett 233:337–339
14. Schatz JF, Simmons G (1972) Thermal conductivity of Earth materials at high temperatures. J Geophys Res 77(35):6966–6983
15. Cawthorn RG (1975) Degrees of melting in mantle diapers and the origin of ultrabasic liquids. Earth Planet Sci Lett 27:113–120
16. Robie RA, Hemmingway BS, Fischer JR (1978) Thermodynamic properties of minerals and related substances at 298.15°K and 1 bar (10^5 Pascals) pressure and at higher temperatures. U.S. Geolog. Survay Bulletin, N 1452
17. Bottinga Y, Steinmetz L (1979) A geophysical, geochemical, petrological model submarine lithosphere. Tectoniphysics 55:311–347
18. Wyllie PJ (1979) Magmas and volatile components. Am Mineral 64:469–500
19. Hirose K (1997) Melting experiments in lherzolite KLB-1 under hydrous conditions and generation of high-magnesian andesite melts. Geology 25(1):42–44
20. Turcotte DL, Schubert G (1982) Geodynamics: application of continuum physics to geological problems, vol 1. Wiley, New York
21. McKenzie D, Bickle MJ (1988) The volume and composition of melt generated by extension of the lithosphere. J Petrol 29(3):625–679
22. Hirth G, Kohlstedt DL (1996) Water in the oceanic upper mantle: implications for rheology, melt extraction and the evolution of the lithosphere. Earth Planet Sci Lett 144:93–108
23. Asimov PD, Hirschmann MM, Stolper EM (2001) Calculation of peridotite partial melting from thermodynamic models of minerals and melts, IV. Adiabatic decompression and the composition and mean properties of Mid-ocean Ridge basalts. J Petrology 42(5):963–998

24. Braun MG, Hirth G, Parmentier EM (2000) The effect of deep damp melting on mantle flow and melt generation beneath mid-oceanic ridges. Earth Planet Sci Lett 176:339–356
25. Hirschmann MM (2000) Mantle solidus. Experimental constraints and the effect of peridotite composition. Geochem Geophys Geosyst 1. doi:10.1029/200GC000070
26. Galushkin YuI, El Maghbi A, El Gtlawi M (2014) Thermal regime and amplitude of lithosphere extension in the Sirte Basin, Libya: numerical estimates in the plane basin modeling system. Izvestiya Phys Solid Earth 50(1):259–272
27. Makhous M, Galushkin YuI, Lopatin NV (1997) Burial history and kinetic modelling for hydrocarbon generation. Part I: The GALO Model. AAPG Bull 81(10):1660–1678
28. Galushkin YuI (1997) Numerical simulation of permafrost evolution as a part of basin modeling: permafrost in Pliocene-Holocene climate history of Urengoy field in West Siberian basin. Canad J Earth Sci 34(7):935–948
29. Peaceman DW, Rachford HH (1955) The numerical solution of parabolic and elliptic differential equations. J of Soc Indus Appl Math 3(1):28–41
30. McKenzie DP (1981) The variation of temperature with time and hydrocarbon maturation in sedimentary basins formed by extension. Earth Planet Sci Lett 55:87–98
31. Sclater JG, Christie PAF (1980) Continental stretching: an explanation of the Post-Midcretaceous subsidence of the central North sea basin. J Geophys Res 85(B7):3711–3739
32. Galushkin YI, Kutas RI (1995) Dnieper_Donets Paleorift: thermal evolution and oil_and_gas bearing capacity. Geofizichesky Zhurnal 17(3):13–23 (in Russian)
33. Guidish TH, Lerche I, Kendall CG, O'Brien JJ (1984) Relationship between eustatic sea level changes and basement subsidence. AAPG Bull 68(2):164–177
34. Vail PR, Mitchum RM, Thompson S (1977) Global cycles of relative changes of sea level. AAPG Mem 26:83–97
35. Volozh YA, Antipov MP, Varshavskaya NE, Lipatova VV, Bobylova EE (2004) Sedimentary stratigraphy: determination, modern state of the problem. In: Leonov YG, Volozh YA (eds) Sedimentary basins: the study methods, structure and evolution. Moscow, Nauchny Mir, pp 388–402 (in Russian)
36. Turcotte DL, Bernthal MJ (1984) Synthetic coral-reef terraces and variations of Quaternary sea level. Earth Planet Sci Lett 70:121–128
37. Su D, White N, McKenzie D (1989) Extension and subsidence of the Pearl River Month basin, northern South China Sea. Basin Res 2:205–222
38. Watts AB, Weissel IK, Larson RL (1977) Sea floor spreading in marginal basins in the western Pacific. Tectonophysics 37:167–181
39. Hegarty KA, Weissel JK, Mutter JC (1988) Subsidence history of Australian's southern margin: constraints on basin models. AAPG Bull 72:615–633
40. Artyushkov EV (1993) Physical tectonics. Nauka, Moscow (in Russian)
41. Artyushkov EV, Merner NA (1997) Fast subsidence of sedimentary basins—indication to temporary decrease of the lithosphere strength. Doklady Akademii Nauk RAN 356(3):382–386 (in Russian)
42. Artyushkov EV, Lindstrem M, Muzylev NG, Popov LE, Chekhovich PA (1998) Role of tectonic and eustatic factors in fast variations of the sea depth in sedimentary rocks. In: Tectonics and geodynamics: general and regional aspects, vol 1. Moscow, GEOS, pp 30–32 (in Russian)
43. Touloukian YS, Ho CY (1981) Physical properties of rocks and minerals. McGrew-Hill
44. Wood BJ, Yuen DA (1983) The role of lithospheric phase transitions on sea floor flattering at old ages. Earth Planet Sci Lett 66:303–314
45. Yamasaki N, Nakada M (1997) The effect of the spinel-garnet phase transition on the formation of rifted sedimentary basins. Geophys J Int 130:688–692
46. Forsyth DW, Press F (1971) Geophysical tests of petrological models of the spreading lithosphere. J Geophys Res 76:7963–7972
47. McKenzie DP (1978) Some remarks on the development of sedimentary basins. Earth Planet Sci Lett 40:25–32

48. Royden L, Keen CE (1980) Rifting processes and thermal evolution of the continental margin of eastern Canada determined from subsidence curves. Earth Planet Sci Lett 51:343–361
49. Takeshita T, Yamaji A (1990) Acceleration of continental rifting due to a thermomechanical instability. Tectonophysics 181:307–320
50. Ziegler PA, Cloetingh S (2004) Dynamic processes controlling evolution of rifted basins. Earth-Sci Rev 64:1–50
51. Newman R, White N (1997) Rheology of the continental lithosphere inferred from sedimentary basin. Nature 385:621–624
52. Huismans RS, Podladchikov YuY, Cloetingh S (2001) Transition from passive to active rifting: relative importance of asthenospheric doming and passive extension of the lithosphere. J Geophys Res 106(B6):11271–11291
53. Galushkin Y, Shreider AA, Bulychev AA, Shreider AA (2006) Heat flow and thermal evolution of the lithosphere of the Black Sea basin Oceanology, Moscow, Maik Nauka/Interperiodica Publishing, vol 46, issue 2, pp 274–291
54. Karter N, Tsenn MC (1987) Flow properties of continental lithosphere. Tectonophysics 136:27–63
55. Kruse S, McNutt M (1988) Compensation of Paleozoic orogens: comparison of the Urals to the Appalachians. Tectonophysics 154:1–17
56. Lobkovsky LI (1988) Geodynamics of spreading zones, subduction, and two-level plate tectonics. Nauka, Moscow (in Russian)
57. Burov EB, Diament M (1995) The effective elastic thickness (Te) of continental lithosphere: what does it really mean? J Geophys Res 100:3905–3927
58. Bassi G, Bonnin J (1988) Rheological modeling and deformation instability of lithosphere under extension—II. Depth-dependent rheology. Geophys J 94:559–565
59. Byerlee JD (1968) Brittle-ductile transition in rocks. J Geophys Res 73:4741–4750
60. Brace WF, Kohlstedt DL (1980) Limits on lithospheric stress imposed by laboratory experiments. J Geophys Res 85(B11):6248–6252
61. Thibaud R, Dauteuil O, Gente P (1999) Faulting pattern along slow-spreading ridge segments: a consequence of along-axis variation in lithospheric rheology. Tectonophysics 312:157–174
62. Kirby SH (1983) Rheology of the lithosphere. Rev Geophys Space Phys 21:1458–1487
63. Jaoul O, Tullis J, Kronenberg AK (1984) The effect of varying water contents on the creep behaviour of Heavitree quartzite. J Geophys Res 89:4298–4312
64. Ord A, Hobbs BE (1989) The strength of the continental crust, detachment zones and the development of plastic instabilities. Tectonophysics 158:269–289
65. Meissner R, Kusznir NJ (1987) Crustal viscosity and the reflectivity of the lower crust. Annal Geophys 5B(4):365–374
66. Shelton G, Tullis J (1981) Experimental flow laws for crustal rocks: EOS. Trans Am Geophys Union 62:396
67. Ranalli G, Murphy DC (1987) Rheological stratification of the lithosphere. Tectonophysics 132:281–295
68. Takeshita T, Yamaji A (1990) Acceleration of continental rifting due to a thermomechanical instability. Tectonophysics 181:307–320
69. Chopra PN, Paterson MS (1981) The experimental deformation of dunite. Tectonophysics 78:453–473
70. Chopra PN, Paterson MS (1984) The role of water in the deformation of dunite. J Geophys Res 89:7861–7876
71. Ranally G (2000) Rheology of the crust and its role in tectonic reactivation. J Geodyn 30(1–2): 3–15
72. Artemjev ME, Kaban MK, Kucherenko VA, Demyanov GV, Taranov VA (1994) Subcrustal density inhomogeneities of northern Eurasia as derived from the gravity data and isostatic models of the lithosphere. Tectonophysics 240:249–280

Chapter 2
The Lithosphere Extension and Hydrocarbon Generation in the Eastern Continental Passive Margin of India

Abstract The chapter analyzes the changes in the tectonic and thermal evolution of the lithosphere in the transition from shallow to deep-water shelf for the example of passive continental margin of India in the Bay of Bengal. The study bases on numerical reconstructions thermal evolution of 10 sedimentary sections, five of which locate within shallow offshore with water depth of 10–90 m and five others in the deep offshore with water depth of 1900–2800 m. The difference in the amplitude of the crust thinning, thermal and maturation conditions of the main sedimentary formations of sedimentary sections in shallow and deep-water offshore are discussed in detail. The consequences of these differences in the generation of different fractions of hydrocarbons by probable source rocks of the basin are considered also.

Keywords Passive margin · Bay of Bengal · Tectonic subsidence · Lithosphere extension · Maturity level · Hydrocarbon generation · Thermal activation of basin

2.1 Geological History of the Krishna-Godavari and Mahanadi Basins

2.1.1 Tectonic History of the Bay of Bengal

The eastern seaboard of India is a rifted divergent margin that evolved since Late Jurassic related to the break up and drifting of Indian and Antarctic plates during the breakup of eastern Gondwanaland [1–3]. The margin is geomorphologically and tectonically segmented by major faults and Visakhapatnam, Nayudupeta and Chingleput highs into the Bengal, Mahanadi, Krishna-Godavari, Palar and Cauvery Basins [4]. At the same time two great part of the margin are considered: a rifted northern part and southern sheared (transformed) part. Whereas the rifted northern part, including the Bengal, Mahanadi and Krishna-Godavari seaboard is characterized by sedimentary basins having coast parallel horst-graben structures,

Y. Galushkin, *Non-standard Problems in Basin Modelling*,
DOI 10.1007/978-3-319-33882-8_2

the Cauvery basin along the sheared segment shows development of pull-apart basins and intervening ridges oblique to the N-S shore-line [1].

In the pre-break up reconstructions of Gondwanaland, Enderby Land and Mac Robertson Land of Antarctica are placed against east coast of India [4, 5]. Evolution of sedimentary basins in the eastern passive margin of India started in the Permian-Triassic with the stage of early rifting, formation of system of aulacogens along the Mahanady, Godavary, Krishna and Cavery rivers which flow along the dead branches of R-R-R triple junctions [1, 2, 6]. These aulacogens are aligned in a NE-SW trend (or in a NNE-SSW trend in the south), parallel to the Eastern Ghats of Precambrian age. During the Jurassic, rifting continued with formation of a set of rift triple junctions. Graben subsidence and its infill by sediments continued, block faulting was still active. The Godavari and Mahanadi grabens had continuity with the rift-like structures in the Enderby Land and the Lambert rift, respectively [7].

Cauvery Basin was initiated in the Late Jurassic, in response to development of Natal Basin between Africa–India (with Madagascar)—Antarctica at the rift propagating from the South. This crustal extension resulted in counter clockwise movement of Sri Lanka [4]. During Late Jurassic-Early Cretaceous (Kimmeridgian-Valenginian) the west Australia-India rift propagated further to the North–West. This extension was oblique and resulted in formation of horsts (Bapatla, Tanaku, Yanam horsts) and grabens (Krishna, West Godavari and the East Godavari sub-basins) in the Krishna-Godavari Basin [4]. The major Godavari rift extends both onland and offshore. On land, it is exposed near Wardha towards the north-western direction and extends to the sea in the south-east direction [8]. In the seaward portion, it crosses the shelf and enters the deep sea. The basin is dominated by deltaic plains near the sea–land boundary. Development of Mahanadi Basin was also initiated during this period. Mailaram high (rift shoulder) delivered sediments into the newly formed grabens/basins [4]. The three failed arms of the R-R-R triple junctions are Bengal-Purnea, Mahanadi-Hasdo and Lambert grabens, while along the two other arms (Bengal-Bangladesh-Assam and Krishna-Godavari-Mahanadi arms) rifting progressed and led to separation [4].

The oblique extension of the India and west Australia rift up to Krishna-Godavari Basin in the Early Cretaceous (Barriasian-Hauterivian) followed by asymmetric seafloor spreading [9], resulted in a transpression along the junction between Antarctica and Sri Lanka-India. This led to development of a NNW-SSE trending transcurrent fault along which Antarctica moved southward. The angular unconformity within synrift sediments in the Penar area of the Krishna-Godavari Basin marking beginning of mobilization is considered as the period of initiation of transcurrent movement between India and Antarctica. Ramana et al. [9] have identified magnetic anomaly of the Mesozoic crust to be 133–118 Ma old in the Bay of Bengal. As a whole, the breakup of India and east Antarctica could not be older than M0 whereas most of the oceanic crust in the Bay of Bengal evolved during the Cretaceous Normal Superchron (120–84 My; [10]).

Syntectonic infill of the aulacogens and main rift arms by sediments continued in Early Cretaceous. The latter culminates in seafloor spreading between India and Australia-Antarctica as Eastern Gondwana broke up about 140–125 Ma. It appears that the relative timing of crustal extension initially was earlier in the northern part than in the southern part and also the magnitude of extension was more in north than in south [6]. As a whole, splitting of eastern Gondwana in Upper Jurassic-Lower Cretaceous can be divided into two stages [3]. The first break-up occurred with separation of Greater India from Australia and East Antarctica during the Early Cretaceous [11]. Additional thinning of the crust assumedly along the Kakinada Trough, which is a half-graben parallel to the coast [12], subsequently became a favorable breakup zone, which occurred because of a northward ridge jump [13] and resulted in the separation of the Elan Bank from India at M2. The crust thinning is confirmed by the gravity-derived crustal models. They indicate that the crust at the eastern Indian shield margin is 39–41 km thick and thins to as much as 20–23 km at the Ocean Continent Transition (OCT). In addition, there are several structural highs within the offshore that could be a continental fragment left behind during the breakup between India and the Elan Bank [14].

In the second stage of the splitting, micro-continent of Elan Bank, which presently lies on the western margin of the Kerguelen Plateau, got detached from the eastern margin of India at about 120 Ma (Fig. 2.1; [13, 14]). Therefore, the most part of the oceanic crust in the Bay of Bengal was formed during the Cretaceous Magnetic quiet period (120–84 Ma) that explains the lack of pronounced magnetic anomaly in the Bay of Bengal [3]. In the Late Cretaceous, the Crozet hotspot had emplaced the 85° E Ridge and some isolated structural highs on oceanic crust that was already formed during the Cretaceous quiet period. The 85° E Ridge has begun its formation about 85 My ago in the northern Bay of Bengal on the oceanic crust of about 35 My old [3, 16].

In the Middle and Later Cretaceous, early drift, volcanic activity, drainage of aulacogens along the Mahanadi and Godavari rivers toward the East continued. Sea floor spreading and subduction of the Tethyan Ocean beneath southern Tibet continued forcing the Indian plate northwards towards Eurasia. The spreading rate of Indian Ocean floor increased further from 84 Ma onwards and reached maximal value about 66–64 Ma [2, 6, 14]. At the end of Cretaceous, when the rifting ceased, some parts of the basins were risen above sea level and underwent by erosion.

In the Early Paleocene, the first soft collision took place as continental India collided with the Eurasian continental margin. Rifting has ceased and India was drifting northwards. In the Middle Eocene, the hard collision took place as continental India collided with continental Eurasia. In Oligocene, a slightly northern shift of direction occurred as continental India also collided with the Indochina plate. In the Early Miocene, continuing shift of India to the North led to rise of the Himalayas to the extent when deposition of sediments of the Ganges began to affect the sedimentation of all the eastern coast of India [1, 4].

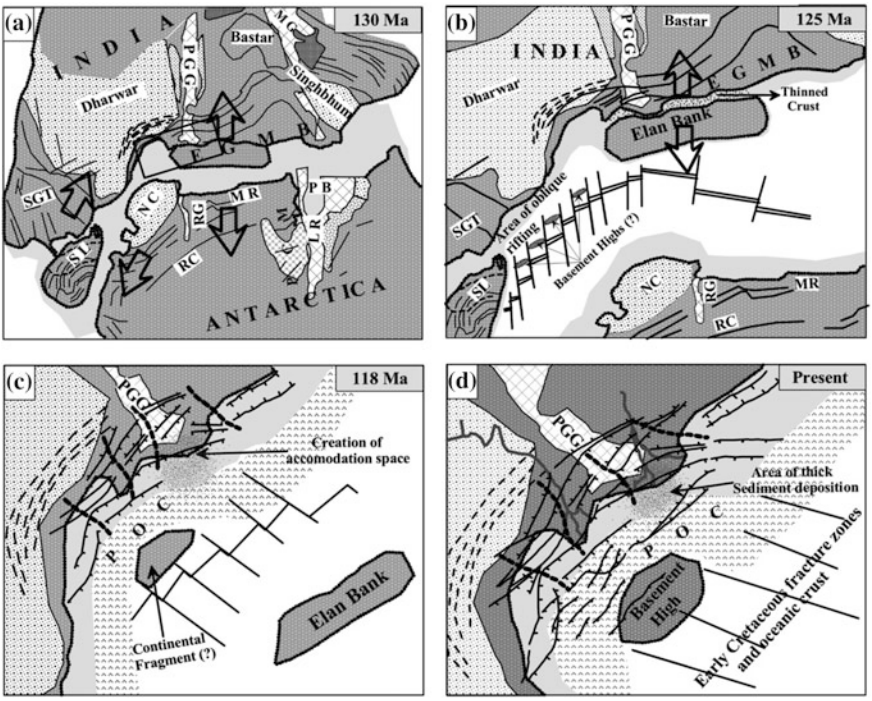

Fig. 2.1 Schematic representations of the rifting history and the double breakup events between the East Coast of India, Elan Bank and the Eastern Antarctica, and the development of the Krishna-Godavari (K-G) basin (after [14]). **a** Pre-breakup scenario just before M9 (130 Ma) showing the sense of future breakup. Area shown in rectangle is already under subsided condition, due to the pre-existing NW-SE trending Pranhitae-Godavari Graben (PGG) and NE-SW trending Jurassic rift systems developed along the coast. **b** Breakup of East Antarctica with the southern part of East Coast of India led to the development of oblique fracture zone trends and generation of late Mesozoic (younger to M4) crust at the margin. Formation of basement highs during the early breakup is indicated as inferred by Krishna et al. [15]. Significant thinning of the crust took place during this time between India and the Elan Bank. **c** Ridge jump at M2 gave rise to splitting of Elan Bank from India. Instabilities in spreading segments caused a small portion of the Elan Bank to be left behind with the Indian plate. K-G Basin was taking shape, the coastal cross trends helped to further segment the basin. The two cross trends along the PGG created a major accommodation space in the Godavari offshore. **d** The K-G Basin with its present geological features. *SGT* Southern Granulite Terrain, *EGMB* Eastern Ghat Mobile Belt, *MG* Mahanadi Graben, *MR* Mac. Robertson Land, *PB* Prydz Bay, *LR* Lambert Rift, *RG* Robert Glacier, *NC* Napier Complex, *RC* Rayner Complex, *PCM* Prince Charles Mountains

2.1.2 Sedimentation History

The sediments of the Pre-Break stage are absent in the basins of the East Coast of India except of deepest local areas of grabens [4]. Therefore, we begin the discussion of sedimentary blanket of the region with syn-rift sediments. As a whole,

the East Coast sedimentary supergroup of the eastern passive margin of India can be subdivided into two major tectono-stratigraphic sequences: (1) Late Jurassic-Early Cretaceous syn-rift megasequence, comprised largely of non-marine units, overlain by (2) Early Cretaceous (Aptian)—Cenozoic post-rift megasequence, comprised of marine sedimentary formations [2, 6]. The thickness of syn-rift sediments is controlled by the structural geometry, which in these basins is characterized by a series of NE-SW trending horsts and grabens, while post-rift sediments show an overall thickening seawards.

The syn-rift sedimentary infill is essentially fluvial and lacustrine (Fig. 2.2). Sedimentary sequences of Aptian-Albian age (Andaman and Palk Bay formations) belong also to sin-rift deposits). They were coarse sand eroded from the higher horst block and deposited in the intervening lows. Mailaram High (rift shoulder) initiated about 144 Ma [17] delivered sediments into the newly formed grabens/basins of the Krishna-Godavari and Mahanadi Basins. During Late Jurassic-Early Cretaceous (Kimmeridgian-Valenginian), deposition of *Nellore claystone, Krishna Formation and Pennar shale* took place in Krishna-Godavari Basin and deposition of Athgarh sandstone—in Mahanadi Basin [4]. As result of uplift of Nellore high, *Nellore claystone, Bapatla sandstone and Pennar shale* were deposited in the southern part of Krishna-Godavari Basin, while in Kakinada Bay area, the *Golapalli sandstones* were deposited.

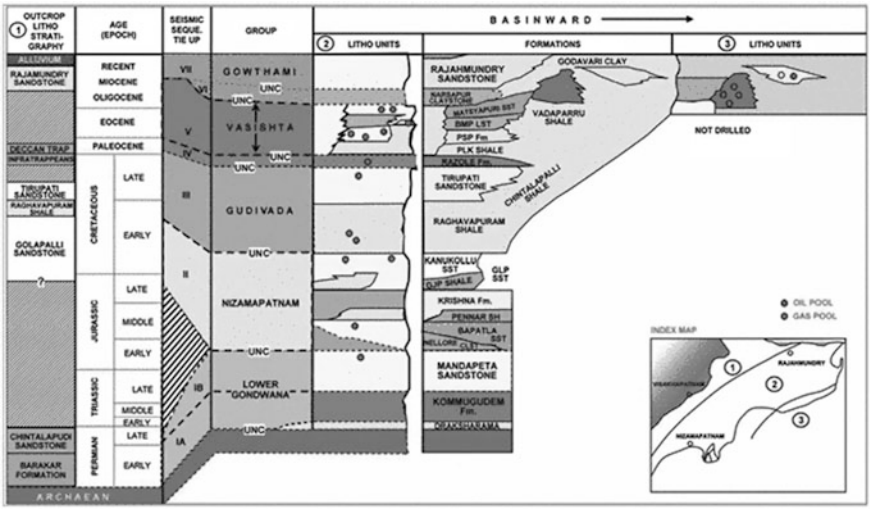

Fig. 2.2 The generalized stratigraphy of Krishna–Godavari basin (after [18, 19]). The Godavari Graben is filled with a maximum of 2.8-km-thick Early Gondwana (Late Permian to Early Triassic) sediments [20]. In between the horst structures, three sub-basins are, namely, Krishna, West Godavari and the East Godavari. The basin is dominated by deltaic plains near the sea–land boundary

Karai Shale Formation ranges in age from Albian to Cenomanian. It consists of a basal limestone unit, which is corralline and reefoidal at some places, overlain by grey to dark grey calcareous, pyritiferous shales with phosphatic nodules. The uppermost part of the formation consists of siltstone and sandstones [1, 4]. The first basin-wide marine transgression took place during Cenomanian and continued up to Maastrichtian. The post-rift thermal subsidence continued throughout remainder of the Cretaceous and Tertiary. This event is represented by extensive marine sedimentation in the rock record of the East Coast basins [6].

The rift-drift (spreading) transition is also marked by the volcanic activity in the Gulf of Mannar, which had started in Cenomanian and continued till Santonian. During early thermal subsidence stage, spanning from Cenomanian to Maastrichtian, these half-grabens were gradually invaded by the sea and were occupied by interconnected seas (Fig. 2.2). *The Paravay Formation*, ranged in age from Turonian to Coniacian, consists of grey to dark grey, hard, compact, massive, fine to medium grained calcareous sandstones. Variegated clays and limestones occur frequently within the sandstone. *Trichinopoly Formation* is confined to Santonian age. It consists of two members, the basal brown, compact, arenaceous shelly limestone with intervening sandstones and grey to brown clays and the upper yellow to brown argillaceous, fossiliferous limestone interbedded with marls and gypseous clays. *The Llakkudi Formation* is of Campanian age. It consists of yellowish to grey and white, fine to medium grained sandstones. *Kallankurichi Formation* is of Early Maastrichtian age. It is made up of limestones ranging from grainstone to wackestone [2, 6, 14]. The lower part is sandy. *Kallamedu Sandstone Formation* belongs to Late Maastrichtian age. The sandstone is yellowish white to white. It grades upwards into ferruginous claystone. The early thermal subsidence stage is marked in the basin by marine transgression. The dark gray shales of *Dhananjayapur Formation* of the Upper Cretaceous age were deposited during this phase. The lithology of the Cretaceous section in the subsurface is predominantly clastic with thin limestone layers over most of the basin. A thick dolomite unit is present over a part of the Pattukottai horst [2, 6, 14]. Eastwards of the horst along the East Coast of India a blanket of Paleocene sediments filled any Cretaceous topography.

In the Middle Eocene, the hard collision of continental India with continental Eurasia took place. In the Early Miocene, continuing shift of India to the North led to rise of the Himalayas to the extent when deposition of sediments of the Ganges began to affect the sedimentation of all the eastern coast of India. *The Niniyur Formation* ranges in age from Paleocene to Early Eocene. It consists of a lower, purple to greyish white sandstone overlain by buff to cream coloured, fossiliferous limestone [2, 14]. Himalayas rose to a great height in the Middle Miocene and sedimentation of the fan of the Ganges dominates deposition processes in offshore zone of the eastern coast. *The Cuddalore Formation* ranges in age from Middle Miocene to Pliocene. It consists of non-marine pebbly sandstone strata in the western part. Towards the coast, this formation becomes more argillaceous with increasing marine influence.

Finally, coastal and deltaic plains of Quarternary age consisting of yellow to grey, fine grained sands and clays are seen over a major part of the land area of the basin between the Precambrian outcrops and the coast line. The shallow marine area of Cauvery coastline is marked by deposition of sands, parallel to the coast, by along shore currents [2, 6, 14]. Mazumdar et al. [21] note that higher smectite contents in sediments of the Krishna-Godavary Basin compared to the Mahanadi Basin suggests a contribution of weathered Decan basalts to sedimentary rocks of the Krishna-Godavari Basin.

2.2 Thermal, Burial and Maturity Histories of the Krishna-Godavari and Mahanadi Basins

2.2.1 Input Data for Modeling

In this chapter we analyze the changes in tectonic, thermal, maturation and generation histories of the basin rocks at transition from the shallow to deep areas of the eastern offshore of India on the example of the Krishna-Godavary and Mahanadi Basins. Consequently, we study burial, thermal, tectonic and maturation histories of the basins on the example of five wells 1, 3, 5, 7, 9 in the shallow offshore (water depth is 10–90 m) and five pseudo-wells located in the deep-water offshore (water depth is 1900–2800 m). Locations of these wells and conjugate pseudo-wells are shown in Fig. 2.3. The first six modeling areas (1–6) are divided from others areas

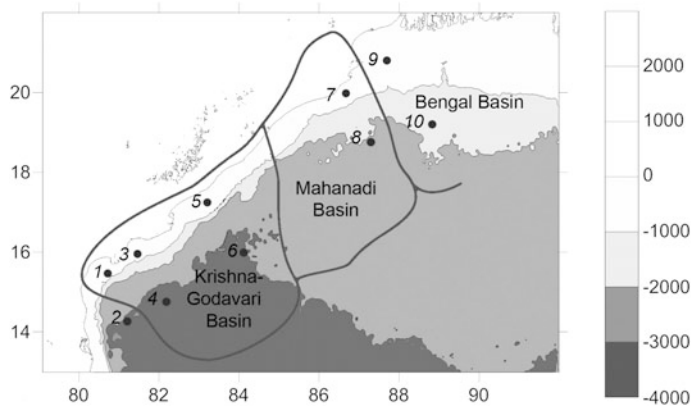

Fig. 2.3 Location of pseudo-wells (*1*, *3*, *5*, *7*, *9*) in shallow offshore near the coast with water depth of 10–90 m) and the pseudo-wells (*2*, *4*, *6*, *8*, *10*) in deep offshore (water depth is 1900–2800 m)

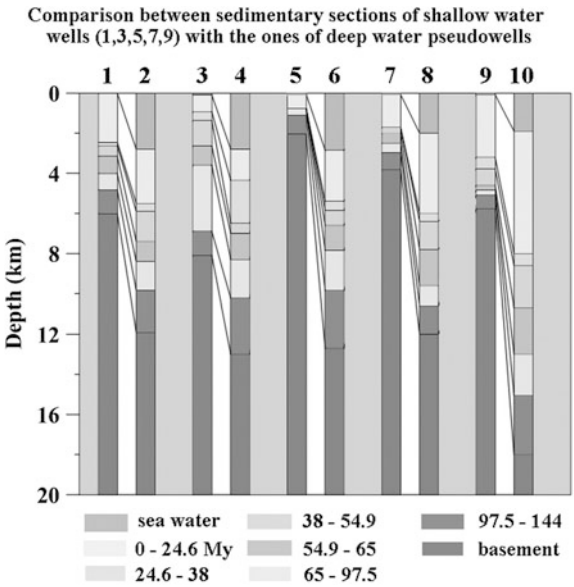

Fig. 2.4 Comparison of thickness of sedimentary formations of different age in shallow-sea (wells *1*, *3*, *5*, *7*, *9*) with the ones in deep sea areas of the north-eastern offshore of India (pseudo-wells *2*, *4*, *6*, *8*, *10*). (The locations of pseudo-wells are shown in Fig. 2.3.)

(7–10) by the 85° E Ridge [2]. Areas 1 and 2 are in the boundary of the Krishna-Godavary and Palar Basins, and areas 9 and 10 belong to the boundary between the Mahanadi and Bengal Basins (Fig. 2.3; [1]).

A significant part of initial data for modeling consists of description of sedimentary sections of the basins. For the wells: GS-41-1 (1), GS-5-1 (3), KB-4-1B (5), MND-5 (7), NEC-1 (9), these sections were constructed on the base of drilling data for the horizons with reasonable burial depth and seismic data for the deepest horizons of the sections. The sedimentary sections in the deep-water offshore (pseudo-wells 2, 4, 6, 8, 10) are constructed on the base of seismic profiles crossing the areas of these pseudo-wells. Figure 2.4 demonstrates correlations of sedimentary deposits of different age in the areas near coast (wells 1, 3, 5, 7, 9) with the ones in the deep offshore areas (2, 4, 6, 8, 10). Transition from the first group to the second one is accompanied by increase in thickness of sedimentary blanket largely due to contribution of the Miocene-Pliocene section that trends to increase towards the North and the ocean (Fig. 2.4).

The GALO program computes the distribution of temperatures with depth and time from numerical solutions of one-dimensional non-steady heat transfer equations during compaction history of sediments (Sect. 1.1). The domain for temperature calculation has mobile upper boundary that changes during sedimentation or erosion. Petrophysical attributes of the rocks in heat transfer equation change with depth and time (see Sect. 1.1). The GALO system uses a so-called “flat basin approach” which considers variations of temperature only with depth and time and neglects variations in the horizontal (x, y) plane. In spite of this limitation, this approach has some advantages compared to other basin modelling systems because

Table 2.1 Initial model of the continental lithosphere of India (before stretching) used in our modeling as initial model of the margin lithosphere [22–24]

Layer	Granitic			Basaltic	Mantle
Depth of the layer base (km)	1.0	11.0	20	40.0	>40
Density (g/cm^3)	2.75	2.75	2.75	2.90	3.30
Heat conductivity (W/m K)	3.30	3.15	2.80	1.90	K = f(T)
Radiogenic heat production (mkW/m^3)	3.30	1.40	0.20	0.10	0.00

Remark Dependence heat conductivity K on temperature T in the mantle (function K = f(T) is determined according to Sect. 1.1.2)

it allows you to set the lower boundary of the domain for temperature calculation at great depth (Sect. 1.2).

We simulate heat transfer in the sedimentary section, the underlying lithosphere and asthenosphere down to depths of ZM = 90–120 km. The temperature TM = 1150–1170 °C is maintained at low boundary of the domain (at depth ZM). The principles of computation of the parameters TM and ZM are discussed in Sect. 1.1.4. The model of the lithosphere used in our reconstructions differs from the standard continental lithosphere in Table 1.1 by presence of the thicker granitic layer in the crust. Structure of the lithosphere shown in Table 2.1 is constructed on the base of the data of geological and geophysical studies in the region [22–24].

The gravity-derived crustal models suggests the crust at the eastern Indian shield margin 39–41 km thick, which thins to as much as 20–23 km at the Ocean-Continent Transition in offshore [14]. On the base of this information, the initial crustal thickness of 40 km was taken in our model. It corresponds to the present-day thickness of consolidated crust in undeformed regions of central India. Densities and heat conductivity of the consolidated crust and mantle rocks are presented in Table 2.1 for normal conditions (P = 1 atm, T = 0 °C). They change with pressure and temperature at numerical simulation of the basin development (Sects. 1.2 and 1.3). Heat conductivity and heat capacity of the mantle rock in our modeling change with temperature according to recent analysis of heat transfer in the mantle (Sect. 1.1.2). The basement described in Table 2.1 was subjected to intense stretching in the Lower and Upper Cretaceous (see below). Radiogenic contribution of the initial consolidated crust is about 23.1 mW/m^2. It can be significantly less in the modern lithosphere of the passive margin at the areas of the pseudo-wells 2, 4 and 6, where amplitude of the lithosphere stretching could reach 2 and more (Table 2.2).

The temperatures corresponded to paleoclimatic condition (the mean annual temperatures at the sea bottom) are taken at upper boundary of the domain, Z = 0. These temperatures are shown in upper parts of Figs. 2.5 and 2.6. They were determined on the base of the paleoclimate data in [25], changes in paleo-lattitude of the region under study [2, 6, 14, 26] and variations in the sea depth during the Basin history (curves 4 in Fig. 2.7). Paleoclimate curve of shallow-water offshore areas (wells 1, 3, 5, 7 and 9) reflects just linear increase of the surface mean annual temperature from 15 °C in the Lower Cretaceous to 26 °C at the present time.

Table 2.2 Tectonic and maturation history of the sedimentary basins in the eastern passive margin of India: comparison between shallow and deep shelf

Well number	1 (GS-41-1)	2	3 (GS-5-1)	4	5 (KB-4-1B)	6	7 (MND-5)	8	9 (NEC-1)	10
Zsea (m)	10	2800	90	2800	70	2850	75	2000	80	1900
Zg-h (m)	0	378	0	388	0	366	0	379	0	329
β	1.21	1.92	1.27	2.13	1.04	2.29	1.21	1.61	1.13	2.70
tb (My)	144	144	144	144	286	144	144	144	144	144
zs (m)	6000	9100	8,000	10,200	3800	9850	3700	10,000	5700	16,100
Ro (%)	2.07	2.48	3.88	3.32	1.05	3.49	0.76	2.41	1.13	4.69
Zow (km)	1.89–4.64	2.94–6.61	1.57–4.07	2.60–6.07	1.67–3.80	2.57–5.90	2.35–3.70	3.40–7.45	2.27–5.70	3.10–6.70
tow (My)	15–90	32.6–88	42–70.6	31–74.6	129–286	25–79.6	63.5–144	17.3–64.3	9–144	4.9–38

Remarks Numbers of the wells correspond to Fig. 2.3. tb, zs and Ro are the age, depth and maturity (vitrinite reflectance) of sedimentary rocks at the base of sedimentary cover. *Zow* and *tow* the depth and age of the rocks at roof and base of "oil window" ($0.50 \leq \text{Ro} \leq 1.30$ %), *Zsea* modern depth of sea bottom, β is total amplitude of thinning of the consolidated crust. *Zg-h* depth of lower boundary of zone for the methane gas hydrate stability (its upper boundary is the sea bottom, z = 0 m)

Paleoclimatic curve in the deep shelf (pseudo-wells 2, 4, 6, 8, and 10) is determined mainly by change in bottom temperature related to the variations in the sea depth (Figs. 2.5 and 2.6).

The distribution of the basement and sediment rock densities with depth is calculated at each time step of the Basin development over entire depth interval of computation. In addition, variations in tectonic subsidence of the Basin are computed during its burial history by two methods (Sects. 1.2 and 1.3; Fig. 2.7). In the first (solid line 2 in Fig. 2.7), tectonic subsidence is calculated by removing sediment and water load on the basement surface according to Eq. (1.11). In the second method (dashed line 3 in Fig. 2.7) changes in amplitude of the tectonic subsidence relative to its initial value are computed by considering the time-dependent variations in density distribution of the basement rocks (Eq. (1.13)). If isostatical response of the lithosphere on external and internal load is assumed, both tectonic variations presented by the curves 2 and 3 in Fig. 2.7 must coincide. We fit the amplitude and duration of thermal activation and stretching of the lithosphere to ensure this coincidence (Sect. 1.3). Therefore, the GALO program allows an analysis of the thermal evolution of the basins which had been undergone by repeated phases of the lithosphere heating and extension, and is not limited to simple models of the lithosphere cooling (see Sect. 1.3).

2.2.2 *Thermal and Maturation Histories of Sedimentary Basins in the Eastern Shelf of India: Results of Modeling*

The reconstructed thermal history of the margin lithosphere is demonstrated in Fig. 2.8 on the example of the well 1 (well GS-41-1) and pseudo-well 2 presented shallow and deep shelf of the Krishna-Godavari Basin correspondingly (Fig. 2.3). Figure 2.8a, c show variations in heat flow through the surfaces of sedimentary blanket (solid line) and the basement (dashed line). In our reconstructions, heat flow at the Basin initiation was about 120 mW/m^2. It is close to mean heat flow in axial zones of continental rifting. The history of the Basin tectonic subsidence differs considerably in the deep and shallow-water offshore areas (Figs. 2.7 and 2.8). According to our analysis, an amplitude of lithosphere extension, β, is 1.21 in the area of the well 1 (GS-41-1) with sea depth of about 10 m, whereas β reaches 1.92 in the pseudo-well 2 with sea depth of about 2800 m (Fig. 2.7; Table 2.2). In the lithosphere of the deep shelf, the crustal thickness reduces from an initial value of 40 to 29 km at present time. The later includes 9.1 km of the modern sedimentary cover (see "MOHO" line in Fig. 2.7b). This reduction in thickness of the consolidated crust ensured the deepening of the sea up to 2.8 km in the Cretaceous. At the same time, the crust in the shallow-water offshore reduces only to 38 km with thickness of sedimentary blanket 6 km (left Fig. 2.7b). High amplitude of lithosphere stretching in the deep shelf corresponds to great sea depth (Table 2.2).

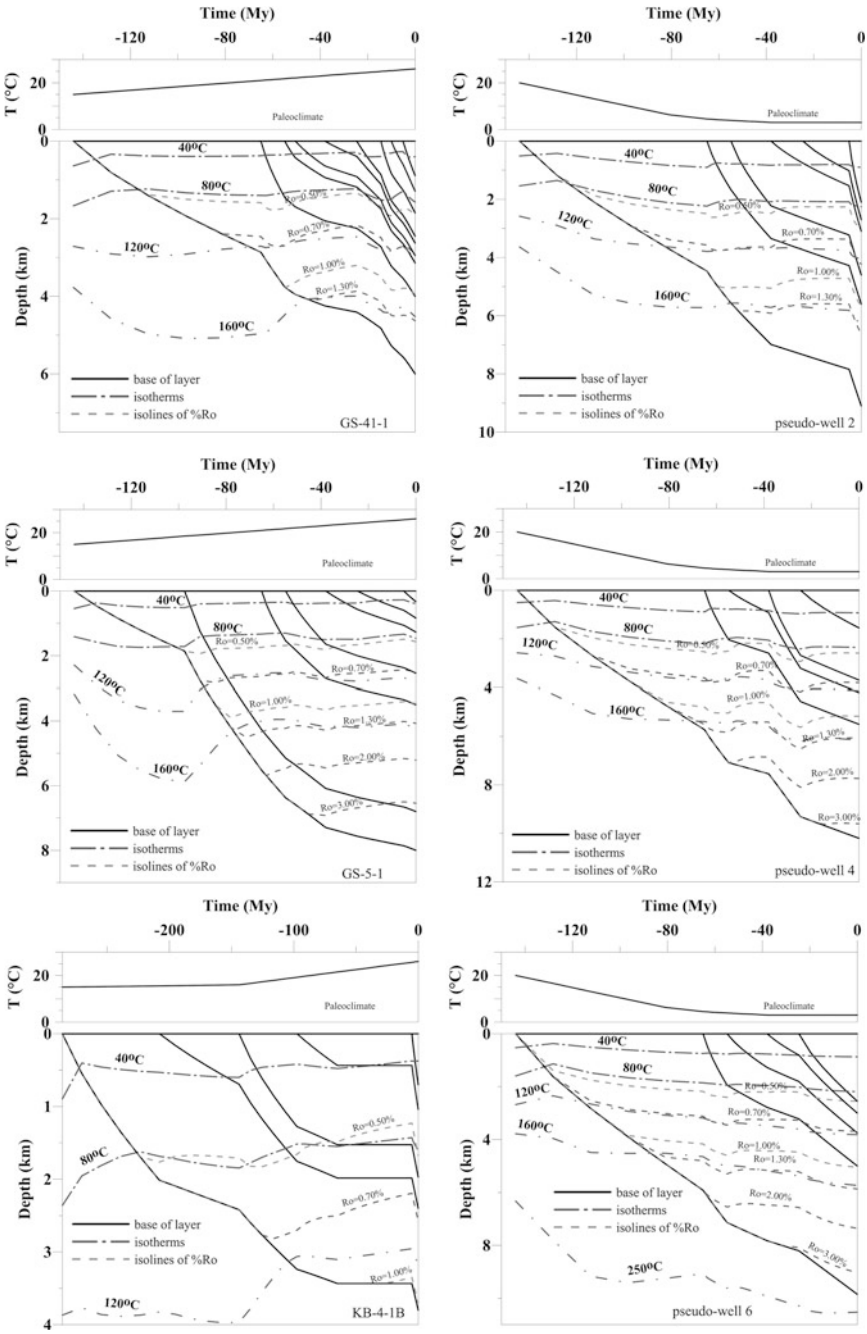

Fig. 2.5 Variations in mean-annual surface temperature (mean-annual temperature at sea bottom) (*upper figures*) and burial, thermal and maturation histories (*lower figures*) of sedimentary sections in the Krishna-Godavari Basin (wells *1*, *3*, *5*, pseudo-well *2*, *4*, *6*; Fig. 2.3)

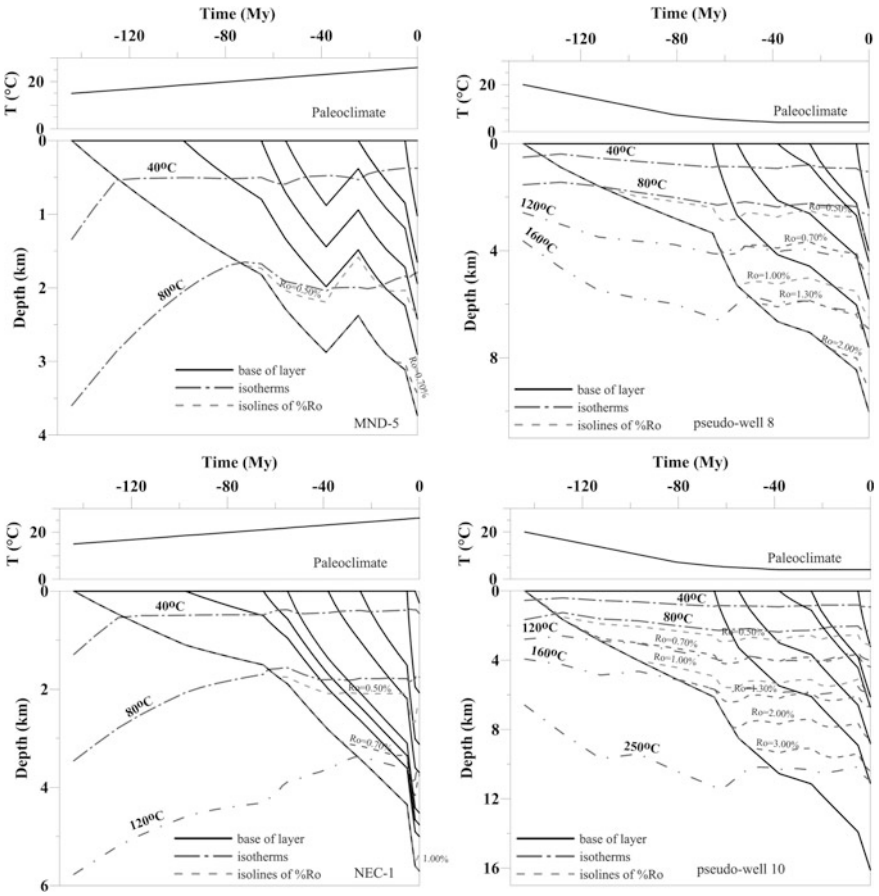

Fig. 2.6 Variations in mean-annual surface temperature (mean-annual temperature at sea bottom) (*upper figures*) and burial, thermal and maturation histories (*lower figures*) of sedimentary sections in the Mahanadi Basin (wells *7*, *9*, pseudo-well *8*, *10*; Fig. 2.3)

But highest amplitude of extension $\beta = 2.7$ is reached in pseudo-well 10 in north-western part of the Bay of Bengal with sea depth of 1900 m. Such amplitude corresponds to depth of the Mochorovich boundary about 31 km and is related partly to anomalous thickness of sedimentary section (more than 16 km).

The calculated temperature distribution in present-day sedimentary section of the area 1 (GS-41-1) is shown in Fig. 2.9. by solid line. Two temperatures measured in the GS-41-1 well are shown by stars. The GS-5-1 and GS-41-1 wells are located in a relatively narrow area (may be local fracture) of the south-eastern coast of India with a high modern heat flow [27, 28]. They are characterized by higher temperatures at the same depth compared with pseudo-wells 2 and 4.

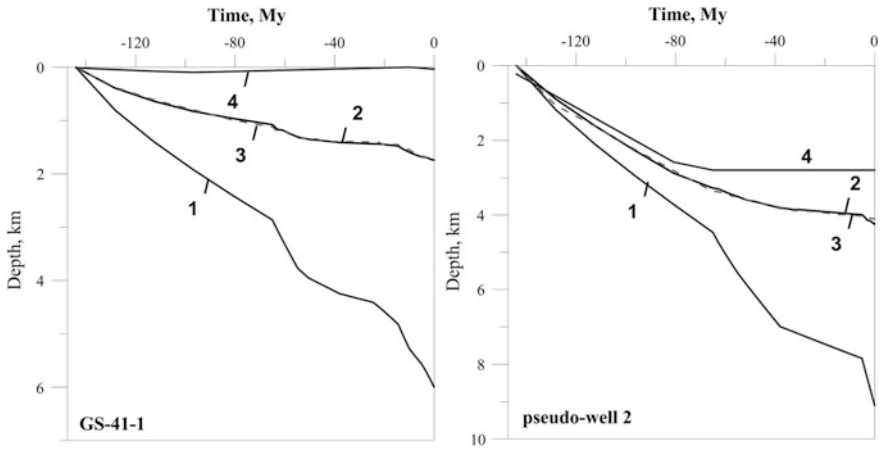

Fig. 2.7 Tectonic subsidence of the basement surface in the areas of the well 1 (well GS-41-1) and pseudowell 2 located in the shallow and deep shelf of the Krishna-Godavari Basin (Fig. 2.3) and calculated in the local isostasy approach. *1* depth of the base of sedimentary cover (or the depth of the basement surface) computed by usual "backstripping" procedure; *2* (*upper solid line*)—tectonic subsidence of the basin calculated by removing the sediment and water load from the basement surface (Eq. (1.11)); *3* (*upper dashed line*)—tectonic subsidence calculated by consideration of time-variations in density profile in the basement (Eq. (1.13)); *4* sea depth

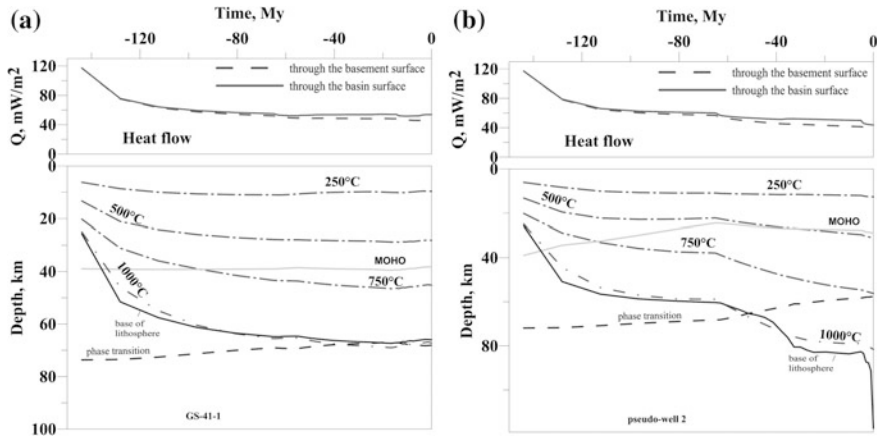

Fig. 2.8 Variations in heat flow (**a**) and thermal state of the lithosphere (**b**) reconstructed numerically in the GALO system for the well 1 (well GS-41-1) and pseudowell 2 located in shallow and deep shelf of the Krishna-Godavari Basins (Fig. 2.3). **a** The heat flows through the sediment and basement surfaces; difference between the flows is mainly due to radiogenic heat generation in sediments. **b** *Long dashed* lines are isotherms. *The "moho"-line* is the base of the crust. *The "phase transition" line* is the location of "spinel peridotite—garnet peridotite" compositional transition in the mantle (Eq. (1.16)). *Base of the lithosphere*—depth of intersection of the current geotherm of the lithosphere with the solidus of peridotite with 0.2 % H_2O (Eq. (1.4))

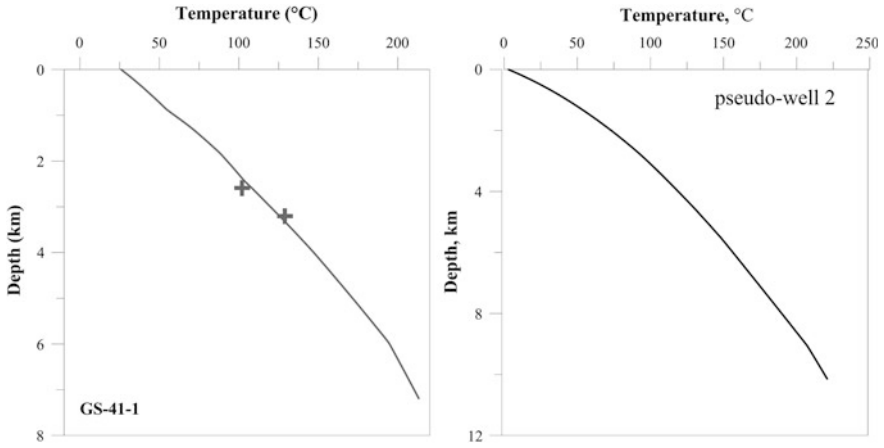

Fig. 2.9 Calculated (*solid lines*) and measured (*crosses*) temperatures with depth in the modern sedimentary sections of the well 1 (well GS-41-1) and pseudowell 2 located in the shallow and deep shelf of the Krishna-Godavari Basin (Fig. 2.3)

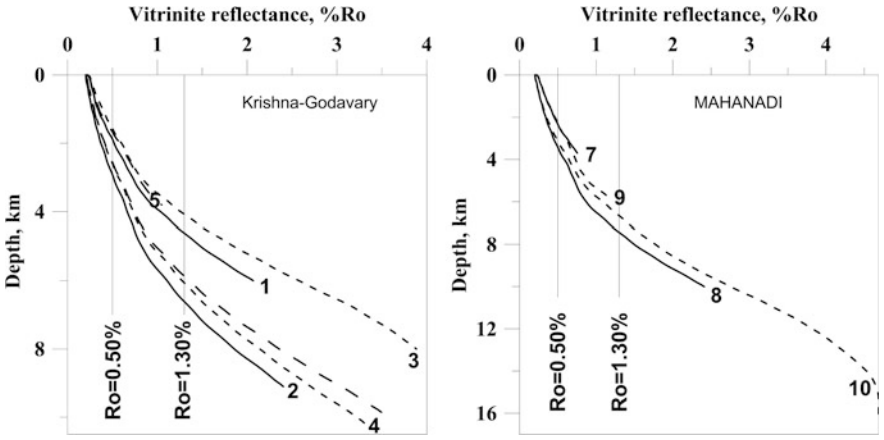

Fig. 2.10 Calculated variations in vitrinite reflectance with depth in modern sedimentary sections of Krishna-Godavari Basin (wells 1, 3, 5, pseudo-wells 2, 4, 6; *left figure*) and Mahanadi Basin (wells 7, 9, pseudo-wells 8, 10; *right figure*). Numbers correspond to numbers of wells and pseudo-wells in Fig. 2.3. The oil window ($0.50 \leq Ro \leq 1.30$ %) is shown by *vertical lines*

Main results of the modeling in different areas of the Krishna-Godavary and Mahanadi Basins are presented in Figs. 2.5, 2.6 and 2.10, Table 2.2. They give an opportunity to compare changes in temperature regime of sedimentary sections and degree of maturation of organic matter in sedimentary rocks at the transition from shallow to deep-water offshore.

Our modeling suggests that sedimentary rocks in the shallow shelf are hotter than the rocks at the same depth in the deep shelf. However, the

situation is reversed for rocks of the same age. These rocks in deep-water offshore are characterized by greater depth, temperatures and maturity level, than the rocks of the same age in the shallow shelf. This trend is obvious for areas 5–10 but it is less obvious for areas 1–4 because the wells 1 and 3 are located in a local region of elevated heat flow [27, 28]. The modeling shows that intensive sedimentation from the Gang River in the Miocene-Pliocene led to considerable subsiding of "oil window" in both basins (Table 2.2), but its influence is more pronounced in the Mahanadi basin, especially in the pseudo-well 10 (Figs. 2.5, 2.6 and 2.10, Table 2.2). Top of the "oil window" (Ro = 0.50 %) in present section is deeper in the deep offshore than in the shallow one by nearly 1 km, whereas base of the "window" (Ro = 1.30 %) is deeper by 1–3.5 km in comparison with the shallow shelf. As a whole, the rocks located within the "oil window" are younger in the deep shelf areas (Figs. 2.5, 2.6 and 2.10; Table 2.2). Summing up the results of the section, we note that the deepening of the "oil window" with distance from the coast, and with approach to the mouth of the Ganges River is mainly due to increase of the Miocene sedimentation rates (Figs. 2.4, 2.5 and 2.6).

2.3 A Comparison Temperature and Maturation Histories of the Probable Source Rocks in the Basins in the Shallow and Deep-Sea Areas

This section gives a short comparison between temperature and maturation conditions in the probable source rocks of the shallow- and deep-sea areas in the Krishna- and Mahanady-Basins. It is often found in the literature an assessment of maturation degree of organic matter not only by computation or measurement of vitrinite reflectance, but also by estimation of the transformation degree in clay minerals (smectite to illite transition). We used the results of our simulation to compare both methods of maturity estimation.

2.3.1 Estimation of Smectite/Illite Ratio During Diagenesis of Clays

Evaluation a degree of transformation smectite to illite computing a ratio smectite/illite is often used together with calculation of vitrinite reflectance to estimate organic matter maturity. Smectite to illite transition is the most important mineral reactions during diagenesis of clay. Usually, smectite is found in fine-grained sediments at shallow depths. During diagenesis and deeping, smectite generally turns into illite, releasing silicon, water and cations. Earlier one-step

models of the smectite to illite transformation [29–31] did not demonstrate a good agreement with observations at application to geological time scale. The two-step model of smectite transformation proposed in the papers [32–34] describes geological situation considerably better than the previous one-step models. We use the two-step model of Velde and Vasseur [32–34] to compute a change of fraction of mectite in mixture smectite/illite during burial history of the probable source formations. Our results give an opportunity to compare the values of vitrinite reflectance, Ro%, with corresponding ratios Smectite/Illite and estimate a possibility to use this relationship in basin analysis. In the model of [33], take a place two reactions: X → Y (the first reaction) and Y → Z (the second reaction). At the first reaction, smectite layer belong to X becomes illite. Therefore X disappears but the new illite joints with nightbouring smectite forming new sub-row Y consisted of one smectite + one illite. This reaction is clear to correspond to transformation of initial mineral (R = 0) with non-ordering smectite to ordering mineral (S = 1). If only the first reaction (X → Y) would be active, it could lead to the mineral R = 1 with 50 % smectite. But there is the second reaction (Y → Z) when smectite layer belong to Y becomes illite and forms sub-layer Z (two illites). This reaction describes the process of gradual illitization of mineral R = 1 and it competes with the first reaction. Then, the equations ruled the reactions can be described as:

$$dX/dt = -\,k_1 \cdot X; \quad \text{where } k_1 = A_1 \cdot \exp(-E_1/RT(t))$$

$$dY/dt = k_1 \cdot X - k_2 \cdot Y, \quad \text{where } k_2 = A_2 \cdot \exp(-E_2/RT(t))$$

Then, total content of smectite in rock is:

$$S(t) = X(t) + (Y(t)/2)$$

Initial values $X = X_0$, $Y = Z = 0$.
Solution of the above equations is:

$$X(t) = X_0 \cdot \exp[-\int_0^t k_1(t') \cdot dt']$$

$$Y(t) = X_0 \cdot \exp[-\int_0^t k_2(t') \cdot dt'] \times \int_0^t k_1(t') \cdot \exp(\int_{'0}^{t'} [k_2(t'') - k_1(t'')] \cdot dt'') \cdot dt'$$

Parameters of two reactions (A_1, E_1, A_2, E_2) are determined from comparison of geological data with the values S calculated in the model. According to [34] they are:

$$\mathrm{Ln}(A_1) = 24.4 \pm 0.6 \cdot \mathrm{Ln}\,(\mathrm{Ma}^{-1}); \quad E_1 = 76.8 \pm 1.7 \text{ kJ/mole}$$

$$\mathrm{Ln}(A_2) = 3.6 \pm 0.6 \cdot \mathrm{Ln}\,(\mathrm{Ma}^{-1}); \quad E_2 = 22.2 \pm 2.0 \text{ kJ/mole}$$

The two-step model with the above parameters was used in our computations. It describes the observed geological data (S) better than the previous one-step model.

2.3.2 *Comparison of Thermal and Maturation Histories of the Probable Source Rocks*

Figure 2.11 demonstrates a comparison in temperature histories of the main probable source rocks in the shallow (w. GS-41-1) and deep (pseudo-well 2) shelf of the Krishna-Godavary Basin.

Figures 2.12 and 2.13 demonstrates similar comparison for maturity degree of organic matter and transformation degree in clay minerals. The comparison shows that the probable source rocks of Cretaceous and Eocene are buried at greater depth and characterized by more high temperatures in the deep-sea areas than in the shallow-sea ones.

The comparison shows that the probable source rocks of Cretaceous and Eocene located at great depth in the deep shelf are characterized by more high maturity level and clay transformation ratios than in the shallow shelf.

Figures 2.14, 2.15 and 2.16 demonstrate similar comparison for two areas of the Mahanadi Basin. The great difference in the burial histories of the NEC-1 and pseudo-well 10 areas (Fig. 2.6) results in considerable difference of these areas in thermal and maturity histories of the formations.

The probable source rocks of Cretaceous and Eocene are burryed at greater depth and characterized by more high temperatures in the deep-sea areas in the Mahanadi Basin than the rocks in the shallow-sea areas of the Basin. This effect is especially considerable close to the Gange mouth.

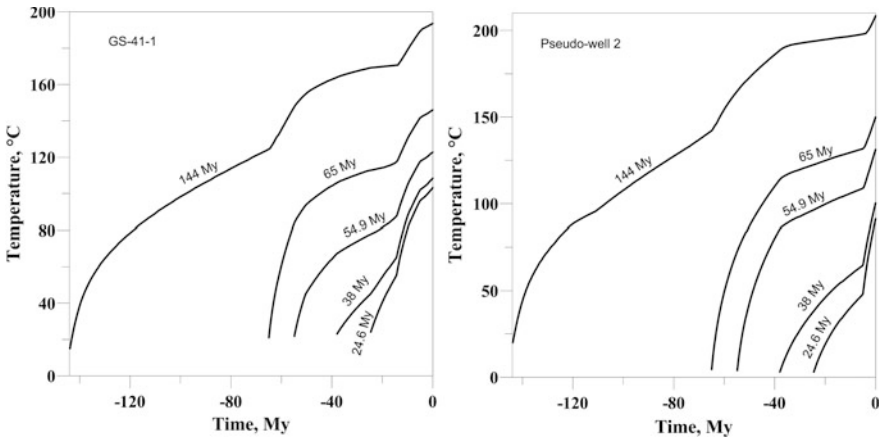

Fig. 2.11 Comparison between temperature histories of probable source rocks in the shallow (w. GS-41-1) and deep (pseudo-well 2) sections of the Krishna-Godavary Basin

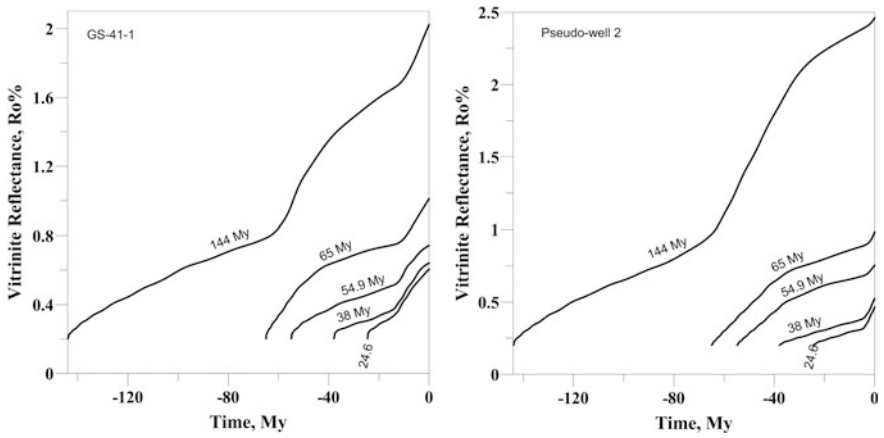

Fig. 2.12 Comparison of catagenesis history of probable source rocks in the Krishna-Godavary Basin in the shallow (GS-41-1) and deep (pseudo-well 2) areas

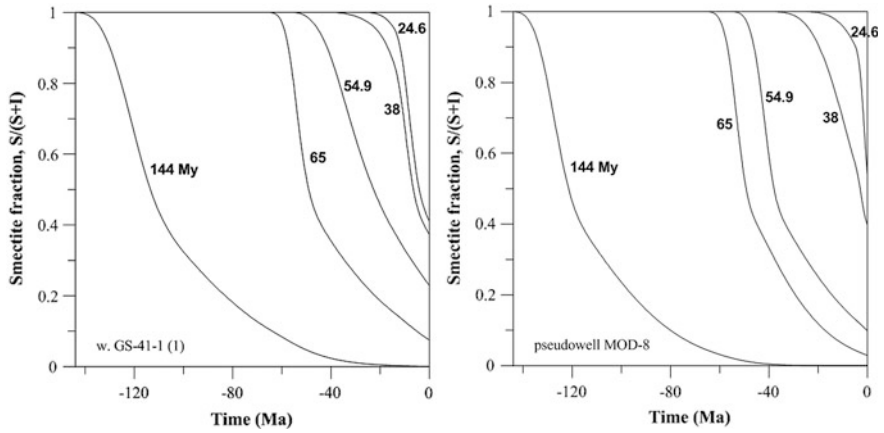

Fig. 2.13 Comparison between smectite content in the burial history of the probable source rocks in the Krishna-Godavary Basin in the shallow (GS-41-1) and deep (pseudo-well 2) areas

2.3.3 Correlation Between Smectite/Illite Transformation and Ro%

It would be interesting even for the basins of the Eastern shelf of India to establish whether there is a definite correlation between vitrinite reflectance %Ro and the ratio S/(S + I) in clays. Correlation between Smectite/Illite ratio and rock temperatures can be seen from comparison of results in Figs. 2.11 and 2.14 with Figs. 2.13 and 2.16. Hunner [35], analyzing the process in the Mexico Bay says that the start of the smectite to illite transformation corresponds to the temperatures from 58 to 92 °C.

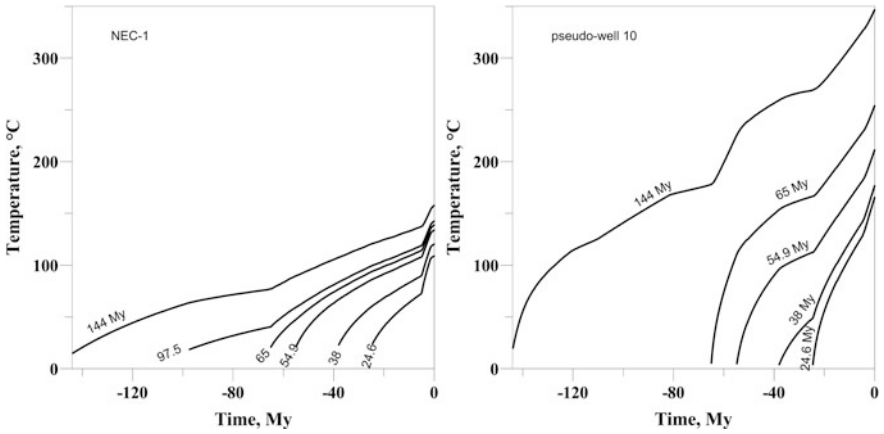

Fig. 2.14 Comparison of temperature histories of probable source rocks in the Machanady Basin in the NEC-1 and pseudo-well 10 areas

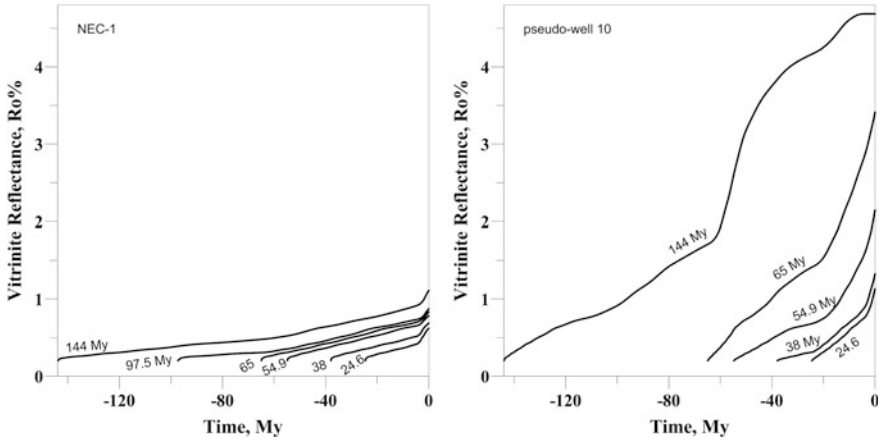

Fig. 2.15 Comparison of catagenesis histories of probable source rocks in the Machanady Basin in the NEC-1 and pseudo-well 10 areas

Our calculations suggests temperatures from 50 to 70 °C. For finish of the transformation Hunner [35] suggests wide temperature interval: from 88 to 142 °C. He says that smectite loses last water layer at the temperatures from 172 to 192 °C. The latter is in a rather good agreement with our calculations in the two-step model of clay transformation. But it is necessary to keep in mind that the process of transformation of smectite to illite is kinetic and must be ruled not only by temperature but the time too. By this reason, the correlation of smectite/illite transformation with temperature must be very approximate. It is more interesting to consider the correlation of the smectite/illite ratio with vitrinite reflectance Ro% because both

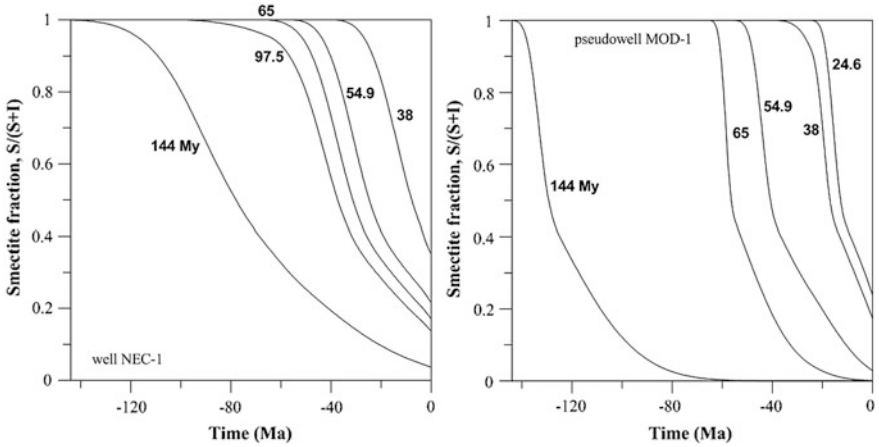

Fig. 2.16 Comparison between smectite content in the burial history of the probable source rocks in the Machanady Basin in the NEC-1 and pseudo-well 10 areas

processes of smectite transformation and vitrinite maturation are the kinetic processes. Figure 2.17 presents the fraction of smectite in Smectite/Illite mixture calculated in two-step model of smectite transformation as a function of vitrinite reflectance for different sedimentary formations of the GS-41-1 well (left Fig. 2.17) and for the Low Cretaceous formations of southernmost and northernmost areas under study (wells GS-41-1, Nec-1, and pseudo-wells 2 and 10 (right Fig. 2.17).

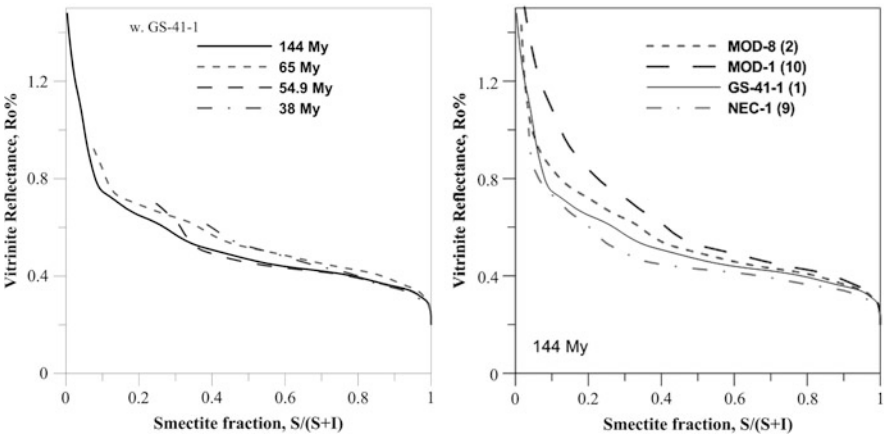

Fig. 2.17 The fraction of smectite in Smectite/Illite mixture calculated in two-step model of smectite transformation as a function of vitrinite reflectance for different sedimentary formations of the GS-41-1 well (*left figure*) and for the Low Cretaceous formations in the southernmost and northernmost areas under study (wells GS-41-1, Nec-1, pseudo-wells 2 and 10; *right figure*)

Figure 2.17 shows that at quality agreement of the curves in the left Fig. 2.17 there is considerable scattering in Ro% data at fixed ratio S/(S + I) for burial histories in different areas of the Basins (right Fig. 2.17). Figure 2.17 demonstrates that different kinetics of vitrinite maturation and Smectite/Illite transformation do not suggest an single universal relationship between Ro% and the S/(S + I) ratio.

2.4 Hydrocarbon Generation by Probable Source Rocks in Shelf Areas of the Krishna-Godavary and Mahanady Basins

Large prospects of oil and gas generation follow from the study of the source rocks in the East coast of India [8, 18, 36]. Geochemical study shows that the Cretaceous source rocks of the margin are characterized by TOC = 0.75–3.00 % and contain predominantly kerogen of type III with initial potential 100–300 mg HC/g TOC [26, 36, 37]. The Early Cretaceous shales of the Pennar formation are believed to be source rocks for the overlaying Krishna formation. As mentioned above, shales of the Middle Cretaceous Raghavapuram formation mark the first marine transgression and start of spreading. The shales of the Middle and Upper Cretaceous contain predominantly organic matter of type III with little admixture (30 %) of type II with TOC about 1.5 % [18, 36]. They are considered as good source rocks. It is believed that initial potential of these source rocks was HI = 225 mg HC/g TOC. In particularly, the Late Cretaceous shales of the Chintalapalli formation are believed to be source rocks for hydrocarbon accumulations in the Tirupati sandstones [8, 18]. Paleocene shales in the Krishna-Godavari Basin contain kerogen of type III with modern TOC $\approx$ 1.4 % whereas the same rocks in the Mahanadi Basin contain an organic matter of type III mixed with type II with TOC approximately 2 % [12]. The Eocene/Oligocene shales of the Vadaparru formation are considered as source rocks for hydrocarbon accumulations in the Ravva formation of the Miocene-Pliocene age. The Eocene shales in both basins are characterized by kerogen of type III with TOC = 1.5 % in the Krishna-Godavari Basin and 2 % in the Mahanady Basin. The Oligocene shales contain kerogen of type III with TOC = 2 % in the Mahanady Basin and the same kerogen mixed with type II with TOC = 2.5 % in the Krishna-Godavari Basin. Kerogen of type III with TOC = 1.3–1.5 % is typical for Miocene shales in both basins [12, 26, 37, 38].

As mentioned above, the content of organic matter in present-day sedimentary section of the Eastern margin of India can range widely: from 0.3 to 6 % [8, 18, 36]. TOC = 1.5 % was accepted in our assessments as reasonable mean value of the TOC (Tables 2.3 and 2.4). The calculated values of TOC at initiation of burial history of the formations are shown in Tables 2.3 and 2.4 in the TOCinit column. Difference between TOCinit and TOC depends on type of kerogen, its initial hydrocarbon potential and realization degree of this potential (maturity level of organic matter) [39–41]. In accordance with the above information, we suggest that

Table 2.3 Maturity level and realization history of hydrocarbon potential in sedimentary sections 1–6 in the Krishna-Godavary Basin (results of modelling)

t	Z	T	Ro	Hi	Ht	Hho	Hlo	Hoil	Hgas	TOC	TOCinit	$t_{0.5}$	$t_{1.30}$
My	m	°C	%	mg HC/g TOC						mg OM/g rock		My ago	
Pseudo-well 1 (well GS-41-1) sea depth 10 m													
144	6000	194	2.04	160	134	7.6×10^{-4}	1.02	1.02	80.6	1.5	1.73	113	42
65	4000	146	1.02	225	130	33.9	42.1	76	27.8	1.5	1.72	52	–
54.9	3140	123	0.72	225	34.9	27.3	41.2	31.5	3.2	1.5	1.55	17	–
38	2630	109	0.64	160	3.14	2.59	0.177	2.77	0.365	1.5	1.50	8.5	–
24.6	2450	103	0.61	225	5.49	4.07	0.896	4.97	0.524	1.5	1.51	6.5	–
Pseudo-well 2 sea depth 2800 m													
144	9100	207	2.37	160	144	6.7×10^{-5}	0.021	0.021	91	1.5	1.75	120	51
65	5600	149	0.96	225	114	46.8	30.1	76.9	20.4	1.5	1.69	48	–
54.9	4600	130	0.75	225	36.3	28.4	4.27	32.7	3.34	1.5	1.56	34	–
38	3100	99.5	0.52	160	0.533	0.463	0.0092	0.473	0.06	1.5	1.50	0.55	–
Pseudo-well 3 (well GS-5-1) sea depth 90 m													
144	8000	249	3.85	160	160	0	0	0	106	1.5	1.79	97	74
97.5	6800	224	3.15	225	223	0	0	0	135	1.5	1.90	87	64
65	3500	139	1.00	225	124	36.4	38.6	75	25.6	1.5	1.71	53	–
54.9	2540	111	0.70	225	21.7	17	2.69	19.7	1.96	1.5	1.52	35	–
38	1270	73	0.43	160	0.0269	0.0235	2.4×10^{-4}	0.0239	0.003	1.5	1.50	–	–
Pseudo-well 4 sea depth 2800 m													
144	10,200	230	3.28	160	158	0	0	0	104	1.5	1.78	–	–
65	5500	147	1.10	225	145	10.9	58.1	69.1	37.8	1.5	1.76	–	–
54.9	4200	129	0.75	225	37.6	29.3	4.45	33.8	3.48	1.5	1.56	–	–
38	3700	110	0.68	160	4.72	3.8	0.35	4.15	0.559	1.5	1.51	–	–
24.6	1550	58	0.35	225	0.00314	0.00184	0.00105	0.00289	0.00026	1.5	1.50	–	–

(continued)

Table 2.3 (continued)

t	Z	T	Ro	Hi	Ht	Hho	Hlo	Hoil	Hgas	TOC	TOCinit	$t_{0.5}$	$t_{1.30}$
Pseudo-well 5 (well KB-4-1B) sea depth 70 m													
286	3800	134	1.03	160	51.1	10.5	17.2	27.7	12.7	1.5	1.58	223	–
208	2400	101	0.66	160	3.59	2.94	0.226	3.17	0.421	1.5	1.51	100.5	–
144	1970	91	0.57	160	1.21	1.05	0.0245	1.075	0.136	1.5	1.50	68.5	–
Pseudo-well 6 sea depth 2850 m													
144	9850	240	3.45	160	159	0	0	0	105	1.5	1.78	133	86
65	5000	144	0.97	225	116	45.3	31.3	76.6	21.2	1.5	1.70	49	–
54.9	3750	118	0.71	225	22.7	17.8	2.79	20.6	2.05	1.5	1.52	17	–
38	3000	100	0.57	160	1.41	1.22	0.0343	1.25	0.16	1.5	1.50	5.7	–
24.6	2550	90	0.50	225	0.745	0.494	0.184	0.678	0.068	1.5	1.50	–	–

Remarks t age of the formation in My. *z* depth in m. *T* calculated temperature in °C. *Ro* calculated value of vitrinite reflectance in % (z, T, Ro-values belong to the present-day section of the basin, t = 0 in Figs. 2.5 and 2.6). *Hi* initial potential of HC generation by the rocks of the formation; *Ht* total realization of the potential, *Hho*, *Hlo* and *Hoil* generation of heavy and light oil and total oil correspondingly; *Hg* gas generation (in mg HC/g TOC). The values of Ht, Hho, Hlo, Hoil and Hgas present total generation of corresponding hydrocarbons to present time computed under condition that generated hydrocarbons have not leaved the porous space of the source rocks. t_1, t_2 times of enter and leaving the "oil windows" (0.50 % $\leq$ Ro $\leq$ 1.30 %) by the rock. In the Tables 2.3 and 2.4, initial potential HI = 225 mg HC/g TOC corresponds to the mixture of 30 % standard marine kerogen of type II with initial hydrocarbon potential 377 mg HC/g TOC and 70 % standard kerogen of type III with initial hydrocarbon potential 160 mg HC/g TOC; HI = 160 mg HC/g TOC corresponds to the standard kerogen of type III with initial hydrocarbon potential 160 mg HC/g TOC. The kinetic spectra for HC generation by standard kerogen of types II and III in the frame of 4-th fraction system (heavy and light oil, gas and coke) were used in computations of HC generation (see text)

Table 2.4 Maturity level and realization history of hydrocarbon potential in sedimentary section 7–10 in the Mahanady Basin (results of modelling)

t	Z	T	Ro	Hi	Ht	Hho	Hlo	Hoil	Hgas	TOC	TOCinit	$t_{0.5}$	$t_{1.30}$
My	m	°C	%	mg HC/g TOC						mg OM/g rock		My ago	
Pseudo-well 7 (well MND-5) sea depth 75 m													
144	3730	125	0.75	160	10.4	7.92	1.11	9.03	1.31	1.5	1.52	70.5	–
97.5	2900	103	0.59	225	4.3	3.15	0.737	3.89	0.414	1.5	1.51	11.5	–
65	2420	92	0.51	225	0.975	0.659	0.226	0.885	0.090	1.5	1.50	0.5	–
54.9	1940	83	0.44	225	0.197	0.122	0.0582	0.181	0.017	1.5	1.50	–	–
Pseudo-well 8 sea depth 2000 m													
144	10,000	211	2.37	160	145	6.6×10^{-5}	0.0206	0.0206	91.4	1.5	1.75	107	46
65	7600	179	1.34	225	175	0.284	71	71.3	53.2	1.5	1.82	54	0.6
54.9	5800	139	0.82	225	64.5	47.5	8.45	55.9	6.67	1.5	1.60	27	–
38	4400	115	0.64	160	3.08	2.55	0.171	2.72	0.357	1.5	1.50	4.4	–
24.6	4000	107	0.58	225	3.90	2.85	0.671	3.52	0.375	1.5	1.51	2.0	–
Pseudo-well 9 (well NEC-1) sea depth 80 m													
144	5700	158	1.12	160	66.2	6.19	25.5	31.7	18.4	1.5	1.61	59.5	–
97.5	5000	143	0.88	225	85.2	54.4	14.4	68.8	10.7	1.5	1.64	35.5	–
65	4760	139	0.83	225	70.9	50.6	9.88	60.5	7.7	1.5	1.61	30.5	–
54.9	4520	134	0.79	225	52.7	40.3	6.38	46.7	5.11	1.5	1.58	24	–
38	3700	121	0.69	160	5.81	4.63	0.477	5.1	0.694	1.5	1.51	7	–
Pseudo-well 10 sea depth 1900 m													
144	16,100	342	4.69	160	160	0	0	0	106	1.5	1.79	138	80.7
65	11,100	251	3.32	225	224	0	0	0	136	1.5	1.93	56.5	27
54.9	8800	209	2.08	225	206	5.7×10^{-4}	0.863	0.864	118	1.5	1.89	39	7.7
38	6700	175	1.29	160	94.1	0.678	38.4	39.1	29.8	1.5	1.66	16.5	–
24.6	6100	164	1.10	225	148	14.1	57.9	72.0	37.9	1.5	1.76	12.6	–

See remarks to Table 2.3

kerogen of type III with HI = 160 mg HC/g TOC was typical for Lower Cretaceous (144 My) and Upper Eocene (38 My) rocks, whereas mixture of 30 % kerogen of type II (HI = 377 mg HC/g TOC) with 70 % kerogen of type III (HI = 160 mg HC/g TOC) characterizes organic matter of the Middle and Upper Cretaceous (65 My), Upper Paleocene (54.9 My) and Upper Oligocene (24.9 My) rocks in Tables 2.3 and 2.4 and Figs. 2.11, 2.12, 2.13 and 2.14. Algorithms for computing the yields of different hydrocarbon fractions are discussed in detail in [42, 43] and Chap. 3.

Tables 2.3 and 2.4 show the capacity of the main source rocks in the Eastern continental margin of India to generate heavy and light oil and gas estimated in the GALO system of basin modeling. In addition to age, the depth, temperature and maturation level of the rocks, computed for present-day section of the basin, are in these Tables. Ht, Hho, Hlo, Hoil, and Hgas in Tables 2.3 and 2.4 are total generation of hydrocarbons, heavy and light oil, oil and gas to present time, computed in the frame of the 4-fractional model of kerogen cracking (light and heavy oil, gas and coke). We used the kinetic spectra for cracking of kerogen of types II and III in the 4-fractional model, that was developed in the French Oil Institute (Paris) and are applied in a widespread modeling package MATOIL. Note again that Tables 2.3 and 2.4 present the total generation of hydrocarbons of different types reached to current time. Parameters $t_{0.5}$ and $t_{1.30}$ in the tables are the calculated times of entering in "oil window" (Ro = 0.50 %) and leaving it (Ro = 1.30 %). Now we consider shortly the generation properties of the source rocks beginning with the Cretaceous.

Variations in maturity level of organic matter during burial history of the rocks at the base of the Cretaceous proposed by modeling for different areas of the East margin are shown in Figs. 2.5 and 2.6. These figures and Tables 2.3 and 2.4 allow comparison of maturity levels of rocks in the shallow- and deep-water offshore. The modeling shows that organic matter in the Lower Cretaceous rocks reached rather high maturity level (Ro > 2.3 %) in all considered areas of the deep-water offshore (pseudo-wells 2, 4, 6, 8, 10). Such maturity level corresponds to total destruction of heavy and light oil as result of secondary cracking (Fig. 2.11; Tables 2.3 and 2.4). Destruction of oil occurred in deep offshore not later than the Oligocene (Fig. 2.18). Close situation is for the pseudo-wells 1 (w. GS-41) and 3 (w. GS-5-1) located in the shallow offshore within the deep aulocagen in the region with the non-typical high modern heat flow (Fig. 2.18; Table 2.3). Here, the Low Cretaceous rocks are gas prone (Table 2.3). But in others pseudo-wells of shallow offshore (5, 7, 9), these rocks are characterized by a considerable lower maturity level of organic matter (especially in the KB-4-1B well, located on local horst) and could be oil prone (Fig. 2.18; Tables 2.3 and 2.4).

Figure 2.19 presents a history of realization of hydrocarbon potential of the Upper Cretaceous source rocks on the example of the same pairs of pseudo-wells: 1, 2 and 9, 10. Tables 2.3 and 2.4 and Fig. 2.19 show that the Upper Cretaceous rocks are oil prone. They are actively generating oil. The exception is the pseudo-wells 5, 7 and 10. In the first two, organic matter of the Upper Cretaceous rocks is immature. In pseudo-well 10, the Upper Cretaceous rocks occur at the

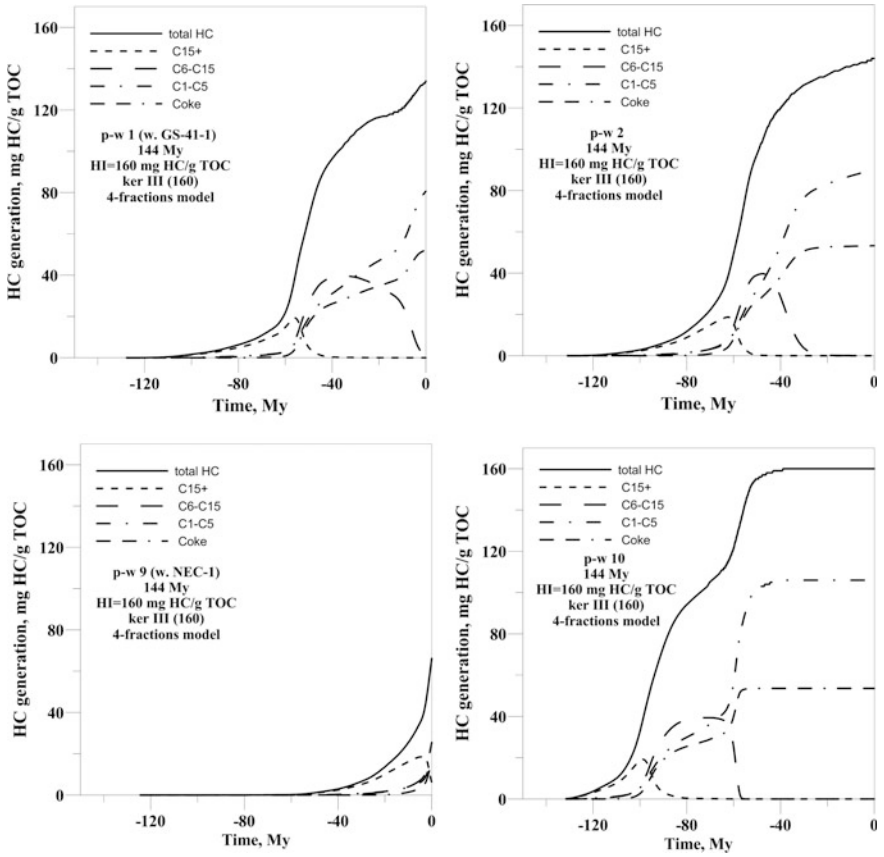

Fig. 2.18 Realization of hydrocarbon potential by the probable Lower Cretaceous source rocks of the Krishna-Godavary and Mahanadi Basins: comparison between the shallow (pseudo-wells 1 and 9 (wells GS-41-1 and NEC-1) and deep (pseudo-wells 2 and 10) areas of the eastern passive margin of India. Computations were carried out in the 4-fractions model of kerogen cracking (heavy and light oil, gas and coke)

depth more than 11 km. Their organic matter is over-mature and rocks are gas prone (Fig. 2.19; Table 2.4).

Realization of hydrocarbon potential of the Upper Paleocene source rocks is shown in Tables 2.3 and 2.4 and Fig. 2.20. In pseudowell 5 (w. KB-4-1B), located on local horst, and in shallow pseudo-well 7 (w. MND-5), maturity level of organic matter of the Upper Paleocene rocks does not exceed 0.50 % and hydrocarbon generation here is negligible (Tables 2.3 and 2.4). In pseudo-wells 1 (w. GS-41) and 3 (w. GS-5-1), located within the deep aulacagen in the region with high modern heat flow, and also in pseudo-wells 2, 4, 6, 8, 9 (w. NEC-1) maturity level ranges from 0.7 to 0.8 % and the Upper Paleocene rocks generate predominantly heavy oil. In the pseudo-well 10, these rocks are buried up to depth of 8000 m due

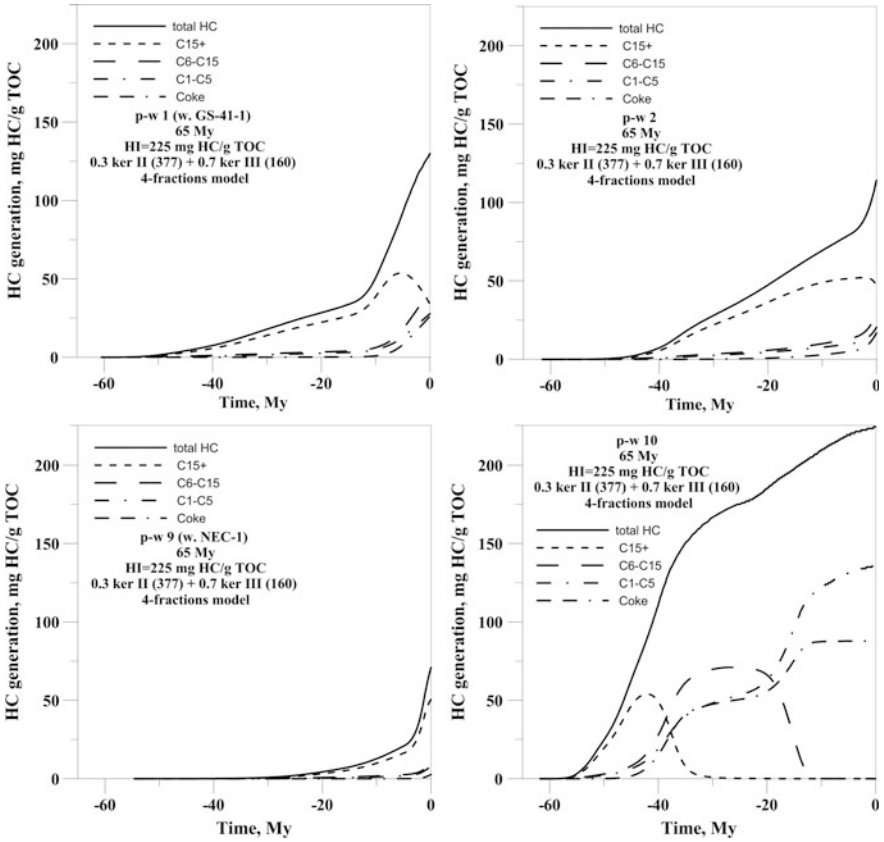

Fig. 2.19 Realization of hydrocarbon potential by probable Upper Cretaceous source rocks of the Krishna-Godavary and Mahanadi Basins: comparison between the shallow (pseudo-wells 1 and 9 (wells GS-41-1 and NEC-1)) and deep (pseudo-wells 2 and 10) areas of the eastern passive margin of India. Computations were carried out in the 4-fractions model of kerogen cracking (heavy and light oil, gas and coke)

to fan sediments of the Gang River and are gas prone at present time. However, it is possible that these rocks have generated significant volume of light oil that could migrate into upper horizons and thus avoid secondary cracking in matrix of the source rocks. Figure 2.20 shows that this possibility is quite likely in the sedimentary section of the pseudo-well 10, because the destruction of light oil remaining in the matrix of the source rocks of the Upper Paleocene, took place relatively recently, in the last 5–8 million years.

Hydrocarbon generation by the Eocene and Oligocene probable source rocks is very limited in all considered areas of the shallow and deep offshore due to low maturity level of organic matter in these rocks that does not exceed 0.70 % (Tables 2.3 and 2.4). The exception is again the area of pseudo-well 10, where avalanche sedimentation from the fan of the Gang River buried the Oligocene and

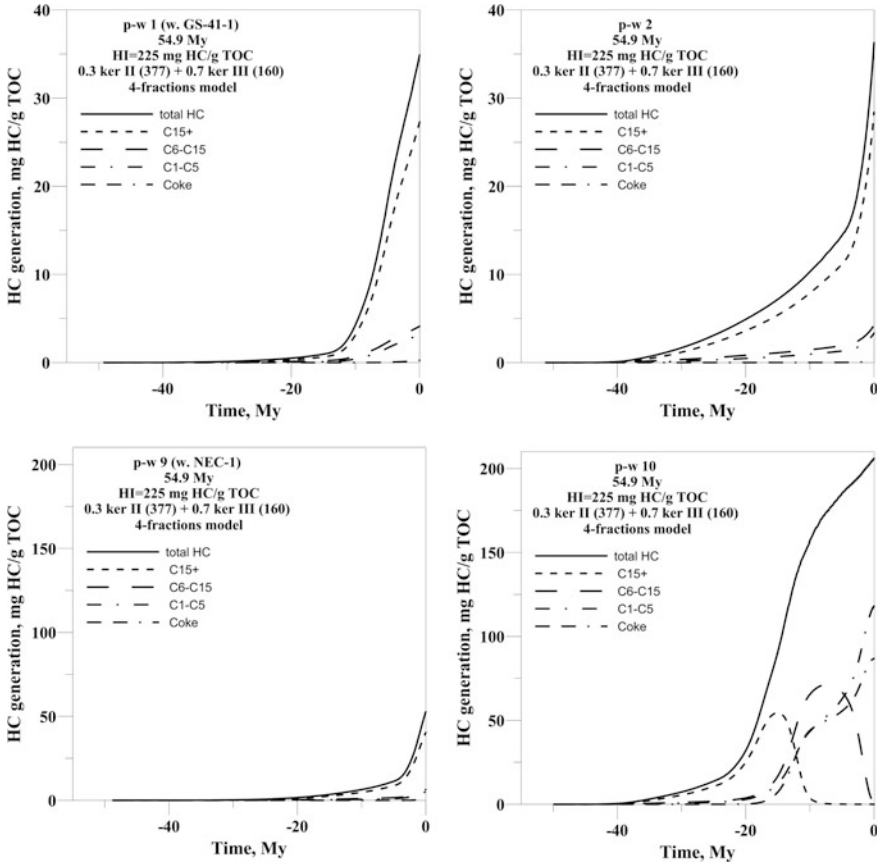

Fig. 2.20 Realization of hydrocarbon potential by probable Upper Paleocene source rocks of the Krishna-Godavary and Mahanadi Basins: comparison between the shallow (pseudo-wells 1 and 9 (wells GS-41-1 and NEC-1)) and deep (pseudo-wells 2 and 10) areas of the eastern passive margin of India. Computations were carried out in the 4-fractions model of kerogen cracking (heavy and light oil, gas and coke)

Eocene rocks at depth more 6 km and increased maturity level up to 1.1 % (Table 2.4). Table 2.4 and Fig. 2.21 show that the rocks of the Upper Eocene with kerogen of type III can generate light oil and gas, whereas the Upper Oligocene rocks with admixture of kerogen of type II generate more light oil than gas.

As a whole, Tables 2.3 and 2.4 and Figs. 2.18, 2.19, 2.20 and 2.21 demonstrate great variations in hydrocarbon generation and maturity level of probable source rocks depending on the age of formation and position of the area under study within the offshore of the Eastern continental margin of India.

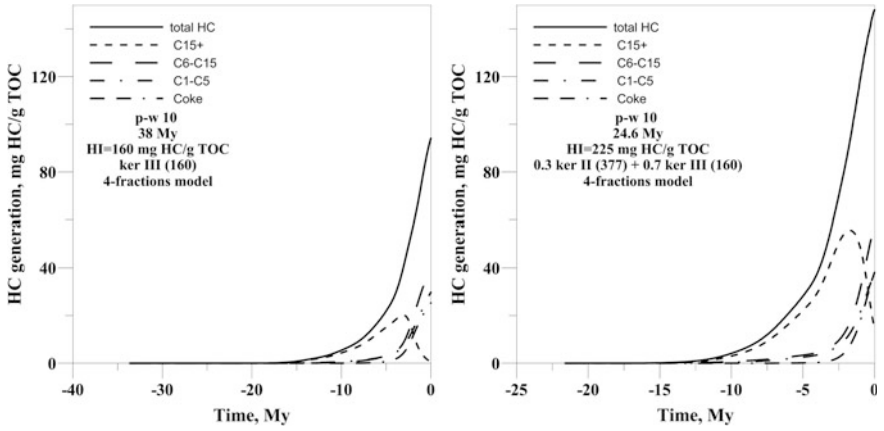

Fig. 2.21 Realization of hydrocarbon potential by the Upper Eocene and Upper Oligocene probable source rocks of the pseudo-well 10 in deep offshore of the Mahanadi Basin. Computations were carried out in the 4-fractions model of kerogen cracking (heavy and light oil, gas and coke)

2.5 Conclusion

Analysis of the basin tectonic subsidence suggests that the amplitude of the lithosphere stretching increases from $\beta = 1.03–1.3$ in shallow-water offshore to $\beta = 1.7–2.9$ in the deep-water offshore. As a result, the crustal thickness in the deep-water area reduced from initial value of 40 km to 25–29 km at present time (including rather thick sedimentary cover). At the same time, the sea depth increased from 50–100 m to 2–3 km. The degree of the lithosphere stretching and also the distance of the studied area from the fan of Gang River are the main factors caused the difference in burial, thermal and maturation histories of sedimentary sections in the shallow and deep-water offshore. The modeling suggests that maturity level of organic matter increases considerably toward the ocean together with the burial depth of rocks. Intensive sedimentation from the river Ganges in the Miocene-Pliocene led to considerable subsiding of "oil window" in the Krishna-Godavary and Mahanadi Basins. The rocks within the "oil window" are younger in the deep-water shelf.

References

1. Biswas SK (2012) Status of petroleum exploration in India. Proc Indian Nat Sci Acad 78 (3):475–494
2. Radhakrishna M, Rao SG, Nayak S, Bastia R, Twinkle D (2012) Early Cretaceous fracture zones in the Bay of Bengal and their tectonic implications: constraints from multi-channel seismic reflection and potential field data. Tectonophysics 522–523:187–197

3. Swamy KV, Radhakrishna Murthy IV, Krishna KS, Murthy KSR, Subrahmanyam AS, Malleswara Rao MM (2009) Magnetic anomalies of offshore Krishna–Godavari basin, eastern continental margin of India. J Earth Syst Sci 118(4):405–412
4. Lal NK, Siawal A, Kaul AK (2009) Evolution of east coast of India—a plate tectonic reconstruction. J Geol Soc India 73(February):249–260
5. Smith AG, Hallam A (1970) The fit of southern continents. Nature 225:139–144
6. Husain R, Mitra T, Gupta RP, Trivedi KB, Glosh A, Baghei SPS (2000) Opening of the East Coast of India vis-a-vis development of cretaceous petroleum systems. Petroleum geochemistry and exploration in the Afro-Asian region. In: 5-th International conference and exhibition, New Delhi, pp 535–540, 25–27 Nov
7. Acharyya SK (2000) Comment on "crustal structure based on gravity-magnetic modelling constrained from seismic studies under Lambert Rift, Antractica and Godavari and Mahanadi rifts, India and their interrelation ship" by D.C. Mishra. Earth Planet Sci Lett 179:595–598
8. Ramachandran K, Rabur V, Beherea BK, Harinarayana T (2013) Source rock analysis, thermal maturation and hydrocarbon generation using Rock-Eval pyrolysis in parts of Krishna-Godavary basin, India: a case study. J Petrol Explor Prod Technol 3:11–20. doi:10.1007/s13202-012-0041-y
9. Ramana MV, Nair RR, Sarma KVLNS, Ramprasad T, Krishna KS, D'cruz M, Subramanyam C, John P, Subramanyam AS, Chandrashekhar DV (1994) Mesozoic anomalies in the Bay of Bengal. Earth Planet Sci Lett 121:469–475
10. Rao GS, Radhakrishna M (2014) Crustal structure and nature of emplacement of the 85ºE Ridge in the Mahanadi offshore based on constrained potential field modeling: implications for intraplate plume emplaced volcanism. J Asian Earth Sci 85:80–96
11. Curray JR, Emmel FJ, Moore DG, Russel WR (1982) Structure, tectonics, and geological history of the northeastern Indian Ocean. In: Nairn AE, Stehli FG (eds) The ocean basins and margins, the Indian Ocean, vol 6, pp 399–450, Plenum, New York
12. Gupta RP, Husain R, Maurya SN, Venkataramatah V, Rawat S (1999) Deliberate search for subtle traps within Raghavapuram Shale: agenda for future exploration in West Godavary subbasin, Krishna-Godavary Basin. In: Proceedings of workshop on integred exploration for subtle and stratigraphic traps, Dehradun, ONGC Bulletin, vol 36, Issue 1, pp 27–37
13. Gaina C, Muller RD, Brown B, Ishihara T (2003) Microcontinental formation around Australia. In: Hillis Rand Muller RD (eds) The evolution and dynamics of the Australian plate. Joint Geological Society of Australia. America Special Paper, vol 22, pp 399–410
14. Radhakrishna M, Twinkle D, Nayak S, Bastia R, Rao SG (2012) Crustal structure and rift architecture across the Krishnae Godavari basin in the central Eastern Continental Margin of India based on analysis of gravity and seismic data. Mar Pet Geol 37:129–146
15. Krishna KS, Michael L, Bhattacharyya R, Majumdar TJ (2009) Geoid and gravity anomaly data of conjugate regions of Bay of Bengal and Enderby Basin—new constraints on breakup and early spreading history between India and Antarctica. J Geophys Res 114(B03102):21. doi:10.1029/2008JB005808
16. Ramana MV, Subramanyam V, Chaubey AK, Ramprasad T, Sarma KVLNS, Krishna KS, Mariadesa, Murty GPS, Subramanyam C (1997) Structure and origin of 85°E ridge. J Geophys Res 102(B8):17995–18012
17. Veevers JJ, Tewari RC (1995) Gondwana master basin of peninsular India between Tethys and the Gondwana province of Pangea. Geol Soc Am Mem 187:1–73
18. Gupta SK (2006) Basin architecture and petroleum system of Krishna Godavari basin, east coast of India. Lead Edge 25:830–837. doi:10.1190/1.2221360
19. Ramachandran K, Babu V, Behera BK, Harinarayana T (2013) Source rock analysis, thermal maturation and hydrocarbon generation using Rock-Eval pyrolysis in parts of Krishna-Godavari basin, India: a case study. J Petrol Explor Prod Technol 3:11–20. doi:10.1007/s13202-012-0041-y

20. Kaila KL, Murty PRK, Rao VK, Venkateswarlu N (2005) Deep seismic sounding in the Godavari Graben and Godavari (coastal) basin. India Tectonophys 173(1):307–317
21. Mazumdar A, Kocherla1 M, Carvalho MA, Peketi A, Joshi RK, Mahalaxmi P, Joao HM, Jisha R (2015) Geochemical characterization of the Krishna-Godavari and Mahanadi offshore basin (Bay of Bengal) sediments: a comparative study of provenance. Mar Pet Geol 60:18–33
22. Gupta MI, Sharma SR, Sundar A, Singh SB (1987) Geothermal studies in the Hyderabad granitic region and the crustal thermal structure of the Southern Indian shield. Tectonophysics 140:257–264
23. Gupta MI, Sundar A, Sharma SR (1991) Heat flow and heat generation in the Archaean Dharwar cratons and implications for the Southern Indian shield geotherm and lithospheric thickness. Tectonophysics 144:107–122
24. Negi IG, Panday OP, Agrawal PK (1986) Super-mobility of hot Indian lithosphere. Tectonophysics 131:147–156
25. Frakes LA (1979) Climates throughout geological time. Elsevier, Amsterdam, pp 1–310
26. Ramani KKV, Naidu BD, Giridhar M (2000) Reassessment of hydrocarbon potential of Cauvery Basin, India—A quantitative genetic model approach. Petroleum geochemistry and exploration in the Afro-Asian region. In: 5-th international conference and exhibition, New Delhi, pp 509–515, 25–27 Nov
27. Atlas of heat flow map of India (1991) Government of India, Delhi 65
28. Gupta ML, Sharma SR, Rao VK (2014) Conductive heat flow in the Godavari sub-basin (Pranhita-Godavari valley), Indian shield and its significance. J Ind Geophys Union 18(3): 394–404
29. Pytte M, Reynolds RC (1989) The thermal transformation of smectite to illite. In: Naeser ND, Mculok TH (eds) Thermal history of sedimentary basins. Springer, pp 132–140
30. Elliott WC, Aronson JL, Matisoff G, Gautier DL (1991) Kinetics of the smectite-to-illite transformation in the Denver Basin: clay minerals, K-Ar data, and mathematical model results. AAPG Bull 75:436–452
31. Huang WL, Longo JM, Pevear DR (1993) An experimrntally derived kinetic model for smectite-to-illite conversion and its use as a geothermometer. Clay Clay Miner 41(2):163–177
32. Vasseur G, Velde B (1993) A kinetic interpretation of the smectite-to-illite transformation. In: Dore AG (ed) Basin modeling and applications, NPF Special Publication, vol 3, pp 173–184
33. Velde B, Vasseur G (1992) Estimation of the diagenetic smectite to illite transformation in time-temperature space. Am Miner 77:967–976
34. Vasseur G, Brigand F, Demongodin L (1995) Thermal conductivity estimation in sedimentary basins. Tectonophysics 244(1–3):167–174
35. Hunner AT (2006) Smectite to illite transformation relevance to pore pressure in the subsurface. Thesis (Internet)
36. Pande DK, Singh RR, Chandra K (2008) Source rocks in deep water depositional systems of east and west coasts of India. In: 2008 AAPG annual convention and exhibition, April 20–23, 2008, San Antonia. Search and Discovery Article #10169 (2008) Posted October 24
37. Mishra PK, Chatter TK (1995) Paleo-environmental significance of petroleum source rock deposition in the Krishna-Godavari, Cauvery and Andaman basins: an integrated approach through the paleontological and geochemical parameters from selected case studies. In: Proceedings of PETROTECH-95, New Delhi, Technology Trends in Petroleum Industry
38. Rangarajy MK, Agrawal A, Prabhakar KN (1993) Tectono-stratigraphy, structural style, evolutionary model and hydrocarbon habitat, Cauvery and Palar basins. In: Biswas SK et al (eds) Proceedings second seminar on petroliferous basins of India, vol 1, Indian Petroleum Publishers, Dehra Dun, 248001, India, pp 371–389
39. Espitalie J, Ungerer P, Irvin I, Marquis E (1988) Primary cracking of kerogens. Experimenting and modelling C1, C2-C5, C6-C15 classes of hydrocarbons formed. Org Geochem 13(4–6): 893–899

40. Ungerer Ph (1993) Modeling of petroleum generation and migration. In: Bordenave ML (ed) Applied petroleum geochemistry, Technip, Paris, pp 397–442
41. Welte DH, Horsfield B, Baker DR (eds) (1997) Petroleum and basin evolution, Springer
42. Makhous M, Galushkin Y (2005) Basin analysis and modeling of the burial, thermal and maturation histories in sedimentary basins. TECHNIP, Paris
43. Galushkin Yu, Eloghbi S, Sak M (2014) Burial and thermal history modelling of the Murzuq and Ghadames Basins (Libya) using the GALO computer programme. J Petrol Geol 37(1):69–92

Chapter 3
Thermal Activation and Stretching of the East Barents Sea Lithosphere, Russia

Abstract In this chapter, the GALO basin modeling system is applied to reconstruct numerically burial, thermal and maturation histories of the East Barents Basin. The analysis carried out on example of two areas (the Admiralteyskaya and Arctic areas) allows to compare the thermal evolution and realization of hydrocarbon potential in contrast regions of the Basin: in the South Barents depression and the Admiralteyskoe rise. Tectonic history of the Basin includes the continental rifting in the Devonian and considerable thinning of the crust in the Permian and Triassic, associated with intensive sedimentation. Radioactive heat from the thick sedimentary cover contributes sufficiently in recent heat flow of the Barentz Depression. The modeling suggests more intensive thermal activation of the lithosphere in the northern areas of the Basin (the Admiralteyskoe Rise) than in the southern ones (the South Barents Depression). According to the modeling, liquid hydrocarbons generated by the Ordovician, Silurian and Devonian deposits in the Admiralteyskoe Rise and by Devonian, Permian and considerable part of Triassic rocks in the South Barents depression were subjected (perhaps, partly) to secondary creaking. Sufficient part of the Permian-Triassic deposits in center of the South Barents depression occurs within the gas generation zone.

Keywords East Barentz Basin · Tectonic subsidence · Maturity level · Vitrinite reflectance · Hydrocarbon generation · Lithosphere extension · Thermal activation of basin

3.1 Short Geological and Geophysical Description of the East Barents Basin

Two deep sedimentary depressions with the depth of the basement surface of 16–18 km up to 20–23 km were discovered seismically in the eastern part of the Barents shelf: the South- and North-Barents basins (Fig. 3.1; [1–4]). The South Barents basin is separated from the North Barents by the Ludlov saddle with depth of the basement at about of 12 km. The trough of the Barents sea paleorift was formed

Y. Galushkin, *Non-standard Problems in Basin Modelling*,
DOI 10.1007/978-3-319-33882-8_3

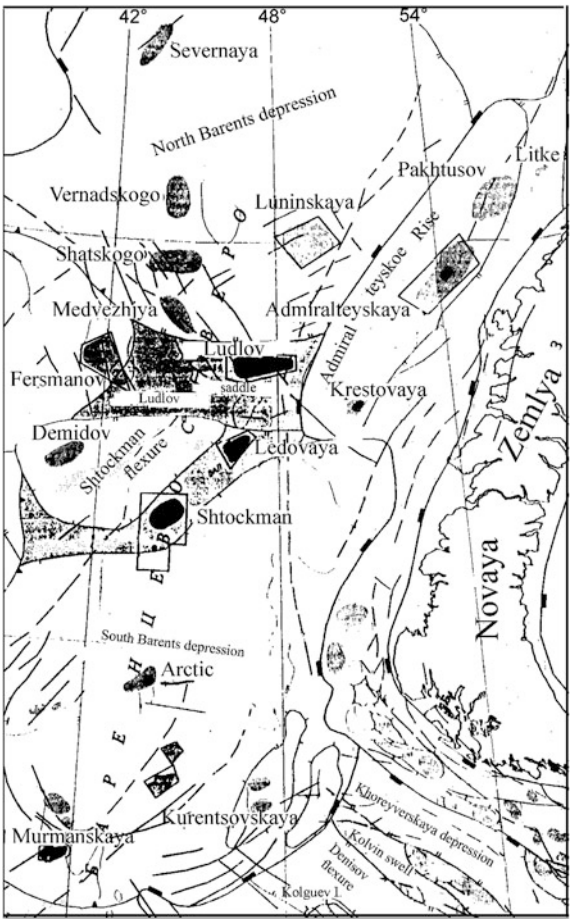

Fig. 3.1 Location of the studied areas and the main tectonic structures in the East-Barents region

in the Middle-Late Devonian across both of the basins from the north to the south at distance about 1,500 km. The width of the rift area ranges from 300 to 600 km. In the axial part of the rift, a considerable thinning of the granite layer (up to total declining) is assumed. The Moho boundary rises here up to depth of 28–32 km in the South Barents depression and to 32–34 km in the North Barents depression. It is equal to 42–45 km in the western, eastern and southern margins of the depressions [5, 6]. Some geologists suppose that the basement is oceanic in rift areas of the depressions [4], but geological majority admit here only significant degree of the continental lithosphere extension within the axial zones of the paleorifts. Neprochnov et al. [5] on the basis of analysis of seismic profiles, crossing the Barents sea paleorift, concluded that granite layer within paleorift really fragmented, but at the same time the thinned consolidated crust includes granite and "basalt" layers with the thickness of 10 and 15 km, respectively. It is confirmed by geothermal study of the region, suggested the modern deep heat flow (at the base of

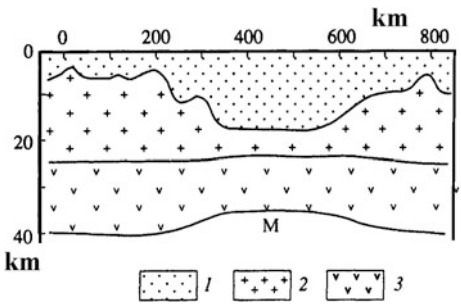

Fig. 3.2 Cross-sections of the crust along the profile from west to east crossed the Ledovaya area. The section was constructed on the base of seismic and gravity data [1]. *1* sediments; *2*granite; *3* "basalt"; *M* Mohorovich boundary

sedimentary blanket) of about 50 mW/m^2 [7, 8]. That is why the geophysics believe that the crust stretching does not result in disappear of granitic layer. It resulted in thinning of granite layer by 10 km compared with the basin flank areas (Fig. 3.2; [5]). The thickness of sedimentary cover in the South and North Barents depressions reached 20–23 km, decreasing to 5–7 km at the flanks of the depressions [6].

The basin evolution began with sedimentation in the Lower Riphean in the Arctic area (Table 3.1) and in the Lower Ordivician in the Admiralteyskaya area (Table 3.2) and finished by long erosion in the Upper Cretaceous—Cenozoic (Tables 3.1 and 3.2). Fast subsidence of the basins in the Late Permian—Early Triassic resulted from intensive extension of the basin lithosphere in the Permian-Triassic [9–11]. The Permian-Triassic complex is the main sedimentary complex in the rift graben where it reach the thickness of 5–10 km (Fig. 3.3; Table 3.1). The sedimentation in the Permian-Triassic was intensive in the rest of the Barents-Karskaya plate too, but with lesser thicknesses of depositions [9]. Composition of the Permian-Triassic depositions is terrigenous and changes physically from lacustrine-continental at the south to shallow marine at the north.

The present heat flow in the Barents Sea region is studied rather well (Fig. 3.4). The high present day heat flow within the Barentz Sea paleorift (about 70 mW/m^2) is in considerable degree due to contribution of radiate heat generation from rather thick sedimentary cover (see below). This contribution is about 20 mW/m^2 similar to the situation in the Gulf of Mexico [12].

3.2 Burial, Thermal and Maturation Histories of the Sedimentary Rocks in the Basin

3.2.1 Calculation of Temperature Distribution with Depth in Sedimentary Sections of the Basin

Figures 3.5 and 3.6 demonstrate an evolution of the depth of sedimentary layers during burial history of the East Barentz Sea Basin on the Arctic and Admiralteyskaya areas. The Arctic sedimentary section includes the rocks of age

Table 3.1 Main stages of evolution of the Barents Sea Basin and lithology of sedimentary layers in the Arctic area

N	NN	Z (km)	Time (My)		Lithology					
			t1	t2	shale	alevr.	sandst.	limest.	dolom.	Corg
1	1	14.600	1650	416	0.300	0.000	0.300	0.000	0.400	0.000
2	1	11.000	416	387	0.200	0.000	0.150	0.300	0.300	0.050
3	2	9.600	387	385	–	–	–	–	–	–
4	1	9.600	385	359.2	0.300	0.200	0.200	0.300	0.000	0.000
5	1	8.800	359.2	274	0.220	0.000	0.070	0.400	0.310	0.000
6	2	7.900	274	270.6	–	–	–	–	–	–
7	1	7.900	270.6	254	0.600	0.000	0.250	0.100	0.000	0.050
8	4	0.800	254	251	–	–	–	–	–	–
9	1	6.400	251	245	0.750	0.100	0.150	0.000	0.000	0.000
10	1	4.900	245	228	0.800	0.100	0.100	0.000	0.000	0.000
11	1	4.450	228	203.6	0.400	0.200	0.350	0.000	0.000	0.050
12	1	3.825	203.6	199.6	0.050	0.250	0.700	0.000	0.000	0.000
13	2	3.540	199.6	196.5	–	–	–	–	–	–
14	1	3.540	196.5	178	0.050	0.300	0.650	0.000	0.000	0.000
15	1	3.050	178	170	0.100	0.120	0.780	0.000	0.000	0.000
16	2	2.695	170	160	–	–	–	–	–	–
17	1	2.695	160	157	0.200	0.300	0.500	0.000	0.000	0.000
18	1	2.450	157	145.5	1.000	0.000	0.000	0.000	0.000	0.000
19	2	2.380	145.5	140.2	–	–	–	–	–	–
20	1	2.380	140.2	125	0.850	0.150	0.000	0.000	0.000	0.000
21	1	1.870	125	97	0.500	0.400	0.080	0.000	0.000	0.020
22	1	0.710	97	92	0.450	0.500	0.050	0.000	0.000	0.000
23	4	0.500	92	1.81	–	–	–	–	–	–
24	1	0.375	1.81	0.00	0.500	0.000	0.500	0.000	0.000	0.000

Remarks *N* number of the basin evolution stage; *NN* type of evolution (*1* sedimentation, *2* interruption, *4* erosion); *Z* depth of base of the layer in the present-day section or erosion amplitude (in km); *t1* and *t2* times of initiation and finish of the stage (in My); in columns of "lithology" the relative fractions of every lithological unit in the rock of given layer are shown
Abbreviations: *alevr.* alevrolite; *sandst.* sandstone; *limest.* limestone; *dolom.* dolomite

from the Lower Riphean, whereas the Admiralteyskaya section—the rocks from the Ordovician (Tables 3.1 and 3.2; Figs. 3.5 and 3.6). The consolidation of sediments is considered in accordance with the principles discussed in Chap. 1, when a change in matrix volume due to compression is considered as negligible in comparison with the deformation of porous media [13]. The parameters of rock consolidation and the rock's thermal attributes depended on rock lithology. The rocks of sedimentary sections in the studied region are presented by different fractions of clays, shales, aleurolite, sandstones, limestones and dolomites (Tables 3.1 and 3.2). According to seismic data, thickness of sedimentary cover in the Arctic areas located within the

Table 3.2 Main stages of evolution of the Barents Sea Basin and lithology of sedimentary layers in the Admiralteyskaya area

N	NN	Z (km)	Time (Ma)		Lithology		
			t1	t2	shale	sandst.	limest.
1	1	5.900	488.0	392.0	0.200	0.800	0.000
2	1	4.900	392.0	380.0	0.300	0.700	0.000
3	1	4.600	380.0	374.0	0.400	0.200	0.400
4	1	4.500	374.0	359.0	0.200	0.000	0.800
5	1	3.864	359.0	345.0	0.300	0.000	0.700
6	4	0.500	345.0	311.0	0.300	0.000	0.700
7	1	3.814	311.0	299.0	0.100	0.000	0.900
8	1	3.764	299.0	271.0	0.400	0.100	0.500
9	1	3.564	271.0	251.0	0.500	0.500	0.000
10	1	3.138	251.0	245.0	0.500	0.500	0.000
11	1	0.135	245.0	200.0	0.500	0.500	0.000
12	4	1.000	200.0	176.0	0.500	0.500	0.000
13	1	0.000	176.0	100.0	0.500	0.500	0.000
14	4	0.800	100.0	1.8	0.500	0.500	0.000
15	1	0.006	1.8	0.0	0.500	0.500	0.000

Legend see in Table 3.1

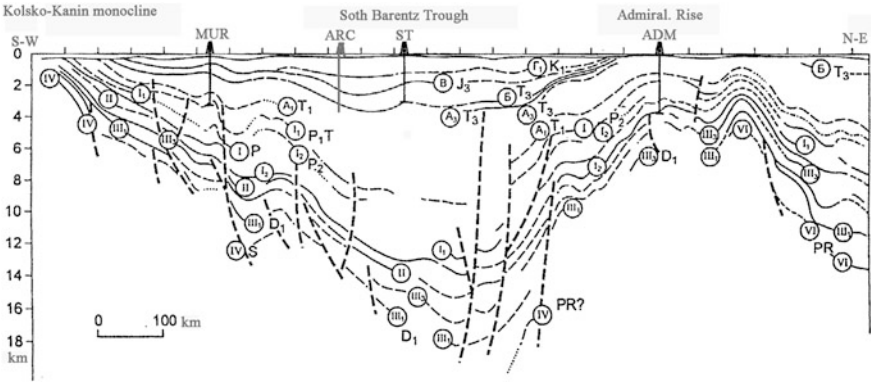

Fig. 3.3 Geological-geophysical profile from *S-W* to *NE* across the East-Barentz Basin (according to [2] with little changes). *Symbols in circles* numbers of seismic layers. Abbreviations: *MUR*, *ARC*, *ST* and *ADM* Murmanskaya, Arctic, Stockman and Admiralteyskaya wells; *Admiral. Rise* Admiralteyskoe Rise

East Barentz Trough exceeds 14 km and ranges from 5 to 9 km at the areas of the Admiralteyskoe rise (Fig. 3.3).

Both areas analyzed here are characterized by maximal sedimentation rates in the Lower Triassic. These rates increase toward southern part of the East Barents Basin.

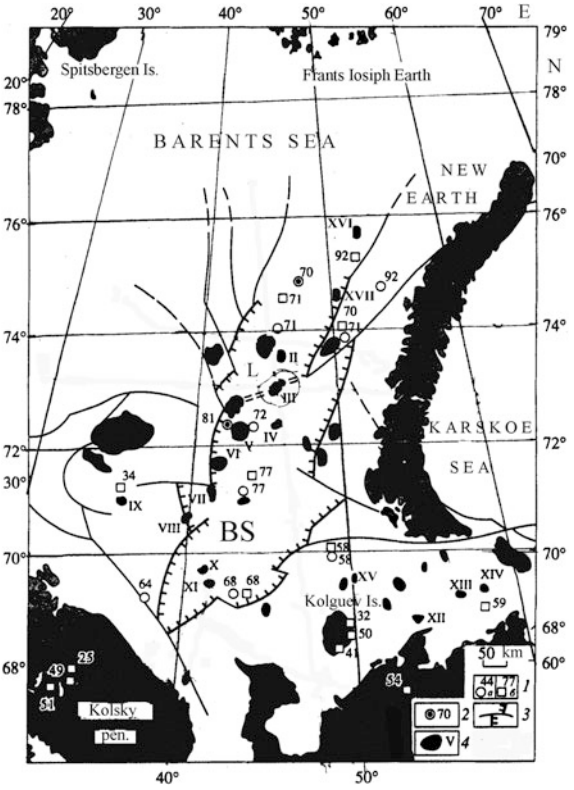

Fig. 3.4 Heat flow map of the East Barenz Basin with approximate location of the East Barentz Trough and some faults (according to [8] with little changes). Legend (*bottom right*): *1*, *2* points of the heat flow measurements and values of heat flow (in mW/m^2). *3* faults and shifts; *4* oil and gas fields and wells: *I* Fersman, *II* Ludlov, *III* Ledovoe, *IV* Britvinskoe, *V* Stokman, *VI* Teriberskoe, *VII* Severo-Nadezhdinskoe, *VIII* Nadezhdinskoe, *IX* Severo-Kildinskoe, *X* Severo-Murmanskoe, *XI* Murmanskoe, *XII* Pomorskoe, *XIII* Severo-Gulyaevskoe, *XIV* Prirazlomnoe, *XV* Peschanoozerskaya, *XVI* Admiralteyskaya, *XVII* Krestovaya, *BS* Barentz Sea paleorift, *L* Ludlov saddle

As whole, the sedimentation rates diminish considerable in the Jurassic, Cretaceous and Cenozoic up to considerable erosion in the Cenozoic (Figs. 3.5 and 3.6). Burial history of the Admiralteyskoe Rise is not as intense as the history of the Arctic area, but it is more complicated. It includes three periods of erosion: in the Carboniferous, Upper Triassic-Lower Jurassis and Cenozoic (Fig. 3.6).

As result of such burial histories, the Devonian and Carboniferous deposits occur at depth of 8000–11000 m in the Arctic area and $3600 \leq z \leq 5000$ m in the Admiralteyskaya area (Tables 3.1 and 3.2; Figs. 3.5 and 3.6).

As mentioned in Chap. 1, the temperature distribution within the sedimentary cover and underlying lithosphere is found from numerical solution of heat-transfer Eq. (1.1), scribed in the frame related with the basement: Temperature at the upper boundary of the domain of temperature computation (Z = 0) changes with geological time according to paleoclimate conditions of the basin development (see upper parts of Figs. 3.5 and 3.6). For the Carboniferous—Late Cretaceous the paleoclimate curve was constructed on the base of data in [15, 16], whereas the data of the papers [17, 18] are used for the Cenozoic. The steady temperature Tlow $\approx$ 1160 °C was maintained at the base of the domain at the depth of 93–115 km (see Sect. 1.1.4). Initial temperature distribution corresponded to the values of surface temperature

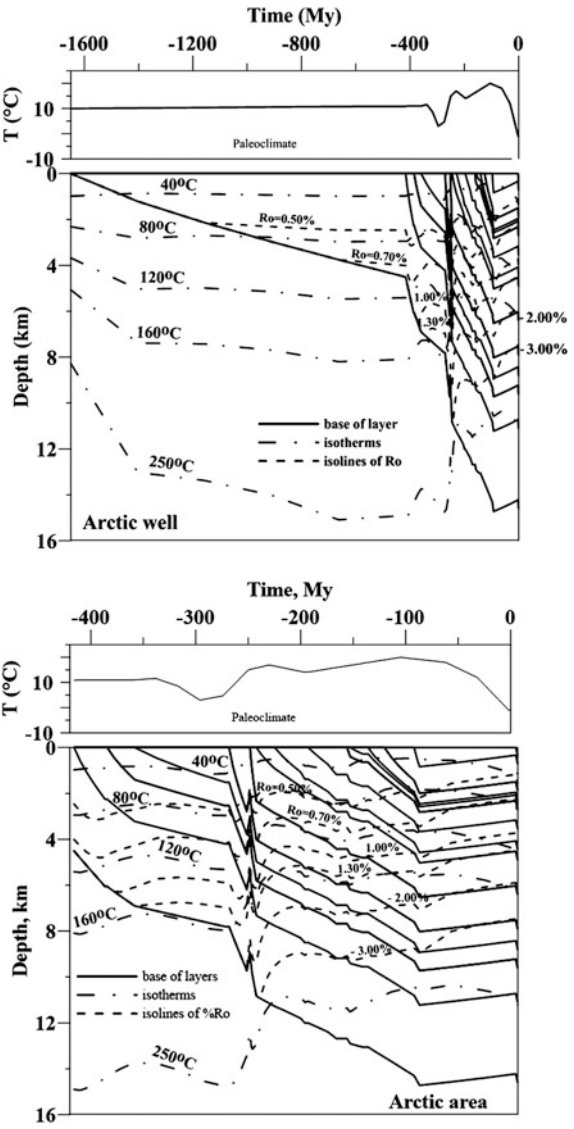

Fig. 3.5 Changes in rock temperatures and maturity degree of organic matter during burial history of the East Barentz Basin in the Arctic area (results of modeling). The *bottom figure* shows in more detail the burial history from Devonian. Depth of the %Ro-isolines were computed with use of the %Ro EASY model of vitrinite maturation [14]

and heat flow during initiation period of the basin evolution. The initial heat flow was equaled to 85 mW/m^2 in the Arctic area and 67 mW/m^2—in the Admiralteyskaya area. These heat flows are in accordance with variations in tectonic subsidence of the basement surface (Sect. 1.2; see below). Non-steady heat transfer equation was solved using the non-apparent finite-difference scheme adapted for variable thermal physical parameters in the equation and for non-steady time and depth steps (Sect. 1.1.5). The depth steps (Δz) change continually from 1 to 2 m near

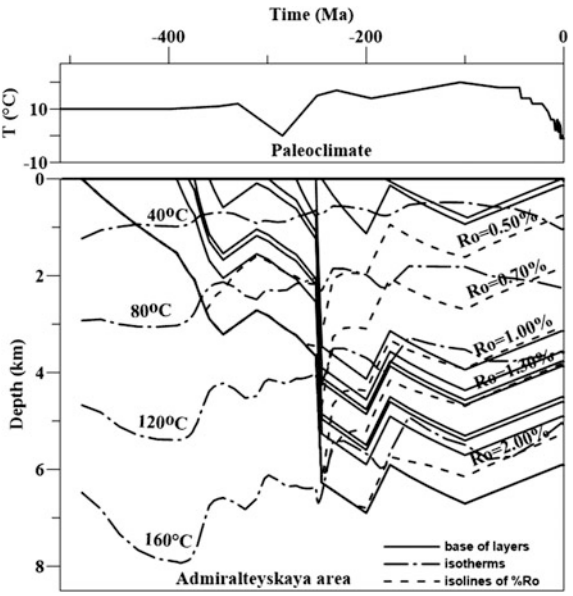

Fig. 3.6 Changes in rock temperatures and maturity degree of organic matter during burial history of the East Barentz Basin in the Admiralteyskoe Rise (results of modeling)

surface of the basin to 10–30 m at its base. Within the basement, Δz increase linearly up to 1–1.2 km at the base of the computed domain ($Z \approx 93$–115 km).

The thermal physical parameters in the heat transfer Eq. (1.1) are determined by lithological rock composition, rock porosity and temperature. These values change considerable with time of the basin evolution and depth. For example, heat conductivity of argillaceous sandstone increases from 1.2–1.5 mW/m^2 at small depths to 3–3.5 mW/m^2 at the depth of more than 4–5 km. Such variations in heat conductivity resulted in significant variations in thermal gradient at all stages of the basin development including its modern stage (Figs. 3.7 and 3.8). At whole, heat conductivities computed in our model were in a good agreement with the measurements in [19, 20].

As mentioned in Sect. 3.1, contribution of radiogenic heat generation from sedimentary rocks into surface heat flow is rather high in the Arctic area reaching here to 15 mW/m^2 due to thick sedimentary cover (Fig. 3.9a). It is about 7 mW/m^2 for thinner covers of the Admiralteyskaya area. The contribution of radiogenic heat generation from sedimentary rocks is the main reason of difference in heat flows through the surface of sediments and the basement in Figs. 3.9a and 3.10a.

As whole, the modeling suggests rather high thermal regime of sedimentary blanket in tne East Barentz Basin. So, the temperatures of the rocks at the base of sedimentary sections in the Arctic reach 310. It equals to 160 °C at the depth about of six kilometers in the Admiralteyskaya area (Figs. 3.7 and 3.8). As whole, thermal evolution of sedimentary cover is in agreement with the thermal variations of the lithosphere (Figs. 3.9 and 3.10) but it is complicated by variations in climate and sedimentation rates (Figs. 3.5 and 3.6).

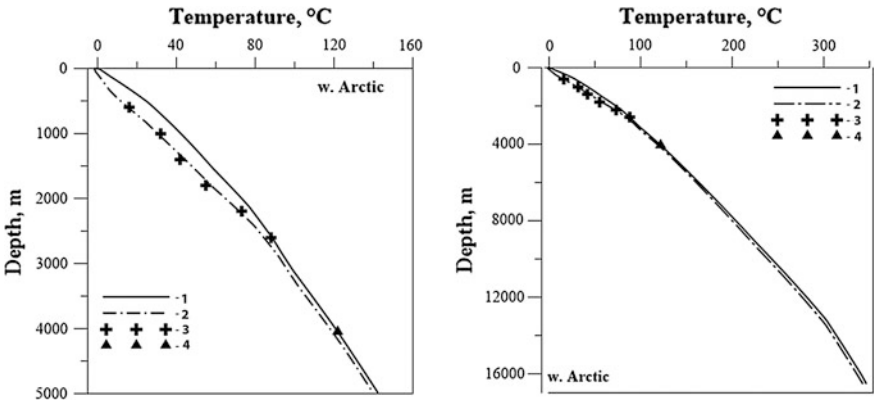

Fig. 3.7 Calculated and measured temperatures in the present-day sections of the Arctic area in the East Barents Sea Basin. *1* profile computed with paleoclimate curves from Fig. 3.5. *2* temperature profile computed with detailed climate curves for the last 3 My (see Chaps. 9 and 10 for details), *3* measured temperatures from [19]; *4* measured formation temperature (private report)

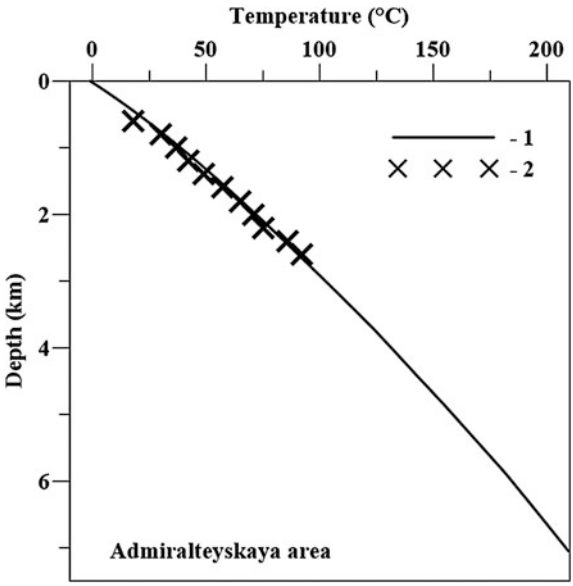

Fig. 3.8 Calculated and measured temperatures in the present-day section of the Admiralteyskaya area of the East Barents Sea Basin. *1* temperature distribution calculated without accounting of detail climate variations during last 3 My. *2* temperatures measured in sedimentary section of the Admiralteyskaya area [19]

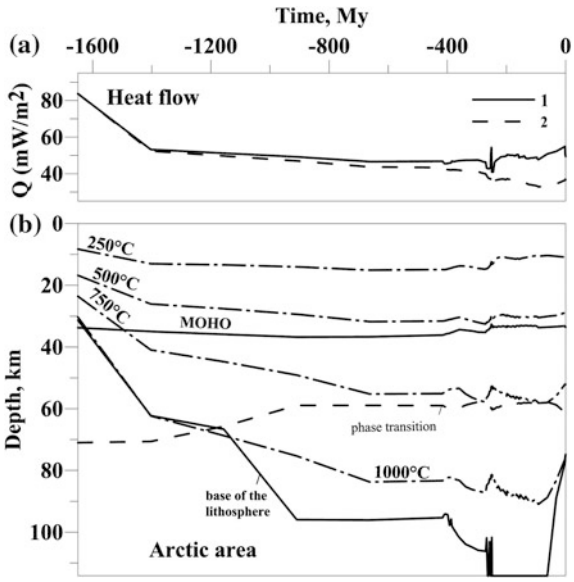

Fig. 3.9 Heat flow (**a**) and thermal history (**b**) of the Basin lithosphere in the Arctic area. **a** Calculated variation in heat flow. *1* heat flow through the sediments surface; *2* heat flow through the basement surface. **b** Reconstruction of thermal history of the lithosphere. *The MOHO line* base of the crust (the crust thickness increases during sedimentation and decreases during extension of the lithosphere, for example in the Permian-Triassic). *Dashed-dotted lines* isotherms. *Dashed line* phase transition of spinel to garnet peridotite (see Sect. 1.2.2, Eq. (1.16)). The "base of the lithosphere" line—the base of the lithosphere determined by intersection of the current geotherm with peridotite solidus (1.4) (see Sect. 1.1.3)

3.2.2 *Calculation of Maturity Degree of Organic Matter in Sedimentary Section of the Basin in the EASY%Ro and Basin%Ro Models of Vitrinite Maturation*

Numerical reconstruction of the thermal history of the Basin is used in the model, to assess a degree of maturity level of organic matter in sedimentary rocks. For this purpose, the values of vitrinite reflectance, *%Ro*, are calculated using the kinetic spectrum of vitrinite maturation published in [14] and modified kinetic spectrum the *Basin%Ro* model of [21]. The values of vitrinite reflectance are computed by calculation of transformation ratio *Tr* of vitrinite [14]:

$$Tr(t) = \sum_{1}^{n} X_{i0} \cdot \{1 - EXP\,[-\int_{to}^{t} K_i(t') \cdot dt')]\} \tag{3.1}$$

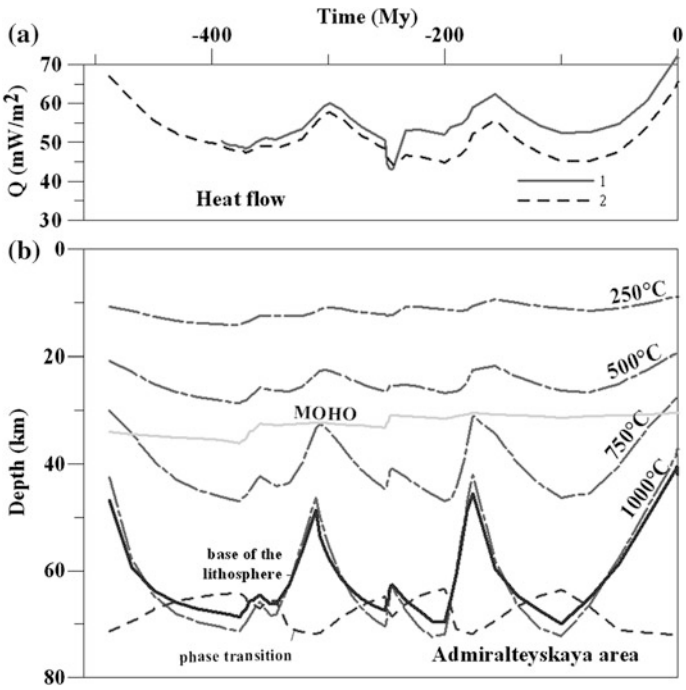

Fig. 3.10 Heat flow (**a**) and thermal history (**b**) of the Basin lithosphere in the Admiralteyskoe Rise (see legend in Fig. 3.9)

where rate of the *i*-th kinetic reaction of Arhenius

$$Ki(t) = A_i \, exp(-Ei/R\,T(t)) \tag{3.2}$$

In (3.2), frequency factor of reactions $Ai = 1.0 \times 10^{-13}$ 1/s in both models (the *EASYRo* model of [14] and the modified model of [21]). $T(t)$ is the temperature history of the rock sample (in °K), t is the burial time, R is the ideal gas constant. Activation energies *Ei* and initial potential of reaction, *Xio*, are shown in Table 3.3 for both models of vitrinite maturation. In the *EASYRo* model the values of vitrinite reflectance are obtained from relationship [14]:

$$R\% = EXP(-1.6 + 3.7 \cdot Tr) = 0.202 \cdot EXP(3.7 \cdot Tr) \tag{3.3}$$

Expression (3.3) describes the rather good correlation between transformation ratio *Tr* and the values of *%Ro*, which result from analysis of data from the North Sea basin, the French Central Basin, the Pannonian Basin and Mahakam Delta Basin [14, 22]. Thus, the Eqs. (3.1) and (3.3) are based on the laboratory spectrum of vitrinite maturation (Table 3.3) and correlation ratios obtained for different sedimentary basins of the world. The Eq. (3.3) suggests that $R\% = 0.202$

Table 3.3 Parameters of the *EASY Ro* model of vitrinite reflectance of [14] and the *Basin%Ro* model of [21]

Ei (Kcal/mol)	*Xio*	
	Model *EASY Ro* [14]	Modified model [21]
34	0.03	0.0185
36	0.03	0.0143
38	0.04	0.0569
40	0.04	0.0478
42	0.05	0.0497
44	0.05	0.0344
46	0.06	0.0344
48	0.04	0.0322
50	0.04	0.0282
52	0.07	0.0062
54	0.06	0.1155
56	0.06	0.1041
58	0.06	0.1023
60	0.05	0.0760
62	0.05	0.0593
64	0.04	0.0512
66	0.03	0.0477
68	0.02	0.0086
70	0.02	0.0246
72	0.01	0.0096
	Σ *Xio* = 0.85	Σ *Xio* = 0.9215

for immature matter ($Tr = 0$), whereas $Ro\% = 4.69$ % for overmature matter ($Tr = 0.85$).

Nielsen et al. [21] derived the new vitrinite reflectance model that is consistent with the data from 22 wells in the East China Sea and the Nova Scotian Shelf, one pseudo-well, and six laboratory pyrolysis experiments. The model allows an explanation of the general behaviour of vitrinite reflectance with burial depth described by [23], when %Ro change linearly with depth from 0.2–0.25 % Ro at the surface to 0.6–0.7 % Ro; then increases rapidly to ~1.0 %Ro; and then increases again linearly but more rapidly than in the upper segment. In the *Basin% Ro* model of [21], the relationship between *Tr* and *%Ro* is rather close to Eq. (3.3):

$$R\% = EXP(-1.56 + 3.7 \cdot Tr) = 0.2104 \cdot EXP(3.7 \cdot Tr) \tag{3.4}$$

The difference of the new model from the EASY%Ro is only in wages of reactions Xio (Table 3.3). According (3.4) and Table 3.3, R% = 0.2104 for immature matter (Tr = 0), whereas Ro% = 6.365 % for overmature matter (Tr = 0.9215). A comparison of both models in [21] shows that the widely used easy%Ro-model can overestimate vitrinite reflectance in the interval 0.5–1.7 %Ro by up to 0.35 %.

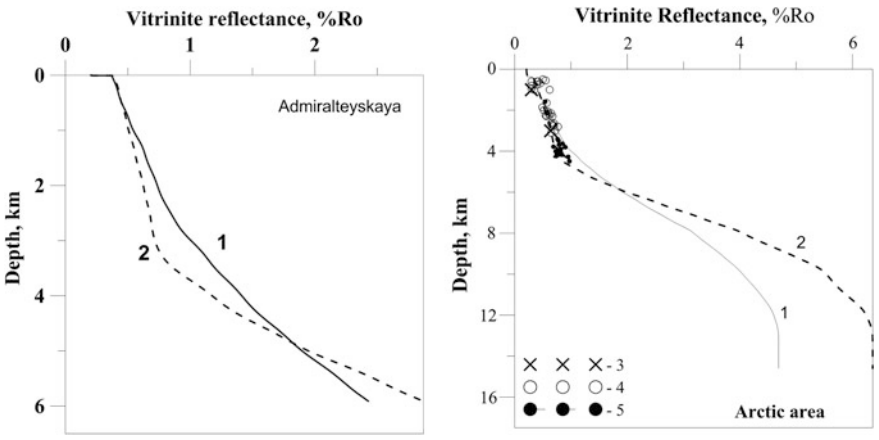

Fig. 3.11 Computed distribution of vitrinite reflectance with depth, %Ro(z), in present-day section of the Admiralteyskaya and Arctic areas and comparison with measured values. *1* %Ro computed in the EASYRo model [14] of vitrinite maturation; *2* %Ro computed in the %RoBasin model [21]; *3* data from [10]; *4* data from report 2002; *5* from report 2009

This can be seen also in Fig. 3.11 on example of the %Ro distributions computed for the present-day sedimentary sections of the Admiralteyskaya and Arctic areas. In region of Ro < 2 %, the values of Ro calculated by the EASY %Ro model 1 exceed the values obtained in the %Ro Basin model. When Ro > 2 %, the situation is reversed. The right Fig. 3.11 demonstrates rather good agreement between the Ro values measured in the Arctic area and the ones computed in the % Ro Basin model (curves 2 in Fig. 3.11), whereas the values calculated in the EASY %Ro model [14] (lines 1 in Fig. 3.11) exceed the measured ones. It is necessary to note that the dashed lines in Figs. 3.5 and 3.6 are isolines of %Ro, computed in the EASY%Ro model of [14].

Figure 3.5 shows that the quick subsidence of the basin in the Permian-Triassic resulted in significant increase of rock temperatures and early maturation of organic matter in the Devonian and Triassic formations of the Arctic area. Even the Low Jurassic rocks at depth from 3050 to 3540 m in present-day section are characterized here by rather high catagenesis in the EASY%Ro model (Ro ≈ 0.77–0.87 %) and more moderate maturation in the BASIN%Ro model (Ro = 0.64–0.68 %). We emphasize that regardless of model [14] or [21] of vitrinite maturation such values of Ro indicate significant hydrocarbon generation in rocks with organic matter of type II (Table 3.4). The Triassic-Devonian rocks in the Admiralteyskaya area locate at moderate depths and are characterized by lesser degree of maturation (Fig. 3.6; Table 3.4).

Table 3.4 Calculated values of maturation level (effective %Ro), temperature and realization of hydrocarbon potential for the probably source rocks in the present-day sedimentary sections of the East Barents Sea Basin in the Admiralteyskaya and Arctic areas

T	Z	T	Ro	Hi	Ht	Ho	Hg	t1	texp	t2
My	m	°C	%	Mg HC/g Corg				Million years ago		
Admiralteyskaya area										
488	5900	180.6	2.306	377	377	0	221	362	247	241
392	4900	154.5	1766	268	253	6.2	162	273	244	230
374	4500	143.6	1.558	668.5	662	388	151	249	245	217
359	3864	126.6	1.297	377	377	273	84	247	242	0
299	3764	123.8	1.253	377	377	284	79	246.5	241	–
271	3564	118	1.173	268	237	164	69.2	246	234	–
251	3138	105.6	1.014	268	223	164	59	245	222	–
Arctic area										
359-t	8800	206.2	3.49	450	449	0	247	260	247	226
359-d	8800	206.2	3.49	627	627	0	317	260	248	226
290-a	8070	196.3	3.12	627	626	0	316	256	246	210
262	6430	173.8	2.44	450	441	0.0007	240	245	218	137
247+	5400	126.6	1.30	160	107	29.8	75.4	184	–	0
247−	5400	126.6	1.30	250	219	130	79	184	97	0
205	3861	102.7	0.89	160	50.9	16	34.9	132	–	–
157	2450	77.8	0.67	450	30.5	25.1	5.4	102	–	–
151	2387	73.6	0.65	450	17.2	14.1	3.1	98	–	–

Notes t formation age (My). *z* depth (km). *T* temperature in °C. *Ro* vitrinite reflectance computed by the %R-EASY model [14]. (*z*, *T*, *Ro* computed values in the present-day section); *Hi* initial potential of HC generation by the formation rock; *Ht* total HC generation by formation rocks to present time; *Ho* oil generation and *Hg* gas generation (in mg HC/g Corg) to present time; *t1*, *t2* times of rock enter in the "oil" (Ro = 0.50 %) and "gas" (Ro = 1.30 %) "windows"; *texp* the time of expulsion threshold for liquid HC (see text)

The following types of kerogene are assumed for probably source rocks

Ordovician (t = 488 My): Corg = 0.4 %, kerogen of type II with Hi = 377 mg HC/g Corg

Middle Devonian (t = 392 My): Corg = 0.4 %, the mixture 50 % kerogene of type II (HI = 377) and 50 % kerogene of type III (HI = 160) with summary initial potential Hi = 268 mg HC/g Corg

Upper Devonian (t = 374 My): Corg = 2 %, the mixture 50 % kerogene of type I (HI = 710) and 50 % kerogene of type II (HI = 627) with summary Hi = 668.5 mg HC/g

Upper Devonian (t = 359 My): in the Admiralteyskaya area: Corg = 0.3 %, kerogen of type II with Hi = 377 mg HC/g. In the Arctic area; Corg = 2 %, the mixture 62 % kerogene of type II (HI = 627) and 38 % kerogene of type III (HI = 160) with summary Hi = 450 mg HC/g

Carboniferous (t = 359 /290 My): in Admiralteyskaya area: Corg = 0.4 %, the kerogene of type II with Hi = 377 mg HC/g Corg; In the Arctic area: kerogen of type II (HI = 627 mg HC/g)

Lower and Upper Permian (t = 299/288, 271/263, 255, 248 My): in the Admiralteyskaya area: Corg = 0.4 %, the mixture 50 % kerogene of type II (HI = 377) and 50 % kerogene of type III (Hi = 160) with summary Hi = 268 mg HC/g. *In Upper Permian* (262 My) in the Arctic area: Corg = 2 %, the mixture 62 % kerogene of type II (HI = 627) and 38 % kerogene of type III (HI = 160) with summary Hi = 450 mg HC/g

Lower Triassi (247 My): in the Arctic area: kerogen of type III with HI = 160 mg HC/g TOC

Middle Triassic (247 My) in the Arctic area: the mixture 41 % kerogene of type II (HI = 377) and 59 % kerogene of type III (HI = 160) with summary Hi = 250 mg HC/g

Upper Triassic (205 My) in the Arctic area: kerogen of type III with HI = 160 mg HC/g TOC

Upper Jurassic (157 and 151 My) in the Arctic area: Corg = 2 %, the mixture 62 % kerogene of type II (HI = 627) and 38 % kerogene of type III (HI = 160) with summary Hi = 450 mg HC/g

3.2.3 *Realization History of Hydrocarbon Potential of Probable Source Rocks of the East Barentz Basin*

Table 3.4 gives a general review of calculated values of maturation level (effective %Ro), temperature and realization of hydrocarbon potential for the probably source rocks in the present-day sedimentary sections of the East Barents Sea Basin in the Admiralteyskaya and Arctic areas. Calculations of HC generation were carried out based on reconstructions of thermal history of the Basin discussed above and kinetic spectrum of primary and secondary creaking of kerogens of different types. Algorithm of calculations is described in [22, 24, 25]. Secondary creaking of liquid HC can result in total destruction of oil as is the case in the Devonian, Carboniferous and Permian formations in the Arctic area and in the Ordovician and Lower Devonian formations in the Admiralteyskaya area (Table 3.4; Fig. 3.12). On the other hand, there are examples when liquid HC transform to gaseous fraction only partly (the Upper Devonian formations of the Admiralteyskaya area, the Upper Permian, Lower and Middle Triassic formations of in the Arctic area (Table 3.4; Fig. 3.13).

In our computations, we use the three component kinetic spectra with reactions of primary and secondary creaking of standard kerogenes of types I, II and III [22, 26, 27]. Type and composition of organic matter in the probable source rocks are presented in Note to Table 3.4.

The values of Corg take a part in assessment the start times of primary migration of liquid HC from source rocks (texp in Table 3.4). These times are noted by vertical lines 4 in Figs. 3.12 and 3.13. They are very approximate because it is known that the expulsion threshold depends on many factors including content of

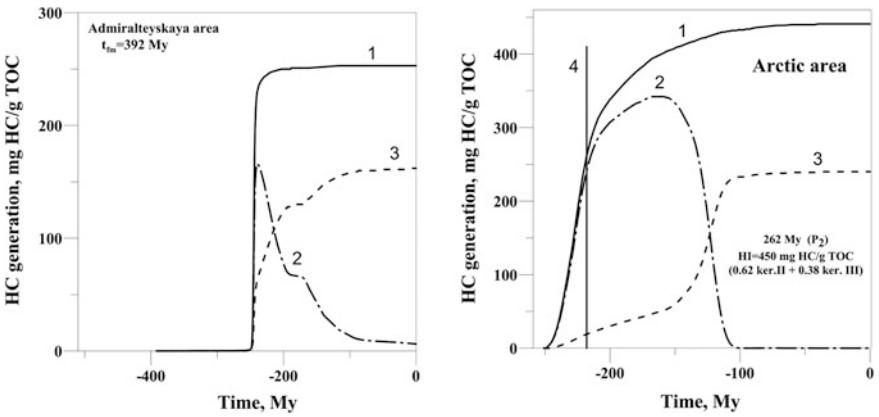

Fig. 3.12 Hydrocarbon generation by the rocks of the Lower Devonian and Middle Permian formations with active secondary cracking of oil. *1* total HC generation; *2* generation of liquid HC; *3* generation of gaseous HC; *4* expulsion threshold for primary migration of oil determined by the condition that 20 % of porous space is filled by oil [22, 24]

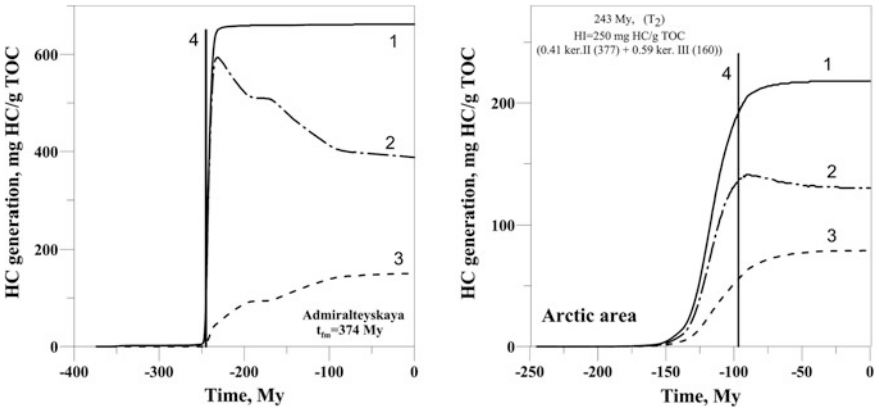

Fig. 3.13 Hydrocarbon generation by the rocks of the Upper Devonian and Middle Triassic formations with moderate secondary cracking of oil

gaseous HC in rock pores [22, 27]. The time of initiation of primary migration of liquid HC was determined in our model from condition that liquid HC's fill 20 % of porous volume in source rocks.

3.3 Thermal Evolution and Two Stage of Stretching of the Basin Lithosphere

3.3.1 Heat Flow and Thermal State of the Basin

In the simulation, it was assumed that the basement of the East Barents Sea Basin before extension in the Devonian and Permian-Triassic is presented by standard continental lithosphere of Table 1.1 with 15 km of granite layer and 20 km of the pseudo-basalt. Radiogenic contribution of the consolidated crust into surface heat flow before extension was about 25 mW/m^2. According to the modeling, amplitude of the lithosphere extension in the Arctic area located in southern part of the paleorift axis (Fig. 3.1) reached to 1.8, whereas it consists about 1.38 in the Admiralteyskoe Rise. The present-day heat flow from the mantle can be roughly assessed by reducing the radiogenic contribution of thinned crust (about 14 mW/m^2 in the Arctic area and 18 mW/m^2 in the Admiralteyskaya area) from the calculated heat flow through the basement surface (Figs. 3.9 and 3.10). The latter is equaled to 36.6 mW/m^2 in the Arctic area and 65.2 mW/m^2 in the Admiralteyskaya area. Therefore, modern mantle heat flow is now about 23 mW/m^2 in the Arctic area and considerable higher (about 47 mW/m^2) in the Admiralteyskaya area. The increase in the heat flow through the mantle surface (the MOHO boundary) at transition from the southern Arctic area to the northern Admiralteyskaya one can be related

with approach to the modern spreading centre (the Gakkel ridge) located to the north from the region under study.

In this connection, it is necessary to say that high values of heat flow measured in the region contradict relatively low values of deep temperatures and moderate degree of organic matter maturation, measured in the wells. Indeed, the heat flow measured in the Ledovaya, Shtockman and Arctic areas is about 70 and about 90 mW/m^2 in the Admiralteyskaya area [7, 8, 28]. These values exceed the ones calculated in our model (50–58 mW/m^2 in the Ledovaya, Shtockman and Arctic areas and 72 mW/m^2 in the Admiralteyskaya area). On the other hand, the deep temperatures calculated in the model are in reasonable agreement with the reliable measured ones (see Figs. 3.7 and 3.8). For example, the calculated temperatures at the depth z = 2,600 and 4,050 m in the Arctic area are T = 88 and 119 °C, whereas measured values T = 90 and 122 °C, correspondingly (Fig. 3.7). If we take in the Arctic area surface heat flow 69 mW/m^2 we get the heat flow through the basement surface 54 mW/m^2 and the temperatures T = 115 and 159 °C at the same depths that exceed considerably measured temperatures. Similar situation takes place for rock maturation (vitrinite reflectance, %Ro). For heat flow q = 69 mW/m^2 we obtain Ro = 2.02 % (in both models [14, 21]) at the depth of 4,050 m whereas measured Ro is 0.90 % (see above). Therefore, application of the high measured heat flow led to overestimation of temperatures by 30–40°C and considerable overstating in the %Ro values. Corrections on the Quaternary climate variations must only enhance the above contradiction. The authors [28, 29] faced a similar problem, conducting two-dimensional modeling of the thermal field in the East Barentz Basin. They came to the conclusion that the above contradiction is related to the hardness of heat flow measurement in the Barentz shelf, because numerous distortions of heat flow by exogenic and near surface factors led to considerable scatter in the measured values of heat flow. The authors of [28, 29] concluded that the reliable method of heat flow measurement is only its measurement in deep wells. In this regard, note also that the above contradiction could not be due to errors in determination of thermal parameters of the rocks. Indeed, the measured heat conductivities of aleurolite and sandstone samples from depth of 1,440 and 3,100 m in the Shtockman area are in agreement with the values computed in our basin modeling with a precision of 10–20 %. The measurements of deep temperatures in the well with enough time after drilling stops (the Arctic and Admiralteyskaya wells; [19, 20]) are more reliable for modeling control than the heat flow measurements. That is why we used the deep temperature measurements but no the heat flow measurements to control the modeling results.

3.3.2 An Analysis of Tectonic Subsidence of the Basin

Our modeling uses an analysis of the Basin's tectonic subsidence as one of the control factors in addition to comparison of measured and computed temperatures and maturation degree in present-day sedimentary section (see Sect. 1.2; Fig. 3.14).

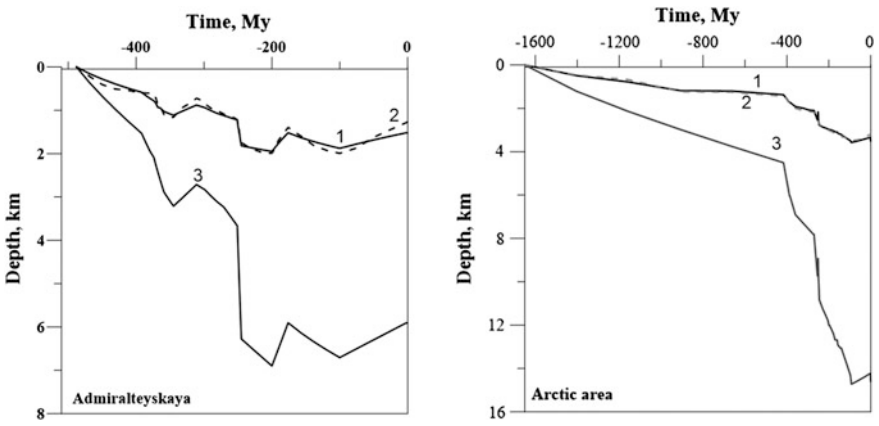

Fig. 3.14 Tectonic subsidence of the basement surface in the Admiralteyskaya and Arctic areas of the East Barents Basin calculated in the local isostasy approach. *1* (*upper solid line*) calculated by removing sediment and water load. *2* (*upper dashed line*) calculated by consideration of time-variations in density profile of the basement. *3* (*lower solid line*) the depth of the basement surface received by usual "backstripping" procedure

This analysis suggested an isostatic response of the basement on the external and internal load. The base of the domain for temperature calculation ($Z \approx 95$–115 km) is considered as isostasy level. It is located within the deep, heated horizons of the mantle. Here the rocks are rheologically weak and able to flow under rather small strength difference (Sect. 1.4). Deviations from isostasy should not be great. A weakening of the lithosphere during its heating or extension contributes to the state of isostasy. This state is reached also for sedimentary load when the typical horizontal size of sedimentary cover exceeds considerably the effective elastic thickness of the lithosphere (Sect. 1.4).

An analysis of tectonic subsidence of the basement is used in our modeling to estimate the sequence and amplitude of tectonic-thermal events, which could occur during the basin evolution (Sect. 1.3). For this aim the variations in the basement tectonic subsidence are computed by two independent methods. The first calculates the response of the lithosphere caused by removing of water and sediments load. These variations in the basement tectonic subsidence are shown in Fig. 3.14 by solid lines 1. In the second method, tectonic subsidence is determined from the time-variations in density distribution with depth within the basement (Sect. 1.2). In this method, changes of the basement rock densities due to thermal expansion of rocks during thermal activation of the lithosphere, the lithosphere stretching, phase transitions in the mantle and other processes considered in Sects. 1.2 and 1.3 are taken into consideration. The corresponding variations in the basement tectonic subsidence are shown in Fig. 3.14 by dashed lines 2. Both of the tectonic curves (1 and 2) must coincide at local isostasy response of the basin lithosphere on

internal and external load. The assumed thermal reactivation or extension of the lithosphere changes the density distribution in the basement. An amplitude and duration of the event are chosen to ensure coinciding the dashed tectonic line (2) with the solid one (1), provided that the chosen parameters do not contradict to available geological and geophysical information about structure and evolution of the region (Fig. 3.14; Sect. 1.3).

The analysis of variations in the basement tectonic subsidence in Fig. 3.14 allowed an assessment of intensity and duration thermal activations and extension amplitudes of the lithosphere in southern and northern part of the East Barentz Basin. Thermal activation in the Cenozoic explains erosion of 500 m of sedimentary section in the Arctic area and 800 m in the Admiralteyskaya area. In addition, tectonic analysis suggests two thermal activations, that explain the 500 m erosion in Carboniferous and erosion of the 1000 m of sediments in the Lower Jurassic in the later area (Fig. 3.6; Table 3.2). The analysis of tectonic subsidence of the Basin assumes a more intensive thermal activation of the basin lithosphere in the Cenozoic in the northern areas of the Basin than in the southern (Figs. 3.9 and 3.10). As mentioned above, this is in accordance with increase of heat flow to the North with approach to the Gakkel Ridge.

The modeling suggests two main stage of the lithosphere extension occurred in the northern and southern parts of the Basin. The first stage with extension amplitude $\beta = 1.15–1.17$ lasted during all Devonian in the Arctic area and during the Upper Devonian in the Admiralteyskaya area. After the first period, the second stage of the lithosphere extension with amplitude $\beta = 1.20$ occurred in the Upper Permian—Lower Triassic in both areas of the East Barentz Basin. In the Arctic area, the third period of extension took place. It had the same integral amplitude and lasted from Triassic to Lower Cretaceous. The subsidence of the Basin in this time can't be explained by simple thermal cooling of the lithosphere (Figs. 3.5 and 3.14). Referring to tectonic analysis, it should be noted that the estimates of the duration and amplitudes of thermal and tectonic events described above are based on the chronology of the layers in the sedimentary sections which is rather approximate for the deep horizons of the Permian, Carboniferous and Devonian. More accurate definition of the rock age in these sections at further study of the Basin can correct our estimates.

Evolution of thermal regime of the lithosphere in the East Barents region is shown in Figs. 3.9 and 3.10 on the example of the Arctic and Admiralteyskaya areas. This evolution includes the Devonian continental rifting and considerable crust thinning in the Permian-Triassic. The modern value of the crust thickness is about 34 km in the Arctic area and 31 km in the Admiralteyskaya area including 14.6 and 5.9 km of sedimentary cover. Therefore, the consolidated crust decrease from initial thickness 35 km to the modern values 19.5 and 25 km in the first and second areas due to the lithosphere extension.

3.4 Conclusion

Tectonic history of the Basin includes the continental rifting in the Devonian and considerable subsiding of the Basin in the Permian and Triassic, associated with intensive sedimentation. According such history, our modeling suggests two main stage of the lithosphere extension occurred in the northern and southern parts of the Basin. The first stage with extension amplitude $\beta = 1.15–1.17$ lasted during all Devonian in the Arctic area and during the Upper Devonian in the Admiralteyskaya area. After the first period, the second stage of the lithosphere extension with amplitude $\beta = 1.20$ occurred in the Upper Permian—Lower Triassic in both areas of the East Barentz Basin. The modeling suggests more intensive thermal activation of the lithosphere in the northern areas of the Basin (the Admiralteyskoe Rise) than in the southern ones (the South Barents Depression). This is in accordance with increase of heat flow to the North with approach to the Gakkel Ridge. These conclusions are confirmed by analysis in paper [30] where modeling of three wells in the Admiralteyskoe Rise and 4 wells in the East Barentz Depression are considered. According to our modeling, sufficient part of the Permian-Triassic deposits in the South Barents Depression occurs within the gas generation zone. Liquid hydrocarbons generated by the Ordovician, Silurian and Devonian deposits in the Admiralteyskoe Rise and by Devonian, Permian and considerable part of Triassic rocks in the South Barents Depression were subjected totally or partly to secondary creaking.

References

1. Shipilov EV, Mossur AP (1990) Anomalous seismic horizons in the sedimentary cover of the Barents Sea. Geotectonica 1:90–96 (in Russian)
2. Bogdanov NF, Khain VE (eds) (1996) Remarks to tectonic map of the Barents Sea and northern part of the European Russia. Map and geological-geophysical profiles. The RAN Lithosphere Institute
3. Kogan LI, Murzin RR (1997) The East Barents Sea depression is the one of ancient in the Earth (according to seismic data). In: Geologia morey I okeanov. XII International geological school. Abstracts, vol 1, GEOS, pp 253–254 (in Russian)
4. Aplonov SV (2000) Geodynamics of the deep sedimentary basins. S.-P, TsGI TETIS (in Russian)
5. Neprochnov YuP, Semonov GA, Sharov NV, Yliniemi J, Komminaho K, Luosto U, Heikkinen P (2000) Comparison of te crustal structures of the Barents Sea and the Baltic Shield from seismic data. Tectonophysics 321:429–447
6. Kogan LI, Malovitskiy YP, Murzin RR (2002) Deep structure of the East Barents depression by the data of wide angle seismic sounding. Razvedka I Okhrana Nedr (8 August):52–58 (in Russian)
7. Verzhbitsky EV (2000) Geothermal regime and origin of the eastern part of the Barents Sea region. Okeanologiya 40(3):448–455 (in Russian)
8. Verzhbitsky EV (2002) Geothermal regime, floor tectonics and temperature conditions for HC generation in the eastern part of the Barents Sea. Geotectonica 1:86–96 (in Russian)

9. Gramberg IS (1997) The Barents Sea Permian-Triassic paleorift and its significance for oil-gas bearing problems in the Barents Karskoe plate. Dokl RAN 352(6):789–791 (in Russian)
10. Gramberg IS, Evdokimova NK, Suprunenko OI (2001) Catagenesis zoning of sedimentary blanket of the Barents Sea shelf in relation with the oil and gas prospecting of the region. Geologiya I Geophizika 42(11–12):1808–1820 (in Russian)
11. Korotaev MV, Nikishin AM, Shipilov EV, Cloetingh S, Stefenson RA (1998) Geological history of the East Barents Sea region in the Paleozoic-Mesozoic by the data of computer modeling. Doklady RAN 359(5):654–658 (in Russian)
12. Mckenna ThE, Sharp JM (1998) Radiogenic heat production in sedimentary rocks of the Gulf of Mexico Basin, South Texas. AAPG Bull 82(3):484–496
13. Perrier B, Quiblier J (1974) Thickness changes in sedimentary layers during compaction history: methods for quantitative evaluation. AAPG Bull 58(3):507–520
14. Sweeney JJ, Burnham AK (1990) Evolution of a simple model of vitrinite reflectance based on chemical kinetics. AAPG Bull 74(10):1559–1570
15. Frakes LA (1979) Climates throughout geological time. Elsevier, Amsterdam
16. Welte DH, Horsfield B, Baker DR (eds) (1997) Petroleum and basin evolution. Springer
17. Velichko AA (1987) Climatic variations in Meso-Cenozoic by the data for East Europe. In: Climates of the Earth in geological history. Moscow, Nauka, pp 5–43 (in Russian)
18. Velichko AA (ed) (1999) The climate and landscape during the last 65 Ma (Cenozoic: from Paleocene to Holocene). Moscow, GEOS (in Russian)
19. Tsybulya LA, Levashkevich VG (1992) Heat flow in the Barents Sea region. Appatite (in Russian)
20. Tsybulya LA (1993) Geothermal conditions in the Barents-Karsky region and their influence on formation of oil and gas accumulations. In: Gavrilov VP (ed) Geodynamics and oil and gas bearing in Arctic, Nedra, pp 146–159 (in Russian)
21. Nielsen SB, Clausen OR, Mc Gregon E (2015) Basin % R_o: a vitrinite reflectance model derived from basin and laboratory data. First published 24 Oct 2015. doi:10.1111/bre.12160
22. Tissot BP, Pelet R, Ungerer P (1987) Thermal history of sedimentary basins, maturation indices, and kinetics of oil and gas generation. AAPG Bull 71(12):1445–1466
23. Suggate RP (1998) Relations between depth of burial, vitrinite reflectance and geothermal gradient. J Pet Geol 21:5–32
24. Makhous M, Galushkin Y (2005) Basin analysis and modeling of the burial, thermal and maturation histories in sedimentary basins. Editions TECHNIP, Paris
25. Welte DH, Horsfield B, Baker DR (eds) (1997) Petroleum and basin evolution. Springer
26. Ungerer P, Burrus I, Doligez B, Chenet P, Bessis F (1990) Basin evolution by integrated two-dimensional modeling of heat transfer, fluid flow, hydrocarbon generation, and migration. AAPG Bull 74:309–335
27. Ungerer P (1993) Modeling of petroleum generation and migration. In: Bordenave ML (ed) Applied petroleum geochemistry. Technip, Paris, pp 397–442
28. Khutorskoy MD, Podgorny LV (2001) Three dimensional model of geothermal field of the Barents Sea region. Doklady RAN 377(1):96–100 (in Russian)
29. Podgorny LV, Khutorskoy MD (1998) Thermal evolution of the lithosphere in the zone of joint of the Baltic shield and the Barents Sea plate. Phizika Zemli 4:3–9 (in Russian)
30. Galushkin YI, Yakovlev GE, Sitar KA (2014) Comparative analysis of hydrocarbon generation by probable source rocks in the deep and uplifted parts of the East Barents Basin: results from basin modeling. AAPG 3P Polar petroleum potential conference and exhibition, Stavanger, Norway, 15–18 Oct 2013. Search and Discovery Article # 10566, 1–33 (2014). Posted January 27, 2014

Chapter 4
Thermal Regime and Extension of the Lithosphere in Different Tectonic Structures of the Sirte Basin, Libya

Abstract Numerical reconstruction of burial, thermal and maturation histories are carried out for eight sedimentary sections along the profile from the Cyrenaica Platform on the eastern coast of the Sirte Basin to the Hun Graben on the western border of the Sirte paleoift. The interval of depths for temperature calculations included the sedimentary. The analysis of variations in the tectonic subsidence of the basin is used to estimate the amplitudes and duration of the events of thermal activation and extension of the lithosphere occurred during evolution of the Sirte Basin. The modeling suggests that thermal activations of the lithosphere in the Albian–Cenomanian and Oligocene–Pleistocene are common for all tectonic structures of the Sirte Basin and the Cyrenaica Platform. A relatively high temperature regime is also typical for modern state of the lithosphere in the Sirte Basin and Cyrenaica Platform. Such a regime is caused mainly by the thermal activation of the lithosphere during the last 10 Ma. The intensity of this activation is highest in the western part of the Basin, where it is accompanied by the highest erosion amplitudes. The analysis of the variations in the basin tectonic subsidence suggests that two intervals of significant extension of the lithosphere in the Upper Cretaceous and Paleocene are common for all areas within the basin. The total amplitude of the crustal extension attains 1.5 in the central part of the Sirte Basin (the Ajdabiya and Maradah troughs and Zelten and Dahra platforms), is equal to 1.3 in the Hameimat and Zallah troughs, and is minimal (1.11–1.17) in the periphery of the basin (within the Hun Graben and Cyrenaica Platform).

Keywords Sirt sedimentary basin · Cyrenaica platform · Tectonic subsidence · Vitrinite reflectance · Hydrocarbon generation · Lithosphere extension

4.1 Tectonic and Geological History of the Basin

The tectonic structure of the Sirte Basin, its thermal history, and catagenetic transformation of its organic matter (OM) have been studied by many authors in relation to the problem of hydrocarbon (HC) generation [1–8]. Abadi et al. [7]

Y. Galushkin, *Non-standard Problems in Basin Modelling*,
DOI 10.1007/978-3-319-33882-8_4

carried out the backstripping analysis for about 200 sedimentary sections (borehole columns) and, based on this, estimated the amplitudes and duration of the intervals of the lithospheric extension in the burial history of the Sirte Basin. These authors distinguish four tectonic stages in the evolution of the Basin from the Late Jurassic to the present. At the same time, the thermal history of the basin and maturity evolution of organic matter in sedimentary rocks are interpreted quite loosely in the works quoted above. Namely, it is assumed that the temperature gradient remained constant throughout the entire history of the basin, that is the time and depth variations in the gradient were neglected. However, they also note that the tectonic and thermal history of the Sirte Basin is characterized by numerous intervals of thermal activation and extension of the lithosphere, which alternated with the intervals of relative tectonic quiescence and thermal cooling of the lithosphere. In this chapter, we apply the GALO system for basin modeling to study the influence of the intervals of activation and lithospheric extension on the formation of the thermal regime of the basin. This system is suitable for analyzing variations in the tectonic subsidence of the basin and assessing, on this basis, the duration and amplitude of the events of thermal and tectonic activation (extension) of the lithosphere, which took place during the basin evolution (see Sects. 1.2 and 1.3).

The comparative analysis of the data of drilling and two-dimensional sedimentary sections presented in [1, 3, 4, 6–9] was used here for constructing the refined sedimentary columns in pseudo wells. They reflect the sedimentary sections of the main tectonic structures of the Sirte Basin: the Cyrenaica, Zelten, and Dahra platforms and Hameimat, Ajdabiya, Murabah, Zallah, and Hun grabens (Fig. 4.1). All the sedimentary sequences analyzed in this Chapter included the Lower Cretaceous complex as the oldest formation of the sedimentary cover (Figs. 4.2 and 4.3). The analysis of two_dimensional sections was also used for a rough estimation of the amplitudes of erosion, which was not once in the Basin history. It is marked in sedimentary section by unconformities at rifting stage in the Lower Cretaceous, at the boundary of the Lower and Upper Cretaceous, in the Lower and Middle Eocene, and in the Upper Miocene–Pleistocene [4].

The history of geological evolution of the Sirte Basin has been the focus of studies of many scientist [3, 4, 6–11]. According to these works, the Basin was developing on the triple junction of continental rift faults on the northern margin of Africa. Rifting started in the Early Cretaceous, peaked in the Late Cretaceous, and ceased in the Early Tertiary, having formed the triple junction of the Sirte, Tibesti, and Sahrir arms within the Basin [3, 12]. The Late Cretaceous rifting was characterized by the formation of a series of northwest striking horsts and grabens deepening (in a stepwise manner) to eastwards, so that the Sirte Trough is the deepest part of the Basin. In the north, these horsts and grabens continue in the complex marine blocks, which include the Ionic abyssal plateau in the northeast [3]. The plateau is underlain by the oceanic crust, which is subducted northwards and eastwards beneath the Hellenic Arc. The marine provinces in the west and the pull-apart formations of the Sabratah Basin, which stretch along the Cyrenaica southern fault zone and Cyrenaica Platform in the east, are strongly affected by the extensional tectonics. The Nubian Uplift located in the south is an example of a

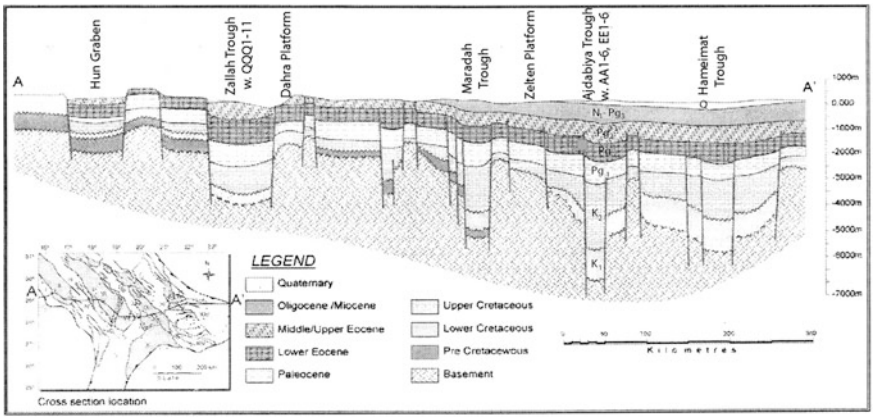

Fig. 4.1 Location of the main structures of the Sirt Basin analyzed in the paper (after [10] with little changes)

stable continental basement. It is considered as the prerifting lithosphere for the rift basins considered above [3].

In the Cenomanian, the marine transgression in Libya was controlled by the sharp horst and graben relief, which was preserved after the crumpling of the Sirte Arc [4]. Initially, shallow marine sediments were deposited in the grabens. However, with the development of the transgression, deep_sea marine condition propagated into the grabens, whereas shallow-water sediments were gradually accumulated on the surface of the horsts [4]. In the Late Cretaceous, extension again becomes a predominant regime along the southern margin of Thetis. In the end of the Cretaceous, the Sirte Basin grabens were largely filled with sediments, and most of the horsts were covered by shallow-water marine deposits. Some of these deposits form important reservoirs for thydrocarbons [4]. The Early Tertiary time in Libya was marked by the uplifting of the surface and regression of the sea in the western regions. Simultaneously, the previous Cretaceous grabens of the Sirte Basin gradually subsided. Major subsidence occurred in the Ajdabiya Trough (Fig. 4.1). At that time, vast carbonate platforms with the rifts in the marginal parts of the sea were formed. The Paleocene–Eocene carbonates are the main reservoirs for hydrocarbons in Libya [3, 4]. Subsidence in the Hun Graben took place in the Oligocene [4]. In the Neogene, marine sediments were accumulated in the Ajdabiya Trough and on the Cyrenaica Platform. Large volumes of basaltic magmas were erupted by the volcanoes chaining along the axis of the ancient Tripoli–Tibesti uplift. Thus, the geological evolution of the Sirte Basin suggests the differences in the subsidence histories of the horst and graben structures of the Basin, the presence of recurrent intervals of thermal activation and the extension of the lithosphere, which were accompanied by unconformities in the sedimentary sequences or periods of fast accumulation of sediments. In next section, the GALO system will be used to consider these events in detail.

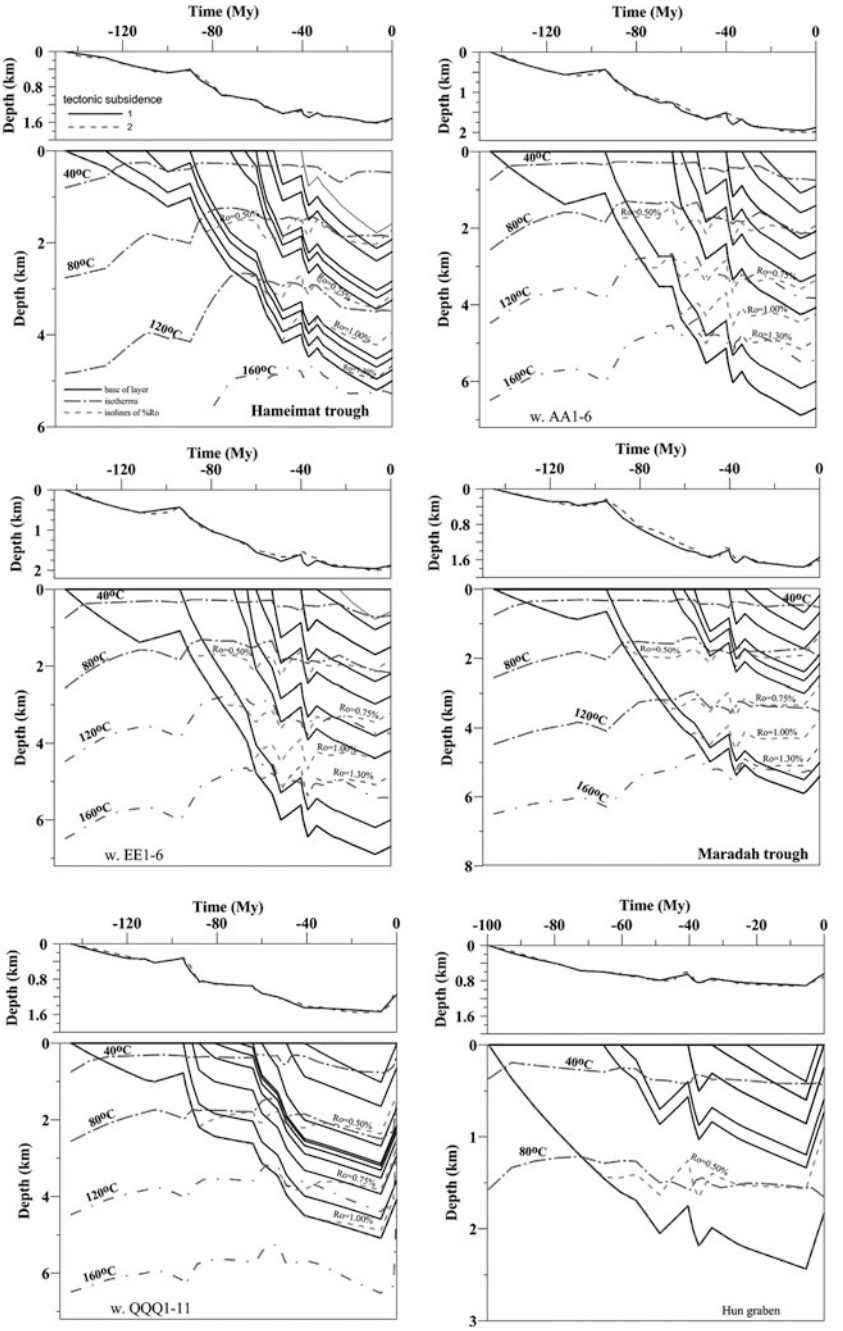
Time (My)
-120
-80
-40
0
Depth (km)
tectonic subsidence
1
2
40ºC
80ºC
120ºC
160ºC
Ro=0.50%
Ro=0.75%
Ro=1.00%
Ro=1.30%
base of layer
isotherms
isolines of %Ro
Hameimat trough
w. AA1-6
w. EE1-6
Maradah trough
-100
-60
w. QQQ1-11
Hun graben

◀ **Fig. 4.2** Variations in tectonic subsidence (*upper figures*) and burial, thermal and maturation histories (*lower figures*) of grabens and troughs in the Sirt Basin. *Upper figures*: *1* (*solid line*) tectonic subsidence of the basement surface calculated in the local isostasy approach by removing sediment and water load (see Sect. 1.2.1); *2* (*dashed line*) tectonic subsidence of the basement surface calculated by consideration of time-variations in density profile in the basement (see Sect. 1.2.2). *Lower figures*: legend at lower left angle of the first figure

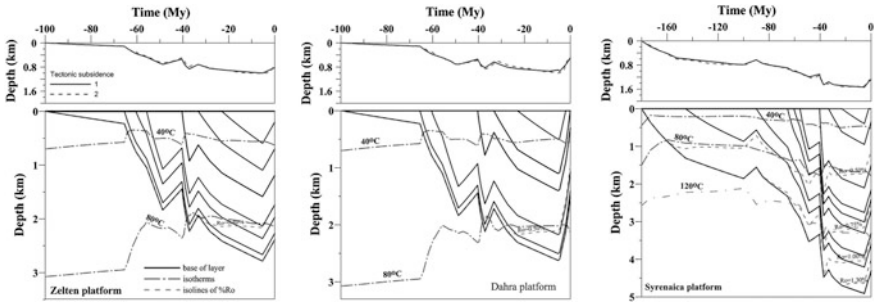

Fig. 4.3 Variations in tectonic subsidence (*upper figures*) and burial, thermal and maturation histories (*lower figures*) of the Zelten, Dahra, and Cyrenaica Platforms. Legend in Fig. 4.2

4.2 Temperature and Maturation Histories of the Sirte Basin

4.2.1 The Principles of Thermal History Computation

Figures 4.2 and 4.3 show the results of numerical reconstructions of burial and thermal history of the Sirte Basin for sedimentary sections typical of the graben (Fig. 4.2) and platform (Fig. 4.3) structures of the Basin. The reconstructions are based on the information about the structure and geological evolution of the region, drilling and seismic tomography data, as well as the measurements of deep temperature and vitrinite reflectance in the modern section of the Basin. The principles and algorithms of numerical reconstruction of the thermal history of the basin are described in detail in Sect. 1.1. According to Chap. 1, the temperature distribution in the rocks is obtained by solution the one-dimensional (z) non-steady heat transfer equation in the area whose boundaries vary during the erosion and accumulation of sediments. The thermophysical parameters of the rocks vary with the depth, time and temperature of the buried rocks. The surface of the basin is kept at the temperature corresponding to the paleoclimate in the considered time-interval of the basin evolution. The paleoclimate curve is presented in Fig. 4.4. It is constructed on the base of variations in the paleolatitude of the Basin during its development [4, 6] and annual average temperature on the neutral depth quoted in [13]. Figure 4.4 demonstrates that the annual average temperature quite moderately varied within 22–27 °C from the Early Cretaceous to the present.

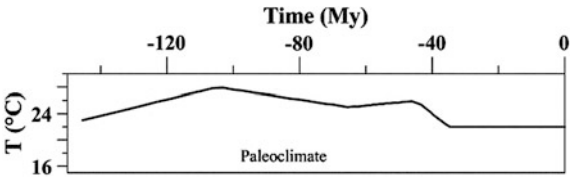

Fig. 4.4 The mean-annual temperature at the Basin surface as a function of time during the Sirt Basin evolution

The sedimentary rocks of the Sirte Basin are represented by a diverse mixture of clay schists, sands, limestones, magnesian limes, marls, salts, and anhydrites [1, 4]. The principles of computation of petrophysical parameters of sedimentary rocks in our modeling are described in Chap. 1. Throughout all time of the Basin development, steady temperature *TM* is maintained at the depth *ZM* (bottom of the domain for temperature calculation). In our reconstructions, it ranged from 1150 to 1160 °C at depth *ZM* = 150–160 km (Fig. 4.5). The values of *TM* and *ZM* and the initial temperature profile are determined according to Sect. 1.1.4.

It is believed that the lithosphere at the initial stage of the Basin development i.e., before the extension, could be presented by the standard continental lithosphere Table 1.1 with little difference concerning with the higher generation of radiogenic heat in the crustal rocks in our model (Table 4.1). Such heat generation is in

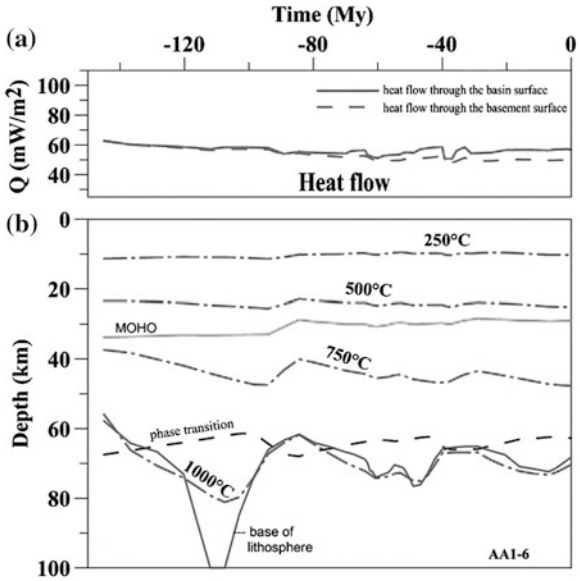

Fig. 4.5 Thermal history of the Sirt Basin lithosphere in the Hameimat trough. **a** Computed variations in the heat flow. **b** Evolution of the thermal regime in the Basin lithosphere. *Dotted-dashed lines* are isotherms. *The "MOHO"-line* is the base of the crust. *The "phase transition"-line* is the location of "spinel peridotite—garnet peridotite" compositional transition in the mantle (Eq. (1.16) in Sect. 1.2.2). The "base of lithosphere"-line is the base of the lithosphere determined by intersection of current geotherm with the solidus curve (1.4) in Sect. 1.1.3

Table 4.1 The structure of continental lithosphere in the North Africa and thermo-physical parameters of the basement rocks

Layer	Гранитный		"Базальтовый"	Мантия
Depth of the layer base (km)	5.0	15.0	35.0	>35
Density (kg/m^3)	2750	2750	2900	3300
Heat conductivity (W/m °K)	2.72	2.72	1.88	K = f(T)*
Heat generation (mkW/m^3)	1.67	1.05	0.54	0.004

*See comments to Table 1.1 in Sect. 1.1.2

agreement with the results of the seismic and thermal studies of the lithosphere in the Hoggar massif and other regions of North Africa [14–18]. According to Table 4.1, radiogenic heat at the stage of basin nucleation contributed 36 mW/m^2 to the surface heat flow, which is far above the corresponding value of 25 mW/m^2 for the standard continental lithosphere Table 1.1. The initial thickness of the crust (35 km) in the lithosphere in Table 4.1 agrees with its estimates in the present-day undeformed regions in the Central Africa [7, 19, 20].

As mentioned above, the temperature *TM* kept at a level of 1150–1160 °C on the bottom of the model at the depth *ZM* = 150–160 km. This temperature differs from the values assumed in other systems. For example, in the models reproducing uniform and nonuniform extension of the lithosphere [7, 21–24], the temperature *TM* = 1333 °C is kept at a depth *ZM* = 100–120 km, which appears to be too high even for the oceanic lithosphere. Indeed, the temperature of the effused lavas is estimated at 1000–1200, 850–1000, and 650–850 °C for basaltic, andesitic, and rhyolitic magmas (Wikipedia). Assuming the temperature gradient γ to be 1 °C per km within the column of molten magma in the interval of 40–70 km (the depth of the melt sources) and 0.5 °C per km in the deeper mantle [25], the temperature growth from the surface (or the bottom of the sea) to a depth of 100–120 km is estimated at 100 °C at most. Then, the temperature of the mantle rocks at a depth of 100–120 km beneath the axial zones of the mid-oceanic ridges is 1100–1300 °C, or *TM* = 1250 °C, assuming the average temperature of basaltic lavas at the surface to be 1150 °C. However, the corresponding temperatures for the continental lithosphere should be noticeably lower since the temperature gradient in the mantle beneath the continents is lower than beneath oceans [25]. Therefore, the *TM* values used in our modeling of the continental lithosphere in the Sirte Basin seem to be quite plausible.

4.2.2 Evolution of the Temperature Regime of Sedimentary Rocks in the Basin

Comparison of computed temperature distribution with measured temperatures is demonstrated in Fig. 4.6 for different sedimentary sections of the Sirt Basin. The temperature gradients and depths presented in the paper [26] were used to construct

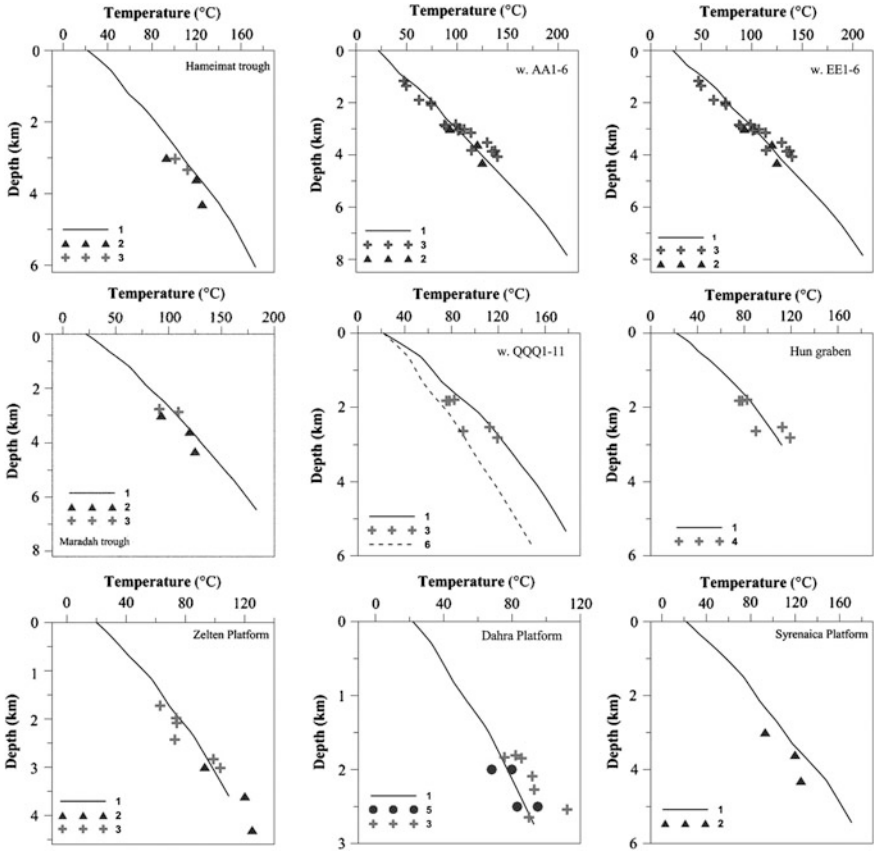

Fig. 4.6 Comparison between computed and measured temperatures. *1* present-day temperature distribution versus depth computed in our modeling; *2* measured temperatures for the eastern part of the Sirt Basin [7]; *3* measured temperatures obtained from the data presented in [26]; *4* the same for w. QQQ1-11; *5* measured temperatures for the western part of the Sirt Basin [26]; *6* temperature distribution for the QQQ1-11 section computed without consideration of hydrothermal activity (see text)

the data base of measured deep temperatures for the wells and pseudowells of our paper. These data were absent only for most western and most eastern parts of the region under consideration, and consequently, the temperatures measured in Zallah trough (in the QQQ1-11 well) were used for control of modeling in the Hun graben (Fig. 4.6), whereas the temperatures measured in the eastern part of the Sirt Basin [7] were utilized for control of modeling in the Syrenaica Platform. As whole, Fig. 4.6 demonstrates rather reasonable agreement between calculated and measured temperatures in the sedimentary sections and the uppermost basement. The high present-day temperatures measured in the QQQ1-11 section can are explained by hydrothermal heating and will be discussed in next section more detailed.

Our calculations support rather high temperature regime of the Sirt Basin and the Syrenaica Platform when temperatures about 100 °C and more are reached at the depths of 2–3 km. Such temperatures are partly resulted from thermal activation of the Basin lithosphere in the last 10 My. This activation was more intensive in the western part of the Sirt Basin where the last erosion was also maximal (Figs. 4.2 and 4.3). Consequently, the temperatures in the Hun and Zallah troughs are considerably higher than the temperatures at the same depths in the eastern areas of the Sirt Basin (Fig. 4.6).

4.2.3 *Maturation History of Organic Matter in the Sirt Basin*

Calculated temperatures of sedimentary rocks as a function of burial time and kinetic spectra of vitrinite maturation from Table 3.3 in Sect. 3.2.2 are applied for estimation of maturation degree of organic matter by means of evaluation of vitrinite reflectance Ro (%). The algorithm is discussed in Sect. 3.3. Dotted lines in Figs. 4.2 and 4.3 demonstrate the depths of Ro-isolines in burial history of the Basin computed by the EASY%Ro model (Eq. (3.3) in Sect. 3.2.2). Figure 4.7 shows a comparison between calculated and measured values of Ro% in present-day sections of the Sirt Basin. As mentioned above, the Ro% values were measured only in the sections of the AA1-6, EE1-6 and QQQ1-11 wells. The rest of the sedimentary sections analyzed in our paper are pseudowells constructed from generalized geological two-dimensional sections of the Sirt Basin presented in papers [3, 4, 6, 7, 10]. They associated with the deepest sites of troughs and shallowest sites of Platforms (Fig. 4.1). Correspondingly, only reconstructions of the above three wells utilized the Ro-values measured in cores of these wells. At the same time, we applied for control of the modeling also the Ro-values from papers [3, 4] where they in turn were used for control of corresponding TTI—reconstructions in the Hameimat and Maradah troughs and the Syrenaica Platform (Fig. 4.7). Typical set of Ro-values measured in the samples of the western parts of the Sirt Basin from the paper [7] were also shown in Fig. 4.7 for the Hun graben and Dahra Platform, despite the fact that the depth of some these measurements exceeds a thickness of the considered sedimentary sections (Fig. 4.7). There are not measurements of Ro-values in central part of the Sirt basin and reconstruction of Zelten Platform was carried out without control by Ro-measurements.

As result of rather high thermal regime of the basin lithosphere (Figs. 4.2, 4.3, 4.4 and 4.6), the Lower Cretaceous rocks at the base of sedimentary section of the Hameimat, Ajidabiya, Maradah and Zallah troughs and the Lower Jurassic organic matter at the base of sedimentary section of the Syrenaica Platform, located at the depth more than 4 km in the present-day section, reach a high maturation level (Ro > 1.20 %; Table 4.2). At the same time, organic matter of the Senomanian

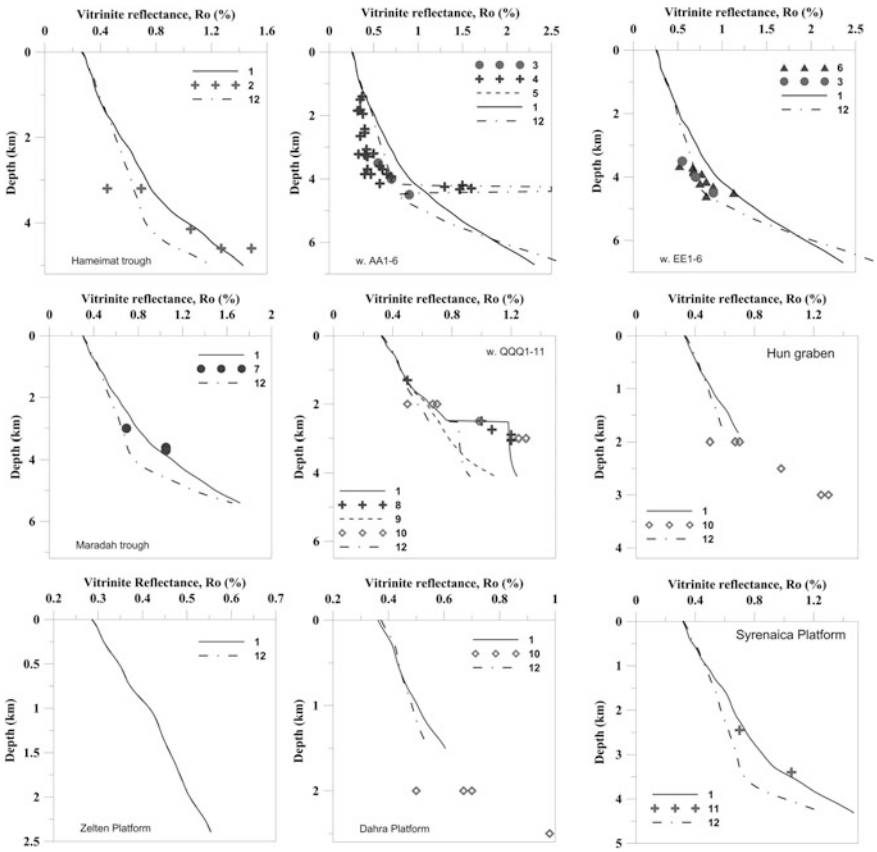

Fig. 4.7 Change of vitrinite reflectance with depth in the present-day sedimentary sections of the Sirt Basin and comparison with measured values. *1* present-day distributions of vitrinite reflectance versus depth computed by the EASY%Ro model (Eq. 3.3, Sect. 3.2.2); *2* the Ro-values taken from TTI—reconstruction of sedimentary section of the Hameimat trough [3]; *3* the mean Ro-values used in paper [7] for the eastern Sirt Basin; *4* the Ro-values measured in w. AA1-6 [1]; *5* present-day distribution of Ro versus depth computed with consideration of intrusion heating (see text); *6* the Ro-values measured in w. EE1-6 [1]; *7* the Ro-values taken from TTI—reconstruction of sedimentary section of the Maradah trough [4]; *8* the Ro-values measured in w. QQQ1-11 [1]; *9* present-day distribution of Ro versus depth computed without consideration of hydrothermal heating (see text); *10* the mean Ro-values used in paper ([7] for the western Sirt Basin; *11* the Ro-values taken from TTI—reconstruction of sedimentary section of the w. A1-36 in the Syrenaica Platform [4]; *12* present-day distributions of vitrinite reflectance versus depth computed by the BASINRo model (Eq. 3.4, Sect. 3.2.2)

rocks at the base of sedimentary sections in the Zelten and Dahra Platforms and the Hun graben at depth of 1.5–2.4 km (in the present-day section) reach only the early stage of maturation (Ro < 0.61 % in the EASY%Ro model and 0.54 % in the BASIN%Ro model; Table 3.3). Then, these Senomanian rocks can't be considered

Table 4.2 Maturity level and realization of hydrocarbon potential in the Sirt Basin and Cyrenaica Platform (results of modeling)

t	Z	T	Ro	Hi	Ht	Ho	Hg	t_1	t_{exp}	t_2	TOC_1	TOC
My	m	ºC	%	Mg HC/g TOC				Million years ago			g TOC/g rock %	
Hameimat trough												
145.5	5000	154.1	1.404	627	609	353	140	82	65.5	18	5.89	3.00
127.6	4760	149.7	1.321	627	606	440	97.8	80	59.8	5	5.86	3.00
109.5	4500	143.6	1.200	627	600	515	58.6	76.4	55.1	–	5.81	3.00
90	4320	140.3	1.147	627	595	535	45.7	74.5	53.8	–	5.76	3.00
72.1	3240	112.7	0.765	627	230	222	8	52.3	5.8	–	3.68	3.00
65.5	3000	106.9	0.726	627	141	136	5.2	49.7	–	–	3.38	3.00
60.5	2830	103.3	0.699	627	99.9	96.1	3.8	47.7	–	–	3.26	3.00
55.8	2190	87.4	0.586	627	21.1	20.4	0.7	19.9	–	–	3.05	3.00
Adjidabiya trough, w. AA1-6												
145	6700	186.7	2.260	627	622	0	312	88.8	76.2	54.4	6.01	3.00
94	6000	171.6	1.845	627	618	0.302	308	81	68.2	39.2	5.98	3.00
64	4073	124.8	0.913	627	495	481	14.3	56.1	31.4	–	4.99	3.00
60	3216	104.5	0.719	627	129	125	4.0	37.5	–	–	3.35	3.00
53	2628	88.7	0.611	627	26.4	25.6	0.8	25.7	–	–	3.07	3.00
Adjidabiya trough, w. EE1-6												
145	6700	187.7	2.313	627	622	0	212	88.6	74.9	57	6.01	3.00
94	6000	172.6	1.891	627	619	0.03	309	80	67.5	50.2	5.99	3.00
70	4194	128.5	0.989	627	536	513	23.4	59.8	48.6	–	5.28	3.00
64	3611	116.2	0.823	627	379	368	11.2	55.4	25.3	–	4.32	3.00
60	2778	96	0.663	627	60.1	58	2.1	37.4	–	–	3.15	3.00
Maradah trough												
145	5400	160.6	1.680	627	616	31.9	291	84.3	70.2	35.6	5.96	3.00
95	5000	151.7	1.475	627	612	246	191	79.3	65.4	22	5.92	3.00
83.2	4000	130	1.092	627	581	543	37.9	63.1	49.1	–	5.64	3.00
74	3200	111.7	0.831	627	384	370	14	55.6	19	–	4.34	3.00
65.5	2500	94.9	0.700	627	102	98	4	38.7	–	–	3.27	3.00
60.5	2150	84.9	0.635	627	37.1	35.5	1.6	31	–	–	3.09	3.00
Zallah trough, w.QQQ1-11												
145	4100	151.8	1.227	627	602	505	65.1	87.6	56.6	–	5.83	3.00
95	3600	139.2	1.185	627	599	521	55.5	76	48.4	–	5.80	3.00
91	2947	122.5	1.169	627	598	526	52.3	58	35.8	–	5.79	3.00
88	2529	112.5	0.765	627	239	231	8.3	51.3	18.2	–	3.72	3.00
81	2324	106.8	0.720	627	137	132	5.1	47.2	0.36	–	3.37	3.00
70	2206	102.9	0.690	627	93.2	89.6	3.6	45.5	–	–	3.24	3.00
64	2151	101.7	0.679	627	80.4	77.3	3.1	44.9	–	–	3.21	3.00
60	1697	84.1	0.563	627	17.6	17.1	0.5	35.2	–	–	3.04	3.00

(continued)

Table 4.2 (continued)

t	Z	T	Ro	Hi	Ht	Ho	Hg	t_1	t_{exp}	t_2	TOC_1	TOC
My	m	ºC	%	Mg HC/g TOC				Million years ago			g TOC/g rock %	
Hun trough												
99.6	1830	84.7	0.684	627	81.1	77.8	3.3	66	–	–	3.21	3.00
86.3	1400	71.6	0.597	627	22.9	22	0.9	38	–	–	3.14	3.00
65.5	730	50.2	0.448	627	6.6	6.58	0.02	–	–	–	3.02	3.00
Zelten Platform												
99.6	2390	85.7	0.624	160	2.24	0.7	1.34	32	–	–	3.04	3.00
65.5	2270	82.9	0.603	160	1.4	0.44	0.96	27.5	–	–	3.02	3.00
60.5	1970	74.7	0.553	160	0.325	0.102	0.223	15	–	–	3.01	3.00
Dahra Platform												
99.6	1520	66.4	0.604	160	1.45	0.453	0.997	27	–	–	3.02	3.00
65.5	1400	63.3	0.580	160	0.89	0.28	0.61	23	–	–	3.01	3.00
60.5	1070	52.9	0.512	160	0.16	0.05	0.11	7.6	–	–	3.00	3.00
Syrenaica Platform												
180	4300	147.2	1.443	160	117	24.9	86.3	156.8	37.1	20.5	–	3.00
145.5	3600	126.1	1.082	160	86.2	26.6	59.6	66.5	–	–	–	3.00
90	3300	116.7	0.927	160	60.3	18.8	41.5	56.3	–	–	4.4	3.00
65.5	2700	102.7	0.780	160	26.7	8.3	18.4	38.8	–	–	3.49	3.00
60.5	2400	94.2	0.724	160	13.3	4.16	9.14	37.4	–	–	3.23	3.00
55.8	2150	87.7	0.676	160	7.34	2.29	5.05	36.5	–	–	3.12	3.00
40.4	1500	73.3	0.582	160	0.939	0.293	0.646	25	–	–	3.01	3.00

Notes Tables 4.3

t formation age in My. *z* depth in km. *T* calculated temperature in °C. *Ro* vitrinite reflectance(%Ro) calculated in the EASY%Ro model (Eq. (3.3) in Sect. 3.2.2); z, T, Ro-values belong to the present-day section of the basin, t = 0). *Hi* initial potential of HC generation by the formation rock; *Ht* total HC generation, *Ho* oil generation and *Hg* gas generation (in mg HC/g Corg). t_1, t_2 the times of enter in the "oil windows" (0.50 % ≤ Ro ≤ 1.30 %) and leaving it by rocks; t_{exp} time of expulsion threshold for liquid HC, determined by the time of filling of 20 % of porous volume in the source rocks by the generated liquid hydrocarbons [27]; *TOC1* and *TOC* initial and present-day values of organic matter content. Standard marine kerogen of type II with initial hydrocarbon potential 627 mg HC/g TOC is assumed in the Table for organic matter in sedimentary rocks in the Troughs and standard kerogen of type III with initial hydrocarbon potential 160 mg HC/g TOC—for the rocks in the Platforms. The calculations were carried out at steady present-day organic matter content equaled to 3 % in all formations

as active source rocks in the above structures. Situation could change at the areas of these structures with deeper subsidence.

The Figs. 4.2, 4.3 and 4.7 demonstrate that in the EASY%Ro model top of the "oil window" (Ro = 0.50 %) is at depth of 0.94–0.97 km in present-day sections of the Hun Graben and Dahra Platform which were subjected to significant erosion and at the depth from 1.85 to 1.94 km in the Ajdabiya trough with minimal amplitude of the Cenozoic erosion. Our estimations of the depth of early maturation zone (Ro = 0.70–0.75 %), the peak oil generation zone (Ro = 1.00 %), and base of the "oil window" zone (Ro = 1.30 %) in Figs. 4.2 and 4.7 are in agreement with results of study of eleven wells in the Hameimat Trough [4] and with the Ro-data

presented in [3]. But the low-mature zone (0.50 < Ro < 0.70 %) in our modeling is shallower by 500–700 m than the one shown in [4]. It can be noted that the Ro-values from interval of low maturity (Ro < 0.50–0.55 %), measured in the Hameimat and Ajdabiya troughs and shown in paper [1], occur at considerable greater depth than the one obtained in all numerical estimations of maturity degree including our modeling (Figs. 4.2 and 4.7) and the assessments in the papers [3, 4, 7]. It can be noted that the vitrinite reflectance measured at depth 1–3 km in the the Ajdabiya trough agree better with the calculations in the BASIN%Ro model (Eq. (3.4) in Sect. 3.2.2). More detailed study of geological and petrophysical conditions of the Sirt Basin formation is required for solution this problem.

Concerning the comparison of Ro-values, it should be noted, that a step-like increase in Ro and following its decrease at the depth of 4.2–4.5 km in the AA1-6 section in Fig. 4.7 can be simulated by intrusion of 50 m thickness into sedimentary layer in the Upper Cretaceous at the depth from 450 to 500 m nearly 68 My ago. In our reconstructions, the conductive part of thermal action of intrusion is simulated by replacement of calculated temperatures on the intrusion temperature (900 °C) within the depth interval of the intrusion emplacement (see Part 2). Of course, the above variant of intrusion is only one of the possible scenarios. It could choice greater depths and later times of intrusion with nearly the same Ro distribution as result.

The reconstruction of the QQQ1-11 section in the Zallah trough is an additional example of anomalous modeling. The step-like increase in vitrinite reflectance in the QQQ1-11 section (Fig. 4.7) and relatively high rock temperature (Fig. 4.6) is explained in the model by hydrothermal heating from convection that comprised the uppermost 400 m of the fractured basement and sedimentary section from its base to the Turonian formation. It is believed that hydrothermal circulation was active nearly from 800 to 200 thousand years ago. The Coniacian and Santonian formations with considerable content of anhydrites limited the convection from above. In the modeling, we do not consider the process of hydrothermal heat exchange in detail, but only simulate its influence on maturation of organic matter, which is mainly due to the increase of temperature in the domain of hydrothermal activity. In our program this process was simulated by replacing existing temperature distribution, T(z,t), by the value T(hyd), that is the rock temperature of the basement at depth of 400 m from its surface (or 4.5 km from the basin surface). Such replacement is made within the depth interval of hydroactivity, $z_1 \le z \le z_2$, at each time step of the process. The depth boundaries of hydrothermal activity, z_1 and z_2, and time interval of the activity are chosen to achieve the best fitting between calculated and measured Ro. This hydrothermal activation helps also to explain rather high present-day temperatures measured at the QQQ1-11 section (Fig. 4.6). Here, similarly to previous example, it can be noted again that the presented variant of hydrothermal activity is only the one of many variants that can explain the peculiarities in distributions T(z) and Ro(z) of the well QQQ1-11 section. It point out only principal possibility of such situation.

The modeling shows that the Palaeocene and Eocene shales at the depth of 2600–3200 m in present day section reach a maturity level of Ro = 0.60–0.72 %

(by the EASY%Ro model) and could generate a little oil in the Ajdabiya Trough, as it was suggested in (Hallet 2002). In the Maradah trough, the maturity level of Ro = 0.70 % in our model is reached close to 2500 m (Figs. 4.2 and 4.7) that is in a reasonable agreement with estimations in [4]. In the western Sirt Basin, in the Zallah trough (well QQQl-11), the model suggests an erosion of 1000 m of sedimentary section during the last 7 My and shows that the Cenozoic rocks in present-day section occupy a depth interval from 0 to 2150 m and are characterized (in absence of intrusion and hydrothermal activity) by maturity from 0.32 to 0.65 % Ro (dashed line 9 in Fig. 4.7). Organic matter of the Upper Cretaceous rocks in the Zallah trough at depth from 2150 to 2950 m has maturity 0.65 < Ro < 0.90 %, and the Lower Cretaceous rocks at depth from 2950 to 4100 m—maturity from 0.90 to 1.09 % (dashed line 9 in Fig. 4.7). Such estimations agree with maturity levels observed in the trough [4]. Consideration of local effect of heating from hydrothermal activity in sedimentary section of the QQQ1-11 well, discussed above, results in increase of maturity level (Ro%) of the Cretaceous rocks by 0.2–0.4 % in the EASY%Ro model or by 0.2 % in the BASIN%Ro model (compare the dashed line 9 with solid line and dotted-dashed line in Fig. 4.7). A maturity plot in Fig. 4.7 shows that the depth of top of the oil window (Ro = 0.50 %) in pseudo-well of the Cyrenaica Platform is around 1100 m in the EASY%Ro and BASIN%Ro models and, of peak generation (Ro = 1.00 %) is at 3430 m and base of the oil window is nearly at depth of 4000 m. These depths in the BASIN%Ro model are nearly 4000 and 4300 m (Fig. 4.7). These results are confirmed by the data from the well A1-36 in the Syrenaica Platform (Fig. 4.7; [4]). Our modeling suggests that the gas shows, encountered in several wells on the Cyrenaica Platform, could be generated by the Lower Cretaceous rocks (Table 4.2).

4.2.4 Realization of Hydrocarbon Potential in the Sirt Basin

In this section, we discuss briefly the influence of the thermal history of the sedimentary cover in the Sirte Basin and change the degree of maturation of its organic matter, discussed above, on the history of the realization of the hydrocarbon potential of the Basin. There are several probable source rocks in the region. For instance, the Jurassic rocks in the Cyrenaica Platform contain organic shales [4]. But, most of the oil in the Sirt Basin was derived from the Campanian Sirt Shale (of age 83–70 My), that is a rich and thick source rock with excellent characteristics [4]. The dominant petroleum system is the Sirt-Zelten system, in which the thick Upper Cretaceous marine shaly synrift sequence contains the principal source rocks, whereas the reservoirs are shallow-marine clastics and carbonate deposits situated on horst blocks [3, 7]. It can be noted, that the Upper Cretaceous organic-rich shale occurs at several levels from the Turonian to the early Maastrichtian (93–65 My; [4]). Kerogen type grades from type III around the Trough margins, to type II in the centre of the Troughs and TOC ranges between 2 and 5 %, but occasionally exceed 10 % [4]. In our estimations, the organic matter

of sedimentary rocks in the Troughs is assumed to be the standard marine kerogen of type II with initial hydrocarbon potential HI = 627 mg HC/g TOC, and the organic matter of the rocks in the Platforms is presented by standard kerogen of type III with HI = 160 mg HC/g TOC. The three-component (oil, gas, coke) kinetic spectra of kerogen are used in computation. The algorithm of computation were taken from the papers [27–30].

Figure 4.8 demonstrates the histories of hydrocarbon generation by main formations in the Ajdabiya and Maradah Troughs and Cyrenaica Platform. The results of modeling for all areas considered in the paper are presented in Table 4.2.

According to Table 4.2 and Fig. 4.8, organic matter in the Low Cretaceous rocks in the Hameimat, Ajdabiya and Maradah troughs reached rather high maturity level

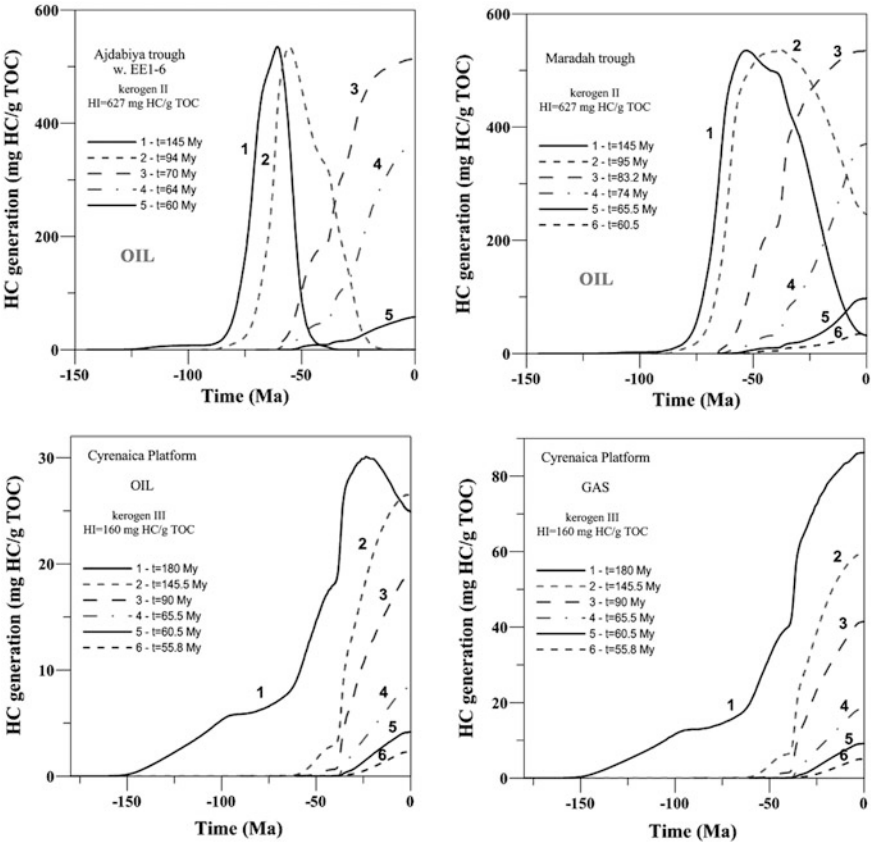

Fig. 4.8 Generation liquid and gaseous hydrocarbons in burial history of the main formations in the Ajdabiya and Maradah Troughs and Cirenaica Platform (see text). *Numbers* mark formations of different age

and generated liquid hydrocarbons could be partly or totally destroyed on gas and coke due to secondary cracking under condition that they could not migrate from source formation to upper horizons with lesser temperatures. In the Zallah trough with more moderate burial depth, these rocks in present-day section locate within the "oil windows" and can generate significant volume of oil (Table 4.2). In spite of considerable erosion (Figs. 4.2 and 4.3), the same rocks in the Hun trough and the Dahra and Zelten Platform are immature with an exception of deepest parts of these structures.

The Upper Cretaceous rocks of age 95–65 My, including the Sirt Shale formation, can be considered as intensive oil generating in all the considered areas (Figs. 4.8; Table 4.2) apart from the Hun graben, Zelten and Dahra Platforms. In the latter structures, they occur in immature or early-mature zones and hydrocarbon generation here is negligible (Table 4.2). In the Zallah Trough, Sirt Shales are early mature (Ro ≈ 0.73 %; Table 4.2) that is confirmed also by an estimations in [4]. The Turonian and Coniacian rocks in the Ajdabiya and partly Maradah trough in the present-day section are over-mature (Ro > 1.30 %) and liquid hydrocarbons generated by these rocks are partly degraded due to secondary cracking (Fig. 4.8; Table 4.2). The source rocks of the Hameimat, Ajdabiya, Maradah and Zallah trough entered into "oil window" (Ro = 0.50 %) in the Pleistocene—Eocene (see column t_1 in Table 4.2) that agrees also with assessments in [4].

Sedimentary section of the Cyrenaica Platform is deeper than the ones in the Zelten and Dahra Platforms (Figs. 4.1, 4.2 and 4.3). As mentioned above, organic matter here is assumed to characterize by terrestrial kerogen of type III that is mainly gas prone. It explains rather limited volumes of liquid hydrocarbons generated by the Jurassic and Cretaceous formations in the Cyrenaica Platforms (Table 4.2) despite the fact that maturity level of the rocks is optimal. A mixture of marine kerogen of type II and kerogen of type III could lead to considerable increase in output of liquid hydrocarbons.

4.3 Variations in Amplitude of the Lithosphere Extension in Different Structures of the Sirte Basin

In Sect. 4.2 the sedimentary section of the Sirte Basin was analyzed including its thermal, maturation and generation histories. The subject of this section is the thermal and tectonic history of the Basin lithosphere and its relationship with tectonic subsidence of the Basin. Some important problems in the analysis of tectonic subsidence of the Basin will be considered in this section and our tectonic analysis will be compared with the approaches in other papers.

4.3.1 Estimation of Amplitude of Tectonic Subsidence

Variations in depth of paleo-sea did not take into consideration in our analysis though the events of marine transgression repeated more than once in the Sirt Basin history (for example, in the Senomanian, Coniacian, Paleocene, Late Eocene and Early Oligocene, [6]). However, the paleowater depth in the Upper Cretaceous and Tertiary is estimated to be less 200 m [7] and it can be considered as negligible in Eq. (1.11). As mentioned above, a great depth of the base of the domain for temperature calculation (Sect. 4.2.1) permits to involve an analysis the variations of the basement tectonic subsidence during basin evolution to estimate the sequence and amplitude of tectonic-thermal events that took a place during the basin evolution (Sect. 1.3). The time intervals of thermal activations and basement stretching in the Sirt Basin assessed from the analysis of tectonic subsidence for 9 sedimentary sections of the Basin are shown in Table 4.3. The events of thermal activation of the Sirt lithosphere in the Albian-Senomanian and the Oligocene-Pleistocene are common for all considered sections excluding the Hun graben and Zelten and Dahra Platforms,. In the latter, the first activation is absent because the start age for these sections was accepted as the Upper Cretaceous; Figs. 4.1, 4.2 and 4.3. The Senomanian thermal activation in latter sections of the Basin was simulated by choice of rather high heat flow at initiation of the basin.

Similarly to [7], the periods of the basement stretching suggested in our modeling help to explain the stages of rather quick subsidence of the Basin. Two considerable periods of lithosphere extension in the Upper Cretaceous and Paleocene are typical for all areas of the Basin. According to our estimations, total amplitude of the basement stretching, β, is maximal in central part of the Sirt Basin (the Ajdabiya and Maradah troughs and Zelten and Dahra Platforms), where it is about 1.5. More moderate values ($\beta \approx 1.3$) were estimated in the Hameimat and Zallah troughs and minimal $\beta \approx 1.11$–1.17—in periphery of the Sirte basin (the Hun Graben and Syrenaica Platform; Table 4.3).

Variations in tectonic subsidence of the Basin computed by the first (Eq. (1.11)) and second (Eq. (1.13)) methods are shown in upper part of Figs. 4.2 and 4.3 by solid and dashed lines. Both of the tectonic curves (solid and dashed) must coincide at the condition of local isostatic response of the basin lithosphere on internal and external loads (Sect. 1.3). The assumed events of thermal reactivation or extension of the lithosphere change the density distribution in the basement (Fig. 4.5). Then, amplitude and duration of the events are chosen to ensure a coincidence the dashed tectonic line with the solid, provided that the chosen parameters of the activations do not contradict to available geological and geophysical information about structure and evolution of the region (Sect. 1.3). The thermal activation of the lithosphere is reproduced in our modeling by gradual uplifting the top of thermal diapir with a temperature 1100 °C. For example, the modeling of sedimentary section of the AA1-6 in the Ajdabiya trough assumes uplift of the 1100 °C isotherm (top of thermal diaper) of 42 km during 20 My (from 114 to 94 My) as simulation of the thermal activation of the mantle in the Albian–Senomanian. Similar uplift in

Table 4.3 Periods of thermal activation and stretching of the lithosphere in the Sirt Basin history assessed from the analysis of tectonic subsidence of the Basin

Structure		Thermal activation		Basement Stretching		
		t_1	t_2	t_{11}	t_{22}	B
Troughs						
Hameimat trough		145	130	125	106	1.03
		105	91	90	72	1.16
		49	40	60	50	1.05
		6	0	–	–	–
Ajdabiya trough	w. AA1-6	114	94	145	115	1.06
		50	40	93	85	1.20
		27	0	60	53	1.08
		–	–	40	28	1.10
	w. EE1-6	113	94	145	115	1.06
		52	40	92	85	1.18
		27	0	75	60	1.10
		–	–	40	28	1.10
Maradah trough		117	95	94	80	1.20
		51	41	70	50	1.13
		38	33	40	38	1.09
		30	0	–	–	–
Zallah trough		113	95	94	88	1.20
		87	64	64	60	1.06
		42	0	–	–	–
Hun graben		50	40	98	77	1.04
		38	32	40	38	1.07
		30	0	–	–	–
Platforms						
Zelten platform		50	40	65	49	1.20
		38	34	40	38	1.15
		26	0	33	27	1.10
Dahra platform		50	40	65	50	1.21
		38	34	40	38	1.15
		30	0	33	25	1.08
Syrenaica platform		155	90	180	156	1.04
		50	40	60	50	1.03
		30	0	40	38	1.09

t_1, t_2 the time of start and finish of thermal activation of the Sirt Basin lithosphere
t_{11}, t_{22} the time of start and finish of stretching of the Sirt Basin lithosphere
β stretching factor

the middle Eocene was nearly 24 km during 12 My. Such thermal activations of the basin lithosphere with different amplitudes and durations explain the periods of erosion or interruption in burial histories in Figs. 4.2 and 4.3 that occurred at the boundary of the Lower and Upper Cretaceous, in the Lower and Upper Eocene and the Upper Miocene-Pleistocene (Table 4.3). In the case of the AA1-6 well, analysis of variations in tectonic subsidence suggests three periods of thermal activation of the Basin and four periods of the basement extension (Table 4.3). The first thermal activation explains rather slow subsidence of the Basin in the Early Cretaceous (Fig. 4.2). Three others activations correspond to the erosion periods. The most significant thermal activation of the Basin lithosphere can be seen by changes in the isotherms depth in Fig. 4.5.

Extension of the lithosphere by finite amplitude β is reproduced numerically in our modeling by a series of n small consequent intervals of adiabatic stretching of the basement by an amplitude $\Delta\beta_i$ such that $\beta = \Delta\beta_1 \cdot \Delta\beta_2 \cdot \ldots \Delta\beta_i \cdot \ldots \Delta\beta_n$ (Sect. 1.3). At duration of the extension events of several million years to 20 My, the stretching rates are slow ($V < 0.06$ mm/year) and such stretching results in variation of the Moho depth whereas the isotherm depths change very little (Fig. 4.5). Slow deformations associated with the stretching of Table 4.3 have no noticeable traces near the basin surface. Listric faults are commonly expected in continental rifting that assumes almost instantaneous stretching with high amplitudes ($\beta = 1.8–2.5$ and higher). These deformation rates exceed those of our modeling by more than an order of magnitude. An assessment of duration and amplitude of the extension and thermal activation of the basin lithosphere is conducted in successive order starting from the basin initiation. In addition, the structure and thermal state of the lithosphere before start of current stage of activation are the result from action of all previous stages of activation and relaxation of the basin lithosphere (Fig. 4.5).

4.3.2 *Comparison with the Model [7] of Tectonic Subsidence*

Abadi et al. [7] studied in detail the history of tectonic subsidence of the Sirte Basin based on a backstripping analysis of more than 200 wells located within the Basin. The curves of tectonic subsidence have been modeled to quantify the variation in timing and the magnitude of crust rifting. Tectonic analysis in [7] uses an assumption of local isostatic response of the Basin lithosphere on load similarly to our approach. It would be interesting to compare results of our estimations of lithosphere stretching with the results obtained in the model of uniform stretching of lithosphere [7]. Such comparison will be carried out for the Dahra and Zelten Plaforms and the Hameimat, Ajdabiya, Zallah and Hun grabens. According to Table 4.3, a total amplitude of lithosphere extension β in our model is equaled 1.26, 1.27, and 1.11 for the Hameimat and Zallah Troughs and in the Hun Graben, correspondingly. In paper [7] it is estimated by the values of $\beta = 1.21–1.31$, 1.24

and 1.09 for the same structures. Then, there is rather good agreement between results of two models in the above structures. But β-values differ one from other in the central part of the Sirt Basin. So, a total amplitude of extension, β, in Zelten and Dahra Platforms and Ajdabiya trough consists 1.48–1.51 in our modeling (Table 4.3). At the same time, it is 1.12 and 1.20 in the Platforms and 1.16–1.35 in the Trough by estimations in [7]. It can be assumed that a neglect of erosion in the latter model could be a reason of this disagreement. In order to verify the assumption, we conducted numerical experiment and replaced erosion periods in the subsidence histories of the Ajdabiya trough in Figs. 4.3 by interruptions (no sedimentation, no erosion) and repeated the modeling procedure with new burial history. As result of neglecting of erosion, total amplitude of lithosphere extension, β, decreased up to 1.27 and 1.32 for sedimentary sections of the AA1-6 and EE1-6 wells instead $\beta = 1.50$ with consideration of erosion. The above reduced values are close to the estimations in [7]. The considered example shows that estimations of amplitude of lithosphere extension are sensitive to suggested erosion amplitudes. Indeed, erosion leads to an increase in sedimentary thickness that must be deposited at the stage preceding this erosion. Then, corresponding amplitude of extension must be increased also to explain an increase in subsidence (and sedimentation) rate. In neglecting of variations in paleosea depth (see above) the extension period in tectonic analysis will always correspond to increase in subsidence (and sedimentation) rate ([7]; see for example Table 4.3 and Figs. 4.2 and 4.3).

4.3.3 Analysis of Tectonic Subsidence in Other Models

Estimations of extension amplitudes in the papers [7, 31] are based on the forward modeling technique [31]. In this approach, initial lithosphere of the Sirt Basin is assumed to be a homogenous continental plate of thickness 100 km. Steady temperature 1333 °C was held up during the modeling at the base of the plate. It is believed that every stage of fast sedimentation corresponds to extension event of the basin lithosphere. Correspondent amplitude of extension, β, was determined from the condition that tectonic subsidence computed with assumed value of β must coincide with the one determined by the "backstripping" procedure, that is by removal of sediment and water load from the basement surface. As whole, the approach of uniform stretching of flat basin [21, 23] and assumption of local isostatic response of the lithosphere on the surface and internal load that were used in [7, 31] are similar to the approach in the GALO system with one difference. This difference is that the forward modeling technique of [31] does not consider heat transfer problems which are very important in the modeling of the Sirt Basin characterized by several periods of thermal activations of the basement (Table 4.3). In contrast to the automatic basin modeling system of [7, 31, 32], calculation of density distribution in the basement column at every time step in the GALO system gives a possibility to analyze variations in thermal state of the Basin lithosphere during as stretching events as the events of thermal activation of the lithosphere

(Table 4.3). An analysis of real sedimentary section of the basin and detailed structure of its basement, consideration of dependence of density, heat conductivity, heat capacity and heat generation of the rocks in sedimentary cover, consolidated crust and the mantle on temperature and pressure, and finally, a consideration of latent heat effect during fusion or solidification of the mantle are an additional useful attributes of the GALO system applied in our modeling (see Sects. 1.1–1.3).

At this point it can be noted that the "two-dimensional inverse modeling systems" suggested by Kooi and Cloetingh [33] and applied in [34, 35] are more advanced in comparison with the forward modeling system [31]. They allow an analysis of multiple rifting events with finite duration of the process and consideration of thermal evolution of the lithosphere. In these systems, a numerical domain is split along the horizontal direction into vertical columns. Each column is assigned crustal (δ) and mantle (β) thinning factor. An aggregate of these factors is determined later by inverse statistic procedure from the condition of closeness of calculated and observed burial histories of the basin [34]. A general algorithm of solution of the inverse statistical task is similar to the one applied in determination of parameters of kinetic reactions from the Rock-Eval data or in computation of angular rates of the lithosphere plate movement from the measured rates at the plate boundaries. The 2-D modeling systems [33–35] utilize a regional (flexure) isostasy instead of local isostasy in the 1-D systems applied in the papers [7, 31] and also in the GALO system (Sects. 1.2 and 1.3). The 2D-flexure models assume that a vertical deflection of top of the crust, is described by the equation of bending of thin elastic plate. Correspondingly, the effective elastic thickness of lithosphere plate (Te) is a critical parameter of the 2-D modeling. Depth of necking level (Z_{neck}) is other critical parameter of the modeling, affected strongly on the field of strain rates and history of the basin subsidence. For example, the values Te = 30 km and Z_{neck} = 0–15 km were used in the modeling of the Gulf of Lions margin [33], Te = 0 km and Z_{neck} = 10–17 km in the Dnieper-Donets Basin [34], Te = 5 km and Z_{neck} = 15 km in the Viking Graben [36], Te = 15 km and Z_{neck} = 15 km in the Tano Basin, Ghana [37]. A main advantage of the automated 2-D inverse modeling systems [33–35] in comparison with the 1D one, relates with their ability to consider the basins with finite strength of the lithosphere. But this advantage is decreased considerably due to assumption of steady values of Te and Z_{neck} during all of the time of the basin development. Effective elastic thickness of lithosphere plate (Te) must change strongly during thermal activation of the basin or its cooling from initial rift stage. Distribution of strength of the lithosphere rocks with depth together with parameter Te can change also due to increase of sedimentary load on the basement surface (Sect. 1.4). Therefore parameter Te can't remain steady during basin evolution.

Other problem in the modeling systems [33–35] is related with using of high asthenosphere temperature Ta = 1300–1333 °C. In the 2-D systems, thermal activation of the basin lithosphere associated with the extension period is simulated by filling of thinned volume of the mantle in the lower part of the lithosphere by the mantle rocks with temperature Ta. The thinned volume is determined in turn by expression $(1–1/\beta) \times t_{mi}$ where t_{mi} is thickness of the mantle before current stage of

non-uniform stretching. In the examples of modeling considered in the papers [33, 34, 36, 37], the parameter of the mantle extension, β, varies from 2 to 4–5 and then the isotherm of 1333 °C rises up to depth 10–20 km under Moho boundary. Such high temperature at this moderate depth is unreal especially in the continental lithosphere (see Sect. 1.1). In other models of non-uniform stretching of the lithosphere [22, 23, 31], thermal activation of the lithosphere is simulated by rising of the 1333 °C isotherm due to choice of δ-parameter presented a degree of attenuation of the lithosphere (in contrast to the β-factor reflected the crust thinning; [23]).

We believe that a great number of indefinite initial parameters in the "2-D inverse modeling systems" [31] makes more preferable the using of the GALO system for analysis of the Sirt Basin. As mentioned above, the GALO system calculates temperature distribution taking into account change in thermal state during as stretching as thermal activation of the lithosphere. The main limitation of the system is related with an assuming a local isostasy response of the Basin lithosphere on surface and internal loads. Deviations from the state of local isostasy can be suggested in the relative short periods of the lithosphere compression. But they can't change considerably the results of tectonic analysis because isostatic equilibrium is restored rather quickly after finish of the compression stage especially during following thermal activations of the Basin when its lithosphere becomes weak. Fracturing and deposition of thick sedimentary cover contribute also into weakening of the basin lithosphere (Sect. 1.4). Rather moderate gravity anomalies observed in the Sirt Basin (no more 20 mgl, [8]) confirm the fact that the state of the present-day lithosphere of the Sirte Basin is close to isostatic equilibrium.

In the finish, we say some words about possible influence of the flat basin approach in heat transfer modeling in the GALO system on our maturity estimations. For the profile of Fig. 4.1 in the Sirt Basin, we don't expect significant deviations of results in the 1-D modeling of the Basin thermal regime from the ones in the 2-D modeling. Indeed, the main 2-D heterogeneities concentrate in the upper 5–7 km of the section, whereas the crust and mantle below are relatively homogenous. In addition, cross sizes of the graben and horst structures exceed their depth by 5–10 times and the wells and pseudowells under analysis locate enough far from boundaries of the structures (Fig. 4.1).

4.4 Conclusion

Analysis of tectonic subsidence of the Sirte Basin suggests that thermal activations of the lithosphere in the Albian–Cenomanian and Oligocene–Pleistocene are common for all tectonic structures of the Sirte Basin and the Cyrenaica Platform. A relatively high temperature regime is also typical for modern state of the lithosphere in the Sirte Basin and Cyrenaica Platform. Such a regime is caused mainly by the thermal activation of the lithosphere during the last 10 Ma. The intensity of

this activation is highest in the western part of the Basin, where it is accompanied by the highest erosion amplitudes. The analysis of the variations in the basin tectonic subsidence suggests that two intervals of significant extension of the lithosphere in the Upper Cretaceous and Paleocene are common for all areas within the basin. The total amplitude of the crustal extension attains 1.5 in the central part of the Sirte Basin (the Ajdabiya and Maradah troughs and Zelten and Dahra platforms), is equal to 1.3 in the Hameimat and Zallah troughs, and is minimal (1.11)–(1.17) in the periphery of the basin (within the Hun Graben and Cyrenaica Platform).

References

1. Gumati YD, Schamel S (1988) Thermal maturation history of the Sirte basin, Libya. J Pet Geol 11(2):205–218
2. Sikander A, Basu SH, Rasul SM (2000) Geochemical source_maturation and volumetric evaluation of lower Paleozoic source rocks in the west Libya Basins. In: The geology of Northwest Libya (Ghadamis, Jifarah, Tarabulus and Sibratah Basins), vol 5, Earth Science Society of Libya, Tripoli, Issue 3, pp 3–53
3. Ahlbrandt TS (2001) The Sirte basin province of Libya–Sirte_Zelten total petroleum system, U.S. Geol Surv Bull 2202–F
4. Hallet D (2002) Petroleum geology of Libya. Elsevier, Amsterdam
5. Gong J (2004) Framework for the exploration of Libya: an illustrated summary, AAPG Datapages, search and discovery article 10061, Tulsa. http://www.searchanddiscovery.com/documents/2004/libya/images/gong.pdf
6. Elakkari TS (2005) Structural configuration of the sirt basin. ITC, Enschede
7. Abadi AM, Van Wees JD, Van Dijk PM, Cloetingh SAPL (2008) Tectonics and subsidence evolution of the Sirt basin, Libya. AAPG Bull 92(8):993–1027
8. Saheel AS, Samsudin ARB, Hamzah UB (2010) Regional geological and tectonic structures of the Sirt Basin from potential field data. Am J Sci Ind Res 1(3):448–462
9. Conant LC, Gondarzi GH (1967) Stratigraphic and tectonic framework of Libya. AAPG Bull 51(5):719–730
10. Abadi AM (2002) Tectonics of the Sirt Basin. P.D. Dissertation, Vrje Universitet (Amsterdam), ITC (Enschede)
11. Gras R, Thusu B (1998) Trap architecture of the early Cretaceous Sarir Sandstone in the eastern Sirt Basin, Libya. In: MacGregor DS, Moody RTJ, Clark-Lowes DD (eds) Petroleum geology of North Africa, vol 317–334. Geological Society London, Special Publication
12. Wilson DH, Guraud R (1998) Late permian to recent magmatic activity on the African-Arabian margin of Tethys. In: MacGregor DS, Moody RTJ, Clark-Lowes DD (eds) Petroleum geology of North Africa, vol 132. Geological Society London, Special Publication, pp 231–263
13. Frakes LA (1979) Climates throughout geological time. Elsevier, Amsterdam
14. Evans TR, Tammemagi HY (1974) Heat flow and heat production in northeast Africa. Earth Planet Sci Lett 23:349–356
15. Morgan P, Boulos FK, Hennin SF, El-Sherif AA, El-Saved AA, Basta NZ, Melek YS (1985) Heat flow in eastern Egypt: signature of a continental breakup. J Geodyn 4:107–131
16. Lesquer A, Bourmatte A, Dautria JM (1989) First heat flow determination from the central Sahara: relationship with the Pan-African belt and Hoggar domal uplift. J Afr Earth Sci 9 (1):41–48

17. Nublade AA, Suleiman IS, Roy RF, Pursell B, Suleiman AS, Doser DI, Keller GR (1996) Terrestrial heat flow in the Sirt Basin, Libya, and the pattern of heat flow across northern Africa. J Geophys Res 101(B8):17737–17746
18. Makhous M, Galushkin YuI (2003) Burial history and thermal evolution of the lithosphere of the northern and eastern Saharan Basins. AAPG Bull 87(10):1623–1651
19. Hadiouche O, Jobert N (1988) Geophysical distribution of surface waves velocities and 3-D upper mantle structure in Africa. Geophys J 95:85–109
20. Plomerova J, Babuska W, Dorbath C, Dorbath L, Lillie RJ (1993) Deep lithospheric structure across the central Africa shear zone in Cameroon. Geophys J Int 115:381–390
21. Mckenzie DP (1978) Some remarks on the development of sedimentary basins. Earth Planet Sci Lett 40:25–32
22. Mckenzie DP (1981) The variation of temperature with time and hydrocarbon maturation in sedimentary basins formed by extension. Earth Planet Sci Lett 55:87–98
23. Royden L, Keen CE (1980) Rifting processes and thermal evolution of the continental margin of eastern Canada determined from subsidence curves. Earth Planet Sci Lett 51:343–361
24. Van Wees JD, Beekman F (2000) Lithosphere rheology during intraplate basin extension and inversion. Inferences from automated modeling of four basins in western Europe. Tectonophysics 320:219–242
25. Turcotte DL, Schubert G (1982) Geodynamics: application of continuum physics to geological problems, vol 1. Wiley, New York, p 376
26. Nublade AA, Suleiman IS, Roy RF, Pursell B, Suleiman AS, Doser DI, Keller GR (1996) Terrestrial heat flow in the Sirt Basin, Libya, and the pattern of heat flow across northern Africa. J Geophys Res 101(B8):17737–17746
27. Ungerer Ph (1993) Modeling of petroleum generation and migration. In: Bordenave ML (ed) Appl Pet Geochem. Technip, Paris, pp 397–442
28. Espitalie J, Ungerer P, Irvin I, Marquis E (1988) Primary cracking of kerogens. Experimenting and modelling C1, C2-C5, C6-C15 classes of hydrocarbons formed. Org Geochem 13(4–6):893–899
29. Ungerer P, Burrus I, Doligez B, Chenet P, Bessis F (1990) Basin evolution by integrated two-dimensional modelling of heat transfer, fluid flow, hydrocarbon generation, and migration. Am Assoc Pet Geol Bull 74(3):309–335
30. Makhous M, Galushkin Y (2005) Basin analysis and modeling of the burial, thermal and maturation histories in sedimentary basins. TECHNIP, Paris
31. Van Wees JD, Stephenson RA, Storba SM, Shymanovsky VA (1996) Tectonic variation in the Dniepr-Donets basin from automated modeling of backstripped subsidence curves. Tectonophysics 268:257–280
32. Van Wees JD, Beekman F (2000) Lithosphere rheology during intraplate basin extension and inversion. Inferences from automated modeling of four basins in western Europe. Tectonophysics 320:219–242
33. Kooi H, Cloetingh S (1992) Lithospheric necking and regional isostasy at extensional basins 1. Subsidence and gravity modeling with an application to the Gulf of Lions margin (SE France). J Geophys Res 97(B12):17553–17571
34. Poplavskii KN, Podladchikov YY, Stephenson RA (2001) Two-dimensional inverse modeling of sedimentary basin subsidence. J Geophys Res 101(106):6657–6671
35. White N, Bellingham P (2002) Two-dimensional inverse model for extensional sedimentary basins: 1. Theory. J Geophys Res 107(B10):1–20
36. Rũpke LH, Schmalholz SM, Schmid EH, Podladchikov YY (2008) Automated thermotectonostratigraphic basin reconstruction: Viking Graben case study. Am Assoc Pet Geol Bull 92(3):309–326
37. Rũpke LH, Schmid DW, Hartz EH, Martinsen B (2010) Basin modeling opf a transform margin setting: structural, thermal and hydrocarbon evolution of the Tano Basin, Ghana. Pet Geosci 16:283–298

Chapter 5
Tectonic History and Thermal Evolution of Sedimentary Basin in the North-Eastern Shelf of Sakhalin Island, Russia

Abstract The burial, thermal and catagenesis histories of rocks in the sedimentary sections of the Kaigan-Vasyukan sector of the Sakhalin-5 area in the north-eastern shelf of Sakhalin are reconstruct numerically using the GALO system for basin modeling. The sedimentary section of the Basin includes the Late Cretaceous complex in addition to the Cenozoic one. The considered area of the shelf locates within the Okhotsk block margin near to the East Sakhalin accretion complex in the region subjected by active fault tectonics. Consequently, two limiting versions of the basin's development are analyzed in this paper: the first with the local_isostatic response of the basin's lithosphere during the basin's entire history and the second with the isostatic behavior of the lithosphere beginning from the time of the Kuril Island Arc's formation (about 34 Ma BP). The computations demonstrate a weak dependency of the lithosphere thermal regime and organic matter maturation in the Cenozoic on the choice of the variants of the basin evolution. Our modeling helped to explain the main problem in the study region—the presence of the low degree of maturation of organic matter in deep rocks of the basin and rather high thermal regime of the basin lithosphere. The modeling shown that the main cause of the above contradiction is the rather high sedimentation rate during the last 10 My. This rate together with thermal activation of the basin lithosphere, assumed by tectonic analysis of the basin, are responsible for the striking non-steady thermal regime of the region. According to maturation and generation modeling, the rocks of the upper half of the Late Cretaceous formation, the Eocene, Machigar, and Daekhurin formations, and the lower half of the Uinin complex could generate oil up to the present time. In contrast, the rocks of the upper half of the Uinin complex and the Dagi, Okobykai, and Lower and Upper Nutov formations are interesting only as the reservoir and cap rocks for the hydrocarbons generated in the lower levels.

Keywords North Sakhalin · Tectonic subsidence · Vitrinite reflectance · Hydrocarbon generation · Lithosphere extension

Y. Galushkin, *Non-standard Problems in Basin Modelling*,
DOI 10.1007/978-3-319-33882-8_5

5.1 Some Problems of the Region Study (Introduction)

On the basis of the seismic, geologic, and geochemical data, the authors of the papers [1–4] came to a conclusion about the high hydrocarbon potential of the North Sakhalin and its shelf. They note that the possibility of formation of oil and gas fields in the studied area depends to a great degree on the ratio between the time of hydrocarbon generation by source rocks and the time of formation of traps for these hydrocarbons. Our modeling confirm the suggestion of Koblov and Kharakhin [3, 4] about the proximity of these times in the Cenozoic history of the Northeast Sakhalin shelf. In literature, there is only one paper devoted to numerical modeling of thermal evolution of the basin in the East Sakhalin. Isaev [5] has studied the temperature history of the Cretaceous and Paleogene deposits in the sedimentary section of the Polyarninskoe oil field. Unfortunately, a direct comparison between modeling in [5] and our results is impossible, because paper [5] consider the Polyarninskaya area of the Lunskaya Depression of Sakhalin Island located on the eastern shore more than 300 km south of the Sakhalin-5 area studied by us. Both areas are characterized by different tectonic histories. Referring to the model [5], it can be noted that the neglecting the change in thermal conductivity during burial of sedimentary rocks, the use of steady heat flow at the base of the sedimentary blanket and evaluation of vitrinite reflectance by a doubtful correlation of paleo-temperatures and %Ro established in the West Siberia basins, make the results of modeling in [5] little reliable for non-steady-state thermal regime of the north-eastern Sakhalin shelf.

In our paper, the petroleum potential of the northeastern Sakhalin shelf are analyzed on the example of four wells (1–4) located within the Sakhalin 5 area (Fig. 5.1). The studied area of the shelf is located within the border of the continental margin of Okhotsk near the complex of the East Sakhalin accretion prism. At present time, the lithosphere of the studied area is close to isostatic equilibrium, which is indicated by the small amplitudes of the isostatic gravity anomalies (10–20 mGal). However, the proximity of the studied area to the complex of the East Sakhalin accretion prism might imply a compression mode of the lithosphere and, consequently, a nonisostatic response of the lithosphere to the load of water and sediments, during the formation of the prism. However, there is much evidence for active fault tectonics within the border of the northeastern shelf of Sakhalin with visible thinning of the lithosphere since the end of the Upper Cretaceous until the present (e.g., see, [6–8]). Due to the uncertainty of the tectonic history of the study area, two limiting versions of the basin's evolution, namely, isostatic and partially nonisostatic are considered in our simulation. In the first one, it is assumed that numerous faults and strike_slip motions along them decreased the strength of the lithosphere. Then, the local isostatic response of the lithosphere to the water and sediments load took place during the entire considered evolution of the basin starting from the Upper Cretaceous. The only exclusions might be for several relatively short periods with compressive stresses. The second and alternative version of the basin's origination implies that a local isostatic response of the lithosphere to the load of water and sediments took place starting from the time of the Kuril Arc formation, which

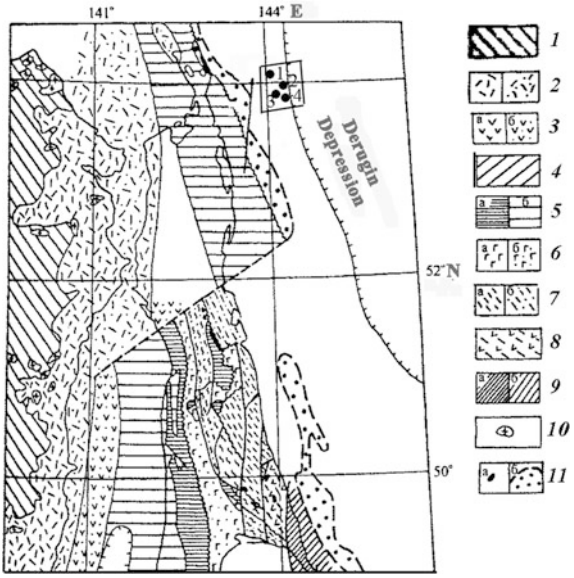

Fig. 5.1 Tectonic zones of the Sakhalin and neighboring areas (according to [6] with little changes). Rectangle drew by solid lines shows approximately the location of the Kaygan-Vasyukan sector of the Sakhalin-5 area with locations of four wells. *1* the Mesozoic and Late Mesozoic structures of the Sikhote-Alin; *2* the Cretaceous-Paleogene volcanic plutonic belt of the Sikhote-Alin continental margin; *3* the Upper Jurassic(?)-Cretaceous structures of the Rebun-Moneron volcanic arc; *4* tuff-terrigenous structures of the Cretaceous Moneron inter-arcs depression; *5* tuff-terrigenous structures of the Cretaceous forearc trough; *6* depositions of the Early Cretaceous accretion complex; *7* the Khidako-Sakhalin terrain; *8* vulcanite of the Upper Cretaceous island arc; *9* the Upper Cretaceous tuff-terrigenous depositions of the fore-arc trough; *10* granitoids; *11* serpentinite mélange; basite and hyperbasite

received the main part of the regional compressive stresses at about 34 Ma B.P. One of the important results of the modeling is that the estimates of hydrocarbon generation insignificantly differ between the isostatic and partially nonisostatic versions of the basin's evolution. This is of great importance for the study of hydrocarbon potential of the region due to the complexity of its tectonic history implying by the close location of the area to the complex of the previously active accretion prism.

5.2 Tectonic and Geological History of the North and Middle Sakhalin

The study area of the northeastern shelf of the Sakhalin is a part of the Okhotsk Sea block, the geological history of which has not a single treatment [6, 7, 9–13]. In some papers this block is considered as a part of continental plate, that was thinned

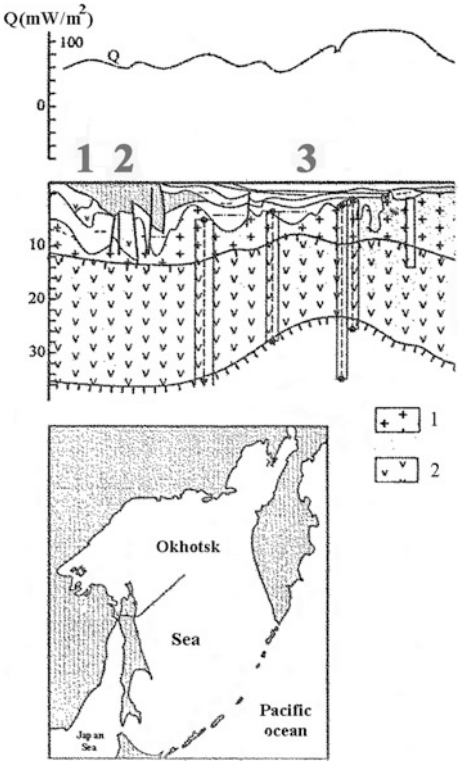

Fig. 5.2 Geoprofile "Amur Lagoon—Central Okhotsk Rise (according to [6] with changes). *Upper figure* heat flow; *middle figure* geoprofile, *lower figure* location of the profile, *1* "granitic" layer, *2* "pseudo-basaltic" layer. Numbers in geoprofile: *1* Amur depression, *2* North-Sakhalin depression, *3* Deryugin depression

during its migration in the Jurassic and Cretaceous [6, 9–11, 14]. If you take this variant of the block evolution, the crust in the Okhotsk Sea shelf in the East Sakhalin must be presented by thinned granite layer in the upper part and by continental pseudo-basalts in the lower part of the crust (Fig. 5.2; [6, 14]). But, according to other models, the Okhotsk Sea block is a part of the oceanic Kula plate, and his volcanic plateau are resulted from the anomalous basalt melting in the Later Jurassic—Early Cretaceous. The latter was caused by movement of the Kula plate above the mantle plume located to the North from the triple junction of the Kula plate with the Faralon and Pacific plates [1, 7, 12, 15]. The volcanic plateau of the Shatsky and Ortong-Java rises were formed at these southern latitudes nearly at the same time and by similar mechanism. Long drift of the Okhotsk Sea part of the Kula plate from southern to northern latitudes led to stopping of the Kula plate subduction under the Okhotsk-Chykotka volcanic plutonic chain [7, 12, 16]. In this variant, when the Okhotsk Sea block was a part of the Kula plate, upper part of the basement crust will be presented by the Cretaceous basalt plateaus and the lower part – by the layers of serpentinized peridotite and gabbro (the third layer of the oceanic crust (Fig. 5.2; [7]).

In the Cretaceous, the Asian continent was bounded from south by island arcs, which can be recognized easy in the rock complexes of the Sikhote-Alin and

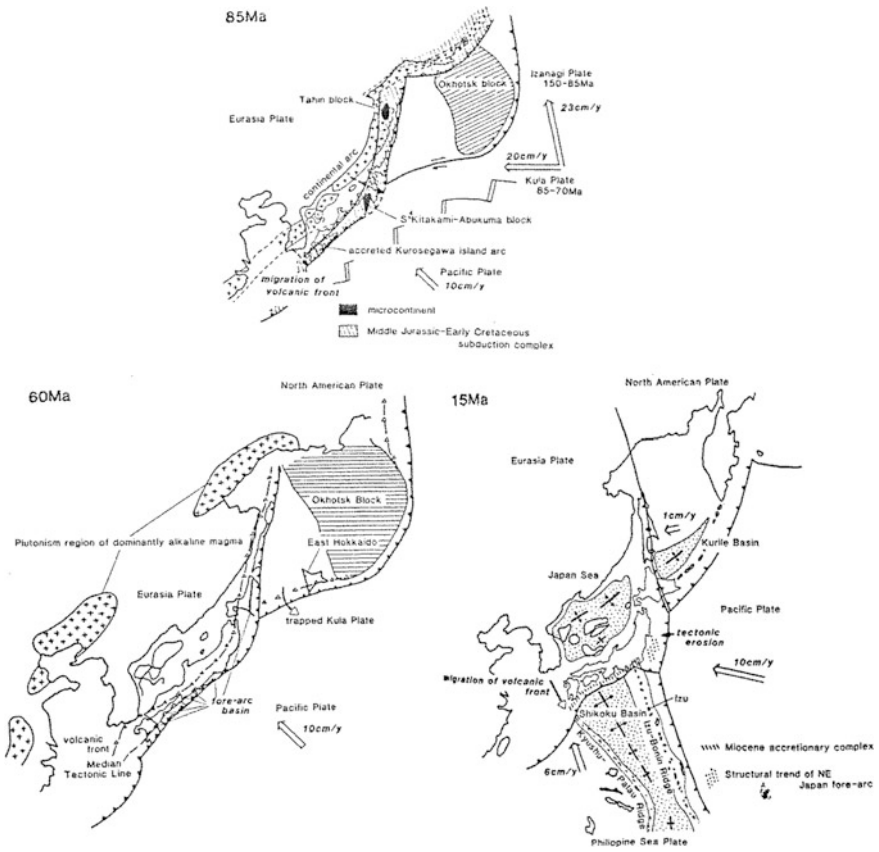

Fig. 5.3 Paleogeographic reconstruction of the eastern margin of the Asia at the times 85, 60 and 15 Ma (according to [11])

Sakhalin (Figs. 5.1 and 5.3; [6, 11, 16, 17]). The Cretaceous rocks in the East Sakhalin mountains belong to the complex of accretion prism. In the Upper Cretaceous, the island arc system was transformed to the active continental margin of Andian type. It included the marginal continental volcanic-plutonic chain of the East Sikhote Alin, the forearc basin and the accretion prism of the East Sakhaline (Fig. 5.1; [16, 17]).

A transition from the subduction of the Kula plate to the one of the Pacific was about 70 Ma (Fig. 5.3; [11, 13]). At this time, active margins of the northeastern Asia shifted to south and east from the Okhotsk Sea block (Fig. 5.1). In the Oligocene, the Kuril island arc arose. It continued to north along the Middle Kamchatka [11, 13, 17]. The Japan Sea, South Kuril and Shikoku-Parese-Vela basins were opened from the Late Oligocene to the Middle Miocene [1, 11–13, 15]. Formation of the basins of rift type in the Sikhote Alin associated with alkaline

basaltic volcanism of the Miocene-Paleocene-Quarternary age and finished due to the Japan Sea opening [9, 11, 13].

In the Late Cretaceous, plates Izanagi and Kula have begun subduction to the west and the Okhotsk block joined with the north-eastern Asia. The Late Cretaceous accretion complex of the North Shimanto and Khidaka was formed at the same time. In the Early Cenozoic, the Pacific plate subduction began, the little sea block between the Okhotsk and West-Hokkaido-Sakhalin bloks (part of the Kula plate) was closed. In the Miocene, the Izu-Bonin arc approached to the Central Honsu and formatted the Shikoku basin. The Japan Sea and Kurile basins were opened just simultaneously. In the Miocene, the accretion complex was created along the Nankai through in the south-western Japan. In contrary, along the Japan through, a tectonic erosion took place [11]. The forearc volcanism developed in relation with the Shikoku block subduction. The Okhotsk Sea block collided with the West Hokkaido block.

The discussion of the tectonic history of the region we finish by a short review of the region fault tectonics (Fig. 5.4). The Sakhalin and its shelf are characterized by the developed fault system. Numerous shifts along these faults in the Cenozoic changed considerable a pattern of the ophiolite chains as well as Mezozoic deep fractures [10]. The main fault of the Sakhalin, the Tym Parany fault, is the boundary between the Mesozoic accretion complex of the Sakhalin at the east and the Cretaceous—Cenozoic sedimentary basin, at the west. This fault of length about of 600 km disappears at the north in the Quaternary sediments. In the South within the Hokkaido Island, it continues in the Khoroenoba fault and the Khidaka mountain chain (Fig. 5.4). Several faults parallel to the Typ Parany fault strike along the eastern coast of the Sakhalin. The northeastern coast of the Sakhalin is divided by several faults of length of some hundred km on several narrow basins (Fig. 5.4) of sediment thickness up to 5000 m. The southwestern cost of the Sakhalin is bounded by the West Sakhalin fault that is also parallel to the Tym Paranay fault (Fig. 5.4). It can be noted, that the Tym Paranay fault is active at present time and explains the main part of earthquakes in the Sakhalin. At the same time, the faults in the East Sakhalin mountains are aseismic now [18].

The opening of the Japan Sea and its initial stage of closure was related mainly with subduction of the Pacific plate. But numerous shifts within the regional strike sleep faults system included the long Hokkaido-Sakhalin (Tym Parana) fault were caused by total tectonic activation of the Asian faults in relation with the collision of Asia with India. Amplitudes of such shift movements in considered region could be rather great. So, the opening of the Japan Sea, beginning 25 My ago requires the shift along the right lateral fault system of total amplitude from 400 to 500 km, The shift along the Tyn Paranay fault is not enough for above amplitude. The latter was realized partly along the faults of the Tatarian strait, characterized by the thinned crust. Other part of the amplitude is realized along the faults of the northeastern part of the Japan arc [18].

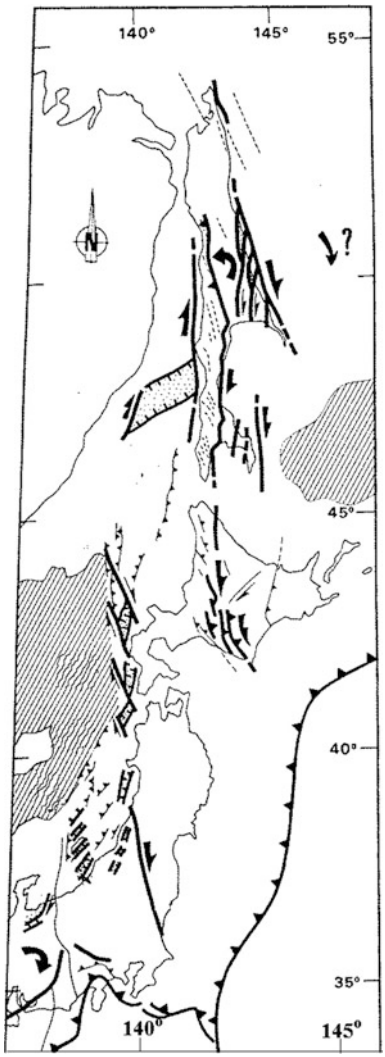

Fig. 5.4 Tectonic map of the Sakhalin—eastern Japan Sea strike slip zone [8]

5.3 Burial, Thermal and Maturation Histories of Sedimentary Rocks

5.3.1 The Initial Data for Basing Modeling

Lithological and stratigraphycal scheme of the sedimentary section of the study basin is shown in Table 5.1 on an example of the well 1. The part of the section from the Quaternary to the Oligocene, including the Daechuriin and partly Michigar formations was constructed by the well data, whereas the thicknesses of the Lower

Table 5.1 The evolution stages of sedimentary section of the North Sakhalin basin (well 1 in the Sakhalin-5 area; according to [2, 19])

N	Stages	Time (Ma)	Depth (m)	Lithology cl::vl::al::sd::lim
1	Sedimentation	99.6–65.5	8000–5030	40:20:00:40:00
2	Interruption	65.5–55.0	5030–5030	–
3	Sedimentation	55.0–34.0	5030–4830	40:10:00:50:00:
4	Sedimentation	34.0–28.5	4830–4430	50:00:00:50:00
5	Sedimentation	28.5–25.0	4430–4130	100:00:00:00:00
6	Interruption	25–23.8	4130–4130	–
7	Sedimentation	23.8–20.5	4130–3930	50:00:05:45:00
8	Sedimentation	20.5–14.0	3930–3430	100:00:00:00:00
9	Interruption	14.0–11.0	3430–3430	–
10	Sedimentation	11.0–9.0	3430–3300	05:00:00:95:00
11	Sedimentation	9.0–6.0	3300–2350	05:00:00:95:00
12	Sedimentation	6.0–2.6	2350–2200	90:00:00:10:00
13	Sedimentation	2.6–2.4	2200–1900	40:00:20:40:00
14	Sedimentation	2.4–1.8	1900–900	75:00:00:20:05
15	Sedimentation	1.8–0.8	900–600	90:00:00:10:00
16	Sedimentation	0.8–0.0	600–0	20:00:00:80:00

Comments: *depth* present-day depths of the base and roof of the sedimentary layer; in the column "Lithology": *cl* clays shales; *vl* vulcanite; *al* aleurolite, *sd* sandstone, *lim* limestone

Oligocene, Eocene and older formations were estimated by seismic data [2, 4, 19–21]. 16 stages in Table 5.1 present the formation history of sedimentary section. The 2-th, 6-th and 9-th of these stages are interruptions and the others are sedimentation. The interruptions in Table 5.1 could be replaced by erosion stages, but erosion amplitudes are indefinite, whereas introduction of erosion with amplitude of 500 m or lesser does not change considerable results of the modeling. Lithology of the rocks in Table 5.1 was taken from the papers [2, 4, 20, 21]. Geological study of the rock composition in the Sakhalin and neighboring regions shown that the Cretaceous deposits consist of terrigenous sandy-clay rocks with admixture of volcanites [2, 4]. In addition to clayey-sandy-volcanic formation of the Eocene, the Cenozoic sedimentary rocks include more six complexes: (1) the Lower Michigar complex (Lower Oligocene), presented by clayey-sandy layer of thickness of about 600 m with considerable contribution of coarse-grained material, (2) the Daechuriin complex (Upper Oligocene) presented by relatively deep-water silicinate-clayey rocks of thickness up to 600 m, (3) the Yinin-Dagin complex (Lower and middle Miocene) of thickness up to 3.5 km presented by delta sandy-clayey formations with little coal interbeds, (4) the Okobykay-Nizhne-Nutov sandy-clayey complex of thickness up to 5.5 km with sandy fraction increasing to the west, where there are the delta complex of the Paleo-Amur (Middle-Upper Miocene—the main oil-gas-fields in the North Sakhalin are related with these complex) (5) the Verchne-Nutov and Pomyr complexes (Pliocene-Quaternary) with thickness up to 4.5 km, presented mainly sands,

Table 5.2 Physical parameters of sedimentary rocks used in numerical reconstruction of burial and thermal history of the sedimentary section of the well 1 (see Table 5.1)

N	$\varphi(0)$	B (m)	K_{S0}	K_m	α (°C^{-1})	C_{vm} (MJ/m^3 °K)	A_m (mkW/m^3)	ρ_{S0}	ρ_m
			(W/m °K)					(kg/m^3)	
1	0.583	2240	1.130	2.738	0.0013	2.560	1.193	1720	2680
2	–	–	–	–	–	–	–	–	–
3	0.577	2190	1.176	2.947	0.0016	2.599	1.264	1730	2680
4	0.600	2060	1.135	2.960	0.0017	2.575	1.465	1690	2680
5	0.700	1800	0.871	2.093	0.0005	2.261	2.093	1530	2700
6	–	–	–	–	–	–	–	–	–
7	0.604	2050	1.126	2.931	0.0016	2.564	1.486	1680	2680
8	0.700	1800	0.871	2.093	0.0005	2.261	2.093	1530	2700
9	–	–	–	–	–	–	–	–	–
10	0.429	2790	1.784	4.044	0.0029	2.857	0.900	1960	2650
11	0.429	2790	1.784	4.044	0.0029	2.857	0.900	1960	2650
12	0.684	1840	0.909	2.244	0.0007	2.324	1.968	1560	2700
13	0.589	2090	1.168	3.044	0.0017	2.596	1.415	1700	2670
14	0.662	1890	0.963	2.449	0.0010	2.409	1.767	1590	2690
15	0.684	1840	0.909	2.244	0.0007	2.324	1.968	1560	2700
16	0.500	2410	1.478	3.647	0.0025	2.763	1.089	1850	2660

Comments Numbers *N* in the first column correspond to *N* in the first column of Table 5.1; $\varphi(0)$ surface porosity (mean porosity of upper 150–200 m of sedimentary rock), *B* is the scale of depth-variation of the porosity: $\varphi(z) = \varphi(0)\,EXP(-z/B))$, K_{S0} heat conductivity of sedimentary rock at the surface; K_m matrix heat conductivity of sedimentary rock at T = 0 °C; α parameter of temperature variation of the matrix heat conductivity: $K_m(T) = K_m/[1 + \alpha \cdot T(oC)]$, C_{vm} is the matrix heat capacity of the rock pro volume unit; *Am* matrix heat generation of sedimentary rock: $A(z) = Am \cdot [1 - \varphi(z)]$; ρ_{S0} and ρ_m surface and matrix densities of rock, correspondingly (see Sect. 1.1.1)

and (6) the Deryugin Quaternary complex, that is clayey in its lower part and sandy in the other part of the complex.

The thermal physical attributes of sedimentary rocks used in our reconstructions of thermal and burial histories of the basin are presented in Table 5.2. These values demonstrate significant variations in porosity, heat conductivity and density during subsidence of the rock in the basin. The calculated values of heat conductivity and heat generation of the sedimentary rocks ranged within the values measured in the study region [5, 19].

For control of basin reconstruction were utilized of the values of vitrinite reflectance (%Ro) and deep temperatures (T) measured in the neighboring areas of the northeastern shelf of the Sakhalin (Fig. 5.5). As it mentioned above, a striking attribute of the study region is the great depths of the initial maturation zone (the rocks with Ro = 0.50–0.64 % locate at depth of 3800–5000 m; Fig. 5.5b), despite the fact that the present-day thermal regime of the lithosphere is rather high (thermal gradient is about 36 °C/km; [14, 19]). The modeling explains this by high sedimentation rates in the region in the Neogene-Quaternary.

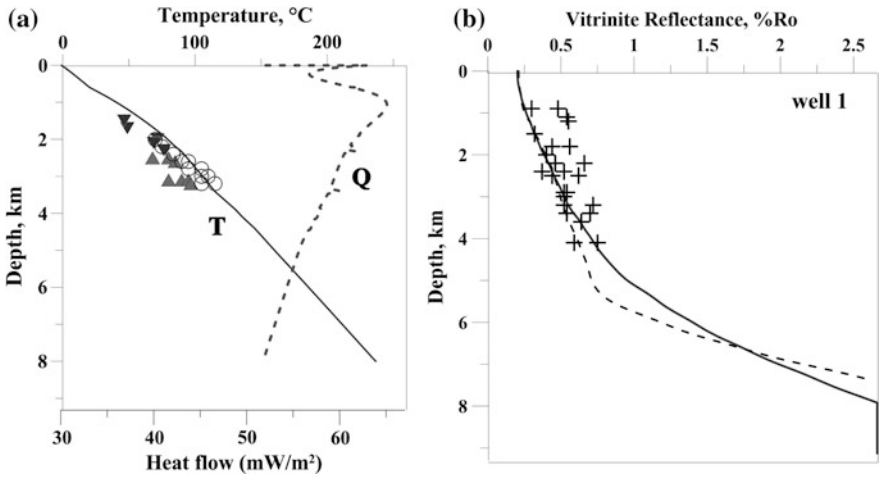

Fig. 5.5 Comparison of the calculated temperatures (*solid line* T in Fig. **a**) and vitrinite reflectance (*solid* and *dashed lines* in Fig. **b**) in the present-day sedimentary section of the well 1 of the Sakhalin-5 area computed in the first variant of the basin development with measured values of T and %Ro. *Symbols* temperatures and vitrinite reflectance measured in the neighboring wells of the northeastern shelf of the Sakhalin). **a** The *solid T-line* and *dashed Q-line* in Fig. **a** demonstrate the present-day distributions of temperature and heat flow with depth, computed with consideration of detailed climate variations during the last 2.5 My (see Sect. 10.7). This figure emphasizes a pronounced non-steady behavior of the heat flow in the study region. The minimum and maximum in the heat flow distribution are the memory about the last periods of warming and cooling of the climate (Sect. 10.7). **b** vitrinite reflectance computed in the EASY%Ro model (*solid line*, Eq. (3.3) in Sect. 3.2.2) and the BASIN%Ro model (*dashed line*, Eq. (3.4) in Sect. 3.2.2)

It can be noted that rather good agreement between calculated and measured values of %Ro is observed for both kinetic spectra of the vitrinite maturation discussed in Sect. 3.2.2.

The mean annual temperatures at the basin surface during its burial history are also included in the block of initial data for basin modeling (see Sect. 1.1.4). These temperatures are determined for study area from the papers [22, 23] and shown in Fig. 5.6a (see also Sect. 11.2).

The initial data for the modeling includes also variations in the sea depth during the basin history. The main part of the Cretaceous and Cenozoic rocks of the Sakhalin-5 area were deposited in the land or shallow-sea conditions [2, 6]. In the North Sakhalin, the rocks of the Michigar, Machituk and Pomyr formations were deposited in the very shallow sea up to sea-coast, lagun and beach environment, whereas the high siliceous deep-water deposits are typical for upper part of the Tumskaya formation (the Upper Oligocene) and in the Pilskaya formation (the Middle Miocene) [2]. The time-variations in sea depth used in our analysis of tectonic subsidence of the basin are shown in the Fig. 5.7a, b by upper solid lines. These figures present the variations in tectonic subsidence of the Basin discussed in detail in Sect. 5.4. It is important that accumulation of the silica rich sediments in

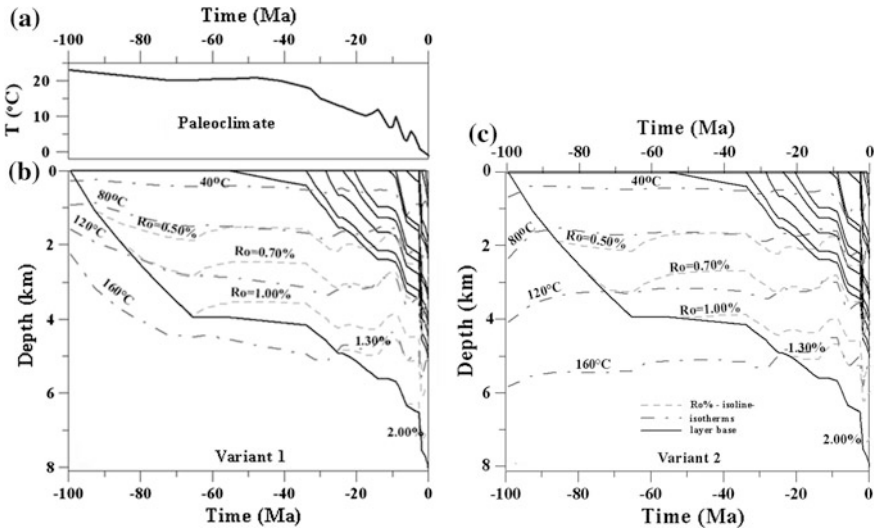

Fig. 5.6 Numerical reconstructions of the burial, thermal and maturation histories of the sedimentary section of the well 1 (Table 5.1) for the two variants of the basin evolution. **a** Paleoclimate (see text and Sect. 10.7). **b** Computations in variant 1 (a high initial heat flow (about 160 mW/m^2), isostatic response of the lithosphere on the water and sediment loads). **c** Computations in variant 2 (a moderate initial heat flow (about 70 mW/m^2), isostatic response of the lithosphere only beginning the time of the Kurile arc formation) (see Sect. 5.3). Comparison of the reconstructions in Fig. **b**, **c** says about rather weak influence of initial heat flow and choice between the above variants of the basin development on the distributions of calculated temperature and Ro% with depth in the modern section of the Basin

the study region does not correlate with eustatic variations in the sea level. That is why the formation of deep water depressions, where such sediments could deposit, is related with different local tectonic movements within the Sakhalin and its shelf ([2]; see also Sect. 1.2.1).

The steady temperature about of 1160 °C was maintained during the modeling at the lower boundary of the domain of temperature calculation (at depth about of 70 km). The problem of its determination is discussed in Sect. 1.1.4. Geological data suggest a rather high initial heat flow in the study area of the Basin (Fig. 5.8a). Indeed, the age of plagiogranite in the South Shmidt hyperbasite shield is estimated by Ka-Ar method by 87.1 Ma and the same method gives 142 ± 12 and 94 ± 10 Ma for age of the intrusive in the eastern ridge of the Shmidt peninsula [6]. As the first and main variant of the basin evolution in the Sakhalin-5 area we consider the variant of the basin formation on the rheologically weak lithosphere (heated and fractured) with high initial heat flow at the boundary of the Upper and Lower Cretaceous (Fig. 5.8a). In the second alternative variant with nonisostatic response of the lithosphere on load in the time from 100 to 34 Ma, the initial heat flow can be accepted (on the base of tectonic subsidence analysis) more low (70 mW/m^2, instead of 160 mW/m^2, in the first variant). Consideration of such

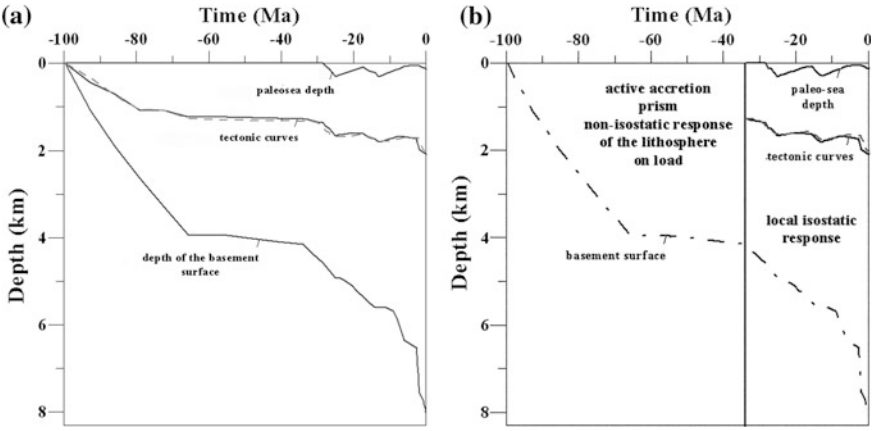

Fig. 5.7 Variations in the tectonic subsidence of the basement for sedimentary section of the well 1 in the Sakhalin-5 area calculated in two variants of the basin development. **a** Variant 1 with local isostasical response of the basin lithosphere on the sediment and water load during all time of the basin evolution. **b** Variant 2 with local isostatical response beginning the time of the Kuril arc formation (during the last 34 My). Tectonic curves: *solid line* tectonic subsidence of the basement surface, computed by remove of the sediment and water load (Eq. (1.11)), *dotted line* the same, calculated from the variations in the density distribution of the basement rocks versus depth (Eq. (1.13))

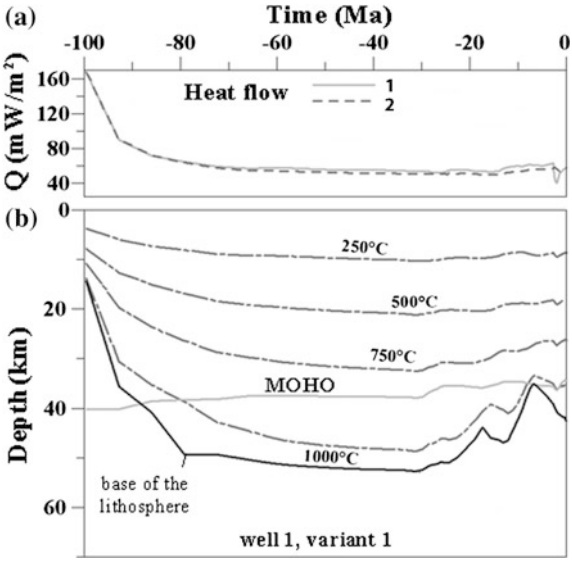

Fig. 5.8 Numerical reconstruction of the thermal history of the basin lithosphere in the north-eastern shelf of the Sakhalin (well-1 in the Sakhalin-5 area; the first variant of the Basin evolution). **a** Heat flows through the sediment (*1*) and basement (*2*) surface. **b** Evolution of thermal state of the basin lithosphere. *Dotted-dashed lines* isotherms; *the MOHO line* the base of the crust. *The base of the lithosphere* was determined by intersection of current distribution $T(z, t)$ and the solidus curve (1.4) in Sect. 1.1.3

variants allows an assessment an influence of initial heat flow in addition to variations in tectonic history of the basin on maturation history of its organic matter. It must emphasize that calculated distributions of temperature and vitrinite reflectance versus depth in present-day section are in agreement with the measured values of T and %Ro in the both variants of the basin evolution (Fig. 5.5).

5.3.2 *Temperature and Maturity Variations in the Sedimentary Blanket of the Basin*

The main results of modeling of thermal and maturation histories of the Basin are demonstrated in Fig. 5.6a, b. The first variant of the basin development, assumes an isostatic response of the lithosphere on the sediment and water load and rather high initial heat flow (about 160 mW/m^2) in the beginning of the Upper Cretaceous. In this variant, intensive subsidence of isotherms in the pre-Cenozoic period of the basin history is caused by cooling of the initially heated lithosphere (Figs. 5.6b and 5.8a, b). A light rise of isotherms in initial stage of the basin development can be seen in Fig. 5.6c, where the second variant of the basin evolution with moderate initial heat flow (about 70 mW/m^2) is presented. This rise is resulted from increase in temperature gradient at transition from the basement rocks with relatively high heat conductivity to the low conductivity sedimentary rocks against the background of weak change in thermal regime of the lithosphere. Comparing results in Fig. 5.6b, c, we can emphasize that the thermal regime of the rocks and maturation history of their organic matter are very close in the both variants of the basement development. It says about weak influence of initial heat flow and choise of tectonic style of the basin development on an assessment of hydrocarbon perspective of the considered area of the basin.

The computed temperature distribution in the modern sedimentary section of the well 1 in the Sakhalin-5 area is shown in Fig. 5.5a together with the values, measured in the neighboring wells of the northeastern shelf of the Sakhalin (the Yuzhno-Vasukanskaya and Udachnaya wells). The temperatures at the depth of 3 and 6.7 km reach 100 and 200 °C, correspondingly, that says about a high thermal regime of the modern basin because these temperatures were achieved in spite of intensive sedimentation during the last 10 My. An influence of the sharp climate variations on temperature distribution in sedimentary blanket will be discussed in Sect. 10.7.

Numerical reconstructions of thermal history of the basin in the Sakhalin-5 area gave an opportunity to calculate variations in organic matter maturation for the main source rocks and assess a realization history of their potential of hydrocarbon generation. A maturation level of organic matter was estimated by the values of vitrinite reflectance (Ro%). Dotted lines in Fig. 5.6a, b show the depths of the %Ro isolines. The Ro values here are computed with use of the EASY%Ro spectrum of vitrinite maturation (Eq. 3.3) in Sect. 3.2.2. Figure 5.5b gives an opportunity to

compare the values of Ro computed by the EASY%Ro model (solid line, Eq. (3.3) in Sect. 3.2.2) and the BASIN%Ro model (dashed line, Eq. (3.4) in Sect. 3.2.2). The measured values of Ro are rather low. That is why that rather good agreement between calculated and measured values of %Ro is observed for both kinetic spectra of the vitrinite maturation discussed in Sect. 3.2.2.

Figure 5.6b, c and Table 5.3 show that the intensive sedimentation in the Miocene-Pliocene led to rather deep subsidence of the catagenesis zones, in spite of the high thermal regime of the Basin. So, the initial stages of organic matter maturation (Ro = 0.50–0.70 %) occurred at the depth of 3,000–4,000 m by the EASY%Ro model and 3,000–4,900 by the BASIN%Ro model in the modern section of the basin (Figs. 5.5b and 5.6b, c; Table 5.3). Figure 5.9 illustrates distribution with depth of generation of liquid and gaseous hydrocarbons (integrated over time) by the basin rocks in the Sakhalin-5 area at the present time. The maturation level (%Ro) is shown right. Similar comparison can be carried out by the data of Table 5.3. The results of modeling in the first (totally isostatic) variant of the basin development are shown in Fig. 5.9 by the 1-lines and the ones in the second variant (partly isostatic)—by the 2-lines. In Fig. 5.9, similarly to Fig. 5.6, we are convinced of weak sensitivity of the modeling results to choice between two variants of the basin development.

5.3.3 *Realization of Hydrocarbon Potential by the Main Formations of the Basin*

In this section, we will analyze a maturation history and oil-gas bearing characteristics of the main formations of the basin using the results of numerical modeling. In this section, only the values of Ro, computed by the EASY%Ro model, will be used for analysis of hydrocarbon generation because namely for them a scale of conformity with hydrocarbon generation is worked out.

(a) The Upper Cretaceous complex (99.6–65.5 Ma)

The Upper Cretaceous complex of thickness about of 3 km is presented by an interbedding of clays and sandstones with appreciable admixture of vulcanites. According to the modeling, a catagenesis level of the rocks ranges from the stage of intensive liquid hydrocarbon generation (Ro = 0.87–0.95 %) at the roof of the complex (at the depth of 4,100–5,000 m) to the stage of dry gas generation (Ro = 2.5–2.8 %) at its base (at the depth of 7,200–8,000 m; Figs. 5.6 and 5.9, Table 5.3). According to maturation level, the rocks in upper half of the complex can continue an intensive oil generation at present time too. The terrigenous clayey deposits of the Cretaceous in the geological expositions of the southwestern frame of the basin and in the Shmidt peninsula are characterized by organic matter content (TOC) > 1 % and low maturity of the organic matter [2, 19]. In our modeling, organic matter in the Upper Cretacous rocks was presented by kerogene of type II

Table 5.3 Calculated values of the organic matter maturation level (Ro%), temperatures and realization of hydrocarbon potential for the probable source rocks in the present-day sedimentary section of the Sakhalin-5 area

t	Z	T	Ro	Hi	H_t	H_o	H_g	t_1	t_{exp}	t_2
Ma	m	°C	%	Mg HC/g TOC				Ma		
Well 1 (variant 1)										
99.6	8000	234.8	2.667	627	624	0	314	87	22.5 (81.6)	25
55	5030	155.7	0.944	627	516	492	24	17	(1.74)	–
34	4830	150.9	0.885	627	477	458	19	15	(1.37)	–
28.5	4430	140.5	0.784	627	289	279	10	9.2	(0.74)	–
23.8	4130	131.3	0.723	627	146	141	5	2.2	–	–
20.5	3930	126.2	0.687	710	45.4	42.2	3.2	1.7	–	–
11	3430	110.4	0.585	377	3.76	3.09	0.67	1.0	–	–
9	3300	107.7	0.561	377	2.33	1.92	0.41	0.9	–	–
6	2350	85.9	0.432	377	0.0413	0.0341	0.0072	–	–	–
Well 1 (variant 2)										
99.6	8000	227.7	2.475	627	623	0	313	85.7	22.4 (72.1)	21
55	5030	151.4	0.894	627	485	465	20	16.7	(1.49)	–
34	4830	146.8	0.844	627	420	405	15	14.7	(1.17)	–
28.5	4430	136.7	0.757	627	221	213	8	8	(0.50)	–
23.8	4130	127.8	0.700	627	109	105	4	2	–	–
20.5	3930	122.8	0.665	710	33.9	31.5	2.4	1.6	–	–
11	3430	107.5	0.562	377	2.34	1.92	0.42	0.9	–	–
9	3300	104.8	0.541	377	1.45	1.19	0.26	0.7	–	–
6	2350	83.7	0.425	377	0.0279	0.0231	0.0048	–	–	–
Well 2 (variant 1)										
99.6	7178	231	2.662	627	624	0	314	92	21.6 (81)	24.4
55	4178	146.4	0.872	627	461	443	18	16.6	(3.27)	–
34	3978	141	0.816	627	362	349	13	14.6	(1.57)	–
28.5	3578	129.8	0.732	627	11	155	6	8.4	(0.18)	–
23.8	3278	119.9	0.663	627	65.3	62.6	2.7	4.2	–	–
20.5	3078	114.3	0.631	710	15.7	14.6	1.1	1.9	–	–
11	2578	96.8	0.508	377	0.488	0.401	0.087	0.25	–	–
9	2458	92.8	0.483	377	0.229	0.188	0.041	–	–	–
7	2080	81.2	0.422	377	0.0234	0.0193	0.0041	–	–	–
Well 3 (variant 1)										
99.6	7430	229.4	2.701	627	625	0	315	92.2	22 (81)	24.8
55	4430	146.6	0.897	627	487	467	20	15.9	(3.31)	–
34	4230	141.2	0.841	627	412	397	15	12.8	(2.09)	–
28.5	3830	130.4	0.748	627	197	190	7	5.8	(0.73)	–
23.8	3530	120.5	0.680	627	84	80.6	3.4	4.2	–	–
20.5	3330	114.9	0.646	710	22.7	21.1	1.6	3.1	–	–

(continued)

Table 5.3 (continued)

t	Z	T	Ro	Hi	H_t	H_o	H_g	t_1	t_{exp}	t_2
Ma	m	°C	%	Mg HC/g TOC				Ma		
11.5	3030	104.9	0.575	377	2.97	2.44	0.53	1.6	–	–
9	2730	97.5	0.522	377	0.788	0.648	0.140	0.8	–	–
6.5	1980	75.4	0.404	377	0.00986	0.00816	0.0017	–	–	–
Well 4 (variant 1)										
99.6	7330	232.7	2.815	627	625	0	315	92.2	21.9 (81)	24.7
55	4330	149.3	0.933	627	511	487	24	16.8	(3.77)	–
34	4130	144	0.871	627	459	441	18	14.7	(2.79)	–
28.5	3730	133	0.765	627	238	230	8	7.8	(1.14)	–
23.8	3430	123.2	0.698	627	106	102	4	4.2	–	–
20.5	3230	117.5	0.658	710	29.7	27.6	2.1	3.3	–	–
11	2730	100.4	0.534	377	1.14	0.938	0.202	1.0	–	–
9	2600	97	0.515	377	0.61	0.502	0.108	0.5	–	–
5.8	2300	86.4	0.446	377	0.0734	0.0605	0.0129	–	–	–

t the formation age (Ma), *z* depth (km), *T* temperature in °C, *Ro* calculated vitrinite reflectance calculated by the EASY%Ro spectra of vitrinite maturation, in % (*z*, *T*, *Ro* calculated values in the present-day section). H_i initial potential of hydrocarbon generation by the formation rocks; H_t realization of the hydrocarbon potential by source rocks to the present time; H_o generation of liquid hydrocarbons; H_g generation of the gaseous hydrocarbon (in mg HC/g TOC). t_1, t_2 the enter times of the rocks into the oil (Ro = 0.50 %) and gas (Ro = 1.30 %) "windows"; t_{exp} the start time of primary expulsion of liquid hydrocarbons (see text). Initial potential HI = 627 mg HC/g TOC corresponds to standard kerogene of type II [24, 25]; initial potential HI = 710 mg HC/g TOC corresponds to the standard kerogene of type I [24, 25]; initial potential HI = 377 mg HC/g TOC corresponds to standard kerogene of type II [24, 25]

with initial potential of hydrocarbon generation HI = 627 mg HC/g TOC [24] with the present-day value of TOC equaled to 0.6 %. Because a maturation of the Upper Cretaceous rocks is rather high (Figs. 5.6, 5.9, 5.10 and 5.11; Table 5.3), the value of modern TOC of 0.6 % corresponds in our modeling to initial values of TOC 1.2 and 1 % for the rocks in the base and roof of the complex, correspondingly. Such TOC is in agreement with measurements in expositions of the Shmidt peninsula (see above).

Figure 5.10 demonstrates the history of realization of hydrocarbon potential by the rocks in the base and roof of the Upper Cretaceous complex in the first variant of the basin development. It can be noted that the oil generating potential of the rocks at the base of the formation remains rather significant up to the Miocene, after that the intensive subsidence and heating of the basin led to total degradation of liquid hydrocarbons due to secondary cracking of oil generated (Fig. 5.10a). This degradation will take place provided, that the generated hydrocarbons did not migrate to horizons with lower temperature. On the contrary, the main oil generation by the rocks at the top of the Upper Cretaceous complex occurred in the Pliocene-Pleistocene (Fig. 5.10c).

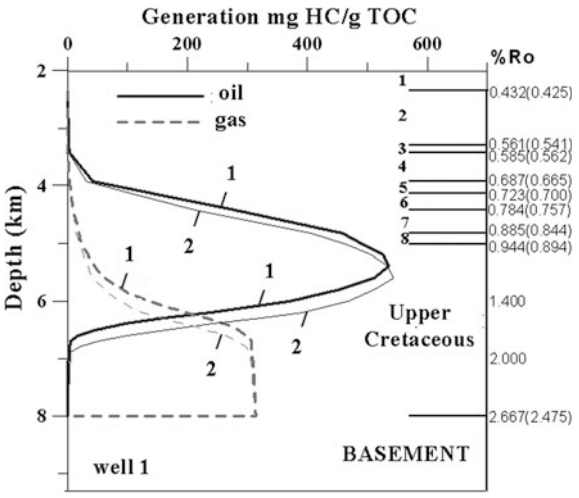

Fig. 5.9 Distribution of integral generation of liquid and gaseous hydrocarbons with depth in the present-day sedimentary section of the well1 in the Sakhalin-5 area. *1* the modeling results for the first variant of the basin development (isostatic response of the lithosphere on load during all basin history). *2* the results for the second variant (isostatic response only beginning the time of the Kurile arc formation about 34 Ma). Numbers from *1* to *8* in the upper right part of the Figure correspond to the different formations of the basin: *1* the Verkhne-Nutov fm., *2* Nizhne-Nutov fm., *3* the Okobyky fm., *4* Dagin fm. *5* Uyninsk fm., *6* Daekhuriinsk fm., *7* Machigar fm., *8* Eocene complex. In the *right*—the values of vitrinite reflectance (by the EASY% Ro spectrum), computed in the variant 1 of the basin development; the calculated Ro (%) values for the second variant are presented in *brackets*

The vertical line in Fig. 5.10a marks the start time of primary migration of liquid hydrocarbons from the rocks in the base of the Upper Cretaceous complex. This time is a formal value that is determined by the time of filling of 20 % of porous volume of the rocks by the liquid hydrocarbons ([24], see Sect. 3.2.3). It is rather conventional value, because a reaching of expulsion threshold depends strongly on the content of gas in generated hydrocarbons [24–27]. Other determination "t_{exp}" suggests that the expulsion threshold is reached when the volume of generated liquid hydrocarbons exceeds 150 mg HC/g TOC. Such determination of expulsion threshold is used for the marine kerogenes of type II in addition to the determination mentioned above [24, 25]. This expulsion time is shown in column "t_{exp}" of Table 5.3 in brackets. It is interesting, that the expulsion threshold, shown in Fig. 5.10a, was reached during a decrease stage of hydrocarbon generation. It is due to relatively low TOC in the rock and, as result of this, with increasing role of decrease of porous volume during subsiding of rock in the reaching of the expulsion threshold. As whole, the results in Figs. 5.6 and 5.10a, c and Table 5.3 say about high potential of the Upper Cretaceous rocks to generate oil during all time intervals beginning with the Maastricht. Moreover, this conclusion does not depend on the choise of the first or second variants of the tectonic basin evolution.

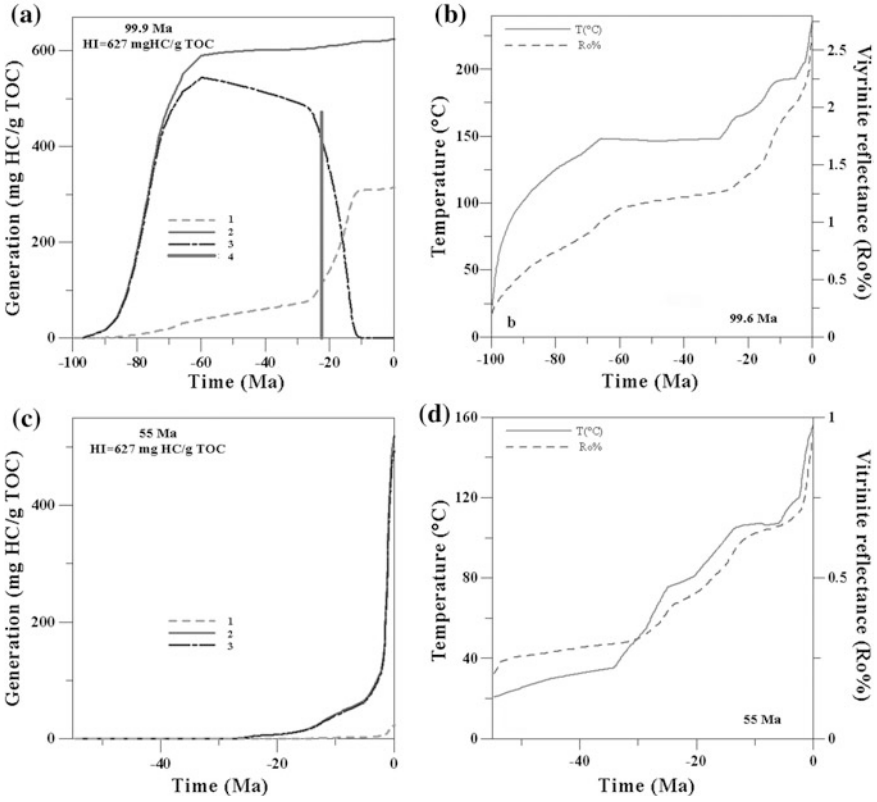

Fig. 5.10 Realization of the potential of oil-gas generation (**a**, **c**) and change of temperature and maturation level (%Ro) (**b**, **d**) in the burial history of rocks at the base (**a**, **b**) and top (**c**, **d**) of the Upper Cretaceous complex (variant 1 of the basin development; well 1 of the Sakhalin-5 area). **a**, **c** *1* generation of gaseous hydrocarbons, *2* total hydrocarbon generation, *3* liquid hydrocarbon generation, *4* the time of expulsion threshold, determined by filling of 20 % of porous volume by liquid hydrocarbons (see text)

(b) The Eocene complex (55–34 Ma)

The Eocene complex has a small thickness (about 200 m) in all of the considered sections (wells) of the Kayga-Vasyukan block of the Sakhalin-5 area. It is presented by mixture of clays, sandstones and vulcanites (Table 5.1; [2, 19]). A level of organic matter maturation ranges from Ro = 0.87–0.95 % at the base of the complex (at the depth of 4,200–5,000 m) to Ro = 0.82–0.87 % at its roof (at the depth of 4,000–4,800 m). The type of organic matter in the Eocene rocks is accepted similar to the one in the Upper Cretaceous complex (kerogene of type II with HI = 627 mg HC/g TOC). The modern values of TOC equaled to 0.6 % corresponds to initial values of TOC equaled to 1 and 0.97 % at the base and roof of the complex, correspondingly. The realization history of hydrocarbon potential of the

complex is close to the one in Fig. 5.10c. The main part of oil generation by the rocks of the Eocene complex occurred in the Pliocene-Pleistocene and the rocks at the base of the complex realized its hydrocarbon potential by 82 % to present time, whereas the rocks at the roof of the complex—by 76 % (Table 5.3). According to these parameters, the oil bearing perspective of the Eocene complex can be assessed as rather high.

(c) The Michigar formation (34–28.5 Ma)

The Lower Oligocene complex of thickness about of 400 m is presented by mixture of clay and sandstones (Table 5.1; [2, 19]). Maturation of organic matter ranges from Ro = 0.82–0.87 % at the base of the complex (at the depth of 4,000–4,800 m) to Ro = 0.73–0.78 % at its roof (at the depth of 3,600–4,400 m; Fig. 5.6; Table 5.3). Organic matter in the rocks of the Michigar complex is again characterized by the kerogene of type II with HI = 627 mg HC/g TOC similarly to the previous complex. The modern values of TOC equaled to 0.6 % corresponds to initial values 0.85–0.97 % at the base of the complex. The realization histories of hydrocarbon potential of the rocks in the base and roof of the Lower Oligocene complex are shown in Fig. 5.11a, b for the first variant of tectonic development of the basin. The main part of oil generation by the rocks of the complex occurred again in the Pliocene-Pleistocene. To present time, the rocks at the base of the complex realized 76 % of its hydrocarbon potential, whereas the rocks at the roof of the complex—46 % (Figs. 5.6, 5.9 and 5.11a, b; Table 5.3). Such level of realization of hydrocarbon potential can be considered as enough for oil field formation, if the conditions for oil migration and accumulation were held.

(d) The Daekhuriinsk formation (28.5–25 Ma)

The Upper Oligocene Daekhuriinsk complex has a thickness about of 300 m in all of the considered sections (wells) of the Sakhalin-5 area. It is presented by the layer of dark gray siliceous argillites (Table 5.1; [2, 19]). A level of organic matter maturation ranges from Ro = 0.73–0.78 % at the base of the complex (at the depth of 3,600–4,400 m) to Ro = 0.66–0.72 % at its roof (at the depth of 3,300–4,100 m; Figs. 5.6, 5.9 and 5.11c; Table 5.3). Sedimentation of clays and siliceous clays took place at relatively deep-water conditions with predomination of marine plankton organic matter and little admixture of continental organic matter. Therefore, the organic matter in the Daekhuriinsk complex is characterized again by the kerogene of type II with HI = 627 mg HC/g TOC. The modern values of TOC equaled to 0.6 % corresponds to initial values of TOC equaled to 0.70–0.76 % at the base of the complex is shown in Fig. 5.11c. The main part of oil generation by the rocks of the complex occurred in the Pliocene-Pleistocene and now the rocks in the base of the complex realized its hydrocarbon potential by 46 %, whereas the rocks at the roof of the complex—only by 23 % (Table 5.3). Such level of realization of hydrocarbon potential can be considered as very moderate, but it can be enough for oil field formation under favorable conditions of oil migration and accumulation.

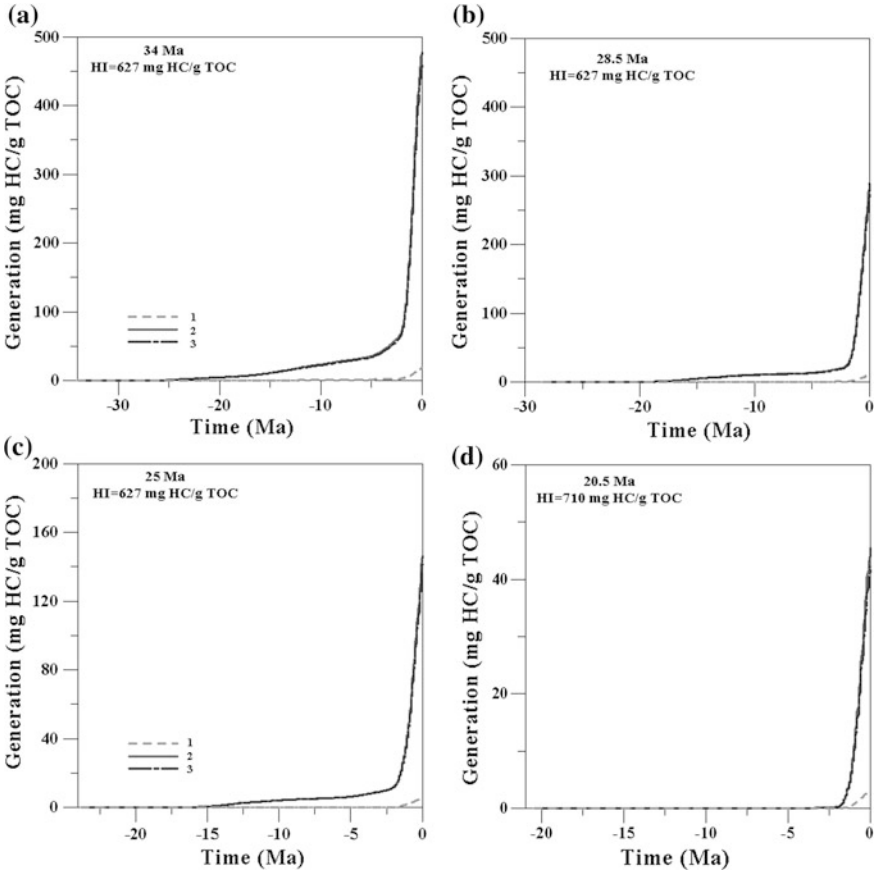

Fig. 5.11 Realization of the potential of oil-gas generation in the burial history of rocks at the base (**a**) and roof (**b**) of the Lower Oligocene (Michigar) sedimentary complex, at the roof of the Upper Oligocene (Daekhuriinsk sedimentary complex **c**) and the base of the Lower-Middle Miocene (Dagin complex **d**) (all computations in variant 1 of the basin development for the well 1 of the Sakhalin-5 area)

(e) The Uyninsk formation (23.8–20.5 Ma)

At the Sakhalin-5 area, the Lower Miocene Uyninsk formation of thickness about of 200 m is presented by alevrite clayey rocks with sandstones interbeds (Table 5.1; [2, 19]). Maturation of organic matter ranges from Ro = 0.66–0.72 % at the base of the complex (at the depth of 3,300–4,100 m) to Ro = 0.63–0.69 % at its roof (at the depth of 3,100–3,900 m; Figs. 5.6 and 5.9, Table 5.3). The organic matter of the Uyninsk complex is characterized again by the kerogene of type II with HI = 627 mg HC/g TOC. The modern values of TOC equaled to 0.8 % corresponds to initial values of TOC equaled to 0.84–0.9 % at the base of the complex. The realization history of hydrocarbon potential by the rocks at the base

of the complex is close to the one in Fig. 5.11c and for the roof of the complex it is shown in Fig. 5.11d. The main part of oil generation by the rocks of the complex occurred in the Pleistocene and now the rocks in the base of the complex realized its hydrocarbon potential by 23 %, whereas the rocks at the roof of the complex—only by 13 % (Table 5.3). Such level of realization of hydrocarbon potential can be considered as moderate-low, and a formation of oil field is possible only under very favorable conditions of oil migration and accumulation.

(f) The Dagin formation (20.5–14 Ma)

The Lower-Middle Miocene Dagin formation of thickness from 300 to 500 m is presented by interbedding of argillite, sandstones, clays with little coal inclusions (Table 5.1; [2, 19]). Maturation of organic matter ranges from Ro = 0.63–0.69 % at the base of the complex (at the depth of 3,100–3,900 m) to Ro = 0.51–0.58 % at its roof (at the depth of 2,600–3,400 m; Table 5.3). The sedimentation environment changes from continental in the western part of the northern Sakhalin to shore and marine in its eastern part. Therefore, the organic matter varies from mainly gumic in the western areas to mainly sapropelic in the eastern ones. In our modeling, the organic matter of the Dagin complex is presented by the kerogene of type I with HI = 710 mg HC/g TOC. The modern values of TOC = 1.1 % in the Dagin formation. The rocks at the base of the complex realized no more than 6 % of its hydrocarbon potential whereas the rocks at the roof of the complex—less than 1 % (Table 5.3).

(g) Okobyky formation (11–9 Ma)

The Okobyky formation (the Upper Miocene) of thickness of 130–300 m is presented by clayey-aleurite rocks with sandstone interbeds (Table 5.1). According the modeling, maturation of organic matter ranges from Ro = 0.51–0.58 % at the base of the complex (at the depth of 2,600–3,400 m) to Ro = 0.48–0.56 % at its roof (at the depth of 2,460–3,300 m; Fig. 5.5b; Table 5.3). The rocks of the Okobyky formation are typically marine formatted at significant influence of the sediments of the Paleo-Amur delta. The rocks in the base of the complex realized no more than 1 % of its hydrocarbon potential and less than 0.6 % at the roof of the complex (Table 5.3). But these rocks are a good reservoirs. The Okobyky formation is the one of the main productive complex of the North Sakhalin.

(h) The Nizhne (9–6 Ma)—and Vetkhne (6–1.8 My)—Nutov formations

The Nizhne-Nutov formation of thickness from 300 to 1000 m is presented by sandstones and sands, but in the Verkhne-Nutov formation of thickness 1200–1400 m the fraction of clay in the rock increases (Table 5.1; [2, 19]). Acording the modeling, maturation of organic matter in the Nizhne-Nutov formation ranges from Ro = 0.48–0.56 % at the base of the complex (at the depth of 2,460–3,300 m) to Ro = 0.44 at its roof (at the depth of 2,350 m). In the Verkhne-Nutov formation maturation of organic matter varies from Ro = 0.44 % at the base of the complex

(at the depth of 2,350 m) to Ro < 0.30 % at its roof (at the depth of about 900 m Fig. 5.6; Table 5.3). These rocks could be interesting only as potential reservoirs.

(i) The probable zones of hydrocarbon accumulation

The absence of regional impenetrable caps in the sedimentary section of the north-eastern shelf of the Sakhalin results in the permeability of the Cenozoic sedimentary blanket and in possibility of migration of the hydrocarbon generated in deeper horizons to the upper layers of the basin [2, 19]. The main part of perspective traps and oil-gas accumulation zones in the northern shelf of the Sakhalin belong to the geological objects of structural type and are arranged for anticline folds of different genesis. They are related often with the regional thrust faults (Vostochno-Ekhabinskaya, Pervomayskaya and other areas; [28]). The structure-lithological caps, related with a replacement of sandy beds in the Nizhne-Nutov formation by clayey beds, spread very widely (the Okhta oil accumulation zone; [3]). The traps of such type were revealed also in the Okobyky-Nizhne-Nutov complex and are suggested in the Dagin complex within the different structures of the North Sakhalin shelf [4]. It is significant that the time of these traps formation coincides practically with the time of intensive generation and migration of hydrocarbons at all of generating depositions, including the Eocene ones (Figs. 5.9, 5.10 and 5.11; [4, 28]). Besides, the main part of the oil accumulations and about half of the gas accumulations in the North Sakhalin are attributed to the natural reservoirs of the layer type, presented by interbedding of sandy, alevrolite and clayey beds. The reservoirs of massif type with fracture and fracture-porous collectors are assumed in the north-eastern shelf of the Sakhalin in the Dayekhuriin horizon and the Pilsky clayey-silica complex. The traps in the Upper Mesozoic basement complex with fissure type of collector associated to the serpentine massif with equivalent open porosity of 5–15 % are considered as very perspective [4]. Such complexes of the low-density serpentinites arose as result of hydrothermal serpentinization of ultramafic rocks of the East Sakhalin ophiolite belt extending along the East Sakhalin crust-mantle fault [4]. Thus, in the absence of the regional caps in the North Sakhalin shelf, there are many possibilities of formation of local hydrocarbon accumulations, generated by the deep oil source rocks of the basin and migrated into different traps in the upper horizons.

5.4 Analysis of Tectonic Subsidence in Two Variants of Tectonic History of the Basin

It was noted in the Sect. 5.1 that there is not one treatment of tectonic history of the region. By this reason, in our paper two “limit” variants of tectonic evolution of the region are analyzed [29, 30]. In the first of the ones, we believe that the numerous faults and shifts along them weakened significantly the lithosphere strength on the study area of the basin (Fig. 5.7a). Then the local-isostatic response of the basin

lithosphere on external and internal loads took place during all of the basin history beginning with the Upper Cretaceous. Possible short periods of duration of some million years with compression regime have not great significance provided that the state of local isostasy was restored after every of these periods.

In the second, alternative variant of the basin evolution (Fig. 5.7b), we believed that the local-isostatic response of the basin lithosphere on external and internal loads took place only beginning with the time of the Kuril arc formation (about 34 My ago), when the arc took itself the main part of regional compression stresses. In this variant, an analysis of the basin tectonic subsidence suggested local-isostatic response of the lithosphere on load is used only for time interval from 34 Ma up to now.

The lithosphere structure of the Okhotsk Sea block in the Sakhalin-5 area was constructed by the geophysical profile "Amur Liman—Central Okhotsk rise" (Fig. 5.2; [6, 7, 14, 20]). In the first variant of tectonic evolution of the region, the Okhotsk Sea block is a part of the continental lithosphere (see Sects. 5.1 and 5.2). Now, the lithosphere of the block is the thinned continental lithosphere with present-day thickness of granite layer of about 5 km and "pseudo-basaltic"layer of about 22 km [6, 14]. In the other variant of tectonic evolution, the block of the Okhotsk Sea is a part of the oceanic Cula plate (see Sects. 5.1 and 5.2). the geophysical data (Fig. 5.2) suggests that the upper part of the consolidated crust can be presented by the Upper Cretaceous basaltic sheets and its lower part—by interbedding of gabbro and serpentinized peridotite (3-th layer of the oceanic crust; [7]). As mentioned in Sects. 5.1 and 5.3, the modeling results will not change considerably at replacement of the first variant of the basin evolution by the second one. One reason for this is that the contribution of radiogenic heat flow in the both variants consists only small part of heat flow in the region (see below).

In the first variant of the basin development, an analysis of tectonic subsidence implies five stages of moderate thinning of lithosphere with total extension amplitude of about 1.52 (Fig. 5.7a). It was believed that these episodes of the crust thinning were local response of the lithosphere on the stress fields within the regional shift zone in the North Sakhalin [8]. They explain a relatively quick subsidence of the basin during these periods of the lithosphere thinning. In the above variant of the basin development, the crust of the basement at the time of initiation of the basin must have a thickness of about 41 km with 7.6 km of "granitic" layer. The present-day thickness of consolidated crust 27 km and granitic layer 5 km will be result from the lithosphere thinning with total amplitude 1.52 in accordance with Fig. 5.2. Physical parameters of such lithosphere, used in the modeling, are shown in Tables 1.1 and 5.4.

In the second, alternative variant of the basin evolution (Fig. 5.7b), we believed that the local-isostatic response of the basin lithosphere on external and internal loads took place only beginning with the time of the Kuril arc formation (about 34 My ago), when the arc took itself the main part of regional compression stresses. In this variant, an analysis of the basin tectonic subsidence suggested local-isostatic response of the lithosphere on load is used only for the time from 34 Ma up to now. In this case, only three periods of the lithosphere thinning of total amplitude of

Table 5.4 The structure of the lithosphere at initiation of the basin evolution [29]

Layer	Granitic		"Pseudobasaltic"	Mantle
Depth of the layer (km)	2.5 (2.1)	7.6 (6.3)	41.0 (34.3)	>41 (>34.3)
Density (kg/m^3)	2,750	2,750	2,900	3,300
Heat conductivity (W/m °K)	2.72	2.72	1.88	$K = f(T)^*$
Heat generation (mkW/m^3)	1.26	0.71	0.21	0.004

"Depth of the layer" points the depth of the base of different layers of the lithosphere in the first variant of the basin evolution (values outside the brackets) and in the second one (values inside the brackets)

Physical parameters of the rocks are taken according to Table 1.1

about 1.27 remain from the above five periods in the first variant. The initial thickness of consolidated crust consists then about 34.3 km and depth of other layers of the initial lithosphere is shown in Table 5.4 in brackets. The present-day thickness of consolidated crust 27 km and granitic layer 5 km will be again the result from the lithosphere thinning with total amplitude 1.27 in accordance with Fig. 5.2.

The thermal history of the basin lithosphere presented in Fig. 5.8b is in agreement with variations of tectonic subsidence of the basin (Fig. 5.7a) and with measured values of temperatures (Fig. 5.5a) and maturation level of organic matter (Fig. 5.5b). In the first variant of the basin development, the tectonic analysis suggests two thermal activation of the lithosphere: in the Early Miocene and the Late Miocene-Pliocene. They led to essential heating of the basin lithosphere at the modern values of surface heat flow 56–57 mW/m^2, which are close to the values 50–60 mW/m^2 measured in the study region [14, 19]. In addition, the analysis of tectonic subsidence in the first variant of the basin evolution suggests five periods of moderate crust thinning: in the Turonian-Santonian (with effective stretching amplitude $\beta \approx 1.14$), the Maastrichtian ($\beta \approx 1.05$), the Upper Oligocene ($\beta \approx 1.1$), the Middle Miocene ($\beta \approx 1.05$) and in the Quaternary ($\beta \approx 1.1$). They correspond to periods of relatively quick subsidence of the basin and are characterized by decrease of the MOHO depth (Figs. 5.6, 5.7a and 5.8b). The second variant of the basin development differs from the first by absence of two periods of the crust thinning—in the Turonian-Santonian and the Maastrichtian (Figs. 5.6c and 5.7b). Correspondingly, the initial lithosphere in the study area of the basin had the crust of thickness of 34.3 km with 6.3 km of the "granite" layer in comparison to 41 and 7.6 km in the first variant of the basin development (Table 5.3).

As whole, the modeling suggests a rather intensive thermal regime of the basin lithosphere during its history. Indeed, the modern heat flow through the basement surface computed in our model consists 55.7 mW/m^2 (Fig. 5.8a). Taking the modern "granite" layer of thickness of 5 km with upper 1.7 km of high-radiogenic rocks and "basaltic" layer of thickness of 22 km (Fig. 5.2; Table 5.4), we can roughly estimate the modern heat flow through the mantle surface by rather high value of 46.6 mW/m^2. In the future this flow can be greater taking into consideration non-steady thermal regime of the region lithosphere ([29]; Figs. 5.5a and 5.8a, b).

Thus, our modeling using the analysis of the tectonic subsidence of the basin, has allowed to solve the contradiction between the limited degree of maturity of organic matter in the sedimentary cover of the basin and high thermal regime of the mantle region.

5.5 Conclusion

Analysis of variations in tectonic subsidence of the Basin permits to assess the amplitudes and duration of the thermal and tectonic (extension) events in the evolution of the Basin lithosphere and obtain the numerical reconstructions of the burial, thermal and maturation history of sedimentary blanket within the eastern part of the North Sakhalin shelf. The reconstructions were carried out for the entire period of the basin's evolution starting from the Upper Cretaceous ([29, 30]; Figs. 5.6 and 5.8). The location of considered area near to the East Sakhalin accretion complex has led to the need to consider two variants of the Basin evolution. In the first variant the local isostatic response of the basin's lithosphere on internal and external load are assumed to be during entire history of the Basin. In the second variant, such response is suggested only for the time beginning with the Kuril Island Arc's formation that is from about 34 Ma BP up to now. The computations demonstrate a weak dependency of the lithosphere thermal regime and organic matter maturation in the Cenozoic section on the choice of the variants of the basin evolution. The modeling implies a rather high thermal regime of the Basin with modern temperatures of 100 and 200 °C at depths of 3 and 6.7 km, respectively, in spite of intensive sedimentation during the recent 10 Ma (Figs. 5.5a, 5.6 and 5.8; Table 5.3).

The analysis of maturation and generation history of the probable source rocks suggests that the rocks of the Upper Cretaceous, Eocene, Machigar (34–28.5 Ma), Daekhurin (28.5–25 Ma), and Lower Uynin (23.8–20.5 Ma) complexes can be considered as perspective oil bearing rocks [30]. The same analysis supposes that the rocks of the Upper Uynin, Dagi (22–14 Ma), Okobykai (11–9 Ma), Lower Nutov (9–6 Ma), and Upper Nutov (6–1.8 Ma) formations are characterized by low maturity are interesting only for the formation of traps and reservoirs (Tables 5.1 and 5.3).

References

1. Chekhovich VD (1993) Tectonics and geodynamics of the folded framework of small oceanic basins. Nedra, Moscow (in Russian)
2. Gladenkov YB, Bazhenova OK, Grechin VI et al (2002) Cenozoic of Sakhalin and its oil and gas potential GEOS, Moscow (in Russian)

3. Koblov EG, Kharakhinov VV (1997) The regional and local oil-gas field forecast for the sedimentary basins of the Okhotsk Sea, in Geologia i razrabotka mestorozhdeny nefti i gasa Sakhalina I shelfa, Moscow, Nauchny Mir, pp 26–53 (in Russian)
4. Kharakhinov AV (1999) New perspective directions of the oil-gas prospecting in the North Sakhalin shelf. Geologia nefti i gasa 9–10:18–25 (in Russian)
5. Isaev VI (2004) Paleotemperature modeling of the sedimentary section and oil and gas generation. Tikhookeanskaya geologiya 23(5):101–115
6. Bogdanov NA, Khain VE (2000) Comments to the tectonic map of the Okhotsk Sea region of scale 1: 2 500 000 Moscow, ILOVM RAN (in Russian)
7. Bogdanov NA, Dobretsov NL (2002) The Okhotsk volcanic oceanic plateau (in Russian). Geologia I geophisika 43(2):101–114
8. Fournier M, Jolivet L, Huchon Ph, Sergeyev KF, Oscorbin LS (1994) Neogene strike-slip faulting in Sakhalin and the Japan Sea opening. J Geophys Res 99(B2):2701–2725
9. Parfenov LM, Natalin BA (1986) Mesozoic tectonic evolution of northeastern Asia. Tectonophysics 127:291–304
10. Rozhdestvensky VS (1986) Evolution of the Sakhalin fold system. Tectonophysics 127:331–339
11. Maruyama Sh, Seno T (1986) Orogeny and relative plate motions: example of the Japanese Islands. Tectonophysics 127:305–329
12. Sokolov SD, Didenko AN, Grigor'ev VN, Alexyutin MV, Bondarenko GE, Krylov KA (1997) Paleotectonic reconstructions of the north-eastern Russia: problems and uncertainty. Geotectonika (6):72–90 (in Russian)
13. Konstantinovskaya EA (2003) Margins of East Asia: tectonics, structural evolution and geodynamic modeling. Moscow, Nauchny Mir (in Russian)
14. Verzhbitsky EV, Berlin YM, Kononov MV, Marina MM (2006) Bottom age, origin, deep structure and the methods of temperature assessment for hydrocarbon generation in the Okhotsk Sea region. Okeanologia 46(4):572–583 (in Russian)
15. Zonnenshein LP, Kuzmin MI, Natapov LM (1990) Plate tectonics in the USSR area, part 2. Nedra, Moscow (in Russian)
16. Sokolov SD (2003) Accrecionary tectonics: the state of the art. Geotectonika 1:3–18 (in Russian)
17. Melankholina EN (2000) The Late Cretaceous island arcs of the eastern margin of the Euroasia: geological, geochemical and tectonics correlation. Geotectonika (3):41–57 (in Russian):
18. Fournier M, Jolivet L, Huchon Ph, Sergeyev KF, Oscorbin LS (1994) Neogene strike-slip faulting in Sakhalin and the Japan Sea opening. J Geophys Res 99(B2):2701–2725
19. Veselov OV, Gretskaya EV, Iliev AY, Kononov VE, Kochergin EV (2006) Tectonic mapping and hydrocarbon potential of the Okhotsk Sea, Moscow, Nauka (in Russian)
20. Zhigulev VV, Kononov VE, Levin BV (2007) Geological structure of sedimentary cover and an assessment of oil-gas potential of the Derugin depression (the Okhotsk Sea). Tikhookeanskaya geologiya 26(5):3–12 (in Russian)
21. Zlobin TK, Iliev AY, Zlobina LM (2006) The origin and depth of the basin surface in Sea of Okhotsk from deep seismic sounding and CDP seismic reflection evidence. Tikhookeanskaya geologiya 25(4):3–17 (in Russian)
22. Velichko AA (1999) Change in climate and landscapes for the last 65 My (the Cenozoic: from Paleocene to Holocene). Moscow, GEOS (in Russian)
23. Frakes LA (1979) Climates throughout geological time. Elsevier, Amsterdam
24. Espitalie J, Ungerer P, Irvin I, Marquis E (1988) Primary cracking of kerogens. Experimenting and modelling C1, C2–C5, C6–C15 classes of hydrocarbons formed. Org Geochem 13(4–6): 893–899
25. Ungerer P (1993) Modeling of petroleum generation and migration. In: Bordenave ML (ed) Applied petroleum geochemistry, Technip, Paris, pp 397–442
26. Ungerer Ph (1990) State of the art of research in kinetic modelling of oil formation and expulsion. Org Geochem 16(1–3):1–27
27. Welte DH, Horsfield B, Baker DR (eds) (1997) Petroleum and basin evolution. Springer

28. Kharakhinov VV (1998) Tectonics of the Okhotsk Sea oil-gas bearing region (in Russian). PhD thesis, Ocka-na-Sakhaline, SakhalinNIPImorneft', Vladivostok
29. Galushkin YI, Sitar KA, Kunizyna AV (2011) Numerical modeling of the organic matter transformation in the sedimentary rocks of the Northeastern Sakhalin Shelf, vol 51, issue 3. Oceanology, Maik Nauka/Interperiodica Publishing (Russian Federation), pp 491–501 (2011)
30. Galushkin YI, Sitar KA, Kunizyna AV (2011) Realization of the oil generation potential in the estimated source rocks of the sedimentary basin in the shelf of Northeastern Sakhalin: numerical simulation, vol 49, issue 1. Geochemistry International, Maik Nauka/Interperiodica Publishing (Russian Federation), pp 1–12 (2011)

Part II
The Maturation of Organic Matter and Hydrocarbon Generation in the Vicinity of Intrusions and Subtrappean Sedimentary Complexes

Chapter 6
The Trappean Complex of the Siberian Platform

Abstract This chapter is devoted to a study of thermal effect of numerous dolerite intrusions of the Lower Triassic age presented widely in sedimentary basins of the East Siberia platform. The modeling of thermal regime and maturation history of sedimentary basin of the Siberian Platform is conducted on the examples of two sedimentary sections: the Kuyumba-12 well in the Kamo swell containing six sills in sedimentary section and the Kiramkinskaya-1 well of the Kureika Basin with eight intrusive bodies of the Lower Triassic age in sedimentary cover. The modeling allows an estimation of thermal influence of the intrusive complex on the maturation history of organic matter in the host rocks of the basin and hydrocarbon generation by these rocks. The modeling demonstrates that this influence can be both significant and negligible depending on the size of the intrusion and the distance of the host rocks to the surface of the intrusive body. Evaluation of the thermal effect of intrusions was conducted in the framework of a model of instantaneous intrusions and can be considered as the evaluation of such effect to the maximum.

Keywords Siberia platform · Intrusive complex · Intrusive complex · Maturity aureole · Vitrinite reflectance

6.1 Geological Setting

The total thickness of the recent sedimentary cover in the Siberian platform varies between 0 km (within the shields) and 10 km (and possibly more) in the Kureika Basin [1, 2]. The depressions located along the northern and eastern edges of the platform are filled with thick (up to 10 km) Mesozoic terrigenous series (Fig. 6.1). The Riphean and the Vendian-Paleozoic have developed as two distinct tectono-stratigraphic units, characterized by different structural patterns, and separated by a sharp unconformity (see for example Table 6.1). The Riphean has a very complex, blocky structure whereas the Vendian-Paleozoic is structurally less complex (Fig. 6.2).

Y. Galushkin, *Non-standard Problems in Basin Modelling*,
DOI 10.1007/978-3-319-33882-8_6

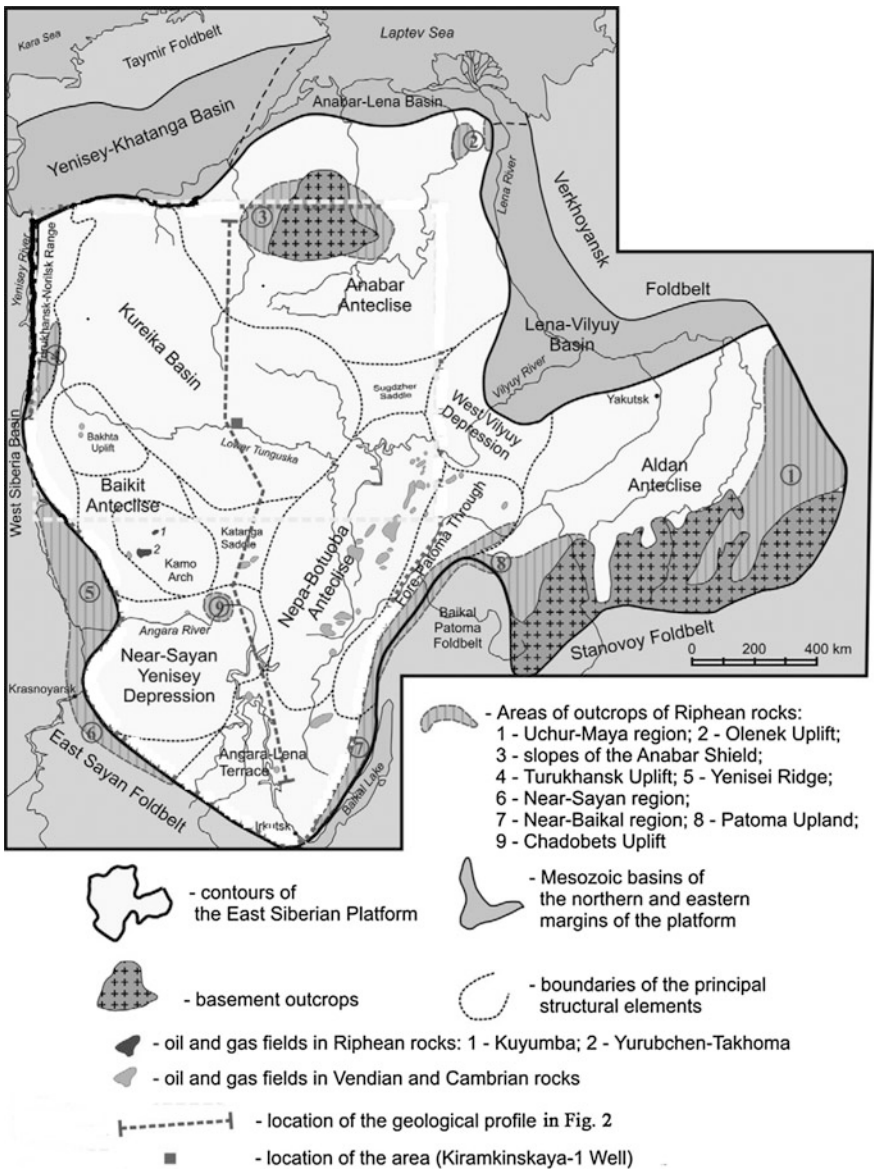

Fig. 6.1 The principal structural elements of the Siberian Platform (according to [1] with little changes)

As whole, the East Siberia platform is unique by its volume of several kilometers thick Meso-Neoproterozoic sedimentary units deposited here over a period of one billion years (1650–650 Ma). The Riphean reservoirs of East Siberia contain the largest portion of oil-and-gas reserves proven in the region. Most researchers

Table 6.1 Main stages of the Basin evolution in the Kuyumba field, well 12

N	Type	t (My)	Z (m)	shale	sand.	dolom	halit	anhyd	marle
1	sedim.	1420–1460	2928–3021	1.000	0.000	0.000	0.000	0.000	0.000
2	sedim.	1210–1420	2418–2928	0.200	0.000	0.800	0.000	0.000	0.000
3	sedim.	850–1210	2166–2418	0.045	0.005	0.950	0.000	0.000	0.000
4	erosion	570–850	1500	–	–	–	–	–	–
5	interrupt.	544–570	2166–2166	–	–	–	–	–	–
6	sedim.	532–544	1911–2166	0.060	0.000	0.840	0.000	0.100	0.000
7	sedim.	529–532	1868–1911	0.150	0.000	0.850	0.000	0.000	0.000
8	sedim.	526–529	1650–1868	0.050	0.000	0.550	0.400	0.000	0.000
9	sedim.	522–526	1300–1650	0.150	0.000	0.750	0.070	0.030	0.000
10	sedim.	519–522	1040–1300	0.050	0.000	0.530	0.400	0.020	0.000
11	sedim.	512–519	700–1040	0.120	0.000	0.790	0.000	0.090	0.000
12	sedim.	503–512	347–700	0.200	0.000	0.680	0.120	0.000	0.000
13	sedim.	502–503	218–347	0.050	0.000	0.950	0.000	0.000	0.000
14	sedim.	500–502	15–218	0.150	0.250	0.150	0.000	0.000	0.450
15	interrup.	480–500	15–15	–	–	–	–	–	–
16	sedim.	420–480	15–15	0.500	0.500	0.000	0.000	0.000	0.000
17	erosion	359–420	400	–	–	–	–	–	–
18	sedim.	305.5–359	15–15	0.500	0.500	0.000	0.000	0.000	0.000
19	sedim.	284–305.5	15–15	0.500	0.500	0.000	0.000	0.000	0.000
20	sedim.	252–284	15–15	0.500	0.500	0.000	0.000	0.000	0.000
21	erosion	175–252	300	–	–	–	–	–	–
22	erosion	20–175	200	–	–	–	–	–	–
23	erosion	1.8–20	500	–	–	–	–	–	–
24	sedim.	0–1.8	0–15	0.500	0.500	0.000	0.000	0.000	0.000

Remarks N is the number of stage of the Basin development, starting with its initiation; *type* type of the stage (*sedim.* sedimentation, *interrup* interruption, erosion). *t* is the start and finish time of the stage in My, Z is the depth of top and base of sedimentary layer in the present-day section or thickness of eroded sediments [1, 2]; *sand.* sandstone, *dolom.* dolomite, *anhyd.* anhydrite

consider Riphean strata as the main source of hydrocarbons for East Siberian oil and gas fields [1, 3, 4]. The discoveries of the large Yurubchen and Kuyumba oil fields led to the understanding that the Riphean series should be the first priority object for oil-and-gas prospecting, and stimulated many detailed studies. These fields contain oil accumulations within reservoirs of weathering crusts in the Riphean carbonates that are sealed by clayey carbonates and evaporates of the Upper Vendian–Lower Cambrian [1].

The basement of the Siberian Platform is composed of highly metamorphosed Archean—Lower Proterozoic rocks. The platform is mainly framed by Paleozoic and Mesozoic orogenic belts: the East-Sayan, Baikal-Patoma and Stanovoy to the south; the Verkhoyansk to the east; the Taymir to the north-west; and the Yenisei Ridge to the south-west ([1], Fig. 6.1). Their junction with the platform is

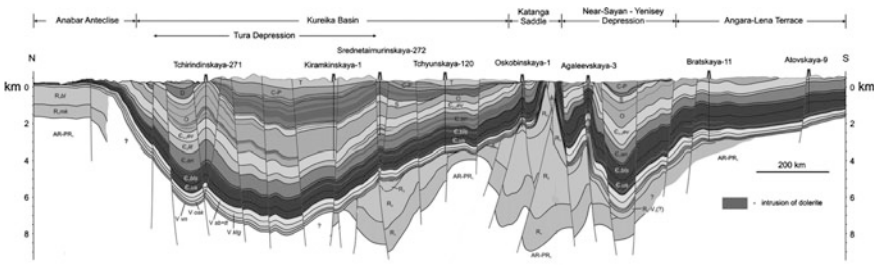

Fig. 6.2 Geological profile across the Siberian Platform showing examples of Riphean/Vendian unconformity (according to [1] with little changes). See Fig. 6.1 for the location of the profile. Stratigraphy indexes: *AR-PR1* Archean-Paleoproterozoic; *R1* Lower Riphean, unspecified; *R1mk* Mukun Group, Lower Riphean; *R1bl* Billyakh Group, Lower Riphean; R2 Middle Riphean; *R3* Upper Riphean; *R3-V1* Upper Riphean-Lower Vendian; *V vn* Vanavara Formation, Vendian; *V osk* Oskoba Formation, Vendian; *V ktg* Katanga Formation, Vendian; *V sb+tt* Soba and Tetere formations, Vendian; *C-1us* Usola Formation, Lower Cambrian; *C-1bls* Bela Formation, Lower Cambrian; *C-1an* Angara Formation, Lower Cambrian; *C-2ltv* Litvintzev Formation, Middle Cambrian; *C-2–3 eV* Evenki Formation, Middle-Upper Cambrian; *O* Ordovician; *S* Silurian; *D* Devonian; *C-P* Carboniferous-Permian; *T* Triassic

characterized by tectonic nappes and thrusted zones. Foreland basins (e.g. the Fore-Patoma and Fore-Verkhoyansk) are developed along these zones. Westward, along the left bank of the Yenisei River, the sedimentary complexes of the Siberian Platform dip under the Mesozoic series of West Siberia. The composition of the sedimentary cover varies throughout the Siberian Platform. The Riphean terrigenous-carbonate series are widespread at its base (see, for example, Table 6.1). They are mostly absent in the Nepa-Botuoba Anteclise, in the Angara-Lena Terrace, and in small areas of the Baikit Anteclise. Vendian deposits, terrigenous at the base and carbonate in the upper part, are generally present, except in the Anabar and Aldan shields. The Ordovician, Silurian, Devonian, and Lower Carboniferous carbonate series are commonly confined within depressions. The Middle Carboniferous—Permian terrigenous coal-bearing deposits reach a maximum thickness in the central and northern parts of the platform.

In this region, Lower Triassic lava and pyroclastic rocks, up to 2 km thick, overlie the sedimentary sequence. Early Triassic dolerites intrusions are present throughout. The amount and the thickness of these sills increase towards the north of the platform and upward in the sedimentary sequence [2]. Last time, an influence of heat from igneous bodies on HC generation draw a great attention in relation with discovering of oil fields formed in vicinity of intrusions emplaced into horizons of immature rocks [5]. We use results of one-dimensional basin modeling (flat basin approach) to reconstruct numerically thermal and maturation histories of the main source formations of sedimentary sections including Kuyumba well in the Kamo arch and the Kiramkinskaya well in the Kureiskaya depression (Fig. 6.1).

6.2 Burial and Thermal Histories of Sedimentary Basins in Kamo Arch of Bayakitskaya Anticline and the Kureika Basin of the Siberian Platform

The present-day sedimentary section of the basin, measured values of deep temperature and heat flow, assessment of maturation level of organic matter together with an analysis of variations in tectonic subsidence of the basin are considered as the main control factors of our numerical models of the basin development (Chap. 1). Then, the input parameters for the modeling include the present-day sedimentary cross-section, estimates of the amplitude and rate of erosion, the lithological composition and petrophysical characteristics of rocks, the structure of the lithosphere (basement) and its rock parameters. In addition, measured values vitrinite reflectance, paleoclimate, sea paleodepth, present-day surface heat flow, measurements of deep temperature and information on the paleotectonics and present-day tectonic setting of the basin are also included in the input data. Part of the data base for the modeling is shown in Tables 6.1 on the example of sedimentary section of the Kuyumba well (Fig. 6.1).

Table 6.1 demonstrates the main stages of the basin evolution together with duration of the stages on the example of the Kuyumba area. Burial, thermal and maturity histories of the basin reconstructed in the GALO system (Chap. 1) are shown in Fig. 6.3 for Kuyumba and Kiramkinskaya areas. Temperature distribution within the sedimentary cover and underlying lithosphere was found out from numerical solution of heat-transfer Eq. (1.1), scribed in the frame related with the

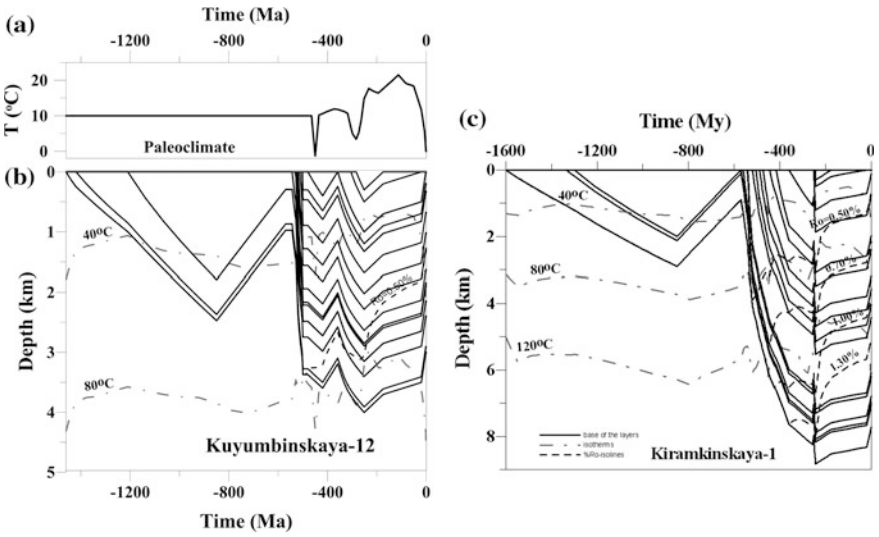

Fig. 6.3 Burial, thermal and maturation histories of sedimentary section of the Kuyumba-12 well and Kiramkinskaya-1 well. The locations of isotherms and isolines of %Ro are computed without consideration of the heat from intrusions

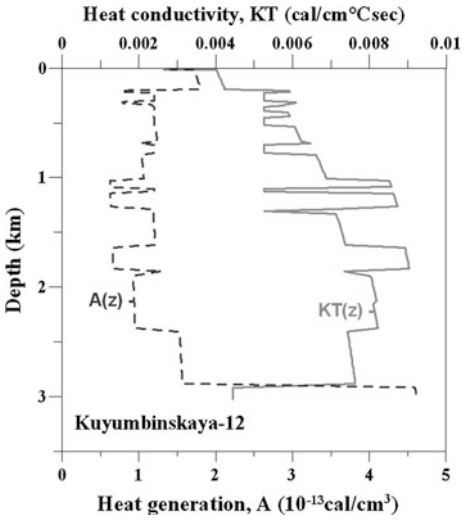

Fig. 6.4 Calculated depth-distributions of heat conductivity and heat generation in present-day sedimentary section of the Kuyumba-12 well (1 cal/cm ° K s = 418.68 W/m °K; 1×10^{-13} cal/cm^3 = 1 HGU = 0.41868 mkW/m^3)

basement. As mentioned in Chap. 1, a significant change of petrophysical parameters in the Eq. (1.1) versus lithological rock composition, porosity φ and temperature T makes the equation considerable nonlinear. Density of sedimentary rocks (ρ_s), their volume heat capacity (*Cvs*), and heat conductivity (*Ks*) are computed by the values for the same parameters for rock matrix (ρ_m, *Cvm*, *Km*) and water (r_w, *Cvw*, *Kw*) (see Sect. 1.1.1). Figure 6.4 shows the calculated variations of heat conductivity and heat generation with depth on example of the present-day section of the Kuyumba-12 well. The values of KT = 0.00526 cal/cm °K s (2.2 W/m °K) and A = 1.2 HGU (0.5 mkW/m^3) were accepted for heat conductivity and heat generation of dolerite intrusions. Maximal heat generation and minimal heat conductivity correspond to the layers with the predominant content of clay (Table 6.1). At whole, heat conductivities computed in our model (Fig. 6.4) are in a rather well agreement with the values measured in the considered region [6].

According to Sect. 1.1.4, temperature at the upper boundary of the computation domain (z = 0) changes with geological time according to paleoclimate conditions during the basin development. Figure 6.3a shows the climate curve used in the basin modeling. The papers [7, 8] gives the paleo-climate data for the Carboniferous—Late Cretaceous and the papers [9, 10]—for the Cenozoic. Cooling periods in the Ordovician, Permian and Cenozoic are considered in construction of this climate curve. Steady temperature T = 10 °C was taken for the Precambrian, in view of the fact that appropriate information about climate in this period of the region development is absent. This simplifying assumption must have a little effect on thermal and maturation history of sedimentary formations of the basin owing to the subsidence did not exceed 3 km in this time interval (Fig. 6.3). The steady temperature Tlow ≈ 1152 °C was maintained at the base of the domain (Z = 103–107 km; Fig. 6.5b). The algorithm of determination of the base temperature Tlow is described in Sect. 1.1.4. Initial temperature distribution corresponded to the surface

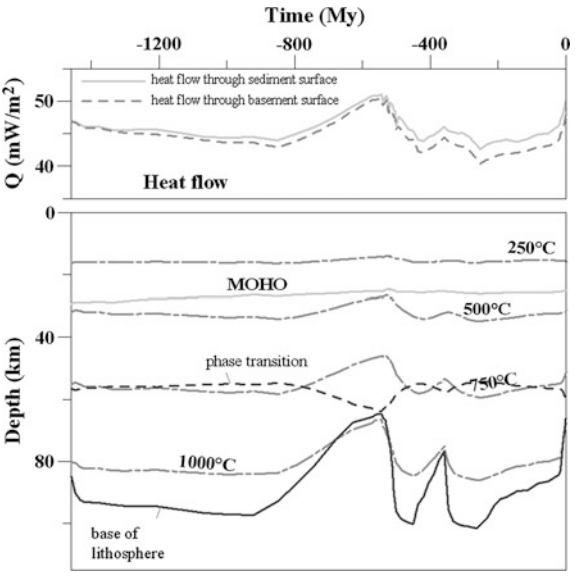

Fig. 6.5 Thermal history of the basin lithosphere in the Kuyumba area (Baykitskaya anticlise, Kamo arch; Fig. 6.1)—numerical reconstructions in the GALO system. **a** Calculated variation in heat flow. **b** Reconstruction of thermal history of the lithosphere (Legend see in Fig. 4.5.)

temperature and heat flow during initiation period of the basin evolution. The initial heat flow was corrected in accordance with variations in tectonic subsidence of the basement surface (Fig. 6.6; Sect. 1.1.4). In considered variant of the basin development it was about 1.12 HFU (47 mW/m^2) in the Kuyumba area of the Kamo arch and 1.5 HFU (62 mW/m^2) in the Kiramkinskaya area of the Kureika Basin whereas the heat flow at present time is estimated by the value of 49 mW/m^2 in the first area and 51.6 mW/m^2 in the second one. The latter values are close to the measured heat flow in the region (50 mW/m^2; [6]). As mentioned above, the distinction of heat flow through the basement surface (dotted line) from the one through the sediment surface (solid line) in Fig. 6.5a is mainly due to radiogenic heat generation in sediments.

The base of the lithosphere, shown in Fig. 6.5b, is determined by intersection of the current geotherm in the lithosphere with the solidus of peridotite with nearly 0.2 % H_2O (Eq. (1.4) in Sect. 1.1.3). This solidus assumes moderately wet mantle. The lithosphere base can be deeper than in Fig. 6.5b, if content of volatile elements is lesser. Long-dashed lines in Fig. 6.5b show isoterms. MOHO-line is the base of the crust. You can see, that the crust thickness reduces slightly during intensive extension of the lithosphere in the Meso- and Neo-Proterozoic in spite of sedimentation in this time period (Fig. 6.3). The phase transition line in Fig. 6.5b shows the depth of the phase transition of spinel peridotite to garnet one (Eq. (1.16) in Sect. 1.2.2). Variations in the depth contribute to a change in amplitude of tectonic subsidence, presented by the lines 3 in Fig. 6.6.

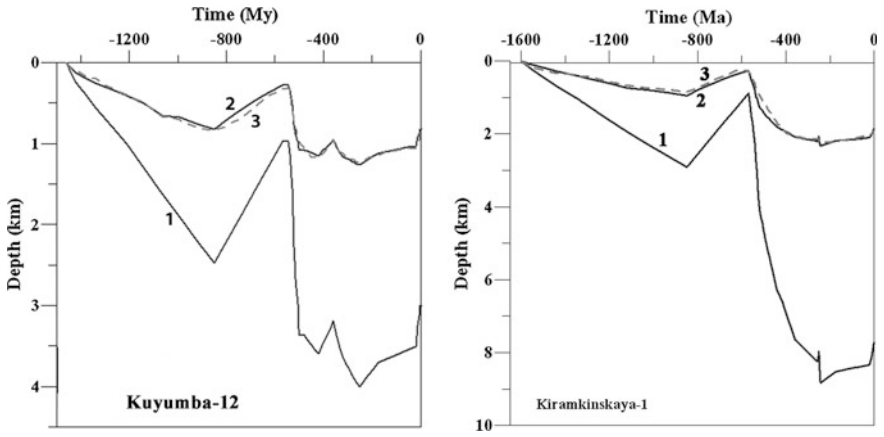

Fig. 6.6 Tectonic subsidence of the basement surface in the burial history of the sedimentary basin (well Kuyumba-12, Kamo arch and well Kiramkinskaya (Fig. 6.1). *1* Position of the basement surface during burial history of the basin, calculated with application of standard "back-stripping" procedure; *2* the tectonic subsidence computed by removal of water and sediment loading on the basement surface (Eq. (1.11) in Sect. 1.2.1). *3* The subsidence calculated from variations in density distribution with depth in the basement during burial history of the basin (Eq. (1.13) in Sect. 1.2.2

In our modeling, a standard continental lithosphere (Table 1.1) of the crust thickness 30 km is assumed for initial stage of the basin evolution (in Lower Riphean). Analysis of tectonic subsidence (Fig. 6.6; Sects. 1.2.1 and 1.2.2) assumes four periods of thermal activation of the lithosphere of different intensity (in the Neo-Proterozoic, the Silurian-Devonian, the Triassic—Oligocene and in the Middle Miocene—Holocene). In the isostasy conditions, these activations correspond to the erosion periods in the basin history (Figs. 6.3, 6.5 and 6.6). In addition, this analysis suggests for the Kuyumba area two periods of the lithosphere extension—in the Meso-Proterozoic with amplitude $\beta = 1.2$ and the Lower Cambrian with amplitude $\beta = 1.1$ (Figs. 6.3 and 6.6). These periods explain the fast subsidence of the sedimentary basin in the Kamo swell in corresponding stage of the basin development. As result from these extensions, the thickness of the crust was reduced up to nearly 25 km to present time, including sedimentary cover on the basement surface (Fig. 6.5). In the Keramkinskaya area of the Kureika Basin analysis of tectonic subsidence suggests the lithosphere extension in the Cambrian—Devonian with amplitude of 1.33 that also explain intensive subsidence of the basin in this period of the basin development and just moderate extension in the Lower Triassic with amplitude $\beta = 1.04$ (Figs. 6.3 and 6.6). As result from the extensions, the crust of the basin lithosphere was reduced up to nearly 29 km to present time, including the 7.76 km of sedimentary cover on the basement surface.

6.3 Evolution of Maturation Degree of Organic Matter During Burial History of the Kuyumba-12 and Kiramkinskaya-1 Sedimentary Sections

Comparison temperature distribution with depth computed for present-day section of the basin with measured deep temperatures requires the consideration of influence of climate variations of the last 3 My on the temperature profile and will be discussed in detail in Chap. 10 for the Kuyumba area. In the Kiramkinskaya-1 well there are not measurements of deep rock temperatures. In this section, distribution of maturity of organic matter with depth is analyzed for both areas and comparison with observed data is conducted for the Kuyumba area where there are estimated values of maturity level. The reconstructions of thermal history of sedimentary rocks discussed in previous section are used to calculate numerically the variations in degree of organic matter transformation. The latter is estimated due to calculation a vitrinite reflectance Ro (%) by using of the EASY%Ro kinetic spectrum of vitrinite (Table 3.3). We use this method for maturation assessment for the rocks of all ages including Riphean in spite of the absence vitrinite in the rocks of such age. The algorithm of calculation is discussed in Sect. 3.2.2.

6.3.1 Formation of Maturity Aureole in the Kuyumba-12 Sedimentary Section Under the Influence of Intrusions

Dotted lines in Fig. 6.3 show the depths of the Ro-isolines during burial history of the basin. Figure 6.3b and curve 3 in Fig. 6.7a demonstrates rather low maturity level reached by the rocks of the Kuyumba-12 section without consideration of intrusions. Such level contradicts the maturity assessment in the area (crosses in Fig. 6.7a).

According to the modeling in Fig. 6.7a carried out in three variants of the basin development, maximal maturation level reached at the base of the section is equaled to 0.665, 0.708 and 0.832 %. These values correspond to following variants of the basin evolution: without intrusions (curve 1 in Fig. 6.7), without intrusion in the basement, but with 6 intrusions in sedimentary section (curve 2 in Fig. 6.7) and with consideration of one intrusive into the basement and 6 intrusions into sedimentary section in the Lower Triassic (curve 3 in Fig. 6.7; see also Fig. 6.3). As it can be seen in Fig. 6.7, only the last variant from tree considered above is in agreement with estimations of maturity level in the present-day sedimentary section. This variant suggests one intrusion of 110 m thickness at depth from 4400 to 4510 m 251 My ago (from 3415 to 3525 m in the present-day section). Therefore, the basement intrusion locates now at the depth from 400 to 510 m beneath the basement surface.

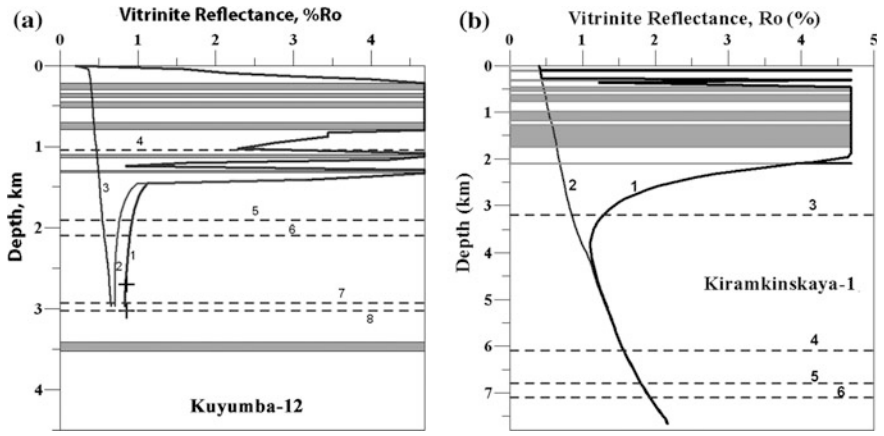

Fig. 6.7 Depth distribution of vitrinite reflectance, %Ro(z), in the present-day sedimentary sections of the Kuyumba-12 well (**a** six intrusions into sedimentary section and one into the basement) and Kiramkinskaya-1 well (**b** eight intrusions into sedimentary section). *1* Ro(z) with consideration of one intrusive into the basement and *6* intrusives into sedimentary section in (**a**) and *8* intrusives into sedimentary section in (**b**); *2* in (**a**)—Ro(z) without consideration of intrusive into the basement, but with consideration of *6* intrusives into sedimentary section in the Lower Triassic; *3* in (**a**) and *2* in (**b**)—Ro(z) without consideration of intrusive activity (see Fig. 6.3); *Light gray strips*—intrusions; *4–8* in (**a**)—probable source formations of age of 519, 532, 541, 1420 and 1460 My, correspondingly; *3–6* in (**b**)— probable source formations of age of 473, 541, 560, 1334 My, correspondingly. Crosses in (**a**)—laboratory assessments of maturation level in the section

Table 6.2 shows the locations of six intrusions in sedimentary section of the basin and one intrusion in the basement (probable intrusion) for several times beginning with the time of intrusions (251 My ago) and finishing with the present time (t = 0.00). This Table gives an opportunity to show the changes in location of intrusions as results of the erosion periods of amplitudes 300 (252–175 My ago), 200 (175–18.2 My ago) and 500 (18.2–1.81 My ago) m, and also the sedimentation period in the Quaternary (Table 6.1; Fig. 6.3). Table 6.2 helps to compare intrusion locations in sedimentary section with thermal histories of the layers in Fig. 6.3 at different times of the basin development.

The thermal effect of latent heat derived as a consequence of melting or solidification of peridotite or basaltic rocks is considered in the enthalpy approach following the Sect. 1.1.3. It is suggested that all sills have intruded instantaneously and simultaneously 251 million years ago. In the GALO system, the effect of the intrusions on the temperature and Ro distributions is computed in three steps. At the first step, the program SED2 in the first propagating calculates and writes to the file the distributions of T(z), Ro(z), φ(z), KT(z), A(z) (temperature, vitrinite reflectance, porosity, heat conductivity, heat generation) for the time just before the intrusions (for t = 251 My ago). At the second step, the program SED23 corrects these distributions taking into consideration the instantaneous basaltic intrusions and their

Table 6.2 Locations of the intrusions in the post-intrusion burial history of the basin at the Kuyumba-12 area

N	1	2	3	4	5	6	7	Z sed
ΔZ (m)	80	48	78	90	40	25	110	
t (My)	Zroof–Zbase (m)							
251	1203–1283	1332–1380	1427–1505	1685–1775	2085–2125	2285–2310	4400–4510	4006
175	903–983	1032–1080	1127–1205	1385–1475	1785–1825	1985–2010	4100–4210	3706
18.2	703–783	832–880	927–1005	1185–1275	1585–1625	1785–1810	3900–4010	3506
1.81	203–283	332–380	427–505	685–775	1085–1125	1285–1310	3400–3510	3006
0.00	218–298	347–395	442–520	700–790	1100–1140	1300–1325	3415–3525	3021

Remarks N intrusion's number; Δ*Z* intrusion thickness (in m); *t* geological time (in My); *Z sed* depth of the base of sedimentary cover; *Zroof*, *Zbase* depth of the roof and the base of the intrusion (in m). t = 0.00 is present-day section

subsequent cooling during about 1 million years. These computations use detailed time step, especially for starting time of intrusion cooling (from 1 day to 1 year) and small depth steps, dz, (0.2–0.5 m in vicinity of intrusions). The program SED23 writes to the special file the distributions T(z) and Ro(z), which were obtained after 1 million years of intrusions cooling. The distributions are used as the initial distributions of these parameters at the third step of our calculations by the program SED2 (in its second propagating), to reconstruct the thermal and maturation history for post intrusion time (from 250 My to present time). The Ro-distributions in Fig. 6.7 are the results of such calculations.

Figures 6.8 and 6.9 illustrate the work of the SED23 program, demonstrating evolution of the T(z) and Ro(z) distributions vs. depth during intrusions cooling. Figure 6.8 shows that significant transformation of thermal field takes place after 5 years of intrusions cooling. Total smoothing of temperature disturbance due to

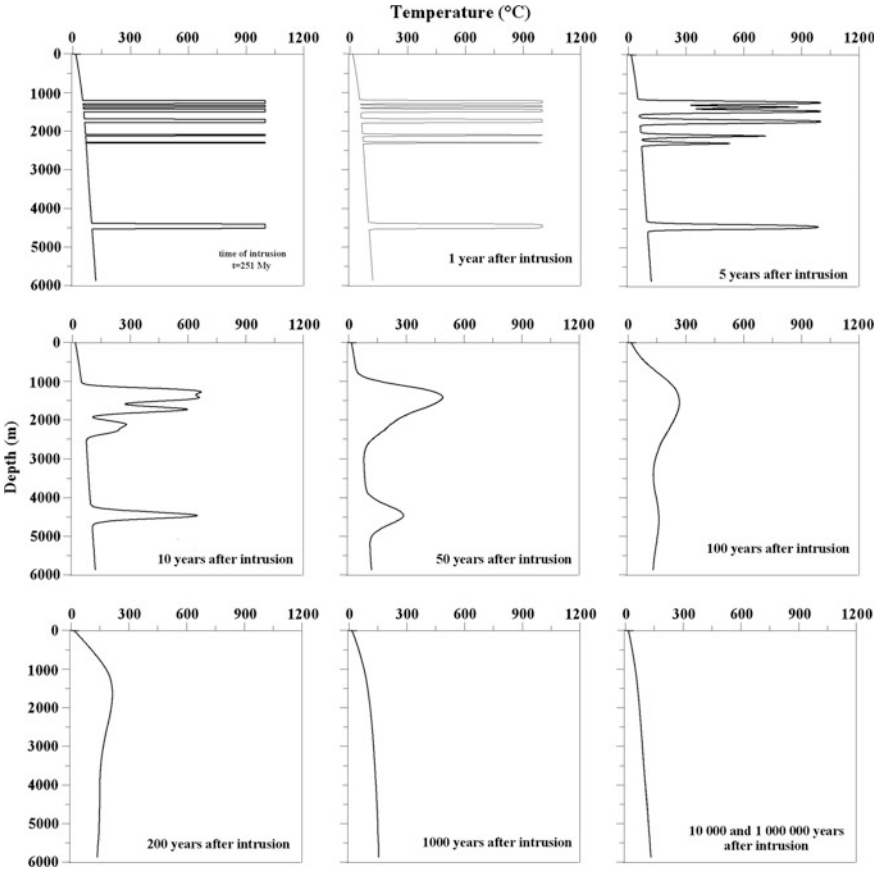

Fig. 6.8 Temperature distributions in upper 6 km of the section for different times of intrusions cooling

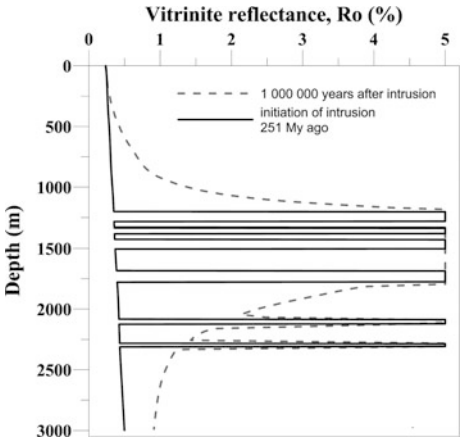

Fig. 6.9 Calculated depth-distribution of Ro in sedimentary section of the Kuyumba-12 well, resulted from 6 intrusions into sedimentary section and one probable intrusion in the basement. The distributions of calculated %R(z) are shown in the Figure for the 0 and 1 million years after instantaneous intrusions 251 My ago. Emphasize that the position of the intrusions is given at the time 250–251 million years ago

intrusions took place after 1000 years of cooling—the distribution T(z) for cooling time 10,000 years does not differ practically from the one for 1 million years of cooling (Fig. 6.8).

Figure 6.9 shows the situation at 251 and 250 My ago. To the present time, the corresponding sedimentary section is reduced by erosion of total amplitude about of 1 km. Therefore, the rocks located in modern section at depth below 1340 m belong to oil-generating rocks according to their maturation characteristics. But it is known that the model of instantaneous intrusion overstates its thermal effect (see next section of the chapter). Then, the rocks located between the intrusions at depth from about 1170–1270 m, which belong to overmature rocks according to the modeling in the frame of the model of instantaneous intrusion, could in practice also belong to oil-generating rocks.

6.3.2 Formation of Maturity Aureole in the Kiramkinskaya-1 Sedimentary Section Under the Influence of Intrusions

The considered area of the Kureiskaya depression has rather thick sedimentary section: present-day depth of the basement surface reaches here 7,760 m. Then, the temperatures and maturation level of organic matter in the Riphean rocks are considerably high (Figs. 6.3c and 6.7b). Intensive erosion of amplitude 2000 m in

the Neoproterozoic Era, intensive basin subsidence in the Cambrian and erosion in the Triassic—Jurassic (amplitude 300 m), the Jurassic—Miocene (200 m) and the most intensive erosion in the last 20 My (of estimated amplitude 500 m) are the main features of the basin burial history in the Kiramkinskaya area. The Lower Riphean rocks in the Upper Permian have reached a maximal depth of about 8250 m (Fig. 6.3c). Dotted lines in Fig. 6.3c demonstrate the depths of the Ro-isolines during burial history of the basin without intrusions. The maturity distribution with depth becomes very complex after emplacement of eight intrusions (Fig. 6.7b). That is why the location of the %Ro-isolines is shown in Fig. 6.3c in the variant without the intrusion action. Figure 6.3c demonstrates rather high maturity level reached by the Riphean rocks even in variant without consideration of intrusions (maximal Ro is 2.74 % at the base of present-day sedimentary section (z = 7760 m), suggesting that the Riphean rocks locates within the condensate and dry gas "windows". Eight intrusions of age of 251 My ago locates at different depths in upper 2100 m of present-day sedimentary section (Fig. 6.7b): (1) 2095–2105 (10 m), (2) 1275–1735 (460 m), (3) 980–1180 (200 m), (4) 630–760 (130 m), (5) 460–540 (80 m), (6) 315–319 (4 m), (7) 304–306 (2 m) and (8) 104–109 m (5 m) (Fig. 6.10). The heating from intrusions ensure very high maturity level of organic matter of host rocks in vicinity of the intrusions (Fig. 6.7b).

Figure 6.10b demonstrates that the intrusions into sedimentary section led to considerable enhance of organic matter maturation up to depth of 4000 m (that is 2000 m under the intrusion complex). Evolution of rock temperature in vicinity of the intrusion during different times of its cooling (up to 1 My) is shown in Fig. 6.10a. The instantaneous emplacement of igneous intrusion resulted in formation of rather wide maturity aureole up to depth about 4000 m. The rocks at the depth from 400 to 2500 m are characterized by overmature organic matter (Ro > 2.5–3.0 %; Figs. 6.7b and 6.10b).

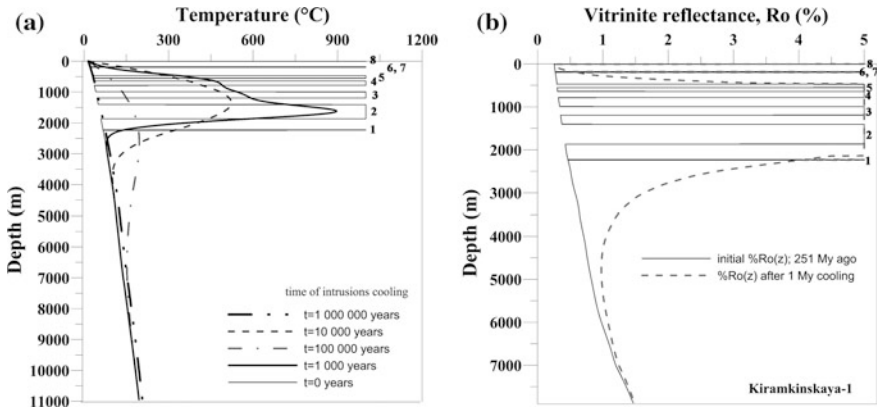

Fig. 6.10 Temperature (**a**) and vitrinite reflectance (**b**) distributions versus depth in the upper section of the Kiramkinskaya-1 area for different times of intrusion cooling. 1–8 numbers of 8 dolerite sills (see text) of different thicknesses of temperature 1000 °C which had intruded instantaneously into the opper 2000 m of at the time t = 0 (251 My ago)

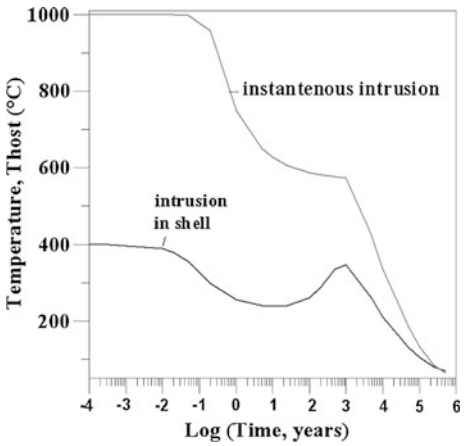

Fig. 6.11 Variations in temperature of host rocks at contact with intrusion in depending on the time of the intrusion cooling. *Instantaneous intrusion*—the model of instantaneous intrusion of dolerite sill of thickness of 460 m at 251 My ago with temperature 1000 °C and its cooling during 1 My. *Intrusion in shell*—the intrusion was formed during 7 days with steady rate of spreading $\Delta Z/\Delta t$ = 460 m/7 days. Temperature at sill axis is increasing linearly from T = 400 °C to 1000 °C during the first 5 days and was steady during next 2 days (up to time t = 7 days). Then the intrusion is cooling during all the rest of time 7 days < t $\leq$ 1,000,000 years

The traditional model of instantaneous intrusion, considered above, over-estimates significantly the scale of its thermal influence. Indeed, the model suggests, that intrusion changes considerably maturity of host rocks up to a distance 1–1.5 thickness of the intrusion and that maximal temperature of host rocks adjoined to the intrusion margin is equaled to the one of melt.

Section 7.1 (see below) says that numerous geological data indicates a more local thermal effect of intrusions. Figure 6.11 presents the results of modeling in the more adequate model "Intrusion in shell". In this model, the temperature of the rocks at the contact of host and intrusive rocks never exceeds 400 °C. A comparison between maturity aureoles computed in the "instantaneous" and "shell" models is considered in Sect. 7.2 of the next chapter. Due to the lack of data on measurements of the degree of maturity of organic matter in the Kiramkinskaya area, below we will discuss only the simulation results under a model of instantaneous intrusion. Just to say that the maturation aureoles calculated in the model of "intrusion in shell" are more narrow by 400–500 m, than the aureoles in the model of instantaneous intrusion (see below in Sect. 7.2). In particularly, the Vendian rocks, located at depth of 3200 m in the present-day section, occur out off zone of the intrusion's influence in distinct of the model of instantaneous intrusion. That is why, the results, received in the latter model and discussed below must be considered as the maximal estimations of maturation level of organic matter. They can be decreased by more detailed analysis of intrusions formation. The Fig. 6.12

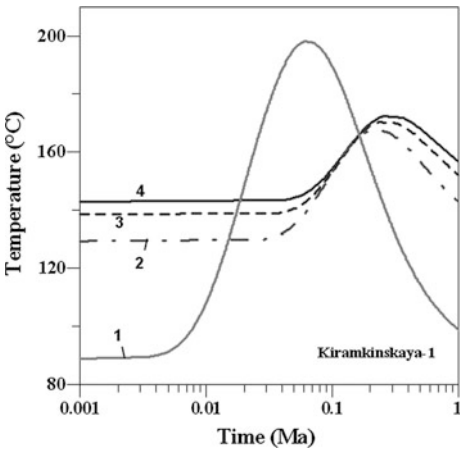

Fig. 6.12 Increase in rock temperature of the probable source formations as result of eight instantaneous intrusions 251 My ago and their cooling during 1 million year. Formation's age: 1 − t = 473 My; 2 − t = 541 My; 3 − t = 560 My; 4 − t = 1334 My

illustrates the increase in rock temperature of the probable source formations in the Kiramkinskaya-1 area as the result of thermal effect from eight instantaneous intrusions 251 My ago and their cooling during 1 million year. An influence of intrusive complex is rather moderate for the Riphean and Vendian rocks, but it is considerable for the Silurian formation (Fig. 6.12; Table 6.4).

6.4 Estimation of Hydrocarbon Generation in Sedimentary Sections with Intrusions

In our computations, there are used the kinetic parameters for reactions of primary and secondary creaking of standard kerogenes of types I, II and III, published in the papers of the Paris Oil Institute and the Lavmore Laboratory [11–17]. In this section, the results of calculations in the three component system (oil, gas, coke) are presented. Calculation algorithms are discussed in detail in [18]. The main results of modeling of hydrocarbon generation are shown in Table 6.3 for the Kuyumba-12 well and Table 6.4 for the Kiramkinskaya-1 well.

The first Lower Riphean (Lower Calymmian) formation of thickness about of 93 m in the Kuyumba area is presented by clay shale. Organic matter of this formation is presented by marine kerogene of type II with initial potential of HC generation Hi = 627 mg HC/g Corg [11]. Modern TOC is about 1 % [1, 2]. In the modeling, this value corresponds to initial TOC = 1.32 % (Tables 6.3). The formation located enough far from the intrusions into sedimentary cover and experienced mainly thermal influence of the intrusion into the basement (Figs. 6.7, 6.8 and 6.9). As result, the OM maturation level in the rocks reaches at present time the value of Ro = 0.831 %. This maturation level for kerogen of type II corresponds to rather intensive liquid hydrocarbon generation and ensures a realization of about 50 % of initial hydrocarbon potential of the formation (Fig. 6.13; Table 6.3). It can be noted

Table 6.3 Calculated values of maturation levet (effective %Ro), temperature and realization of hydrocarbon potential for the probably source rocks in the present-day sedimentary sections of the Kuyumba-12 well in the Kamo arch

T	Z	T	Ro	Hi	Ht	Ho	Hg	t1	Texp	t2
My	M	°C	%	Mg HC/g Corg				Million years ago		
1460	3021	51.1	0.831	627	302	292	9.8	479	250.98	–
				Corg = 1 % Corg (init) = 1.32 %						
1420	2928	49.2	0.833	770	323	316	6.8	470	250.98	–
				Corg = 4.7 % Corg(init) = 6.04 %						
541	2092	38.2	0.900	702	464	450	14.2	2579	250.97	–
				Corg = 2.1 % Corg(init) = 3.2 %						
532	1911	34.3	0.929	268.5	204	158	46.3	251	(250.96)	–
				Corg = 0.55 % Corg(init) = 1.11 %						
519	1040	21.0	2.241	377	377	0.00019	221	251	(250.97)	–
				Corg = 0.9 % Corg(init) = 2.17 %						

Notes t formation age (My). *z* depth (km). *T* calculated temperature in °C. *Ro* calculated value of vitrinite reflectance (in %) (*z*, *T*, *Ro* in the present-day section of the basin, t = 0)). *Hi* initial potential of HC generation by formation rock; *Ht* total HC generation, *Ho* oil generation and *Hg* gas generation (in mg HC/g Corg). *t1*, *t2* the enter and output times of the rock of the "oil windows" (0.50 % $\leq$ Ro $\leq$ 1.30 %); *texp* time of expulsion threshold for liquid HC, determined by the time of 20 % filling of porous volume of the source rocks by the generated liquid hydrocarbons [15]. The values in brackets corresponds to determination of texp by the time when generation of liquid hydrocarbons reach 150 mg HC/gTOC [11]

Table 6.4 Calculated values of maturation level (effective %Ro), temperature and realization of hydrocarbon potential for the probably source rocks in the present-day sedimentary sections of the Kiramkinskaya-1 well in the Kureiska Basin (Results were obtained with consideration of thermal effect from 8 instantanenous intrusions into sedimentary section 251 My ago.)

T	Z	T	Ro	Hi	Ht	Ho	Hg	t1	Texp	t2
My	M	°C	%	Mg HC/g Corg				Million years ago		
1334	7100	119.8	1.871 (1.855)	440	434 (434)	0.0187 (0.0443)	216 (216)	505	441 (441)	250.6 (244.5)
				Corg = 1.7 % Corg (init) = 2.61 %						
560	6800	114.1	1.763 (1.746)	470	462 (462)	2.44 (3.99).	229 (228)	497	428 (428)	241.5 (239)
				Corg = 0.7 % Corg(init) = 1.12 %						
541	6100	103.4	1.543 (1.529)	470	459 (459)	102 (116)	181 (175)	482	399 (399)	226 (220)
				Corg = 0.6 % Corg(init) = 0.95 %						
473	3200	58.0	1.314 (0.841)	430	416 (274)	311 (266)	63.4 (8)	374	250.97 (222.5)	250.9 (–)
				Corg = 0.5 % Corg(init) = 0.64 %						

Notes t formation age (My). *z* depth (km). *T* calculated temperature in °C. *Ro* calculated value of vitrinite reflectance (in %) (*z*, *T*, *Ro* in the present-day section of the basin, t = 0)) The meaning of the parameters Hi, Ht, Ho, Hg, t1, t2, and texp see in Notes to Table 6.3. Values in brackets—calculations without intrusions thermal influence

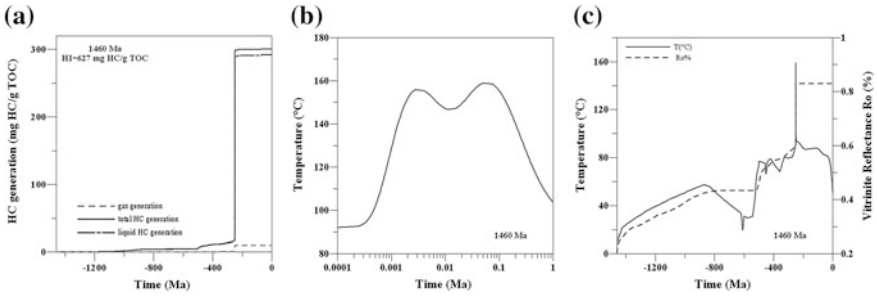

Fig. 6.13 Generation of hydrocarbons (**a**) and change in temperature (**b**) and maturation (**c**) in burial history of the Lower Riphean formation (Lower Calymmian; age t = 1460 My; Kuyumba-12 well). The figure (**b**) shows temperature history of the formation during first million years of intrusions cooling. *Solid line* in figure (**b**) demonstrates the same history during whole burial history of the formation

that generation of oil by the formation rocks remained rather insignificant up to the time of intrusions (251 My ago). The following heating by intrusions led to considerable increase of temperature and maturation (Figs. 6.13b, c) that resulted in significant enhance of oil generation (Fig. 6.13a). Therefore, the main oil generation by the formation's rocks occurred due to intrusion into basement 251 My ago.

The probable source formation of the Lower Riphean (base of Estasian of age 1420 My) in the Kuyumba-12 well is presented by dolomite (80 %) and clays (20 %; Table 6.1). Organic matter of this formation is presented by the mixture 50.5 % kerogene of type I (HI = 911 mg HC/g TOC) and 49.5 % kerogene of type II (HI = 627 mg HC/g TOC) with summary initial potential HI = 770 mg HC/g Corg [1, 2]. Modern TOC is rather high (about 4.7 %). It corresponds to initial TOC = 6.04 % (Table 6.3). This formation locates slightly closly to the sedimentary intrusions complex, than the previous formation, but still enough far from it. Consequently it also experienced mainly the thermal influence of the intrusion into the basement although an effect of sedimentary intrusions reflect in slightly greater Ro values (0.833 % instead 0.831 % in the previous formation; Fig. 6.14c; Table 6.3). The value of Ro = 0.833 % corresponds again to rather intensive liquid

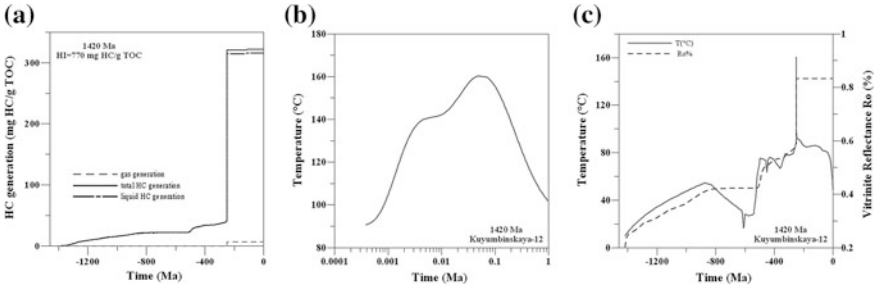

Fig. 6.14 Similar to Fig. 6.13, but for the Lower Estasian formation

hydrocarbon generation and ensures a realization of about 40 % of initial hydrocarbon potential of the formation (Fig. 6.14a; Table 6.3). As in earlier formation, the oil generating potential of the rocks in the formation remained rather insignificant up to the time of intrusions (251 My ago). The following heating by intrusions led to considerable increase of temperature and maturation (Fig. 6.14b, c) that resulted in significant enhance of oil generation (Fig. 6.14a). Therefore, the main oil generation by the formation's rocks occurred due to intrusions 251 My ago.

The probable source formation of the Middle Riphean (of age 1334 My) in the Kiramkinskaya-1 well has the organic matter presented by the kerogene of type II (HI = 627 mg HC/g TOC) normalized on the initial potential HI = 440 mg HC/g Corg;. Modern TOC in the formation is about 1.7 % [2] that corresponds to initial TOC = 2.61 % (Table 6.4). This formation locates relatively far from the intrusions complex (Figs. 6.7b and 6.10b) and influence of the complex on maturity is small (Table 6.4; Fig. 6.7b). The high maturation level leads to total degradation of liquid hydrocarbons due to secondary cracking and ensures a realization about 99 % of initial hydrocarbon potential of the formation (Fig. 6.15a; Table 6.4). The main oil generation by the formation's rocks occurred from the Devonian to Triassic. Participation of the intrusions in this process was very limited (Fig. 6.15, Table 6.4).

The probable source formation of the Vendian (Ediacaran; of age 560 My) in the Kiramkinskaya-1 well has the organic matter with kerogene of type II (HI = 627 mg HC/g TOC) normalized on the initial potential HI = 470 mg HC/g Corg [1]. Modern TOC in the formation is about 0.7 % [2] that corresponds to initial TOC = 1.12 % (Table 6.4). This formation locates relatively far from the intrusions complex (Figs. 6.7b and 6.10b) and influence of the complex on maturity is again small (Table 6.4; Fig. 6.7b). The high maturation level of organic matter in this formation also leads to almost complete degradation of liquid hydrocarbons due to secondary cracking and ensures a realization about 98 % of initial hydrocarbon

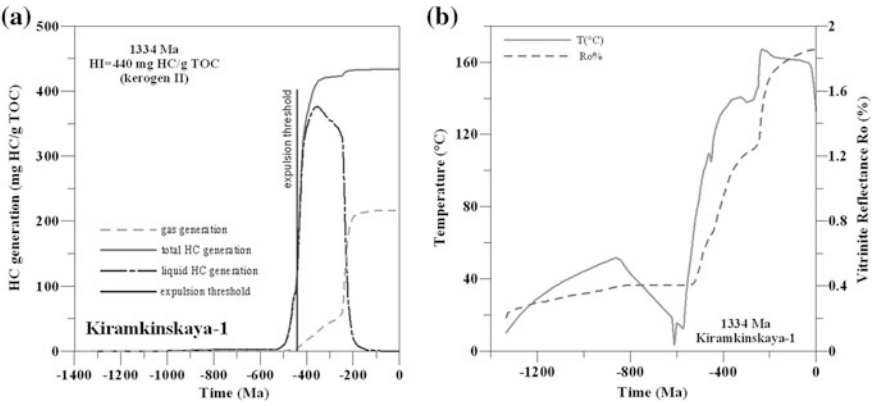

Fig. 6.15 Realization of potential of HC generation (**a**), temperature and OM maturation (**b**) in burial history of the Middle Riphean formation (t = 1334 My). Temperature history of the formation during first million years of intrusions cooling is shown by curve 4 in Fig. 6.12

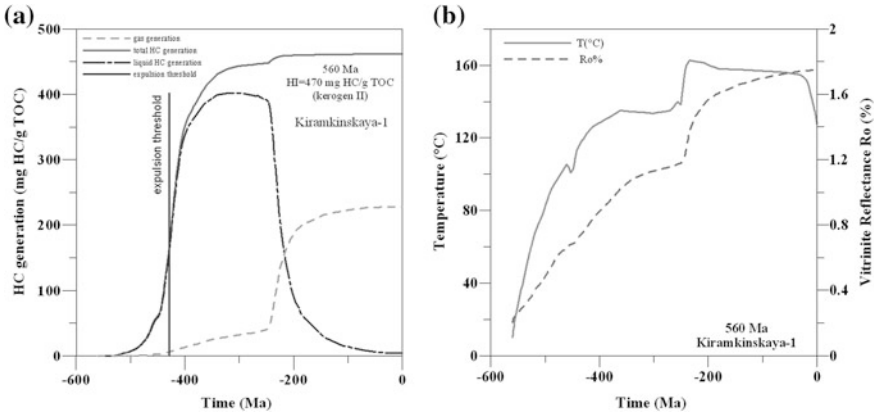

Fig. 6.16 Realization of potential of HC generation (**a**), temperature and OM maturation (**b**) in the burial history of the Vendian formation (t = 560 My). Temperature history of the formation during first million years of the intrusions cooling is shown by curve 3 in Fig. 6.12

potential (Fig. 6.16; Table 6.4). Here, the main oil generation occurred again from the Devonian to Triassic. Participation of the intrusions in this process was very limited (Fig. 6.16, Table 6.4).

The next probable source formation is the layer of the Lower Cambrian (of age 541 My). In the Kuyumba area, organic matter of this formation is characterized by the mixture 26.4 % kerogene of type I (HI = 911) and 73.6 % kerogene of type II (HI = 627) with summary initial potential Hi = 702 mg HC/g [1, 2]. Modern TOC is also rather high (about 2.1 % [1, 2]). It corresponded to initial TOC = 3.2 % (Table 6.3). The formation locates considerable closely to the sedimentary intrusions complex, than the previous formations of this area, and is characterized by greater Ro values (0.900 %; Fig. 6.17c; Table 6.3). This maturity level corresponds to intensive liquid hydrocarbon generation in the present time and ensures a realization of about 66 % of initial hydrocarbon potential of the formation (Fig. 6.17a, c; Table 6.3). As it can be seen from Fig. 6.17a, the oil generation remained here rather insignificant up

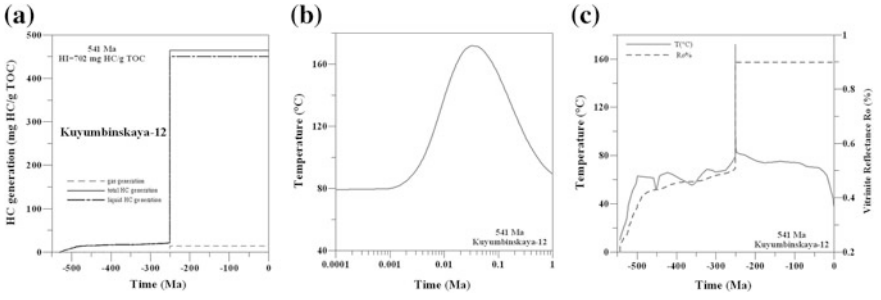

Fig. 6.17 Similar to Fig. 6.13, but for the Lower Cambrian formation of age 541 My

to the time of intrusions (251 My ago). The following heating by intrusions led to considerable increase of temperature and maturation (Figs. 6.17b, c) that resulted in significant enhance of oil generation (Fig. 6.17a). Therefore, the main oil generation by the formation's rocks occurred in the Kuyumba area again due to intrusions. In the Kiramkinskaya area of the Kureika Basin, organic matter of the Lower Cambrian formation is presented again by kerogene of type II (HI = 627 mg HC/g TOC) normalized on the initial potential HI = 470 mg HC/g Corg [1, 2]. Modern TOC in the formation is about 0.6 % that corresponds to initial TOC = 0.95 % (Table 6.4). This formation also locates relatively far from the intrusions complex (Figs. 6.7b and 6.10b) and influence of the complex on maturity is again small (Table 6.4; Fig. 6.7b). The relatively high maturation level of organic matter in this formation leads to degradation of considerable part of liquid hydrocarbons due to secondary cracking and ensures a realization about 97 % of initial hydrocarbon potential (Fig. 6.18; Table 6.4). Here, the main oil generation occurred from the Devonian to Triassic. Participation of the intrusions in this process similarly to previous formations of the area was very limited (Fig. 6.18, Table 6.4).

Organic matter of the Lower Cambrian formation of age 532 My is characterized in the Kuyumba area by the mixture 50 % kerogene of type II (HI = 377 mg HC/g TOC) and 50 % kerogene of type III (HI = 160) with summary initial potential Hi = 268.5 mg HC/g [1, 2]. Modern TOC is rather low (about 0.55 %). It corresponded to initial TOC = 1.11 % (Table 6.3). The formation experienced considerable thermal influence of the intrusion and reaches maturation of Ro = 0.929 % (Fig. 6.19c; Table 6.3). Such maturity level corresponds to intensive liquid hydrocarbon generation in the present time and ensures a realization of about 76 % of initial hydrocarbon potential (Fig. 6.19a; Table 6.3). As in the earlier formations, the main oil generation was due to intrusions 251 My ago.

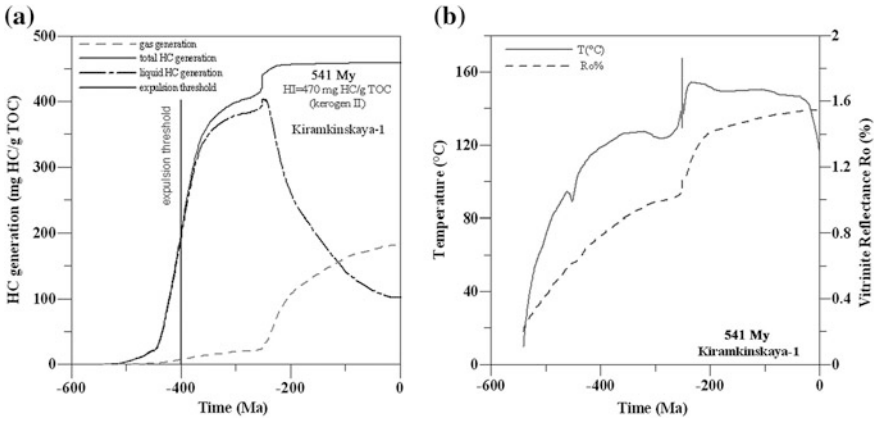

Fig. 6.18 Realization of potential of HC generation (**a**), temperature and OM maturation (**b**) in burial history of the Lower Cambrian formation (t = 541 My) in the Kureika Basin. Temperature history of the formation during first million years of intrusions cooling is shown by curve 2 in Fig. 6.12

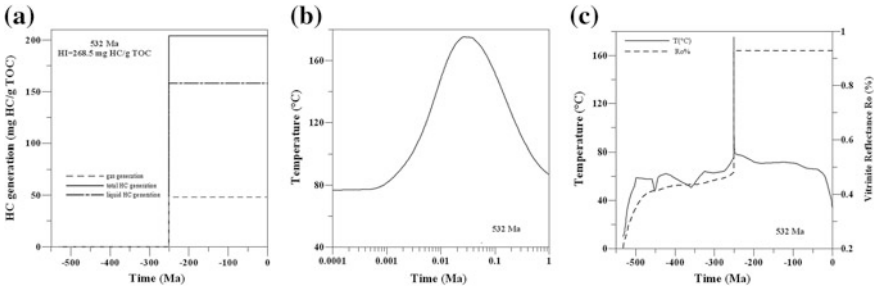

Fig. 6.19 Similar to Fig. 6.13, but for the Lower Cambrian formation (532 My)

Organic matter of the third probable source formation of the Lower Cambrian in the Kuyumba area of age 519 My is presented by kerogene of type II with initial potential Hi = 377 mg HC/g TOC. Modern TOC (about 0.9 % [1, 2]) corresponded to initial TOC = 2.17 % (Table 6.3). The formation most closely to the sedimentary intrusions complex from the other considered formations of the Lower Cambrian and maturity level of the formation organic matter reaches (Ro = 2.241 %; Fig. 6.20; Table 6.3). This Ro corresponds to dry gas generation when liquid hydrocarbons were destroyed quickly during intrusion period due to secondary cracking An initial hydrocarbon potential of the formation was realized totally (Fig. 6.20a; Table 6.3). As above, the oil generation by the rocks remained rather insignificant up to the time of intrusions (251 My ago). The following heating by intrusions led to total destruction of generated oil due to secondary cracking (Fig. 6.20a).

The Lower Ordovician formation in the Kiramkinskaya area of the Kureika Basin, located at depth of 3200 m in present-day section of the basin, experienced significant thermal influence of the intrusions (Figs. 6.7 and 6.12, Table 6.4). As result of subsidence and intrusions influence, the OM maturation level in the rocks reaches at present time (according to modeling) the maturation of Ro = 1.3143 % in variant with intrusions instead the value of 0.841 % in the variant without intrusions. Such maturation level leads to insignificant degradation of liquid hydrocarbons due to secondary cracking (compare Ho + Hg in Table 6.4 with Ht),

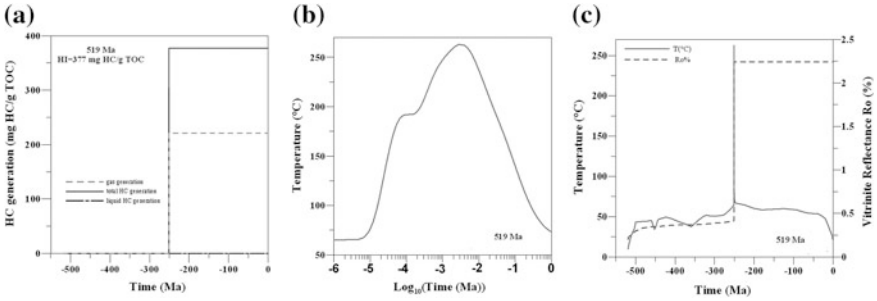

Fig. 6.20 Similar to Fig. 6.13, but for the Lower Cambrian formation (519 My)

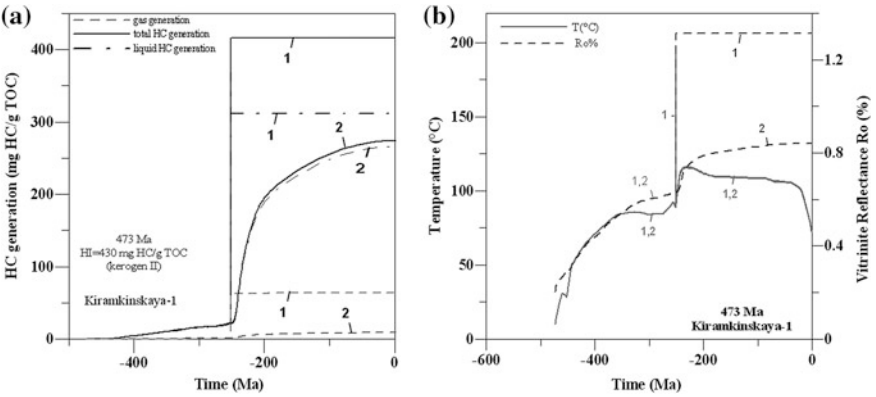

Fig. 6.21 Realization of potential of HC generation (**a**), temperature (*solid line*) and OM maturation (*dashed line*) (**b**); in burial history of the Lower Ordovician formation (t = 473 My). Temperature history of the formation during first million years of intrusions cooling is shown by curve 1 in Fig. 6.12. Number *1* marks the curves obtained in variant with consideration of heating from intrusions; number *2* marks the curves computed without effect from this heating

considerable oil generation and ensures a realization about 97 % of initial hydrocarbon potential of the formation (Fig. 6.21; Table 6.4). It is significant that considerable (but lesser) oil generation could take place in variant without intrusions too (Table 6.4; Fig. 6.21a). In our modeling the organic matter of the Lower Ordovician formation was presented again by marine kerogen of type II with HI = 627 mg HC/g TOC normalized by initial potential of hydrocarbon generation HI = 430 mg HC/g TOC [1, 2]. The present-day value TOC = 0.5 % corresponds in the modeling to initial TOC = 0.75 % (Table 6.4). And again the oil generating potential of the Lower Ordovician formation remains insignificant up to the intrusions (Fig. 6.21a).

6.5 Conclusion

The modeling of thermal regime and maturation history of sedimentary basin of the Siberian Platform conducted on the examples of two sedimentary sections containing six and eight intrusive bodies of the Lower Triassic age allow an estimation of thermal influence of the intrusive complex on the maturation history of organic matter in the host rocks of the basin and hydrocarbon generation by these rocks. The modeling demonstrates that this influence can be both significant and negligible depending on the size of the intrusion and the distance of the host rocks to the surface of the intrusive body. Evaluation of the thermal effect of intrusions was conducted in the framework of a model of instantaneous intrusions and can be considered as the evaluation of such effect to the maximum.

References

1. Frolov SV, Akhmanov G, Kozlova EV, Krylov OV, Sitar KA, Galushkin Y (2011) Riphean basins of the central and western Siberian Platform. Mar Pet Geol 28:906–920
2. Kontorovich AE, Surkov VS, Trofimuk AA (eds) (1981) Geology of oil and gas of the Siberian Platform. Nedra, Moscow (in Russian)
3. Sokolov BA, Egorov VA, Nakaryakov VD, Bitner AK, Zkukovin Y, Kuznetsov LL, Skorobogatikh PP, Zakharyan AZ (1992) Geological and geophysical conditions of formation of oil-and-gas bearing deposits in the ancient rocks of Eastern Siberia. Petroconsultants Australia, Sydney, Australia
4. Kontorovich AE, Izosimova AN, Kontorovich AA, Khabarov EM, Timoshina ID (1996) Geological structure and conditions of the formation of the giant Yurubcheno-Tokhoma zone of oil and gas accumulation in the Upper Proterozoic of the Siberian Platform. Geologiya i Geofizika 37(8):166–195 (in Russian)
5. Rodrigues FM, Villar HJ, Baudino R, Delpino D, Zencich S (2009) Modeling an atypical petroleum system: a case study of hydrocarbon generation, migration and accumulation related to igneous intrusions in the Neuquen Basin, Argentina. Mar Pet Geol 26:590–605
6. Duchkov AD, Lysak SV, Balobaev VT (1987) Heat flow of Siberia. Nauka, Novosibirsk (in Russian)
7. Frakes LA (1979) Climates throughout geological time. Elsevier, Amsterdam
8. Welte DH, Horsfield B, Baker DR (eds) (1997) Petroleum and basin evolution. Springer, Berlin
9. Velichko AA (1987) Thermal change of paleoclimate in the Mezo-Cenozoic by study of the East Europe. In: Velichko AA, Chaplyga AL (eds) The Earth climates in geological past, Moscow, Nauka, pp 5–43 (in Russian)
10. Velichko AA (1999) Climate and landscape variations during last 65 million years (Cenozoic from Paleocene to Holocene). Moscow, GEOS (in Russian)
11. Espitalie J, Ungerer P, Irvin I, Marquis E (1988) Primary cracking of kerogens. Experimenting and modelling C1, C2–C5, C6–C15 classes of hydrocarbons formed. Org Geochem 13 (4–6):893–899
12. Tissot BP, Pelet R, Ungerer P (1987) Thermal history of sedimentary basins, maturation indices, and kinetics of oil and gas generation. AAPG Bull 71(12):1445–1466
13. Ungerer P (1990) State of the art of research in kinetic modelling of oil formation and expulsion. Org Geochem 16(1–3):1–27
14. Ungerer P, Burrus I, Doligez B, Chenet P, Bessis F (1990) Basin evolution by integrated two-dimensional modelling of heat transfer, fluid flow, hydrocarbon generation, and migration. AAPG Bull 74(3):309–335
15. Ungerer P (1993) Modeling of petroleum generation and migration. In: Bordenave ML (ed) Applied petroleum geochemistry. Technip, Paris, pp 397–442
16. Burnham AK, Sweeney JJ (1989) A chemical kinetic model of vitrinite maturation and reflectance. Geochim Cosmochim Acta 53(10):2649–2657
17. Burnham AK, Braun RL (1990) Development of a detailed model of petroleum formation, destruction, and expulsion from lacustrine and marine source rocks. Org Geochem 16 (1–3):27–39
18. Makhous M, Galushkin Y (2005) Basin analysis and modeling of the burial, thermal and maturation histories in sedimentary basins. Editions TECHNIP, Paris

Chapter 7
Duration of the Intrusion Formation and Its Relation to the Size of Thermal and Maturity Aureoles of the Intrusion Bodies

Abstract Maturity aureole of the trap and sill complex considered in this chapter determines the depth of oil and gas windows and an ability of the underlying and host sedimentary rocks to generate hydrocarbons. Our study shows that a size of maturity aureoles of the single intrusions and trap complex decreases considerably with increase of duration of these complex is formation. So, the aureole size in for formation of the trap with total thickness of 1000 m underlain by clay complex reduces from 1150–1067 m for the trap formation during time interval 11.4 years and more shorter to less than 1 m for the traps formed during 1200 and more years under condition of steady rate of the trap formation. The modeling demonstrates that a maturation level of organic matter in sedimentary rocks under trap and within the host rocks of single intrusions can be rather moderate if the time span of formation of these structures (or formation of their single layers) was enough long. The size of maturity aureole of the trap complex formed during several stages can be close to the aureole of single trap layer with maximal thickness. Comparison of computed and measured values of vitrinite reflectance within the thermal aureole of some well-dated intrusions shows that traditional calculations of instantaneous intrusion considerably over-estimate temperatures and maturation of organic matter in the host rocks. Models which consider formation of the intrusive body over time (as distinct from instantaneous intrusion) and especially models of emplacement of the intrusive body in the shell of relatively cool magmatic rocks show better agreement between computed and observed data.

Keywords Formation of intrusions and traps · Temperature · Maturation · Vitrinite reflectance · Maturity aureole

Y. Galushkin, *Non-standard Problems in Basin Modelling*,
DOI 10.1007/978-3-319-33882-8_7

7.1 Difference Between Maturity and Thermal Aureoles in the Models of Instantaneous and Finite Time Intrusions on the Examples of the Well Dated Intrusions

7.1.1 Model with Finite Times of Intrusion Formation

The thermal effects of igneous intrusions into sedimentary blanket of basin have been studied numerically in many investigations [1–4], including the papers [5, 6]. All of the above works except the last two calculate the heat transfer from igneous body in the model of instantaneous intrusion. This model suggests a considerable increase in maturity of host rocks at the distance of 1–1.5 thickness of the intrusion. But detailed study of sills and dykes in the East Siberia Platform indicate that the mean size of a thermal maturity aureole for isolated intrusion is nearly 30–50 % of its thickness, and exceeds 100 % very seldom [7–9]. It is confirmed also by study of coal transformation due to heating from intrusion [10]. As whole, an estimations of the catagenesis and petroleum potential of organic matter in the Riphean and Vendian deposits of the Baikit and Katanga petroliferous areas in the Siberia Platform argue in favour of leading role of regional thermal history in organic matter maturation, whereas the contribution of heating by local sills to the maturation is recognized as rather limited [7, 11, 12]. A limitation of thermal influence by 50–90 % of the intrusion thickness is confirmed by geochemical and petrological studies of rock in vicinity of dikes and sills from many regions of the world [4, 13–15]. In addition, petrological evidences indicate that the temperatures of host rock near contact with magmatic rocks are often less than the temperature of initial liquid magma by 300–500 °C and more. This fact, together with the short duration of heat transfer processes, help to explain an absence of effective rock metamorphism in the contact zone of many dikes and sills [2, 11, 13–16].

Limited size of the thermal aureole of intrusions and the relative low temperatures and metamorphism level of host rocks near the contact zone of intrusion can be explained in the model of intrusion with finite time of sill emplacement (Fig. 7.1), differed from the traditional model of instantaneous intrusion [5, 6]. The point is that an emplacement and cooling of intrusive bodies are essentially an instantaneous events on a geological time scale. However, the duration of magma body formation within the host rocks can play a considerable role in formation of the size of the temperature and maturity aureole near an intrusion [17]. In order to study this problem, we modified the GALO package of computer programs by addition of an algorithm that allows us to analyze the models with finite times of intrusion formation. This algorithm was used previously for the study of accretion of the oceanic crust in axial zones of mid-Oceanic Ridges [18]. According to this approach, the process of sill formation can be described as a sequence of magmatic body accretions by two thin layers of magma rock of width Δz from the sill axis during short time interval, Δt (Fig. 7.1). The host and sill rocks accrued during previous times are moved aside. The temperatures in nodes, calculated to this time,

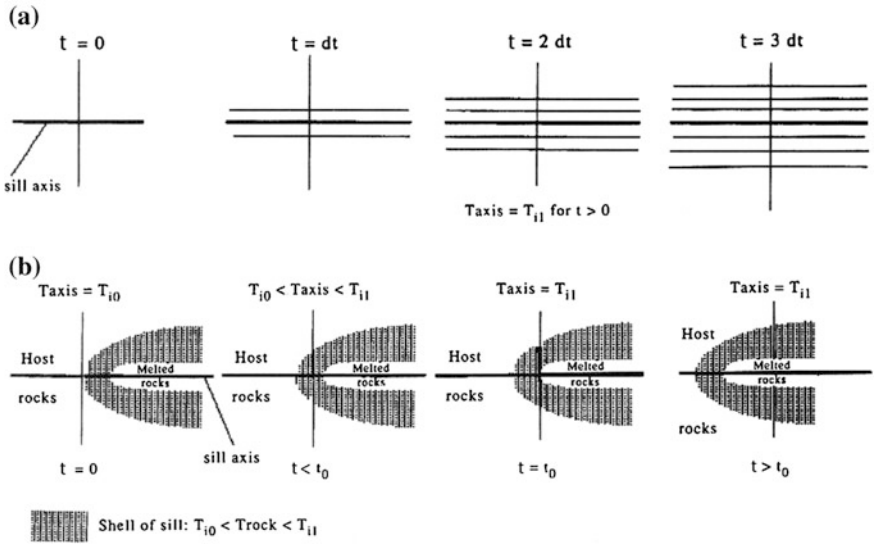

Fig. 7.1 Model of sill intrusion with finite time of emplacement (as distinct from the model of instantaneous intrusions) (according [5] with little changes). **a** model when a temperature at the sill axis (T_{axis}) is equal to the temperature of liquid melt, T_{i1}, during all the time of sill accretion ($0 \leq t \leq t_{int}$). **b** model of intrusion of sill in the shell of cold magmatic rock: temperature at the sill axis in section marked by vertical line increases from $T = T_{i0}$ to $T = T_{i1}$ during time $0 < t < t_0$ in the first stage of sill propagation and it remains to be equal the temperature of liquid melt, T_{i1}, at $t_0 < t \leq t_{int}$ in second stage of the sill propagation. T_{io} is the rock temperature at initial contact of host rocks with the shell of intrusion. Heavy *horizontal lines* in the figure present the sill axis. *Vertical solid lines* show the location of considered section of the sill in different times of sill propagating

move together with their nodes. The temperature at the axis is set to a known value. The temperature profile derived by this method is considered to be the initial temperature distribution required for solution of the heat transfer equation. This information is needed to obtain a measure of thermal relaxation of the temperature regime during time Δt. In the modeling, the temperature at the sill axis, T_{axis}, can be taken to be equal to the initial temperature of liquid melt at the axis (T_{i1}, Fig. 7.1a) or it can increase during some time from some initial temperature, T_{i0} to the temperature of liquid melt, T_{i1} if the model of intrusion in the shell is analyzed (Fig. 7.1b). In the latter, host rocks do not contact with melt matter of the intrusion. They are in contact only with the shell rocks. The temperature of the latter is by 200–400 °C lower than the melt temperature [5].

7.1.2 The 118 m Thick Sill from Midland Valley, Scotland

It is necessary to note that in our analysis of the 118 m thick intrusions of Raymond and Murchison [14], we excluded the Ro data showing a decrease of Ro values near

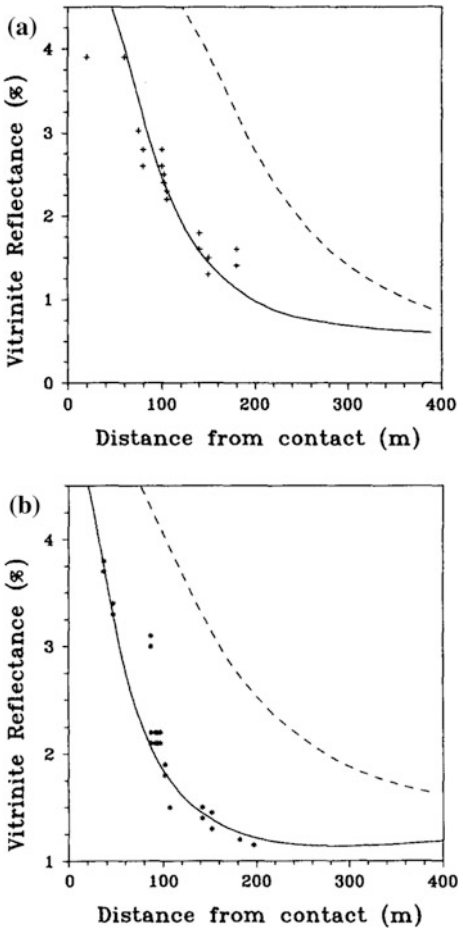

Fig. 7.2 Maturity aureoles above (**a**) and below (**b**) the 118 m-sill from Midland Valley (Scotland) computed in the model of Fig. 7.1b (intrusion in the shell) with a good agreement between observed (*free symbols* [14]) and calculated (*solid lines*) values of %Ro. The temperature at the sill axis increases from 300 to 1100 °C over the first 30 h of the sill formation (propagation). The total time of sill formation is 44 h. Thermal effects of hydrothermal convection above the sill with $Nu = 2.0$ and dehydration reactions are considered in modeling (see [5]). *Dashed lines* demonstrate the corresponding results in the model of instantaneous intrusion

intrusions. The usual decrease of Ro values near intrusions is not a real decrease of maturity, but is related to disturbance of the molecular structure of vitrinite at very high temperatures [13–15].

Figure 7.2 demonstrates application of the model with finite times of intrusion formation in Fig. 7.1b to estimation of maturity aureole of the 118 m thick sill from Midland Valley in Scotland [5]. It is a rather thick sill located at depth from 410 to 528 m in present-day sedimentary section constructed on the base of data from the Rashienhill borehole of central Midland Valley of Scotland [14]. Figure 7.2 shows the Ro profile, calculated for intrusion of the 118 m sill into shales with background values of Ro (before intrusion) ranging from Ro = 0.60 % near the basin surface to Ro = 1.37 % at the depth of 1030 m. The above Ro values are in accordance with the data in [14]. The shell model Fig. 1b describes rather well the observed vitrinite reflectance data in Fig. 7.2a, b. It suggests an increase of axis temperature from 300 to 1100 °C for 30 h, total time of the sill formation about 44 h and hydrothermal

activity above sill with effective Nusselt number Nu = 2.0 above intrusion and Nu = 1 (without hydrothermal activity) below the sill (see [5]). The hydrothermal convection is taken into consideration within the framework of approximate approach when the normal heat conductivity of host rock is increased by Nu times in the corresponding depth and temperature intervals. In the example of Fig. 7.2, hydrothermal convection above the sill with effective Nusselt number Nu = 2.0 helped to explain more wide maturity aureole above the sill in comparison of it below the sill [5]. The effective Nusselt number, Nu, means usually a ratio of total heat flow (sum of convective and conductive heat flows) to the conductive one. It was assumed in the computations that hydrothermal heat transfer was effective only within the temperature interval $100° \leq T \leq 725$ °C. Here, the temperature T = 725 °C was considered as the upper temperature boundary for penetration of hydrothermal convection into host rocks. (upper temperature limit of close of micro-fractures [5, 19]). The following values of parameters were taken in the calculations: temperature of intrusion T_{i1} = 1100 °C, solidus temperature Ts = 950 °C, liquidus temperature Tl = 1150 °C, latent heat of fusion L = 90 cal/g (see [5]). Figures 7.2 a, b demonstrate that the thermal aureoles calculated in the shell model of Fig. 7.1b differ significantly from the results obtained for the same thermal parameters of rocks and the same characteristic hydrothermal activity and dehydration reactions in model of instantaneous intrusion (dashed lines). This calculation also confirms a relatively small contribution of dehydration reactions in the thermal aureole: they decrease the aureole size no more than 10 m [5].

7.1.3 *Example of the 400 m sill in the Kiramkinskaya Well of the Kureika Basin in Siberia Platform*

Unfortunately, we have not measured values of organic matter maturation in the Kiramkinskaya area and this has restricted us in construction more accurate model. We has created an approximate model of formation of the 460 m sill in sedimentary section of Kiramkinskayu well 251 My ago (see Chap. 6) on the base of parameters of the "shell" model of the 118 m-sill from Midland Valley (Scotland) considered in previous Sect. 7.1.2. The approximate model of the intrusion in the Kiramkinskaya well section gives an opportunity to estimate possible errors in determination of maturity aureoles obtained in the model of instantaneous intrusion. The model "Intrusion in shell" was applied to formation of the sill of thickness 460 m, located at depth from 1275 to 1725 m in present-day section of Kiramkinskaya-1 well (Figs. 6.2, 6.3c, 6.7b and 6.10). The intrusion was suggested to form during 7 days with steady rate $\Delta Z/\Delta t$ = 460 m/7 days. Temperature of rocks at sill axis was increasing during the sill formation: from T = 400–1000 °C during the first 5 days and was steady during next 2 days (up to time t = 7 days), when the formation of the intrusion body was completed. The intrusion was cooled during all time 7 days $< t \leq$ 1,000,000 years. As mentioned above, these parameters of the sill formation are not based on the

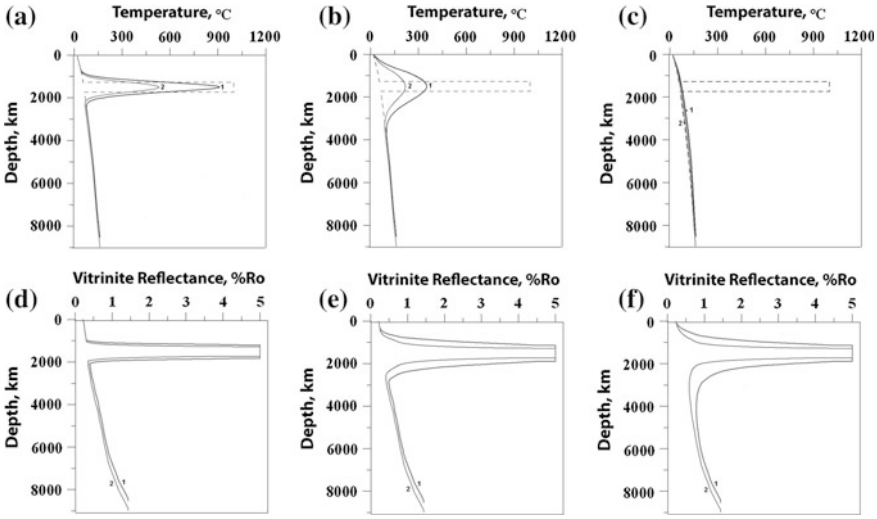

Fig. 7.3 A comparison between temperature and maturation aureoles of the 460 m sill intruded into the Kiramkinskaya-1 sedimentary section (the Siberia Platform), computed in the "instantaneous" (curves 1) and "shell" (curves 2) models of sill emplacement. The results are shown for different times of the sill cooling, t: **a, d** t = 1,000 years, **b, e** t = 10,000 years, **c, f** t = 500,000 years

assessment of maturation level of organic matter in the host rocks of the sill. They were estimated approximately by applying the similarity law to two sills—the first in Fig. 7.2 and the second—in Fig. 6.11 and considered here.

The special program allows a computation of heat transfer within the widening intrusion and in host rocks. It takes into account an actual lithological section of the sedimentary blanket of the basin (Fig. 6.3c). The Figs. 7.3 demonstrate a comparison between temperature and maturation aureoles computed in the "instantaneous" (curves 1) and "shell" (curves 2) models on the example of the 460 m sill intruded into the Kiramkinskaya-1 sedimentary section. Comparison is shown for the times of the sill cooling equaled to 1,000, 10,000, and 500,000 years. Figure 6.11 demonstrates that the temperatures of the host rocks at the contact with the sill boundary computed in the "shell" model do not exceed 400 °C whereas they reach 1000 °C in the model of instantaneous intrusion. Accordingly, the maturation aureoles calculated in the model of "intrusion in shell" are more narrow by 400–500 m, than the aureoles in the model of instantaneous intrusion. In particularly, the model of intrusion in shell gives the distance of maturation with Ro = 1.00 % (from sill surface) by 1 km lesser than the one in the model of instantaneous intrusion. In the model of intrusion in shell, the Vendian rocks, located at depth of 3,200 m in the present-day section (Fig. 6.3c), occur out off zone of the intrusion's influence in distinct of the model of instantaneous intrusion (Figs. 6.7b, 6.10). Then the results,

received in the latter model must be considered as the maximal estimations of maturation level of organic matter that can be decreased by more detailed analysis of intrusions formation.

7.2 Thermal and Maturity Aureoles in Subtrappean Sedimentary Complex—Dependence on the Time of the Trap Formation

The results shown in Figs. 7.2, 6.11 and 7.3 demonstrate clearly that the size of maturation aureole of intrusion depends strongly on the time of its formation. In this section, it will be shown that similar situation takes place also in sediments underlying effusive part of the traps. To analyze thermal and maturity histories of sedimentary rocks in the subtrappean sedimentary complexes, the program for analysis of intrusions in shell (Fig. 7.1a) was modified to the TRAP computer program. The latter allows the calculation of the temperature and vitrinite reflectance distributions with depth, at any time before, during and after the trap formation. The program allows the computation of heat transfer within the widening effusive or intrusive bodies and in the host rocks also. It is important that our calculations take into account the actual lithological composition of the rocks in the sedimentary basin under analysis.

The modeling in this section demonstrates that a maturation level of organic matter in sedimentary rocks under the trap depends strongly on the duration of the trap formation. It can be rather moderate if the time span of the trap formation, or formation of its single layer, was sufficiently long.

7.2.1 The Trap's Provinces in the World

Trap's provinces are widely spread in the world. Many researchers relate their origin with mantle plumes. The trap fields of the Siberia platform in Russia, the Deccan plateau in India and the Parana basin in Brasilia are well known. The Siberian Traps discussed in previous chapter overly the Riphean and Vendian complexes with thickness up to 6 and more km, which are considered as a main oil and gas bearing complexes of the Siberian Platform [7, 8, 11, 19–21]. Almost all of the known oil and gas fields in the Lena-Tungus Province of the Siberia Platform include traps within the upper part of the Lower Cambrian sedimentary complex and hydrocarbon accumulations in the Riphean, Vendian and lower part of the Lower Cambrian complexes [19–24]. Deccan Traps in India is other example of trap province. The thickness of the Deccan Traps ranges from about 100 m in the northeastern part of India to about 1.5 km in the western shelf of India. Geophysical studies have inferred hidden Mesozoic sedimentary complex of thickness up to

2.5 km under trap cover [25, 26]. These sediments are believed to hold rather good hydrocarbon prospects [27, 28]. Just one more example of the basins with sedimentary complex under the basaltic cover is the Parana basin in South America. It is the large Ordovician-to-Cretaceous intracratonic basin [4, 29]. Trap complex consists here of the large basaltic lava flows on continental crust and the thousands of associated intrusive diabase bodies. The effusive and intrusive complexes had effected on hydrocarbon generation by source rocks. The above examples show that an analysis of heating effect of trap intrusions on maturation of organic matter in the sedimentary rocks underlying the trap complex is an actual task of the modern geology.

7.2.2 *Principles and Input Parameters of the Modeling*

The effusive part of traps consists of cold basalt that has been flowing on the basin surface during trap formation. We analyze a temperature distribution and maturation of organic matter in sedimentary complex underlying effusive traps using some modification of the basin modeling system GALO. The main algorithms and working principles of the GALO system are discussed in detail in the papers [5, 6]. Temperature distribution within the trap complex, sedimentary cover and underlying lithosphere was determined from numerical solution of heat-transfer Eq. (1.1). Our modeling considers the processes of sedimentation, interruption, erosion and trap formation. Because of absence the available information about the rate field of groundwater in the study region, convective member in the Eq. (1.1) is not considered in the modeling. But convective heat transfer induced by heat from effusive magma is taken into consideration within the framework of approximate approach with effective Nu-number ([5], see Sect. 7.1.2). As mentioned in Sect. 1.1.1, the main feature of the Eq. (1.1) is significant variations of their petrophysical parameters versus lithological rock composition, porosity, φ, and temperature, T. These variations determine a considerable nonlinearity of the Eq. (1.1) together with change in temperature gradient with depth. The temperatures T = 10 °C at the surface (z = 0) and T = 1160 °C at the base (z = 124–130 km) of the domain for temperature calculation are held during the modeling in all variants of trap formation considered in Sect. 7.2.

The four stages of the basin development were considered in all modeling variants. The sedimentary complex underlying the trap cover was formed during the first stage of the basin development. In this stage, 5 km of clay or sandstone rocks were deposited during the time interval from 460 to 260 My ago. The second stage of the basin development is interruption (no sedimentation, no erosion) during 10 My. The third stage is the trap formation 250 My ago during different time-interval from 0 (instantaneous formation of trap cover) to more than 7000 years (Figs. 7.4 and 7.5). The last (forth) stage of the basin development is interruption from nearly 250 My ago to the present time. The maturation of organic matter in the sedimentary rocks under

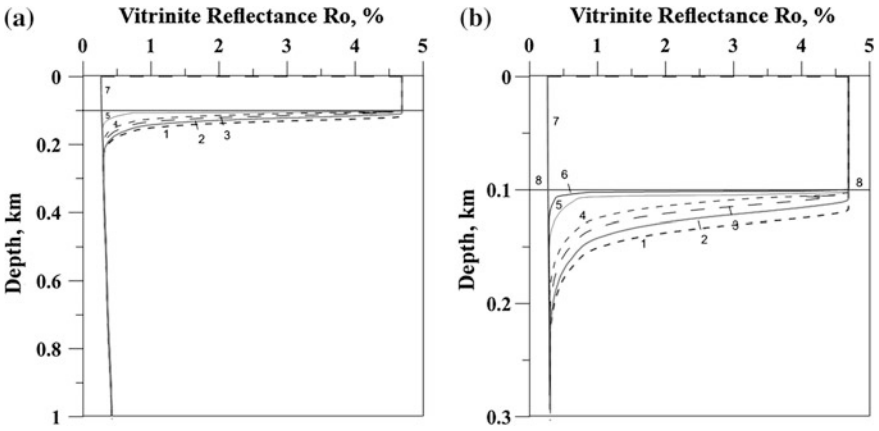

Fig. 7.4 Maturity aureoles of the 100 m trap on the underlying clay sedimentary complex depending on the duration of the trap formation [29]. Figures **a** and **b** differ only by vertical scale. Duration of the trap formation: *1* instantaneous, *2* 102, *3* 204, *4* 409, *5* 2045, *6* 4090 days. *7* background variant (Ttrap = Tsurf); *8* base of the trap

the trap complex changed during all stages of the basin evolution, but especially fast at the stage of the trap formation.

Great differences in duration of the above four stages caused a considerable change in time steps, Δt, used in numerical solution of the Eq. (1.1) at the frame of the non-apparent finite-difference scheme (see Sect. 1.1.5). These steps changed from 1000,000–10,000 years at the sedimentation (first) stage of the basin development to 0.1–1 day during the trap formation (third stage of the basin development). The gradual transition from big time–steps to small ones (and vice versa) took place during 10 My at the second and forth stages of the basin development. The trap formation is simulated in the modeling by successive deposition of 500–1000 elementary layers of melted basalt of thickness 0.2–1 m on the basin surface. Standard continental lithosphere of Table 1.1 is suggested at the basin initiation and in whole history of the basin development. Rather high initial heat flow (80 mW/m^2) was taken at the basement surface at the time of 460 My ago. This heat flow has relaxed during the first 50–70 My of the lithosphere cooling. For this reason, the value of initial heat flow is not a noticeable influence on the modeling results.

The following values of petrophysical parameters were taken in the modeling for the trap rocks: latent heat of fusion L = 90 cal/g (3.768 × 10^5 J/kg); density ρ = 2.6 g/cm^3 (2600 kg/m^3); heat capacity Cp = 0.29 cal/g °C (1.214 kJ/kg °K); heat conductivity at T = 20 °C − K = 0.0045 cal/cm s °K (1.884 W/m °K); solidus temperature Ts = 950 °C; liquidus temperature Tl = 1150 °C and temperature of effusive basaltic magma Ti = 1100 °C. The latter temperature was accepted rather high to explain flowing of liquid trap basalts over great areas. Heat conductivity of basaltic rocks decreased with temperature: $K_m = K_m(T = 0\ °C)/[1 + \alpha \cdot T(°C)]$,

where $\alpha = 5 \times 10^{-4}$ °C^{-1}. The release or consumption of the latent heat during cooling or melting of rocks were considered in usual enthalpy approach [1], when heat capacity Cp in the Eq. (1.1) was replaced by effective heat capacity $Cp' = Cp + L/(Ts - T1)$ within the temperature interval $Ts \leq T \leq Tl$ (see Sect. 1.1.3). This expression suggests linear increase of the melted fraction, f, within the above temperature interval: $f = (T - Ts)/(Tl - Ts)$. Then the effective heat capacity of trap rocks $Cp' = 2.875 \cdot Cp$ at $950 \leq T \leq 1150$ °C and $Cp' = Cp$ at $T < 950$ °C and $T > 1150$ °C.

7.2.3 Maturity Aureole Under Trap: Results of Numerical Modeling

Duration of trap formation is unknown up to now. There are the so called well dated intrusions with detailed measurements of vitrinite reflectance in vicinity of the intruded body like to the example in Sect. 7.1.2 (Fig. 7.2). For such intrusions, it is possibly to estimate the times of the intrusion's formation from comparison between the measured and computed distributions Ro(z) [5, 6]. But similar detailed observed data of Ro is absent for traps. For this reason, we tried to estimate roughly the minimal time of trap formation on the base of the data for the Lakki volcano in Iceland, created the greatest volcanic plateau in recent history. The volume of erupted lava in the Lakki volcano is estimated by 12.5 km^3. The lava covers the area of 565 km^2. This lava was flowing out through fractures during about 3 months (about 90 days). Then the average thickness of the trap cover, d_{trap}, can be approximately estimated to be 12.5 km^3/565 km^2 = 0.022 km. Taken such mean rate of the trap formation (v = 0.022 km/90 days), it can be obtained that the trap complexes of total thickness Δz = 1, 100 and 1000 m can be formed within approximately 4.1, 409 and 4091 days correspondingly. It can be noted that the typical times of conductive cooling of such traps, $\tau \approx \Delta z^2/\kappa$, will be about 11. 6 days, and 322 and 32,200 years, correspondingly taking the rock thermal diffusivity, $\kappa = K/\rho$, $Cp = 10^{-6}$ m^2/s. These times exceed considerably the times of the trap formation.

Figure 7.4 shows the present time maturity aureoles calculated for different formation times of the traps of thickness 100 m. Liquid magma has been flowing out 250 My ago on the surface of sedimentary cover of thickness 5000 m presented by clay rocks. This sedimentary cover has been constructing from 460 to 260 My, on the typical continental lithosphere of Table 1.1. Next stage of the basin development (interruption) lasted from 260 to 250 My was followed by the stage of trap formation. The trap formation was followed in turn by interruption period lasted from about 250 My ago to the present time. All of the maturity aureoles are shown in Fig. 7.4 for final time of the basin evolution i.e. the present time.

Results of the modeling in Fig. 7.4 demonstrate clearly a great role of duration of the trap formation in determination of the size of maturity aureole in the rocks

underlying the trap. The instantaneous formation of trap leads to the widest aureole. The aureoles obtained for the 100 m traps formed during 50 and lesser days almost coincide with the "instantaneous" one. But the size of the aureoles for the sill accreted during 102 and more days will decrease with increasing of the time span of the trap formation. For example, the value of Ro = 1.00 % will be reached at the distance 44, 19 and less than 5 m from the trap base for instantaneous trap formation and its formation during 409 and 2000 and more days, correspondingly (Fig. 7.4b). Very slow accretion of the trap must lead to extra narrow maturity aureole, because the current elementary magma layer will have enough time to cool totally before eruption of next elementary trap layer. In this case, at steady rate of the trap accretion, the size of maturity aureole will be close to the one determined by heating from the current elementary layer of the trap. Distribution Ro(z) for slow accretion of trap coincides with the background one (obtained without heat effect of the trap, i.e. Ttrap = Tsurf) at the main part of depth interval (compare the curves 6 and 7 in Fig. 7.4b). The background distribution Ro(z) presented by curve 7 in Fig. 7.4 was computed under condition that the temperature of the current elementary layer of the trap deposited on the surface was equaled to the surface temperature of the basin (i.e. Ttrap = Tsurf = 10 °C).

Figure 7.5 illustrates the formation of maturity aureole for the trap of 1000 m thickness in the clay and sandy sedimentary complex underlying the trap. The model of the basin formation is similar to one for the 100 m trap, but the time-span of the 1000 m trap formation is longer than the one for the 100 m trap by 10 and more times. The results of modeling in Fig. 7.5 support again a strong dependence of the size of maturity aureole on the duration of trap formation. But in the case of the 1000 m trap, delay of the heat wave generated by current portions of magma

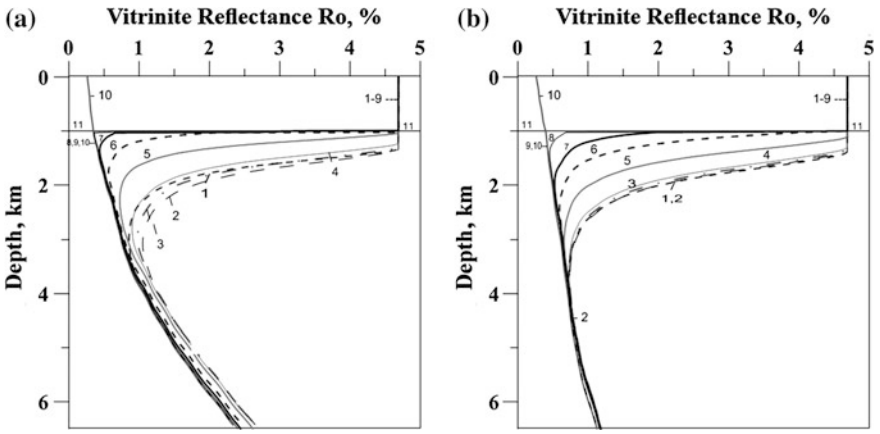

Fig. 7.5 Maturity aureoles of the 1000 m trap in the clay (**a**) and sandy (**b**) sedimentary covers underlying the trap in depending on the duration of the trap formation [30]. Duration of the trap formation: *1* instantaneous, *2* 1.136, *3* *5.68*, *4* 11.36, *5* 56.8, *6* 227, *7* 568, *8* 1420, *9* 7100 years. *10* background variant (Ttrap = Tsurf); *11* base of the trap

and passed through the forming trap becomes considerable. As result, the maturity aureole corresponding to an instantaneous formation of trap (curve 1 in Fig. 7.5a) is a few narrower than the aureoles for the times of trap formation 1.1 and 5.7 years (curves 2 and 3 in the same figure). Note that this effect is less noticeable in Fig. 7.5b with sandy sedimentary rocks of higher thermal conductivity. As whole, all of the aureoles with the formation times $\Delta t \leq 12$ years are close to the "instantaneous" aureole. A considerable difference in the sizes of aureoles begins with 20 and more years of the trap formation. Then the aureole size decreases with increase of time span of the trap formation similarly to the case of the 100 m trap. So, a distance from the trap base to the depth of host rock with Ro = 1.00 % reduces from 1150 m for instantaneous trap formation to 1080, 488, 3, 1.5 and less than 1 m for trap formation during the time interval 11.4, 56.8, 227, 568 and 1200 and more years, correspondingly. Distributions Ro(z) for accretion of the trap during 1000 and more years (curves 8–9 in Fig. 7.5) almost coincide with the background one (curve 10) at the main part of depth interval.

7.2.4 *Influence of Some Factors on Estimated Size of Maturity Aureole*

At first, we will discuss an effect of rock lithology. Figure 7.5b demonstrates results of modeling of maturity aureole from the 1000 m trap formed on the sandy sedimentary cover. These results can be compared with the modeling in Fig. 7.5a for the case of trap formation on the clay sedimentary blanket. The sediments lithology is the only factor of difference in the models of Figs. 7.5a, b. Both Fig. 7.5a, b support the conclusion about decrease of the size of maturity aureole with increasing time span of trap formation. An increase of mean heat conductivity of sandy rocks in comparison with the one in clay rocks results in widening of maturity aureoles in Fig. 7.5b. So, the distance from the depth in the host rocks corresponded to the value of Ro = 1.00 % to the trap base decreases continually from 1370 m for instantaneous trap formation to 1340, 634, 190, 2, and less than 1 m for the trap formation during 11.4, 56.8, 227, 568 and 1300 and more years whereas the same distances in the clay variant (Fig. 7.5a) decrease from 1150 to 1080, 488, 3, 1.5 and less that 1 m, correspondingly. It is interesting that the effect of the aureole widening at transition from clay to sandy rocks is suppressed partly due to considerable decrease of matrix heat conductivity of sandstones with temperature increase (see above).

Hydrothermal heat transfer in sedimentary layers underlying the trap affects considerably the maturity aureole of the trap. No doubt, the hydrothermal activity, induced by trap, lead to widening of the trap maturity aureole (for example compare the aureoles in Fig. 7.2a, b). Figure 7.6 supports also this conclusion. It illustrates an action of hydrothermal convection with effective Nusselt numbers Nu = 1.0 (the variant without hydrothermal convection—curves 1), 1.5 (curves 2) and 2.0 (curves 3)

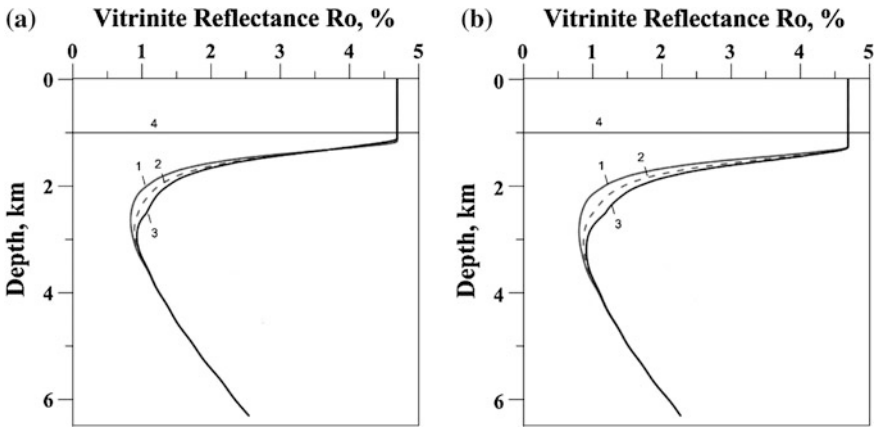

Fig. 7.6 Widening of the trap maturation aureole due to hydrothermal heat transfer induced by the trap of 1000 m thickness in the underlying clay sedimentary cover as a function of the effective Nusselt number, *Nu* [29]. **a** The trap formation during 11.36 years. **b** The instantaneous formation of the trap. *1* $Nu = 1.0$ (without hydrothermal activity); *2* $Nu = 1.5$; *3* $Nu = 2.0$

on the maturity aureole under trap complex. It is believed that the hydrothermal convection was effective only within the temperature interval 150 °C $\leq$ T $\leq$ 725 °C. Here, as above, T = 725 °C is the maximal temperature for penetration of hydrothermal convection into host rocks. The micro-fractiures close at the temperatures above 725 °C [31]. The heat effect of hydrothermal convection is considered in conductive approximation, when usual conductive heat conductivity of rocks is increased by Nu times in corresponding intervals of depth and temperature. Figure 7.6 shows that for our sedimentary section influence of hydrothermal heat transfer on maturity aureole is rather small for marginal parts of the aureole (Ro < 0.7 % and Ro > 2.0 %), but it is considerable for its inner part (0.7 < Ro < 1.5 %). So, a size of maturity aureole corresponded to the value of Ro = 1.00 % increases from 1150 to 1500 m and to 1760 m with increase of the Nu number from 1.0 to 1.5 and to 2.0, correspondingly for the case of instantaneous formation of the 1000 m trap (Fig. 7.6b). The same values for the 1000 m trap formed during 11.36 years are 1080, 1350 and 1610 m (Fig. 7.6a; Table 7.1).

It is interesting to assess an influence of melting parameters of basalt (L—latent heat of fusion, Ts—solidus basalt temperature and Tl—liquidus basalt temperature) on the results of our modeling. An increase of latent heat of fusion or decrease of difference of the liquidus and solidus temperatures lead to increase of latent heat effect due to increase of effective heat capacity $Cp' = Cp\ (1 + [L/(Cp\ (Tl - Ts))]$ (Sects. 1.1.3 and 7.2.2). For example, an increase parameter L from previous value of 90 cal/g to 120 cal/g or replacement of (Tl − Ts) = 200 °C on the (Tl − Ts) = 150 °C leads to transition from previous relationship $Cp' = 2.875 \times Cp$ to the one $Cp' = 3.50\ Cp$. Table 7.1 illustrates the results of such replacement for the traps of thickness 100 and 1000 m formed with the rate typical for the Laki volcano

Table 7.1 The maturity aureole sizes (distance from trap base to the depth in underlying complex with Ro = 1.00 %) for different maturation level, Ro, and different variants of trap formation [30]

Vitrinite reflectance (%)	100 m trap, formed during 409 days on clays (m)	1000 m trap, formed during 11.36 years on clays (m)	1000 m trap, formed during 11.36 years on sands (m)
Ro = 1.00	19–20.5	1067–1260	1273–1440
Ro = 2.00	9.2–11.5	567–660	761–857
Ro = 3.00	6.4–6.7	403–480	549–634

Comments Left numbers are the sizes of maturity aureoles computed in standard variant (L = 90 cal/g, Cp = 0.24 cal/g °K and T1 = 1150 °C, Ts = 950 °C, i.e. Cp′ = 2.875 × Cp). Right numbers are the ones computed in the variants with changed values of L, Ts, T1 (L = 90 cal/g, Cp = 0.24 cal/g °K and T1 = 1100, Ts = 950 °C or L = 120 cal/g, Cp = 0.24 cal/g °K and T1 = 1150 °C, Ts = 950 °C, i.e. Cp′ = 3.50 × Cp)

(22 m/90 days). The table shows the aureole sizes for the Ro values equaled 1, 2 and 3 %. The aureole sizes calculated with traditional parameters (L = 90 cal/g, Cp = 0.24 cal/g °K and T1 = 1150 °C, Ts = 950 °C; i.e. Cp′ = 2.875 × Cp) are shown by left numbers in the Table 7.1. The values of alternating variants (L = 90 cal/g, Cp = 0.24 cal/g °K and T1 = 1100, Ts = 950 °C or L = 120 cal/g, Cp = 0.24 cal/g °K and T1 = 1150 °C, Ts = 950 °C, i.e. Cp′ = 3.50 × Cp) are shown by right numbers in the Table 7.1. Increase of latent heat effect results in widening of maturity aureole by 10–30 %. The data shown in Table 7.1 takes an opportunity to estimate an influence of possible changes in melting parameters of the trap rocks on the modeling results.

A major problem in determining the maturity aureole is the definition of the duration of the trap formation. The models considered above suggested that the trap formation was a continual process. But there are geological evidences that some traps could be formed in several stages, every of which created its layer of the trap [7, 11]. Total duration of trap complex formation is estimated usually by 1–2 My. Let the trap complex of total thickness of 1000 m was formed during 1 My and consists of four trap layers of thickness 250 m. If the rate typical for the .Laki volcano (22 m/90 days) is used in the estimation, the time span for formation of the 250 m trap layer (Δt) is equaled to about 1023 days or 2.84 years. Then, average time interval between successive depositions of the 250 m trap layer can be estimated by the value $\Delta T = (1{,}000{,}000 - 4 \times 2.84)/3 \approx 330{,}000$ years. This time interval is much longer than the typical time of cooling of the layer, equaled $\tau \approx \Delta z^2/\kappa \approx 250^2/10^{-6} \approx 2{,}000$ years. Therefore, previous trap layer had the time to cool totally before the next layer begins its deposition. Such situation will remain for the 100 m trap layers too. In this case, $\Delta T = (1{,}000{,}000 - 10 \times 1.136)/9 \approx 111{,}000$ years, that is much longer than the cooling time $\tau \approx 100^2/10^{-6} \approx 320$ years. For this reason, the maturity aureole of such trap complex will be determined by the aureole of the first trap layer that is nearest to sedimentary complex. In this case, the size of maturity aureole of trap complex must be close to the aureole of single trap layer.

7.3 Conclusion

Maturity aureole of the trap and sill complex determines the depth of oil and gas windows and an ability of the underlying and host sedimentary rocks to generate hydrocarbons. Our study shows that a size of maturity aureoles of the single intrusions and trap complex decreases considerably with increase of duration of these complex is formation. So, the aureole size in for formation of the trap with total thickness of 1000 m underlain by clay complex reduces from 1150–1067 m for the trap formation during time interval 11.4 years and more shorter to less than 1 m for the traps formed during 1200 and more years under condition of steady rate of the trap formation. The modeling demonstrates that a maturation level of organic matter in sedimentary rocks under trap and within the host rocks of single intrusions can be rather moderate if the time span of formation of these structures (or formation of their single layers) was enough long. The size of maturity aureole of the trap complex formed during several stages can be close to the aureole of single trap layer with maximal thickness.

Comparison of computed and measured values of vitrinite reflectance within the thermal aureole of some well-dated intrusions shows that traditional calculations of instantaneous intrusion considerably over-estimate temperatures and maturation of organic matter in the host rocks. Models which consider formation of the intrusive body over time (as distinct from instantaneous intrusion) and especially models of emplacement of the intrusive body in the shell of relatively cool magmatic rocks show better agreement between computed and observed data. An analysis of additional examples of the well dated intrusions and measurements of maturity level in subtrappean rocks help in future to correct the models of formation of the maturity aureoles in the vicinity of the intrusions and traps considered in this chapter.

References

1. Carlslaw HS, Jaeger JC (1959) Conduction of heat in solids. Oxford University Press, New York
2. Delaney PT, Pollard DD (1982) Solidification of basaltic magma during flow in a dike. Amer J Sci 282(6):856–885
3. Fedotov SA (1976) Uplift of mafic magma in Earth crust and mechanism of fracture basalt eruption. Izvestiya ANSSSR Ser Geol (10):5–23 (in Russian)
4. Rodrigues FM, Villar HJ, Baudino R, Delpino D, Zencich S (2009) Modeling an atypical petroleum system: a case study of hydrocarbon generation, migration and accumulation related to igneous intrusions in the Neuquen Basin, Argentina. Mar Pet Geol 26:590–605
5. Galushkin YI (1997) The thermal effect of igneous intrusive bodies on maturity of organic matter—a possible mechanism of intrusion formation. Org Geochem 27(11–12):645–658
6. Makhous M, Galushkin Yu (2005) Basin analysis and modeling of the burial, thermal and maturation histories in sedimentary basins. Editions TECHNIP, Paris

7. Kontorovich AE, Melnikov NV, Staroseltsev VS, Khomenko AV (1987) Effect of trap intrusions on oil and gas generation by the Paleozoic deposits of the Siberian Platform. Geologia i Geophysika 5:14–20 (in Russian)
8. Kontorovich AE, Khomenko AV (2001) Theoretical basis of oil-gas prospecting of sedimentary basins with intensive trap magmatism. Geologia i Geophysika 42(11–12): 1764–1773(in Russian)
9. Verba M, Alexeeva FB (1972) Intrusion effect on the bitumen content in the host carbonate Paleozoic rocks of Norilsk region. In: Voprosy geologii neftegasonosnosty Tungusskoy Sineclizy. Trudy VSEGEI, (308), Leningrad, pp 124–142 (in Russian)
10. Melenevskii VN, Fomin AN, Konyshev AS, Talibova OG (2008) Contact coal transformation under the influence of dolerite dike. Geologia i Geophysika 49(9):886–893 (in Russian)
11. Kontorovich AE, Surkov VC, Trofimuk AA (1981) Oil and gas geology of the West Siberia Platform. Nedra, Moscow (in Russian)
12. Philippov YA, Petrishina YV, Bogorodskaya LI, Kontorovich AA, Krinin VA (1999) Estimation of the catagenesis and petroleum potential of organic matter in the Riphean and Vendian deposits of the Baikit and Katanga petroliferous areas. Geologia i Geophysika 40 (9):1362–1374 (in Russian)
13. Raymond AC, Murchison DG (1988) Development of organic maturation in the thermal aureoles of sills and its relation to sediment compaction. Fuel 67(12):1599–1608
14. Raymond AC, Murchison DG (1989) Organic maturation and its timing in a Carboniferous sequence in the central Midland Valley of Scotland: comparisons. Fuel 68(3):328–334
15. Bishop AN, Abbott CD (1993) The interrelationship of biological marker maturity parameters and molecular yields during contact metamorphism. Geochim Cosmochim Acta 87(15):3661–3668
16. Thrasher J (1992) Thermal effect of the Tertiary Cuillins intrusive complex in the Jurassic of the Hebrides: an organic geochemical study. In: Parnell J (ed) Basins on the Atlantic seaboard: petroleum geology, sedimentology, and basin evolution. Geol Soc Spec Publ (62):35–49
17. Delaney PT, Pollard DD (1982) Solidification of basaltic magma during flow in a dike. Am J Sci 282(6):856–885
18. Galushkin YI, Dubinin EP, Shemenda AI (1994) Thermal structure of the axial zone in mid-oceanic ridges. Part 1. Formation and evolution of axial magma chamber. Phys Solid Earth, Maik Nauka Interperiodika Publishing (Russian Federation) 30(5):385–393
19. Kontorovich AE, Likhanov II, Lepettyukha VV, Khomenko AV, Ten AA (1995) Application of geothermometers to assessment of methamorphic temperatures in sedimentary basin with trap magmatizm. Doklady RAN 345(6):793–796 (in Russian)
20. Kontorovich AE, Pavlov AL, Khomenko AV, Tretiakov GA (1997) Physical—chemical conditions of graphitization of coal bearing rocks (on an example of western part of the Siberian Platform). Geokhimia 6:563–570 (in Russian)
21. Astashkin VA, Khomenko AV, Shishkin BB (1994) Effect of structural trap intrusions on structures of the sedimentary cover of the Siberian Platform. Geologia i Geophysika 35(1):34–40 (in Russian)
22. Frolov SV, Akhmanov G, Kozlova EV, Krylov OV, Sitar KA, Galushkin YI (2011) Riphean basins of the central and western Siberian Platform. Mar Pet Geol 28:906–920
23. Sokolov BA, Egorov VA, Nakaryakov VD, Bitner AK, Zkukovin YA, Kuznetsov LL, Skorobogatikh PP, Zakharyan AZ (1992) Geological and geophysical conditions of formation of oil-and-gas bearing deposits in the ancient rocks of Eastern Siberia. Petroconsultants Australia, Sydney, Australia
24. Kontorovich AE, Izosimova AN, Kontorovich AA, Khabarov EM, Timoshina ID (1996) Geological structure and conditions of the formation of the giant Yurubcheno-Tokhoma zone of oil and gas accumulation in the Upper Proterozoic of the Siberian Platform. Geologiya i Geofizika 37(8):166–195 (in Russian)
25. Biswas SK (1989) Strucrure of the western continental margin of India and related igneous activity. In: Subbarao KV (ed) Deccan flood basalts: geological society of India memoir 10:371–390

26. Kaila KL (1989) Mapping the thickness of Deccan Trap flows in India from DSS studies and inferences about a hidden Mesozoic Basin in the Narmada—Tapti region. In: Subbarao KV (ed) Deccan flood basalts: geological society of India memoir 10:91–116
27. Gombos AM Jr, Powell WG, Norton IO (1995) The tectonic evolution of western India and its impact on hydrocarbon occurrences: an overview. Sediment Geol 96:119–129
28. Kumar B, Patil DJ, Kalpana G, Vishnu VC (2004) Geochemical prospecting of hydrocarbons in frontier basins of India: search and discovery article #10073 (2004). In: Adapted from extended abstract prepared for presentation at AAPG annual convention, Dallas, Texas, 18–21 April 2004
29. Milani EJ, Zala'n PV (1999) An outline of the geology and petroleum systems of the Paleozoic interior basins of Sous America. Episodes 22(3):199–205
30. Galushkin YI, Sitar KA, Frolov SV (2011) Maturity aureole of organic matter in sedimentary rocks underlying trap and its dependence on duration of the trap formation. In: The annual conference of the international association for mathematical geoscience, Salzburg, 5–10 Sept 2011, pp 15, 1–17
31. Hardee HC (1982) Permeable convection above magma bodies. Tectonophysics 84:179–195

Chapter 8
Deccan Trap, India

Abstract The modified GALO program package for basin modeling is used to calculate the temperature and vitrinite reflectance distributions with depth at any time before, during and after the Deccan Trap formation. We consider five specific profiles crossing the Saurashtra and Kutch regions in North-Western India, central part of the Deccan Plateau and western passive margin of India near the Mumbai offshore. Burial, thermal and maturation histories in selected areas of the region are reconstructed numerically. Duration of trap formation is most critical and indefinite parameter in construction of maturity aureole in the sub-trappean sedimentary complex. Our analysis in the frame of the model of continuous formation of traps suggests that a maturation level of organic matter in sedimentary rocks under the trap depends strongly on duration of the trap formation. *Maturity level of organic matter at the distance of* 100–200 m below the base of the trap complex can be rather moderate *even for traps thickness of 1 km or more*, if the trap was formed over fairly a long time.

Keywords Deccan trap · Subtrappean sedimentary complex · Bombay offshore basin · India · Basin modeling · Thermal and maturity history · Tectonic subsidence · Hydrocarbon generation

8.1 Introduction

There are several basins or depressions in the world with substantial sediment thickness under the trap complexes. The Siberian Traps overly the Riphean and Vendian complexes with thickness up to 6 and more km, which are considered as a main oil and gas bearing complexes of the Siberian Platform [1–4]. These traps were considered in Chap. 6 and partly in Sect. 7.1.3. The large Ordovician-to-Cretaceous intracratonic Parana Basin in South America [5, 6] is just one more example of the basin with sedimentary complex under the basaltic cover. In many basins of the world, the sediments underlying the traps are believed to hold rather good hydrocarbon prospect [5, 7]. Chapter 8 considers also the relationships

Y. Galushkin, *Non-standard Problems in Basin Modelling*,
DOI 10.1007/978-3-319-33882-8_8

between, duration of the trap complex formation and size and depth of thermal and maturity aureoles induced in the subtrapean sedimentary complex by heat transfer from the trap. These problems were discussed in Chap. 7, but in this chapter they are considered on the actual examples of sedimentary basins in the Deccan Province of India. The analysis in Chap. 7 shows that the thermal effect of formation of igneous intrusions and trap complex on sedimentary host section together with a size of maturity aureole depend strongly on duration of the formation process and can differ considerably from the effect obtained in the model of instantaneous intrusion. As mentioned in previous chapter, determination of maturity aureoles of traps is significant because these aureoles determine a depth of "oil and gas windows" and an ability of the sub-trappean sedimentary complex to generate hydrocarbons. Numerical estimates of thermal and maturation histories of the rocks carried out in the frame of the basin modeling system with consideration actual lithological composition of overtrappian and subtrappian sedimentary rocks could make more accuracy an assessment of hydrocarbon potential of the basins in the Deccan Trap in India.

8.2 Geological Setting and Rock Lithology

The Deccan Traps are a large igneous province located on the Deccan Plateau of west-central India (between 17–24° N, 73–74° E). Trap is known to extend up to the shelf margin of Bombay Offshore basin and has a volume 512,000 km^3 [8]. Deccan Trap magmas may have erupted through multiple centers, the most prominent of which may have been a shield volcano-like structure in the Western Ghats area [9]. Deccan Trap consists of a series of basaltic lava flows, blanketing all pre-existing rocks. The bulk of the lavas are tholeiitic. The thickness of individual flow ranges from 2 to 40 m [10]. An average density of the basaltic rocks is 2.9 g/cm^3. The flows are generally horizontal with a gentle westerly dip and attain a maximum thickness along the Arabian Sea coast. The geologically estimated thickness of the Trap ranges from 60 m at Belgaum to 1600 m at Mahabaleshwar and 2000 m along the Bombay coast.

For a long time it was believed that the Deccan Traps eruption was associated with a deep mantle plume. Seafloor spreading at the boundary between the Indian and African Plates subsequently pushed India north over the plume, which now lies under Réunion Island in the Indian Ocean, southwest of India. The model of the Deccan trap origin from the hot spot contradicts, however, a number of geological and geochemical factors [11–14]. It is believed now that extension was changed to northeast-southwest during the Late Cretaceous and finally culminated in crustal separation between India and the Seychelles Plateau. This event was associated with extensive magmatism generating the Deccan trap basalts with its locus near the triple junction [15]. Gravity and seismic evidences suggest that most of the west coast is magmatically underplated as a result of Deccan igneous activity [16, 17]. The outcropping basalts are relatively thick near the west coast (up to 2000 m) and thin

toward the east. However, there is relatively little information about the thickness of the offshore basalt series. In the Bombay High region, flood basalts are relatively thin and are directly underlain by Precambrian basement [18]. In the Kutch region, the basalts thicken offshore to about 1.5 km in a westerly direction [19]. After the Deccan volcanic event, the Cambay, Bombay offshore, and offshore Kutch Basin continued to subside, accumulating thick packages of clastics in the Cambay and Kutch basins, whereas the Bombay offshore basin was mainly dominated by carbonates [16, 17]. Late-stage north-south compression as a result of the collision of India with Asia is evident in the Kutch Basin, where Mesozoic sediments are highly folded.

The Late Cretaceous Deccan traps on the Indian peninsula mainly cover Precambrian basement with several rift zones crosscutting the craton, recording the extension history since the Triassic [14, 20]. The main rift zones are the east-west-trending Kutch Basin, the north-south-trending Cambay Basin, the east-west-trending Narmada graben, and the north-northwest-south-southeast Bombay offshore basin (Fig. 8.1). The east-west-trending Kutch Basin was formed in the Early Jurassic or perhaps Triassic [20] as a response to east-west extension and records Cretaceous and Jurassic sedimentation in wells and outcrop, including good reservoir sands and various source rock intervals [14]. Cretaceous and Jurassic sediments are also known from outcrop and drilling on the Saurashtra horst block [21]. Sedimentation continued in the Cretaceous with deltaic sands in the Kutch and Narmada basins, as well as in the south of the Cambay Basin. Early

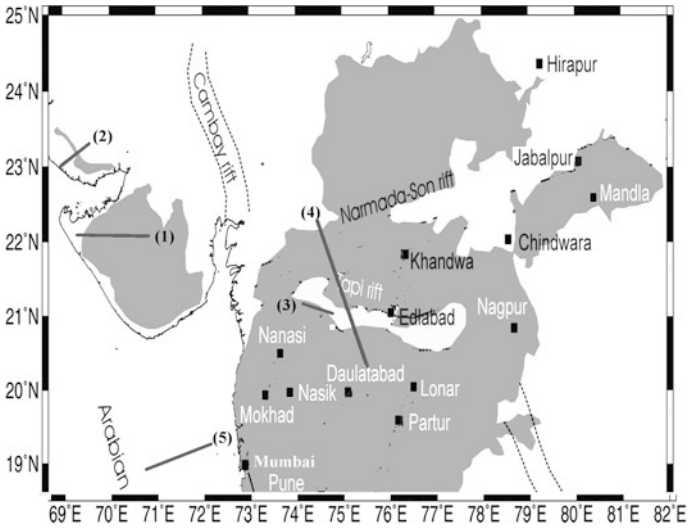

Fig. 8.1 The Deccan Volcanic Province and location of the profiles 1–5 considered in the chapter (after [17] with changing). Profile *1* pseudo-wells (p-w) 3–5; profile *2* p-w. 6, 7; profile *3* p-w. 8–10; profile *4* p-w. 11, 12; profile *5* p-w. 1, 2. Locations of pseudowells in the profiles will be shown below

Cretaceous extension was roughly east-west [22]. As mentioned above, during the Late Cretaceous, extension changed to northeast-south-west and culminated in crustal separation between India and the Seychelles Plateau. This event was associated with extensive magmatism generating the Deccan trap basalts [14, 15].

Several offshore sub-basalt gas discoveries are found in anticlinal traps with a Cretaceous deltaic sandstone reservoir [23] sealed by Deccan trap basalts and shales. Jurassic or Cretaceous gas has probably been sourced from type III source rocks. Potential exists for Jurassic and other Cretaceous reservoirs [14]. Well results from the onshore part of the Kutch Basin suggest that most of the Cretaceous and Jurassic source rock is immature, except for the region west of the median high. On the Saurashtra peninsula, Cretaceous and Jurassic sediments are mainly immature, except for regions in the northwest near the Kutch graben, where light gaseous hydrocarbon concentrations derived from a thermogenic source were encountered in surface soil samples [19]. On the Bombay High, fractured basalt and granites are hydrocarbon bearing, but they have probably been sourced by an Eocene or younger source rock [23].

Gondwana rocks of Permo-Carboniferous to Early Cretaceous age, fluviatile to lacustrine in nature, occur in the Pranhita-Godavari Valley and continue underneath the Trap. Precambrian rocks formed the floor on which Gondwana sediments were deposited. The Gondwana sediments of Lower Permian age consist of diamictite, conglomerates, shales, turbidites, rhythmites and coal seams. Middle Permian sediments are essentially coal free and consist of coarse sandstones and red clays. The Gondwanas of the Upper Permian age are again coal bearing. In the Pranhita-Godavari Graben, the Gondwana sediments of thickness more than 5 km are estimated to occur. Depth computation from DSS data indicates the maximum Gondwana thickness of 1.8 km under the Trap. The Lower Triassic to Lower Jurassic formations essentially consist of alternation of red clays, sandstones and conglomerates. Sediments of Liassic age consist of thick sandstones, siltstones. silty clays, minor red clays with a prominent terrestrial limestone bed towards the base. Lower Cretaceous sediments comprise massive sandstones, conglomerates, white clays, thin coal seams and carbonaceous shales. The overlying Lameta beds consist of marine/brackish water limestones, sandstones, marls and clays [20, 24].

The Lower Gondwana sediments (Barakar Formation in particular), containing abundant organic matter, are thought to constitute good source rocks. Vitrinite reflectance studies indicate that the shale sequences are within the zone of liquid hydrocarbon generation (Satpura fm.: TOC = 10.1 %, Ro = 0.6–1.3 %; Pranhita Godavari fm.: TOC = 3.58–6.41 %, Ro = 0.47–0.67 %; Son—Mahanadi fm.: TOC = 1.06–18.7 %, Ro = 0.4–0.6 %: [24]).

About 2 km thick sedimentary section is sandwiched between the Deccan Trap and the Precambrian basement in a number of depositional basins as revealed by DSS and other geophysical studies. Reservoir facies are well developed in the adjoining Pranhita-Godavari basin in both the Upper and Lower Gondwana sequences, and are expected to be present in the Deccan Syneclise as well. As discussed earlier, gravity-magnetic and DSS data indicate the extension of the Pranhita Godavari and Koyna rift basins towards northwest and north, respectively

and merging with the east-west trending Narmada-Son lineament. This junction of three lineaments enhances the prospectivity of the area. It is considered that heat generation due to Deccan Trap volcanism soon after the Cretaceous sedimentation may have acted as a catalyst in hydrocarbon generation [24].

8.3 The Western Passive Margin of India

8.3.1 Initial Data for Modeling

In this section, the specific profile crossing the western passive margin of India near the Mumbai offshore and containing part of complex of the Deccan Trap will be considered. Two areas near the pseudo-wells P–W-1 and P–W 2 with maximal thickness of the Trap and subtrappean complex on the profile are analyzed in the section (Figs. 8.1 and 8.2). Numerical reconstructions allow us to see burial, thermal and maturation histories typical for evolution of the western passive margin of India. This evolution begins with continental sedimentation in the Upper Carboniferous and includes a stage of the Deccan Trap formation, as well as the stage of post-trappean heatus and sedimentation. The evolution of the Basin in the western passive margin of India considers also stretching of the lithosphere that is responsible for formation of sea of depth about 1–2 km during last 42 My [25]. Duration of the Deccan Trap formation is the most critical and indefinite parameter in reconstruction of maturation history of the rocks in the sub-trappean sedimentary

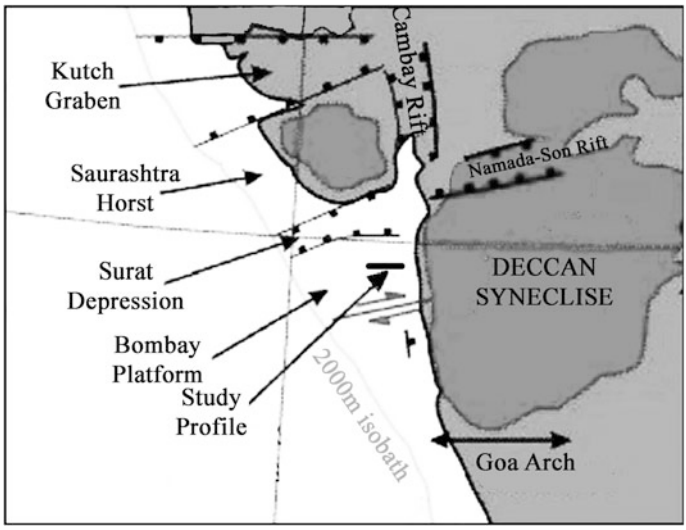

Fig. 8.2 Deccan Volcanic Province and approximate location of the study profile in the western offshore of India (after [24] with changing)

complex. Starting-point in assessment of the duration of the Trap formation was taken the lava eruption of the Lacky volcanic field in 1783 year in Iceland. Here, a thickness of lava cover was increasing with mean rate about V = 0.022 km/90 days (see Sect. 7.2.3). This rate is rather high and actual mean rate of Trap formation can differ from the one. For this reason, the variants with different rates of the Trap formation are presented below. The stage of the Deccan trap formation of finite duration (non instantaneous) was included in our model of the Basin evolution. The developed TRAP computer program that is modification of the GALO program package (see Sect. 7.2.2) is used to analyze the problem of formation of maturity aureole of Deccan Trap. This program allows the calculations of the temperature and vitrinite reflectance distributions with depth as within the effusive and intrusive rocks as in the underlying and overlying host rocks. Calculations are carried out for any time before, during and after the trap formation. It is important that these calculations take into account an actual lithological composition of the rocks in the sedimentary complexes under and over the Trap complex.

Sedimentary section in Fig. 8.3 was constructed using the Gravity, Magnetic and Magneto-Telluric (MT) data along with seismic sounding of the margin [26]. Sedimentary sections of pseudo-wells 1 and 2 correspond to maximal depth of the Basin basement and minimal thickness of the posttrappean complex in the profile of Fig. 8.2. The sections include the trap complex of thickness 2000 and 1900 m, the subtrappean sedimentary complex of thickness of 2700 and 3500 m, and the posttrappian complex of thickness 3300 and 2400 m, correspondingly (Table 8.1, Figs. 8.2 and 8.3).

Table 8.1 demonstrates the main stages of geological history of the Bombay offshore Basin and lithological composition of sedimentary rocks that was constructed in accordance with geological history of the region presented in the papers [7, 10, 16–18, 20, 23, 27, 28] and discussed in Sect. 8.2. The burial history of the Basin includes 6 sedimentation intervals form the Lower subtrappean complex. The rocks of this complex are presented by mixture of 70 % clays and 30 % sandstones. Next 10 sedimentation intervals form the Upper subtrappian complex with the rocks presented to a great degree by limestones (50 %), clays (30 %) and sandstones (20 %). Two heatus (before and after trap formation) and the stage of trap formation

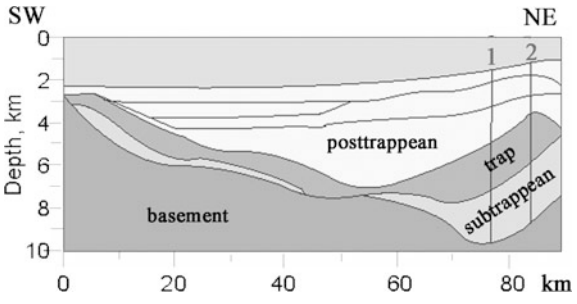

Fig. 8.3 Sedimentary section constructed on the base of Gravity, Magnetic and Magneto-Telluric (MT) data along with seismic sounding crossing the western passive margin of India (after [26] with little changes)

Table 8.1 Sedimentary sections of the Basin in the western passive margin of India near to the 1 and 2 pseudo-wells (Figs. 8.1 and 8.2; [25]) constrained according to [8, 26]

Stage number	Stage type	Z_1 (m)	Z_2 (m)	Lithology			Δt (My)	Number of steps
				Shale.	Sandst.	Limest.		
1	1	8000	7800	0.70	0.30	0.00	310–298 (12)	158
2	1	7742	7468	0.70	0.30	0.00	298–286 12)	158
3	1	7484	7136	0.70	0.30	0.00	286–274 (12)	158
4	1	7226	6804	0.70	0.30	0.00	274–263 11)	146
5	1	6989	6499	0.70	0.30	0.00	263–253 10)	132
6	1	6774	6222	0.70	0.30	0.00	253–245 (8)	106
7	1	6600	6000	0.30	0.20	0.50	245–222 (23)	152
8	1	6433	5780	0.30	0.20	0.50	222–200 (22)	146
9	1	6273	5570	0.30	0.20	0.50	200–178 (22)	146
10	1	6113	5360	0.30	0.20	0.50	178–156 (22)	146
11	1	5953	5150	0.30	0.20	0.50	156–134 (22)	146
12	1	5793	4940	0.30	0.20	0.50	134–112 (22)	146
13	1	5633	4730	0.30	0.20	0.50	112–100 (12)	158
14	1	5546	4615	0.30	0.20	0.50	100–89 (11)	146
15	1	5466	4510	0.30	0.20	0.50	89–78 (11)	146
16	1	5386	4405	0.30	0.20	0.50	78–67 (11)	146
17	2	–	–	–	–	–	67–66 (1)	201
18	1	5300	4300	Basalt (trap)			66–[66 − Δt_{trap}] (Δt_{trap})	1000
19	2	–	–	–	–	–	[66 − Δt_{trap}]–55 (11 − Δt_{trap})	330
20	1	3300	2400	0.00	0.00	1.00	55–25 (30)	148
21	1	1600	1400	0.80	0.20	0.00	25–0 (25)	166

The sections include the trap layers of thickness 2000 and 1900 m

Stage number—number of stage of the Basin development (*1* sedimentation, *2* heatus). Z_1 and Z_2 depth of the base of layer in pseudo-wells 1 and 2 correspondingly. Δt time and duration (in round brackets) of the layer formation or heatus stage (in My), Δt_{trap} duration of the trap formation (see text). *Number of steps* number of time-steps of given stage formation (it is equaled to a number of depth-steps of during sedimentation). In the "Lithology" column: *Sandst.* Sandstone and *Limest.* Limestone. Stages *1–16* subtrappean sedimentary complex, stages *20*, *21* posttrappean sedimentary complex

are included in the Basin history. Two last sedimentation periods in Table 8.1 (20 and 21) are corresponded to formation of the post-trappean complex. The lower part of the complex of the Eocen-Oligocene age is presented by clays, whereas the upper part of the complex—by sandy clays. Table 8.1 has no pretensions to detailed and exact description of rock lithology. It gives only general characteristics of rock composition in the sub- and over-trappean complexes. This information is enough to estimate a general trend in formation of maturity aureole in the subtrappean sedimentary complex and realization of hydrocarbon potential of these rocks.

8.3.2 *Modeling of Burial and Thermal Histories of the Basin*

Figures 8.4a, b show the burial history of the Basin, reconstructed numerically by usual "back-stripping" procedure with consideration of change in porosity with the depth, time and lithological composition of the rock (Sect. 1.1.1). The reconstructions are based on initial data in Table 8.1. The Figures demonstrate rather fast subsidence of the basement in the first initial and last Cenozoic stages of the Basin development and during deposition of the Deccan Trap too. Temperature distribution within the domain included the trap and sedimentary complexes, and the underlying lithosphere of the Basin is determined from numerical solution of the of one-dimensional non-steady heat transfer Eq. (1.1) without convective member. Our modeling considers the processes of sedimentation, heatus, erosion and trap formation. As mentioned above, the most important feature of Eq. (1.1) is significant variations of its petrophysical parameters depending on lithological composition, porosity, φ, and temperature, T of the rocks (Sect. 1.1.1). These variations make Eq. (1.1) considerably nonlinear and determine significant changes in temperature gradient with depth and time of the Basin development. Thermo-physical parameters of basalt were described in Sect. 7.2.2 (Fig. 8.4).

In our modeling, temperature distribution is computed not only in sedimentary sections but in the underlying basement too. Table 8.2 determines the structure and thermophysical attributes of the Indian Shield lithosphere at initial stage of the basin development (before its stretching). This Table was constructed on the base of geological, geophysical and geochemical studies of the present-day lithosphere of the Indian shield [29–31]. It differs from Table 1.1 only by thickness of granitic and "basaltic" layers and radiogenic heat generation. According to Table 8.2,

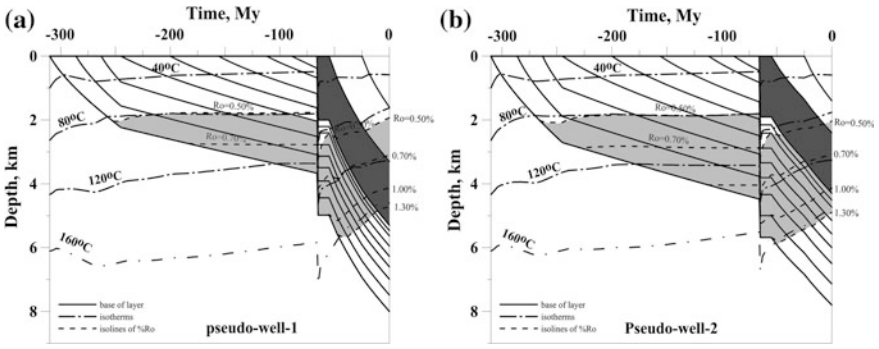

Fig. 8.4 Numerical reconstructions of burial, thermal and maturation histories of sedimentary sections of subtrappean and overtrappean complexes of the pseudo-wells 1 and 2 in the western passive margin of India [25]. Locations of the profile and pseudo-wells are shown in Figs. 8.1, 8.2 and 8.3. The reconstructions shown in Figures a, b were obtained without consideration of contribution of heat of the trap (so called "background" variant). *Dark grey color* marks the position of the Trap, while the *light grey* is the position of the "oil window" ($0.50 \leq$ Ro ≤ 1.30 %)

Table 8.2 Structure and thermophysical parameters of the Indian continental lithosphere used as an initial model of the Indian shield lithosphere before stretching [29–31]

Layer	Granitic			"Basaltic"	Mantle
Depth of the layer base (km)	1.0	11.0	20	36.0	>36
Density (g/cm^3)	2.75	2.75	2.75	2.90	3.30
Heat onductivity (W/m K)	3.30	3.15	2.80	1.90	K = f(T)
Radiogenic heat production (mkW/m^3)	3.30	1.40	0.20	0.10	0.00

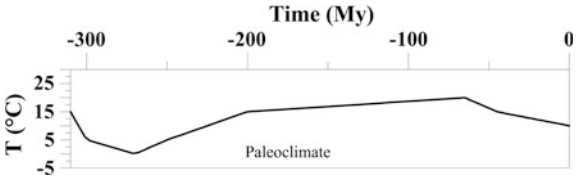

Fig. 8.5 Paleoclimate curve for pseudo-wells 1 (Bombay offshore) constrained with consideration Permian glacial period and variations in sea depth in the Cenozoic (Line 4 in Fig. 8.6). The *curve* presents temperatures at the surface of sedimentary blanket and therefore at the bottom sea when the sea occurs

contribution of radiogenic heat from the rocks of the consolidated crust to the surface heat flow was about 20.7 mW/m^2 at the stage of the basin origination. 80 % of this contribution is provided by the granite layer of thickness 11 km. The release or consumption of the latent heat of fusion during trap formation is considered in enthalpy approach described in Sect. 1.1.3 with parameters of melting of basalt presented in Sect. 7.2.2. By analogy with Sect. 7.2.2 the temperature of basaltic melts is taken rather high (T = 1100 °C). This helps to explain low viscosity of effusive basalts during trap formation and the spreading of the lava over large distances from the crack [32].

In solution of the Eq. (1.1) the temperatures varying with the time of the Basin development were adopted at the top (z = 0) of the domain (Fig. 8.5). These temperatures are corresponded to mean-annual temperatures at the Basin surface (paleoclimate curve). They took in consideration the Permian glaciation and changes in paleosea depth (see curve 4 in Fig. 8.6). In all of the considered reconstructions, the temperature T = 1160 °C was held at the base of the domain for temperature calculation during all the time of the modeling (see Sect. 1.1.4). Depth of the base was about 110 km at the time of the Basin initiation and then increased by the value that did not exceed the thickness of sedimentary cover (Fig. 8.7). It can be noted that a depth of lower boundary of the domain for temperature computation in our modeling was close to the base of the Indian Shield lithosphere. Indeed, geophysical estimates show that the present base of the Indian lithosphere is nearly 117 km and average depth of the MOHO boundary is about 40 km [33].

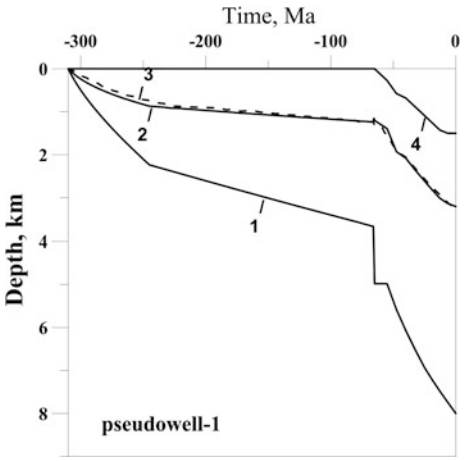

Fig. 8.6 Variations in the tectonic subsidence of the western passive margin of India calculated for sedimentary section of the pseudo-well 1 assuming an isostatic response of the Basin lithosphere to the load. See legend in Fig. 1.3c

Initial temperature distribution needed for solution of the Eq. (1.1) was obtained by solution of the steady-state variant of the heat transfer Eq. (1.1) (see Sect. 1.1.4) with initial heat flow (75 mW/m^2) and heat conductivity, K(z), and heat generation, A(z), of the basement rocks from Table 8.2. Relatively high initial heat flow is in agreement with variations of tectonic subsidence in Fig. 8.6. It was relaxed during the first 50–70 My of the basin development and therefore its value had not a noticeable influence on the modeling results (Fig. 8.7).

In all of the modeling variants, the scheme of the basin formation of Table 8.1 was adopted, that includes 16 stages of formation of under-trap complex of different

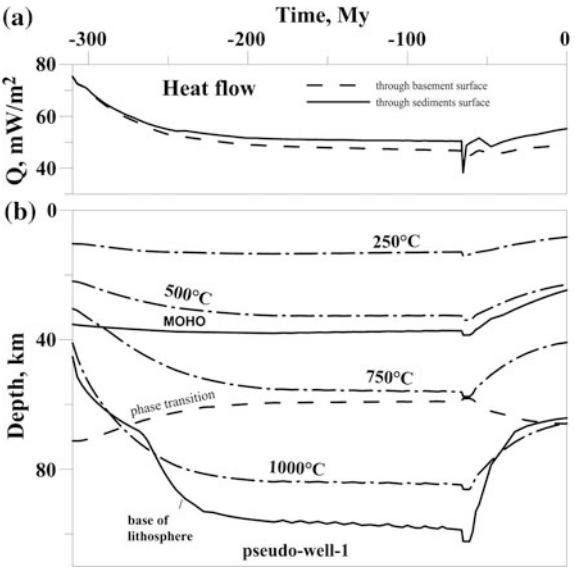

Fig. 8.7 Computed variations in heat flow (**a**) and evolution of the lithosphere thermal regime (**b**) of the Basin in the western passive margin of India (pseudo-well 1 in Fig. 8.3). The thermal history presented in this Figure was reconstructed without consideration of the Trap heat contribution (so called "background" variant). See legend in Fig. 1.3a, b. Sharp decrease in surface heat flow in Fig. a about 65 million years ago is due to the rapid formation of the trap complex

duration. The 17-th stage is an heatus (no sedimentation, no erosion). It lasts for about 1 million years, during which a time step of temperature calculation is gradually reduced from 75 thousand years, typical for the last deposition stage of the subtrappean complex, up to 8 days, typical for the stage of the trap formation (Table 8.1). The 18-th stage is the trap formation. This process is simulated in the modeling by successive deposition of 1000 elementary layers of melted basalt of thickness of 1.9–2 m on the basin surface with time-steps ranged from 2 to 32 days. Duration of the trap formation could range from 1 to 200 years depending on total trap thickness. Variations in duration of trap formation allow consideration of the models with minimal and maximal size of maturity aureole (see Sect. 7.2.3 and below). The 19-th stage of the basin development is again interruption (Table 8.1). It lasted about 11 My. During the stage, time step was gradually increasing from 2–32 days, typical for the stage 18 of the trap formation to 50–200 thousand years, typical for the first deposition stage of the post-trapean complex (Table 8.1). The stages 20-th and 21-th describe a formation of the post-trapean sedimentary complex in the western passive margin of India. The analysis of tectonic subsidence of the Basin in next section shows, that the Basin lithosphere at considered areas of the passive margin was subjected by intensive stretching in the Cenozoic that was accompanied by a significant deepening of the sea. A heating of the Basin lithosphere was also a consequence of this stretching (Fig. 8.7b). This heating led to increase of maturation of organic matter in sedimentary rocks together with the earlier effect of heat from the trap (see below).

8.3.3 Analysis of Tectonic Subsidence of the Basin

Variations in the modelled tectonic subsidence of the Basin in the area of pseudo-well 1 are shown in Fig. 8.6. The solid line 2 represents here the tectonic subsidence obtained by removing water and sediment loading from the basement surface in a conventional "backstripping" procedure (Sect. 1.2.1). The dashed line 3 describes tectonic subsidence determined by the variations with time in depth-density distributions within the basement (Sect. 1.2.2). In the western passive margin of India on the area of the pseudo-well 1, an analysis of variations in tectonic subsidence is in agreement with following factors in the Basin history: relatively high initial heat flow 75 mW/m^2, slow lithosphere extension in the Jurassic-Cretaceous (from 180 to 70 Ma with little total amplitude $\beta = 1.05$) and intensive stretching during post-trapean time (from 60 to 0 Ma with a great summary amplitude $\beta = 2.00$). As result of lithosphere extensions, the thickness of consolidated crust reduces from initial value 36 km to present-day 17 km (see the "MOHO" line in Fig. 8.7b) and the sea depth increases from 0 up to 1500 m (line 4 in Fig. 8.6). As mentioned above, the last intensive stretching is reflected in enhance of thermal regime of the Basin lithosphere (Fig. 8.7b).

The area of the pseudo-well 2 in the western passive margin of India is characterized by lesser sea depth than the pseudo-well 1 area (1100 m instead 1500).

As consequence of this fact, the lithosphere stretching here was more moderate. Similarly to the area 1, an analysis of tectonic subsidence suggests here slow lithosphere extension in the Carboniferous-Permian (from 308 to 250 Ma with amplitude $\beta = 1.04$), extension in the Jurassic-Cretaceous (from 180 to 70 My with the same amplitude $\beta = 1.04$) and intensive stretching in the Cenozoic (from 60 My to present time with $\beta = 1.60$). As a result, the thickness of consolidated crust in the area 2 reduces from initial 36 km to the present-day thickness of 21 km.

8.3.4 *Maturation of Organic Matter in the Over- and Sub-Trappean Sedimentary Complexes*

An estimation of the maturity of organic matter in this section was based on calculations of vitrinite reflectance Ro(%) using the EASY kinetic algorithm (Eqs. (3.1)–(3.3) in Sect. 3.2.2). In Fig. 8.4a, b, the dotted lines demonstrate variations in the depths of the Ro-isolines during the burial history of the Basin. These depths do not take into account the thermal effect of traps, i.e. it is the so-called background version. Figure 8.8 illustrates variations in vitrinite reflectance, Ro%, modelled for present-day sedimentary sections of the western passive

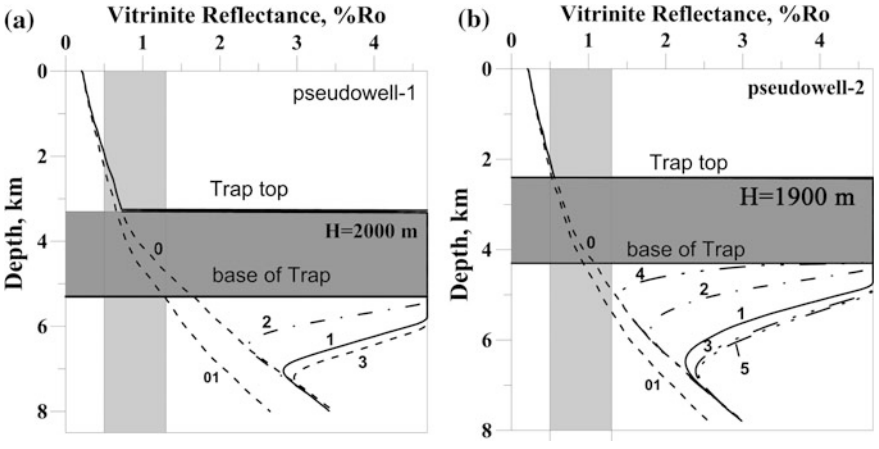

Fig. 8.8 Distribution of vitrinite reflectance versus depth (maturity aureole) in the sub- and over-trappean complexes computed for different durations of the Trap formation in the section of pseudo-well 1 (**a**) and pseudo-well 2 (**b**). *1* variant corresponded to the mean rate of the Trap formation like to the Lakki Lake in Iceland, that is $V_1 = 0.022$ m/90 days (Sect. 7.2.2). Then, the trap of thickness 2000 m (pseudo-well 1) was created within the time-interval $\Delta t = t1 = 22.7$ years, and the trap of thickness 1900 m (pseudo-well 2) was created during the time-interval $\Delta t = t1 = 21.6$ years. *2* and *3* variants of the trap formation within the time $\Delta t = t1 \times 4$ and t1/4. *4* and *5* (in b) variants of the trap formation within the time $\Delta t = t1 \times 16$ and t1/16. *0* "background" variant corresponded to computation without consideration of the Trap heat contribution. *01* the variant 0 but without the Cenozoic stretching of the Basin lithosphere (see text)

margin of India. They are calculated as with consideration of heating effect of the Deccan trap (lines 1–5) as without this effect (lines 0 and 01). As mentioned above, intensive stretching of the lithosphere in Cenozoic led to an additional heating of sediments and increase of maturity level, that can be assessed by comparison between lines 0 and 01 in Fig. 8.8. The lines 0 and 01 reflect the background versions, therefore they are computed without consideration of heat contribution from the trap. In the variant 01, the distribution %Ro(z) is obtained without consideration of the lithosphere stretching, whereas the variant 0 (and 1–5 also) took into consideration the stretching of the lithosphere. The Carboniferous rocks at the base of sedimentary sections located at depth of 8000 and 7800 m in the 1 and 2 areas reach a maturity level Ro = 3.47 and 3.01 % in the "background" variants 0 and only Ro = 2.65 and 2.55 % in the "background" variant 01 when stretching of the lithosphere is not considered (Fig. 8.8a, b).

As mentioned above, duration of the trap's formation is the most critical and indefinite parameter in the modeling. A comparison between the measured and computed distributions vitrinite reflectance Ro(z) as a function of distance from surface of the "well dated" intrusions gives an opportunity to estimate duration of the intrusion's formation (see for example Sect. 7.1.2). The time-interval of the Deccan Trap formation estimated in literature ranges in wide limits from 50,000 to 2,000,000 years [9, 32]. Such estimates are very rough, but detailed measurements of Ro in the sub-trappean complex of the Deccan Trap are absent. For this reason, the modeling uses rough estimate of the minimal time of trap formation on the base of the data for the Lakki volcano in Iceland, considered in Sect. 7.2.3. Taken such mean rate of trap formation (V = 0.022 km/90 days), it can be obtained that the trap complexes of total thickness Δz = 1, 100 and 1000 m could be formed during the time-intervals t1 = 4.1, 409 and 4091 days (11.36 years) correspondingly. It is clear that these times are close to the minimally possible duration of trap's formation but not to its actual values. Note that maturity aureoles received with the formation time t1 or less are close to the ones obtained in the model of instantaneous trap formation (compare lines 1, 3 and 5 in Fig. 8.8b).

The lines 0, 1–5 in Fig. 8.8 give an opportunity to estimate an influence of duration of the Trap formation on maturity aureole. They show that thermal effect of the Trap is widening together with its maturity aureole when duration of the Trap formation reduces. Indeed, the maturity level of the Hauterivian rocks of age 136 My located at the depth of about 5000 m in modern section (700 m below the trap base) is equaled to Ro = 1.35, 1.41, 2.6, 4.25, 4.55 and 4.61 % for duration of the Trap formation 346, 86.4, 21.6, 5.4, 1.35 and 0 years (curves 4, 2, 1, 3, 5 and 0 in Fig. 8.8b). A similar situation takes place in Fig. 8.8a for the pseudo-well-1. Thus, at very slow formation of the Trap, part of the Upper Cretaceous rocks could occur within the "oil window".

In Sect. 7.2.4, the influence of several other factors on the size of maturity aureoles was discussed. The first factor concerned with the continuity of the process of trap formation. There was noted that some traps were formed during several stages every of which created its layer of the trap [1–3]. Total duration of trap complex formation is assessed usually by 1–2 My. This time interval can contain several interruptions. Then, if duration of these interruptions is much longer than the typical

time of cooling of the corresponding trap layer, the maturity aureole of such trap complex will be determined by the aureole of the first trap layer nearest to underlying sedimentary complex (Sect. 7.2.4). In this case, the size of maturity aureole of total trap complex must be close to the aureole of the first single trap layer (under condition that durations of the interruption periods and the thickness of the trap layers are about the same. A change the size of maturity aureole under the influence of such factors as the lithological composition of the rocks in subtrapean complex and variation in the melting parameters of basalt (L—latent heat of fusion, Ts and Tl—solidus and liquidus temperatures of basalt) were discussed in Sect. 7.2.4.

8.3.5 *Realization of Hydrocarbon Potential by Probable Source Rocks of Sub- and Over-Trappean Sedimentary Complexes in the Bombay Offshore*

Several offshore sub-basalt gas discoveries are found in anticlinal traps with a Cretaceous deltaic sandstone reservoir on the Kutch Basin sealed by Deccan trap basalts and shales [23]. Jurassic or Cretaceous gas has probably been sourced from type III source rocks. In general, subtrappean sedimentary complex contains several formations, which are considered as probable source rocks in the Bombay offshore. Among these, there are the Talhir formation of age 290–300 My with TOC = 1–1.9 %, Barakar formation of age 284–285 My with TOC 1–3 %, Pachmarhi formation of age 245–250 My with TOC up to 10 %, Pranhita-Godavary formation of age 200 My with TOC = 3.6–6.4 % [24]. Results of modeling will be used below to calculate variations in hydrocarbon generation by the rocks of the above formations and assess an influence of the Trap formation on the generation process. The calculations are carried out with use of the kinetic spectra for kerogen of terrestrial type III with initial potential HI = 160 mg HC/g TOC in the 4-th fractions model (heavy and light oil, gas and coke). These spectrum was worked out in French Petroleum Institute and applied in the well-known computer package MATOII. Consider the mentioned formations on the example of the pseudo-well-2 section sequentially, starting with the oldest and ending with the younger.

The Talchir fm. The rocks of this formation of age 298 My locate at a depth of 7470 m (3170 m under the base of the Trap; Table 8.1) and reach a maturity level of Ro = 2.85 % in all of the models in Fig. 8.8b. The reason for the same maturity in all variants is that the modern temperature rocks (about 250 °C) exceeds the temperature maximum reached by these rocks during the formation of Trapp. The latter are equaled to 220, 185 and 170 °C in 1-th, 2-th and 4-th versions of the Trap formation (Figs. 8.8b and 8.9a). The histories of realization of hydrocarbon potential by the rocks of the Talchir fm. are also close to each other in different versions of the Trapp formation. Generation of heavy oil decreased slowly before the Trap formation and decreased quickly up to zero during the Trap formation (Fig. 8.9b). Generation of light oil increased and then decreased to zero during 30

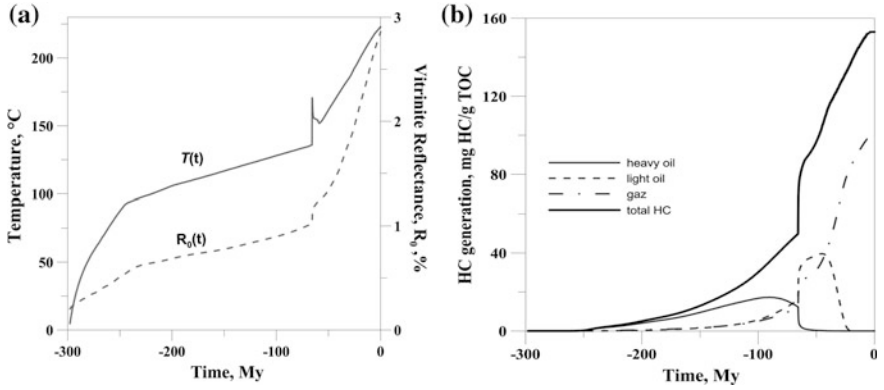

Fig. 8.9 Variations in temperature and maturity level (**a**) and realization of hydrocarbon potential (**b**) in burial history of the Talchir formation the age of 298 My at the pseudo-well-2 area of the western passive margin of India [25]. A variant of the slowest formation of the Trap is presented here (curve 4 in Fig. 8.8b). The parameters of the Talchir fm. in present-day sedimentary section of the Basin: depth from sea bottom—7468 m; depth from the Trap base—3168 m; initial hydrocarbon potential—HI=160 mg HC/g TOC

My of burial history of the formation after the trap formation (Fig. 8.9b). Gas generation increases up to present time.

The Barakar fm. A depth of the Barakar fm. in present-day section is less than the one of previous formation only by 300 m (Table 8.1; Fig. 8.4b). Therefore, the generation history of the Barakar fm. is close to it of the Talchir fm. (Fig. 8.10a, b). The rock temperature before and during the Trap formation was a little lower than in previous fm. (Fig. 8.10a). That is why, a generation of heavy oil continued rising up to the Trap formation (Fig. 8.10b). A degradation of light oil occurred here some later than in Fig. 8.9b. As above, gas generation increases up to present time (Fig. 8.10b).

The Pachmarhi fm. The Pachmarhi fm. of age 253 My is closer to the base of the Trap by 1000 m than previous formations. Therefore, the temperature jumping caused by the Trap formation in the variant 1 is here by 50 °C higher than the present-day temperature of the rock (Fig. 8.11a). Heavy and light oil have degraded totally even during the Trap formation (Fig. 8.11b). At more slow formation of the Trap (variant 2 in Fig. 8.8b), the temperature jumping due to the Trap formation is lesser (Fig. 8.11c) and the light oil degrades later (Fig. 8.11d). And finally, in most slow variant of the Trap formation (variant 4 in Fig. 8.8b), more moderate temperature history (Fig. 8.11e) results in more later degradation of heavy oil, more later generation of light oil and its degradation only during the last 5 My (Fig. 8.10f). Then it would be light oil could be saved if the oil migrated to higher horizons.

The Pranhita-Godavari fm. The Pranhita fm. of age 200 My (boundary between Triassic and Jurassic) is located even closer to the Trap than the previous formation and thermal effect of the Trap is higher here (1270 m from the base of the Trap; Table 8.1; Figs. 8.4b and 8.12a, c, e). The heavy and light oil generated in the 1 and

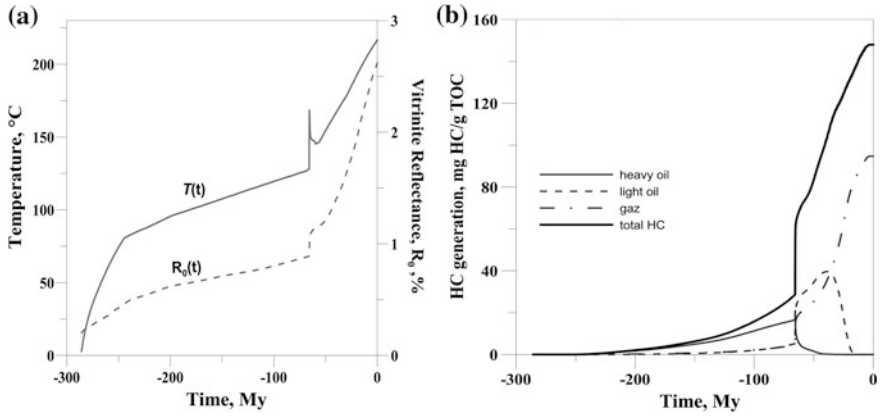

Fig. 8.10 Variations in temperature and maturity level (**a**) and realization of hydrocarbon potential (**b**) in burial history of the Barakar formation the age of 286 My at the pseudo-well-2 area of the western passive margin of India [25]. A variant of the slowest formation of the Trap is presented here (curve 4 in Fig. 8.8b). The parameters of the Barakar fm. in present-day sedimentary section of the Basin: depth from sea bottom—7136 m; depth from the Trap base—2836 m; initial hydrocarbon potential—HI = 160 mg HC/g TOC

2 variants of the trap formation have degraded quickly up to zero during the Trap formation (Fig. 8.12b, d). More moderate temperature regime of the Pranhita fm. in the variant 4 (formation of the Trap during 345 years; Figs. 8.8b and 8.12e) leads to more slow degradation of heavy oil and to maximal generation of light oil during the last 5–10 My (Fig. 8.12f).

And finally Fig. 8.13 demonstrates thermal and maturation history of the the sedimentary formation of the age 134 My that is most close to the Trap base (4960 m from the sea bottom and 640 m from the base of the Trap; Table 8.1; Figs. 8.4b and 8.13). It is suggested in Fig. 8.13 that duration of the Trap formation was 21.6 years (curve 1 in Fig. 8.8b). Temperature about 340 °C and maximal maturity level were reached in these rocks during the Trap formation (Fig. 8.13).

However, it should be emphasized that many of the formations discussed above could be within the "oil window" if the formation of the trap was very slow.

Now we consider shortly the overtrappean complex. The study of sedimentary rocks in the region indicate that Paleocene to early Eocene Panna Formation has good to excellent source rock characteristics in the basinal part of every block in the entire basin. The Panna source rocks have predominantly Type III kerogen in lower horizons and Type II and III mixed kerogen in upper horizons. Initial potential HI = 112–277 mg HC/g TOC is typical for the formation [34]. However, Fig. 8.8a, b shows, that the rocks of the Panna fm. are immature or early mature and hydrocarbon generation by kerogen of type III in the formation is very limited at the areas of Pseudo-wells 1 and 2 in the Bombay offshore.

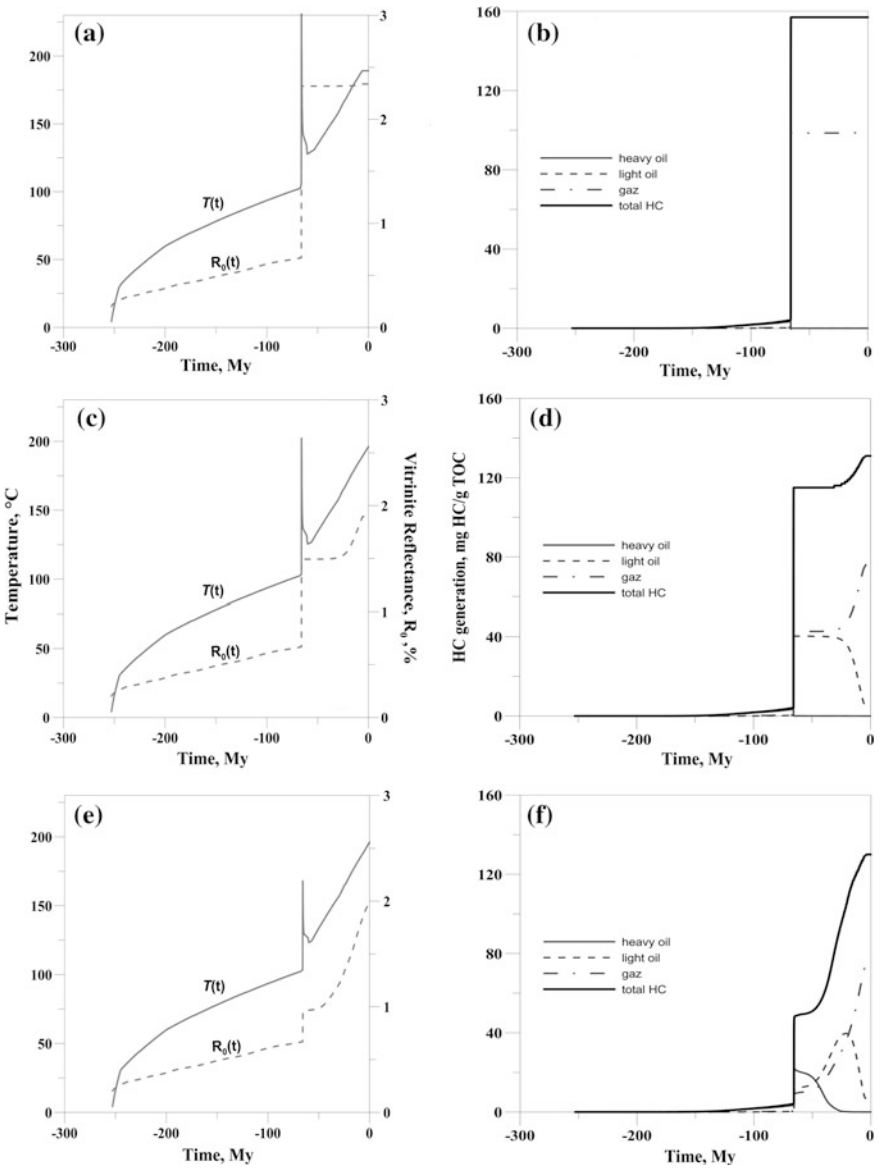

Fig. 8.11 Variations in temperature and maturity level (**a**) and realization of hydrocarbon potential (**b**) in burial history of the Pachmarhi formation the age of 253 My at the pseudo-well-2 area of the western passive margin of India [25]. Calculations were carried out for different durations of the Trap formation: *1* during 21.6 years (Fig. a and b; curve 1 in Fig. 8.8b); *2* during 86.4 years (Fig. c and d; curve 2 in Fig. 8.8b) and *3* during 345 years (Fig. e and f; curve 4 in Fig. 8.8b). The parameters of the Pachmarhi fm. in present-day sedimentary section of the Basin: depth from sea bottom—6222 m; depth from the Trap base—1922 m; initial hydrocarbon potential—HI = 160 mg HC/g TOC. Comparison between pairs Figure (**a**, **b**), (**c**, **d**) and (**e**, **f**) takes an opportunity to estimate influence of duration of the Trap formation on hydrocarbon generation by the subtrappean rocks

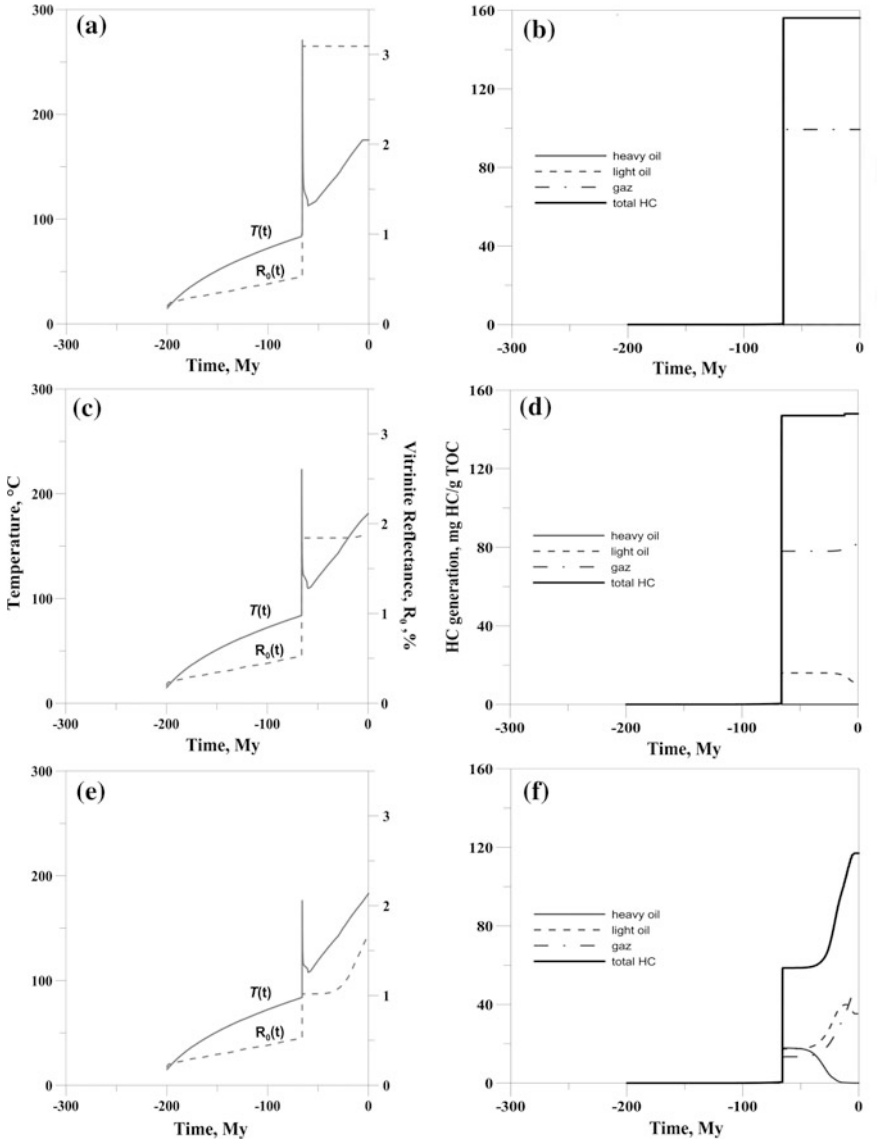

Fig. 8.12 Similarly to Fig. 10, but for the Pranhita formation of age of 200 My. The parameters of the Pranhita fm. in present-day sedimentary section of the Basin: depth from sea bottom—5570 m; depth from the Trap base—1270 m; initial hydrocarbon potential—HI = 160 mg HC/g TOC

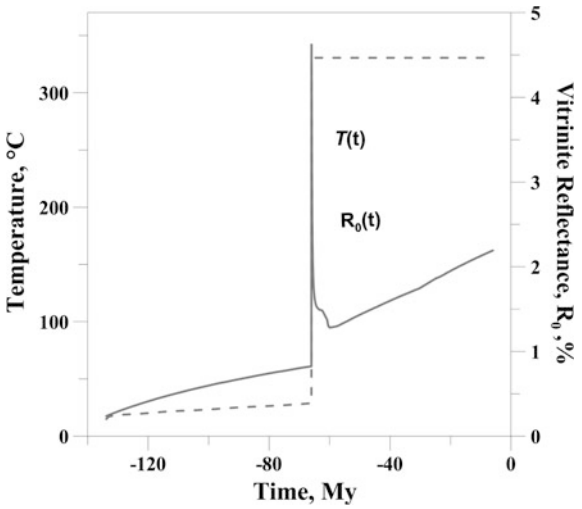

Fig. 8.13 Variations in temperature and maturity level in burial history of the sedimentary formation the age of 134 My [25]. Computation was carried out in variant of curve 1 in Fig. 8.8b. The formation is at depth of 4960 m below the sea bottom and only 640 m below the base of the Trap complex

8.4 The Subtrappean Basins of the Indian Shield

8.4.1 Saurashtra Region, North-Western India (Profile 1)

The pseudo-wells 3–5 locate in the profile 1 crossing the Saurashtra region in the North-Western India (Fig. 8.1). Geological section of the profile is shown in Fig. 8.14. It was constructed on the base of the data from the geo-electrical section along Bhangor, Mulila, Lodhika and Kamalapur in the Saurashtra region of India discussed in detail in [17]. Pseudo-well 3 corresponds to a maximal thickness of the Trap (1300 m) and maximal subtrapean sedimentary complex (2400 m) in the profile 1. Pseudo-well 4 is characterized by more moderate thickness of the trap (700 m) and subtrappean sedimentary complex (1000 m). At last, the pseudo-well 5 corresponds to a total lack of Trap and sedimentary complex of about 1500 m (Figs. 8.14 and 8.15e, f).

In situation of the trap 700 m thick (p-w 4; Fig. 8.15c, d), the Carboniferous rocks at the base of modern sedimentary section (at depth of 1700 m) reaches also a rather low maturity level (Ro = 0.50 %) in the background variant 0 (without heat from trap). The same rocks reach more high maturity level, when duration of the trap formation decreases (Fig. 8.15d). This level increases from Ro = 0.52 % for continuous trap formation during 100 years to Ro = 0.67 % for the formation during the time $\Delta t = t1/4 = 1.99$ years. Recall that the time-interval t1 corresponds to the trap formation with mean rate of the Iceland Lakki Lake formation (V_1 = 0.022 m/90 days). It is about 8 years for the 700 m trap of the p-w 4 (main variant in Fig. 8.15d). Duration of the Trap formation influences on maturity aureole in a considerable degree. Let us consider the "width" of the aureole as the distance from the base of the trap complex to sedimentary rock in subtrappean complex with maturity level of Ro = 1.5 %. Then, increase the duration of the Trap formation

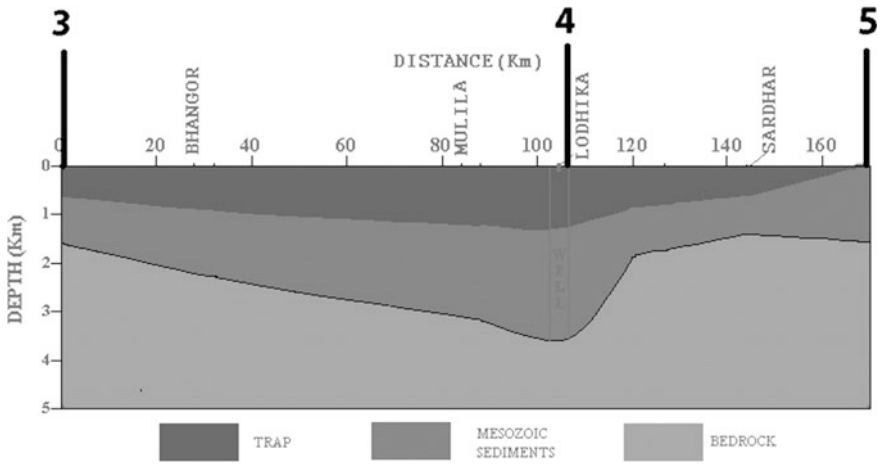

Fig. 8.14 The sedimentary section along the profile 1 (Fig. 8.1) constructed on the base of geo-electrical study of the region along the profil "Bhangor—Mulila—Lodhika—Kamalapur" (after [17] with little changes)

from 2 years (t1/4) to 100 years (12.5 × t1) leads to a decrease the "width" of the maturity aureole from 520 m to about 30 m (Fig. 8.15d). Thus, we see that, the Carboniferous and Triassic rocks occur at present time within the "oil window" at extremely rapid formation of the trap. At the same time, the Jurassic and Cretaceous rocks will generate mainly gas in the variants with the same rates of the Trap formation. Note, that the results for instantaneous formation of the trap don't differ considerably from the ones for the Trap formation during $\Delta t = t1/4$ (Fig. 8.15b, d). In more real variants when the trap was formed during 100 and more years, most of the subtrapean sedimentary complex will be immature, and only sediments within 100 and less 1 m near to the trap could generate gas and oil.

The trap complex of 1300 m (p-w 3) is characterized by a more wide maturity aureole (Fig. 8.15a, b). A maturity of Carboniferous organic matter in the rocks at the base of sedimentary section (at depth of 3700 m) increases from Ro = 0.835 % in the background variant 0 (without heating from trap) to Ro = 0.91, 0.95, 0.99, 1.08 and 1.17 % in the variants with duration of the trap formation 200 (13.5 × t1), 100 (6.8 × t1), 59 (4 × t1), 14.8 (t1) and 3.7 (t1/4) years, correspondingly. Thus, the "width" of the maturity aureole increases from 80 to 360, 865, 1200 and 1570 m, correspondingly (Fig. 8.15b). The Upper Carboniferous to Middle Permian rocks within the lowest 800 m of the modern subtrappean sedimentary section occur in the upper half of the "oil window" in the case of extremely rapid formation of the 1300 m trap ($\Delta t = t1$ and t1/4), whereas the Upper Permian, Triassic, Jurassic and Cretaceous rocks must generate mainly gas. Similar results will be for instantaneous formation of the Trap. In more real variants of the trap formation during 200 and more years, most of the subtrapean sedimentary complex will be within the zone of moderate and intensive oil generation ($0.65 < Ro < 1.3$ %), and only very thin

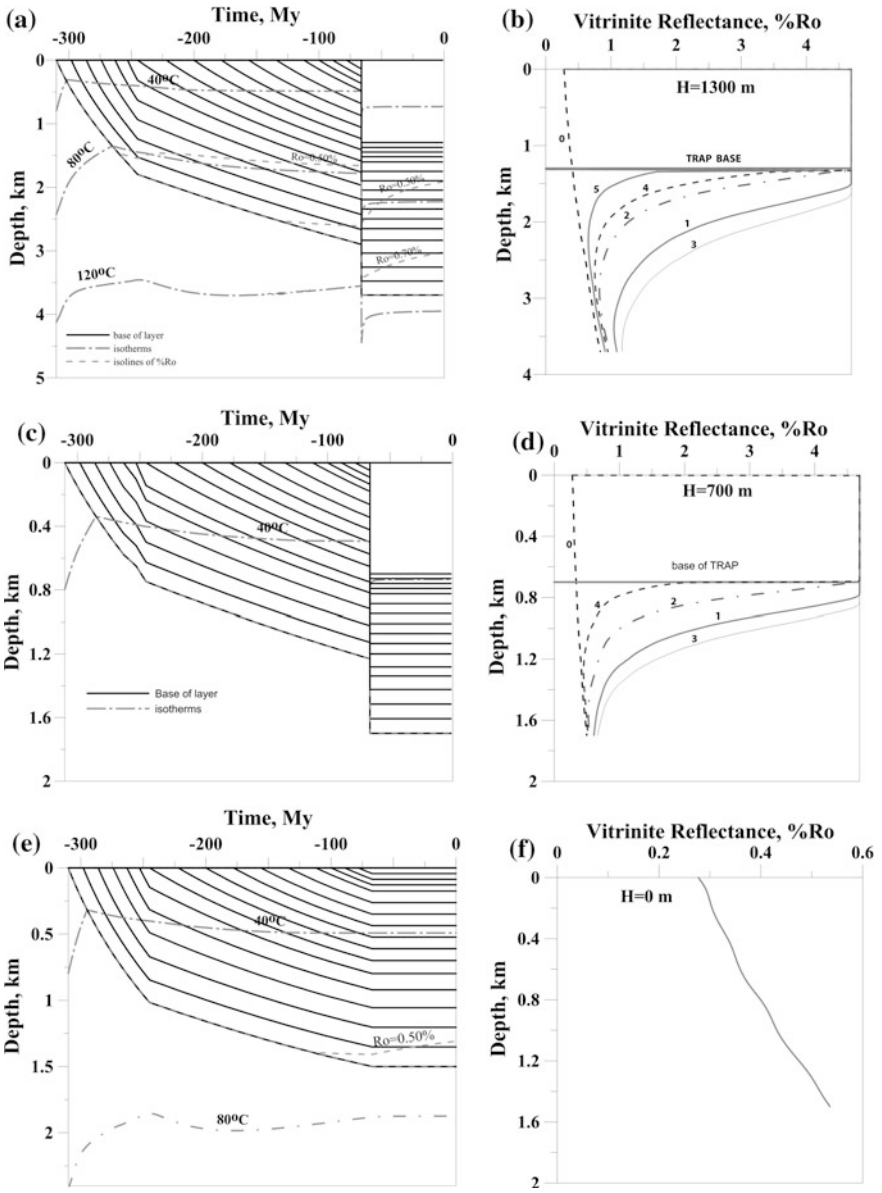

Fig. 8.15 Numerical reconstruction of burial, thermal and maturation histories of pseudo-wells 3–5 along the profile 1 in Saurashtra region of North-Western India (line 1 in Figs. 8.1 and 8.14). **a**, **c**, **e** Burial, thermal and maturation histories of sedimentary sections of subtrappean and trappean complexis received without contribution of the Trap heat (so called background variant). **b**, **d**, **f** Distribution of vitrinite reflectance versus depth (maturity aureole) in the subtrappean complex computed for different duration of the Trap formation: variant 1 (main) corresponds to the mean rate of the Trap formation similarly to the Lakki Lake in Iceland, that is V_1 = 0.022 m/90 days. Then, the Trap of 1300 m (p-w 1) was formed during the time t1 = 14.8 years, whereas the Trap of thickness 700 m (p-w 2) was created within t1 = 7.95 years. Variants 2, 3, 4 and 5—the trap formation during the time $\Delta t = 4 \times t1$, t1/4 and 100 and 200 years, correspondingly. Variant 0 corresponds to computations without contribution of the Trap heat (background variant)

sedimentary layer thickness less than 100 m nearest to the Trap will be within the gas windows.

As mentioned above, the pseudo-well 5 corresponds to a total lack of the Trap complex. The thickness of sedimentary complex is here about 1500 m (Figs. 8.14 and 8.15e, f). Results of modeling shown in Fig. 8.15e, f demonstrate that organic matter in sedimentary rock of the pseudo-well 5 (without trap) is immature at present time (Ro = 0.53 %).

8.4.2 *Kutch Region, North-Western India (Profile 2)*

Profile 2 (Figs. 8.1 and 8.16) in the Kutch region of the North-Western India includes the pseudo-wells 6, 7 under modeling. This profile was constructed using geo-electrical section Suthri-Nakhatrana based on the Deep Resistivity Soundings (DRS) studies in the region [17]. The sections of pseudo-wells 6 and 7 include the Trap of moderate thickness (400 and 670 m) and subtrapean sedimentary complex thickness of 3150 and 3800 m. The sedimentary section of pseudo-well 7 differs principally from the sections 3–6 by presence of post-trappean sedimentary complex—the Oligocene-Neogene sedimentary cover thickness of 300 m (Fig. 8.17c). Figure 8.17b, d demonstrate that a heat influence of the traps on maturation of organic matter is limited by distance of 400–700 m from the trap base in all variants of the traps formations considered in Fig. 8.17. Indeed, the values of Ro at distances over 1 km in Fig. 8.17b and 2 km in Fig. 8.17d from the base of the Trap do not differ from background values. The Carboniferous rocks at the base of sedimentary section reach a maturity level of Ro = 0.97 % at depth of 3550 m in pseudo-well 6 and Ro = 1.37 % at depth of 4770 m in pseudo-well 7. Increase in duration of formation of the 400 m trap from 1.1 to 18.2 years in the section of the pseudo-well 6 leads to decrease in "width" of the maturity aureole from 230 to 96 m and then to less than 5 m for duration 145.4 years (Fig. 8.17b). Thus, a considerable part of the Carboniferous, Permian, Triassic and even Jurassic rocks occur in zone of intensive

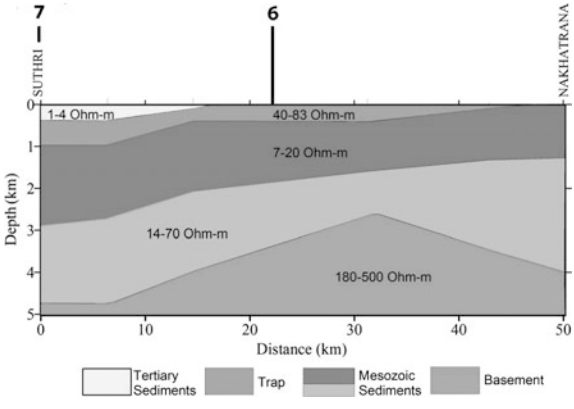

Fig. 8.16 Sedimentary section included pseudo-wells 6 and 7 on the profile 2 in the Kutch region of North-Western India (Fig. 8.1) constructed using the geo-electrical section Suthri-Nakhatrana based on the Deep Resistivity Soundings (DRS) in Kutch region, India (after [17] with little changes)

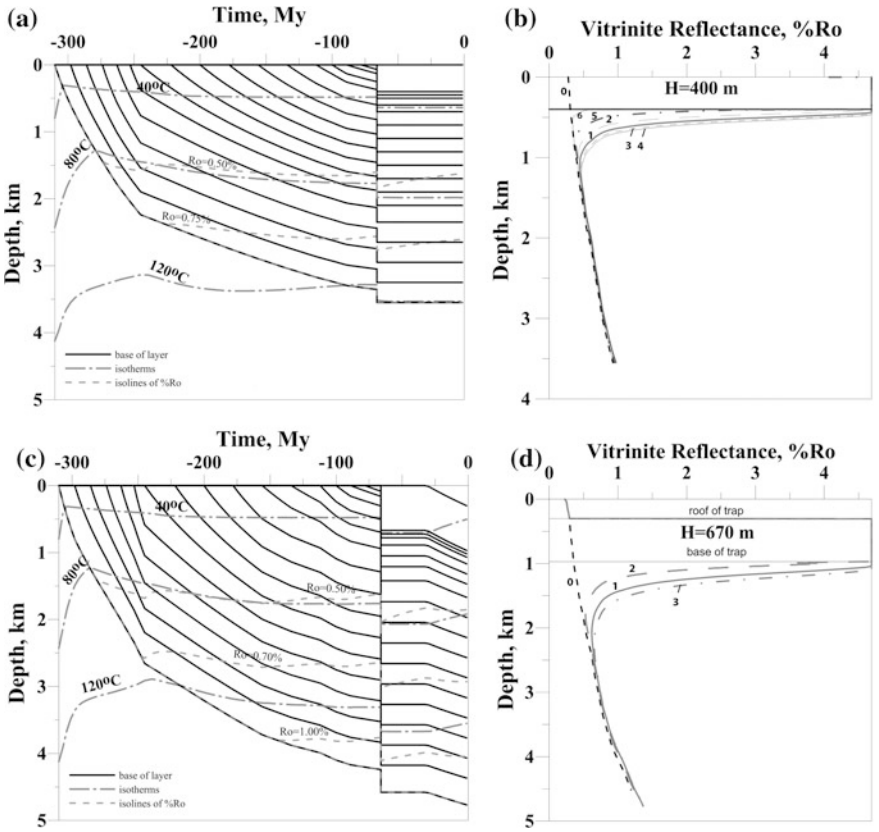

Fig. 8.17 Numerical reconstructions burial, thermal and maturation histories of pseudo-wells 6 and 7 on the profile 2 in the Kutch region of North-Western India (Figs. 8.1 and 8.16). **a**, **c** Burial, thermal and maturation histories of sedimentary sections of subtrapean and trapean complexes received without contribution of heat of the trap (so called background variant). **b**, **d** Distributions of vitrinite reflectance versus depth (maturity aureole) in the sub-trappean complex computed for different durations of the Trap formation: *1* main variant corresponds to the mean rate of the trap formation in the Lakki Lake in Iceland, that is V_1 = 0.022 m/90 days. Then, the trap of 400 m (p-w 6) was formed during the time t1 = 4.55 years, whereas the trap thickness of 670 m (p-w 7) was created within t1 = 7.6 years. Variants 2, 3, 4, 5, 6 in Fig. b—the Trap formation during the time $\Delta t = 2 \times t1$, t1/2, t1/4, $8 \times t1$ and $32 \times t1$. Variants 2 and 3 in Fig. d—the Trap formation during time $\Delta t = 4 \times t1$ and t1/4. Background variant 0 corresponds everywhere to computations without contribution of heating due to the Trap

oil generation according to maturity level reached to present time. In sedimentary section of the pseudo-well 7, the consequence of increasing the duration of formation of the 670 m trap from 1.9 to 30.4 years was the decrease in the "width" of maturity aureole from 440 to about 170 m (Fig. 8.17d). Consequently, all Jurassic, Triassic, Permian and Upper Carboniferous rocks in the present day subtrappean complex are within the "oil windows" in both of the sections 6 and 7 (Fig. 8.17). The Lower Cretaceous rocks can partly enter into this "window".

8.4.3 *Western Part of the Deccan Syneclise, Central India (Profile 3)*

Profile 3 crossing the western part of the Deccan syneclise (Figs. 8.1 and 8.18) includes the pseudo-wells 8, 9 and 10. This profile was constructed with use of the geo-electrical section along the "Vardhe Tembe-Shirpur- Saver" profile and based on the Deep Resistivity Sounding (DRS) studies in the western part of Deccan syneclise [17]. Location of pseudo-well 8 in the profile corresponds to maximal trap thickness. Sedimentary section of this pseudo-well includes 250 m of the Oligocene-Neogene sediments, the Paleocene-Eocene unconformitiy (interruption), trapean complex thickness of 1500 m, and subtrapean sedimentary complex thickness of 1950 m (Figs. 8.18 and 8.19a). Pseudo-well 9 corresponds to a maximal thickness of subtrapean sedimentary complex (Fig. 8.18). The section includes 150 m of the Oligocene-Neogene sediments, the Paleocene-Eocene unconformitiy (interruption), trappean complex thickness of 1000 m, and subtrapean sedimentary complex thickness of 2800 m (Figs. 8.18 and 8.19c). The section of the pseudo-well 10 includes 150 m of the Oligocene-Neogene sediments, the Paleocene-Eocene unconformitiy (interruption), trappean complex thickness of 900 m, and subtrappean sedimentary complex thickness of 1150 m (Figs. 8.18 and 8.19e). In background variant (Fig. 8.19 a, c, e and curves 0 in Fig. 8.19b, d, f), when heat from the Trap is not considered, the Carboniferous rocks at the base of sedimentary section of the pseudo-wells 8, 9 and 10 reach a maturity level of Ro = 0.80, 0.93 and 0.56 % at the depth of 3700, 3950 and 2200 m, correspondingly. Figure 8.19b, d, f demonstrate rather considerable influence of the Trap's heat on maturation of organic matter in subtrappean complex.

An effect of the trap's heat on maturation manifests particularly strong in the section 8 with a maximum thickness of the trap complex (1500 m). Here, maturity level of the Carboniferous rocks at the base of sedimentary section increases from Ro = 0.84 % for continuous trap formation during 274 years to 1.55 % for the formation during 1.06 year (Fig. 8.19b). The last variant does not differ from the version with instantaneous formation of the Trap. Increase the duration of the Trap

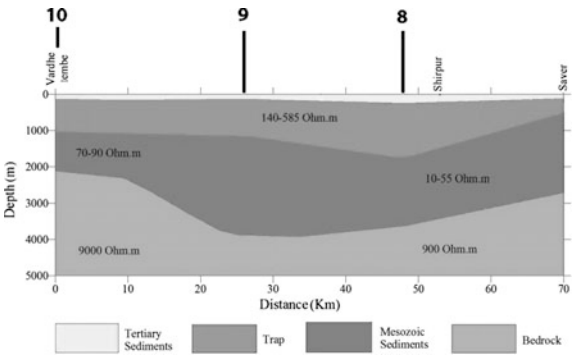

Fig. 8.18 Sedimentary section of profile 3 (pseudo-wells 6–8) in western part of the Deccan Syneclise, central India (Fig. 8.1) constructed with use of the geo-electrical section along the Vardhe Tembe-Shirpur-Saver line and based on the Deep Resistivity Sounding (DRS) (after [17] with little changes)

formation from 1 to 274 years leads to the reduction of the "width" of the maturity aureole from 1950 m (that is total thickness of the subtrappean sedimentary complex) to 50 m (Fig. 8.19b). Thus, the extremely rapid formation of the Trap makes all subtrappean complex gas prone. More real situation with duration of the trap formation 100 and more years puts the subtrappean sedimentary complex within the "oil window" ($0.50 \leq Ro \leq 1.30$ %).

In the section 9 where Trap thickness is lesser (1000 m), the heating effect of the Trap is considerably lesser. The Carboniferous rocks at the base of sedimentary section reach here a maturity level of 1.00–1.06 % in all variants of the Trap formation (Fig. 8.19d). Increase the duration of the Trap formation from 2.84 to 11.4 and to 45.5 years leads to reduction of the aureole "width" from 910 to 690 and to 350 m, correspondingly (Fig. 8.19d). Thus, the Lower Jurassic, Triassic, Permian and Carboniferous rocks of the subtrappean complex occur within the "oil window" even at extremely rapid formation of the trap, including its instantaneous formation. Increase duration of the Trap formation to more real values (100 and more years), makes the Low Cretaceous, Jurassic and Middle and Upper Triassic rocks also oil prone.

In sedimentary section of pseudo-well 10 with the Trap thickness of 900 m, the heating effect of the Trap on organic matter maturation at the base of sedimentary section is considerable because it spreads over lesser subtrappean sedimentary cover. The Carboniferous rocks at the base of sedimentary section reach maturity level, increasing from 0.62 to 0.82 %, when duration of the Trap formation reduces from 40.9 to 2.56 years (Fig. 8.19f). Increase duration of continuous formation of the Trap from 2.56 to 10.2 and 40.9 years leads to reducing of the aureole "width" from 720 to 570 and 290 m, respectively (Fig. 8.19f). Thus, the Middle and Lower Permian and Carboniferous rocks of subtrappean complex occur within the "oil window" even at extremely rapid formation of the trap, including its instantaneous formation. At more real situation with duration of the trap formation 40 and more years, the Low Jurassic, Triassic and Upper Permian rocks become also oil prone in the present day section of the pseudo-well 10 (Fig. 8.19f).

8.4.4 Central Part of the Deccan Syneclise, India (Profile 4)

The profile 4 crossing the central part of Deccan syneclise (Figs. 8.1 and 8.20) is constructed on the base of geological studies of the Thuadara-Sendhwa-Sindad profile [8]. The both of sections in the profile consist of trap complex thickness of 1000 m and subtrapean complex the thickness of which is 1900 m in the pseudo-well 11 and only 200 m in the pseudo-well 12 (Figs. 8.20 and 8.21a, c).

The Carboniferous rocks at the base of sedimentary section of the pseudo-well 11 reach a maturity level Ro = 0.70, 0.76, 0.79, and 0.84 % at the depth of 2900 m in the variant 0 (so called background distribution—without consideration of

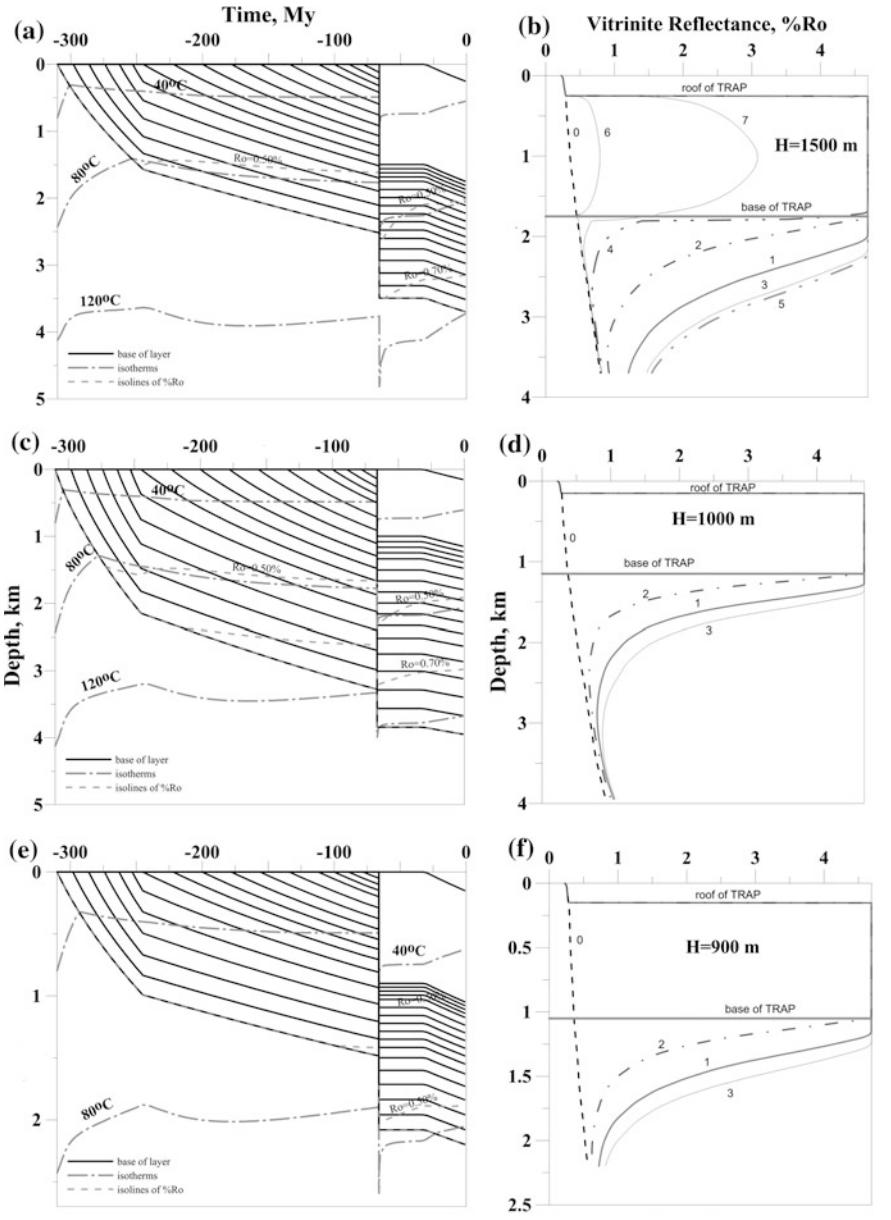
(a)
Time, My
-300
-200
-100
0
40ºC
80ºC
120ºC
Ro=0.50%
Ro=0.70%
base of layer
isotherms
isolines of %Ro
(b)
Vitrinite Reflectance, %Ro
roof of TRAP
base of TRAP
H=1500 m
(c)
Depth, km
(d)
H=1000 m
(e)
(f)
H=900 m

◀ **Fig. 8.19** Numerical reconstructions of burial, thermal and maturation histories of pseudo-wells 8–10 on the profile 3 in western part of the Deccan Syneclise, central India (Figs. 8.1 and 8.18). **a**, **c**, **e** Burial, thermal and maturation histories of sedimentary sections of subtrappean and trappean complexes received without consideration of heating due to the Trap (so called background variant). **b**, **d**, **f** Vitrinite reflectance versus depth (maturity aureole) in the subtrappean complex computed for different durations of trap formation: main variant 1 corresponds to the mean rate of the trap formation similar to the Lakki Lake in Iceland, that is V_1 = 0.022 m/90 days. Then, the trap of 1500 m (p-w 8) was formed during the time t1 = 17 years, whereas the trap thickness of 1000 m (p-w 7) was created within t1 = 11.4 years and the trap thickness of 900 m (p-w 8) was created within t1 = 10.2 years. Variants 2, 3, 4, 5, 6 and 7—the trap formation within the time Δt = 4 × t1, t1/4, 16 × t1, t1/16, 64 × t1 and 32 × t1. Background variant 0 corresponds everywhere to computations without consideration of heating due to the Trap

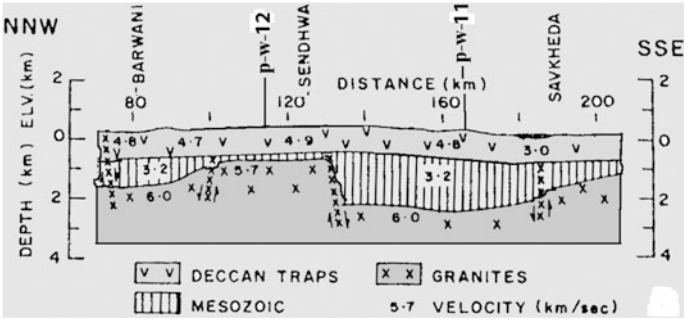

Fig. 8.20 Sedimentary section of profile 4 (p-w 11 and 12) crossing the central part of Deccan Syneclise (Fig. 8.1) and constructed on the base of geological studies of the "Thuadara-Send-hwa-Sindad" profile in central part of the Deccan Sineclise (after [8] with little changes)

heating from trap), and in variants with duration of the Trap formation equaled to 45.5, 11.4 and 2.84 years, consequently. The growth duration of the Trap formation from 2.84 years to 11.4 and 45.5 years leads to reduction of the "width" of the maturity aureole (distance to the rocks with Ro = 1.5 % from the base of the Trap) from 940 to 715 and 354 m, respectively (Fig. 8.21b, d). Thus, even at extremely rapid formation of the trap, including instantaneous formation, the Lower Triassic, Permian and Carboniferous rocks of subtrappean complex occur within the "oil window". At more real situation with duration of the trap formation 50 and more years, the Low Cretaceous, Jurassic and Middle and Upper Triassic rocks become also oil prone.

Sedimentary rocks of the section 12 thickness of 200 m are strongly influenced by the Trapp (Fig. 8.21d). The Carboniferous rocks at the base of sedimentary section of the pseudo-well 12 reach a maturity level Ro = 0.39, 0.64, 1.73, 3.70 and 4.47 % at the depth of 1200 m in the variant 0 (background) and in variants 1–4 with duration of the Trap formation equaled to 181.8, 45.5, 11.4 and 2.84 years,

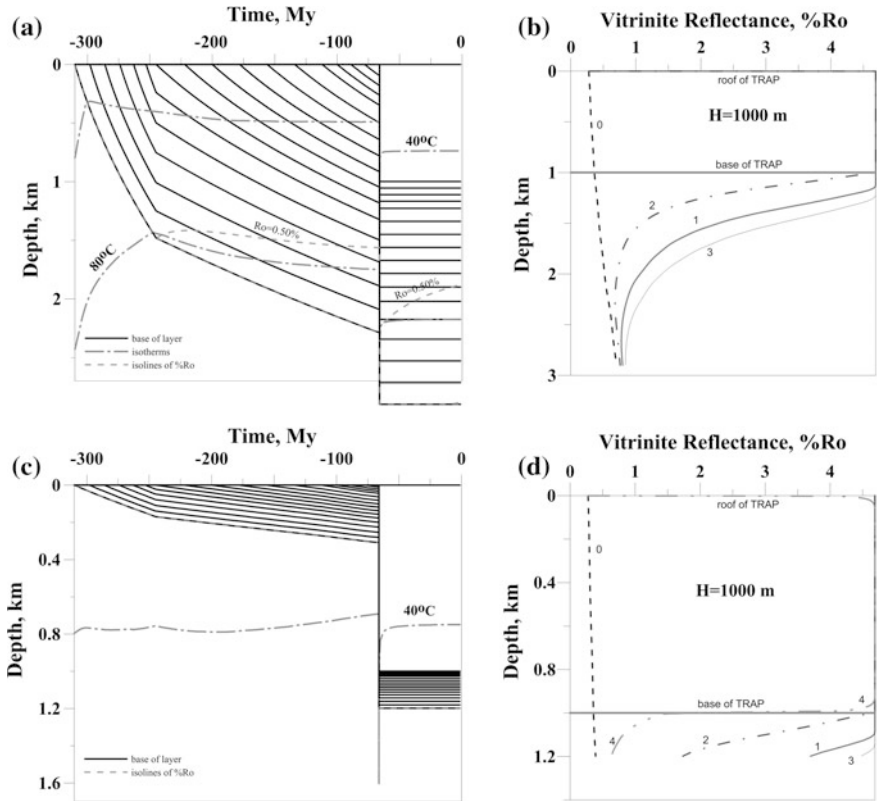

Fig. 8.21 Numerical reconstructions of burial, thermal and maturation histories of pseudo-wells 11 and 12 on the profile 4 crossing the central part of Deccan Syneclise (Fig. 1). **a**, **c** Burial, thermal and maturation histories of sedimentary sections of subtrappean and trappean complexes received without consideration of heat from the Trap (so called background variant). **b**, **d** Vitrinite reflectance versus depth (maturity aureole) in the subtrappean complex computed for different durations of the Trap formation: main variant 1 corresponds to the mean rate of the trap formation similar to the Lakki Lake in Iceland, that is $V_1 = 0.022$ m/90 days. Then, the trap of 1000 m (p-w 11 and 12) was created within t1 = 11.4 years. Variants 2, 3 and 4—the Trap formation during time $\Delta t = 4 \times t1$, t1/4 and $16 \times t1$. Background variant 0 corresponds everywhere to computations without a contribution of heat of the Trap

consequently. In all variants with consideration of heating from the Trap, a main part of sedimentary section is characterized by over-mature organic matter with Ro > 1.70 %. Only variant with most long duration of the Trap formation (during 181.8 years) gives the "width" of the maturity aureole about 4 m and then a greater part of sedimentary blanket will be within the "oil window" (Fig. 8.21d).

8.5 Conclusion

Estimation of hydrocarbon prospects of sedimentary complex underlying the effusive part of the traps is of great interest in the modern geology. Maturity aureole of the trap complex determines a depth of "oil and gas" windows and an ability of the underlying sedimentary complex to generate hydrocarbons. Our study shows that the size of the maturity aureoles in the subtrappean sedimentary complex decreases considerably with increasing duration of the Trap formation. Therefore the duration of the Trap's formation is the most critical and indefinite parameter in the modeling.

There are the "well dated" intrusions with detailed measurements of vitrinite reflectance in vicinity of the intruded body like the example presented in Fig. 7.2 in Sect. 7.1.2. For such intrusions, it is possibly to estimate the times of the intrusion's formation from comparison between the measured and computed vitrinite reflectance Ro(z) at different distances from surface of the intrusion body (Sect. 7.1.2). But similar detailed measurements of Ro are absent for traps. For this reason, we tried to estimate roughly the minimal time of the Trap formation on the base of the data for the Lakki volcano in Iceland, created the greatest volcanic plateau in recent history (Sect. 7.2.3). The mean rate of the trap formation in the Lakki volcano is estimated as V = 0.022 km/90 days. Taken such mean rate of trap formation, it can be obtained that the trap complexes with total thickness Δz = 1, 100 and 1000 m could be formed during the times t1 = 4.1, 409 and 4091 days (11.36 years) correspondingly. These times correspond rather to the minimum possible duration of trap's formation than to actual ones. In addition, the trappean complex can be build during several stages of development each of which is responsible for the formation its layer of the trap complex. Then, the maturity aureole of such trap complex will be determined by the aureole of the first trap layer nearest to the sub-trappean sedimentary complex if the previous trap layer had enough long time to cool totally before the next layer begins its formation. Therefore the size of maturity aureole of such trap complex must be close to the aureole of single trap layer.

As regards the duration of the Deccan Trap formation, there are no reliable estimates of this parameter. An eruption rates is assessed here by 1–2 $km^3\ y^{-1}$ [32]. Taking area of the Deccan Plateau about $(1 - 5) \times 10^5\ km^2$, we obtain average rate of trap formation much lesser than the above rate V, based on the Lakki Lake data. Paleomagnetic constraints indicate an uncertainty of 500,000 years for peak volcanic activity at 65 m.y. in the section of the Western Ghats. They suggest that 90 % of the eruption took place in less than 500,000 years. Calculations of the time scale of plagioclase phenocryst growth in giant plagioclase basalts suggest the possibility of a much shorter interval (perhaps as short as 55,000 years) for the eruption of the entire package of Western Ghats basalts [9]. Thus, we must note the inability to estimate the duration of the formation of the Deccan traps with the necessary accuracy. For this reason, calculations were carried out with a large spread of this parameter.

The modeling presented in this chapter demonstrates that maturation level of organic matter in sedimentary rocks under the Trap can be rather moderate if the time span of the Trap formation (or formation of its single layer) was enough long. The size of maturity aureole of the Trap complex formed during several stages can be close to the aureole of single trap layer. The rocks of sub-trappean complex in the Deccan Plateau and the western passive margin of India can be as oil prone and gas prone depending on the thickness of the Trap and duration of its formation. Uncertainty in the thickness of the layers and the time of the trap formation has noticeable affect results of the modeling. Therefore, further refinement of these parameters can be adjusted results obtained above. Nevertheless, the above reconstructions must help in estimations of hydrocarbon perspective of the rocks in sub-trappean complex of the Deccan Plateau and western passive margin of India.

References

1. Kontorovich AE, Melnikov NV, Staroseltsev VS, Khomenko AV (1987) Effect of trap intrusions on oil and gas generation by the Paleozoic deposits of the Siberian Platform. Geologia i Geophysika 5:14–20 (in Russian)
2. Kontorovich AE, Likhanov II, Lepettyukha VV, Khomenko AV, Ten AA (1995) Application of geothermometers to assessment of methamorphic temperatures in sedimentary basin with trap magmatizm. Doklady RAN 345(6):793–796 (in Russian)
3. Kontorovich AE, Pavlov AL, Khomenko AV, Tretiakov GA (1997) Physical—chemical conditions of graphitization of coal bearing rocks (on an example of western part of the Siberian Platform). Geokhimia 6:563–570 (in Russian)
4. Astashkin VA, Khomenko AV, Shishkin BB (1994) Effect of structural trap intrusions on structures of the sedimentary cover of the Siberian Platform. Geologia i Geophysika 35(1): 34–40 (in Russian)
5. Milani EJ, Zala'n PV (1999) An outline of the geology and petroleum systems of the Paleozoic interiorbasinsof Sous America. Episodes 22(3):199–205
6. Rodrigues FM, Villar HJ, Baudino R, Delpino D, Zencich S (2009) Modeling an atypical petroleum system: a case study of hydrocarbon generation, migration and accumulation related to igneous intrusions in the Neuquen Basin, Argentina. Mar Pet Geol 26:590–605
7. Gombos AM, Powell J, William G, Norton IO (1995) The tectonic evolution of western India and its impact on hydrocarbon occurrences: an overview. Sediment Geol 96:119–129
8. Kaila KL (1989) Mapping the thickness of Deccan Trap flows in India from DSS studies and inferences about a hidden Mesozoic Basin in the Narmada—Tapti region. In: Subbarao KV (ed) Deccan flood basalts: geological society of India memoir (10):91–116
9. Sen G (2001) Generation of Deccan Trap magmas. Proc Indian Acad Sci (Earth Planet. Sci.) 110(4):409–431
10. Patro BPK, Sarma SVS (2007) Trap thickness and the subtrappean structures related to mode of eruption in the Deccan Plateau of India: results from magnetotellurics. Earth Planet Space 59:75–81
11. Sheth HC (2005a) From Deccan to Réunion: No trace of a mantle plume. In: Foulger GR, Natland JH, Presnall DC, Anderson DL (eds) Plates, plumes, and paradigms. Boulder, colorado, geological society of America special paper, vol 388, pp 477–501
12. Sheth HC (2005) Were the Deccan flood basalts derived in part from ancient oceanic crust within the Indian continental lithosphere? Gondwana Res 8:109–127

13. Sheth HC, Pande K, Bhutani R (2001) ^{40}Ar-^{39}Ar ages of Bombay trachytes: evidence for a Palaeocene phase of Deccan volcanism. Geophys Res Lett 28:3513–3516
14. Rohrman M (2007) Prospectivity of volcanic basins: trap delineation and acreage de-risking. AAPG Bull 91(6):915–939
15. White RS, McKenzie D (1989) Magmatism at rift zones: the generation of volcanic continental margins and flood basalts. J Geophys Res 94:7685–7729
16. Singh SB, Babu GA, Singh KP, Negi BC, Srinivas Y, Rao VP (2004) Delineation of basaltic covered sediments in the Saurashtra Region using Deep Resistivity Sounding studies. In: 5th conference & exposition on petroleum geophysics, Hyderabad-2004, India, pp 69–74
17. Singh SB, Babu GA, Veeraiah B, Chakravarthi V (2008) Detection of sub-trappean sediments by Deep Resistivity Sounding studies in India. In: 7th conference & exposition on petroleum geophysics, Hyderabad-2008, India, pp 106–110
18. Rathore SS, Vijan AR, Singh MP, Prabhu BN, Sahu A (2004) Isotopic evidence of Middle Proterozoic magmatism from Bombay High field: implications to crustal evolution of western Offshore of India. Proc Indian Acad Sci 113:27–36
19. Kumar B, Patil DJ, Kalpana G, Vishnu Vardhan C (2004) Geochemical prospecting of hydrocarbons in frontier basins of India. Basaltic article #10073 (2004): adapted from extended abstract prepared for presentation at AAPG Annual Convention, Dallas, Texas, April 18–21 (2004)
20. Biswas SK (1982) Rift basins in western margin of India and their hydrocarbon prospects with special reference to Kutch Basin. AAPG Bull 66(10):1497–1513
21. Dixit MM, Satya Vani N, Sarkar D, Khare P, Reddy PR (2000) Velocity inversion in the Lodhika area, Saurashtra peninsula, western India. First Break 18:499–504
22. Waples D, Hegarty K (1999) Seychelles thermal history hydrocarbon generation traced. Oil Gas J 97(21):78–82
23. Wandrey CJ (2004) Bombay geologic province Eocene to Miocene composite total petroleum system, India. US Geol Surv Bull 2208-F
24. Vardhan CV, Kumar B, Kumanan CJ, Mani1 D, Patil DJ (2008) Hydrocarbon prospects in sub-trappean Mesozoic Deccan Syneclise, India: evidence from surface. Geochemical Prospecting. Search and Discovery Article #10143
25. Galushkin Yu I (2015) Evolution of temperature, maturation level and realization of hydrocarbon potential in subtrappean sedimentary complex of the Bombay offshore—Results of 1-D basin modeling. Mar Pet Geol 67:804–815
26. Fainstein RF, Roy L, Banik N, Rommel B, Piezzhev I, Broetz R (2009) Seismic constrained gravity inversion for sub-basalt exploration in West Coast, India. In: 71-st EAGE conference and exhibition, Amsterdam, The Netherlands, Z046, 8–11 June 2009
27. Biswas SK (1989) Strucrure of the western continental margin of India and related igneous activity. In: Subbarao KV (ed) Deccan flood basalts, geological society of India Memoir, vol 10, pp 371–390
28. Kaila KL (1989) Mapping the thickness of Deccan Trap flows in India from DSS studies and inferences about a hidden Mesozoic Basin in the Narmada—Tapti region. In: Subbarao KV (ed) Deccan flood basalts: geological society of India Memoir, vol 10, pp 91–116
29. Gupta MI, Sharma SR, Sundar A, Singh SB (1987) Geothermal studies in the Hyderabad granitic region and the crustal thermal structure of the Southern Indian Shield. Tectonophysics 140:257–264
30. Gupta MI, Sundar A, Sharma SR (1991) Heat flow and heat generation in the Archaean Dharwar cratons and implications for the Southern Indian Shield geotherm and lithospheric thickness. Tectonophysics 144:107–122
31. Negi IG, Panday OP, Agrawal PK (1986) Super-mobility of hot Indian lithosphere. Tectonophysics 131:147–156

32. Turner S, Hawkesworth C, Gallagher K, Stewart K, Peate D, Mantovani M (1996) Mantle plumes, flood basalts, and thermal models for melt generation beneath continents: assessment of a conductive heating model and application to the Parana. J Geophys Res 101(B5):11.503–11.518
33. Pant PR (1999) Significant inferences on deep crustal structure of Deccan Trap region from spectral analyses of Bouguer anomalies. J Geol Soc India 53:315–328
34. Goswami BG, Singh H, Bhatnagar AK, Sinha AK, Singh RR (2007) Petroleum systems of the Mumbai Offshore basin, India. Posted 27 Sept 2007. Search and Discovery Article #10154

Part III
Change in Heat Flow and Rock Temperature Due to Sharp Climate Variations in the Quaternary

Chapter 9
Evolution of Permafrost and of Gas Hydrate Stability Zone

Abstract In this chapter, permafrost modeling is analyzed as a part of procedure of basin modeling. The temperature on the basin surface corresponded to variations in paleoclimate is taken into consideration beginning with the time of the basin initiation and including the past 3.4 Ma, when formation and degradation of permafrost were repeated many times. The use of real lithological composition of sedimentary rocks distinguishes this approach from previous studies of permafrost evolution. Depth and time variations in thermophysical parameters of rocks (heat conductivity, heat capacity, unfrozen water and salt content, porosity) had a considerable influence on the results of modeling. The calculations demonstrate that the formation and degradation of the zones of stable existence of gas hydrates in the Pliocene-Holocene time are in close correlation with the events of formation and degradation of permafrost layers. All of these events were repeated many times during the Quaternary (Chap. 10). Section 9.3 considers the principles for determining of the base and top of the zones of gas hydrate stability and analyzes the conditions of stable existence of gas hydrates in the land and marine environments.

Keywords Permafrost · Paleoclimate · Temperature · Heat flow · Gas hydrates · Geothermal modeling

9.1 Introduction

Typically, permafrost can occur in the areas where mean annual air temperature stands below −1 °C. This value constitutes the southern boundary of discontinuous permafrost in North America, while the −6 to −8 °C isotherm is considered to be boundary of continuous permafrost [1–3]. The thickest layer of permafrost exists in those areas where freezing has been lasting for the longest time, in the zones where the geothermal heat is the weakest [3]. In northern Canada or Siberia permafrost thickness in the areas of continuous occurrence reaches hundreds of meters [3, 4]. Assume that the deepest permafrost lies in the mountainous area of the Antarctica interior, not covered with land-ice, it is also the oldest permafrost on the Earth [3].

Y. Galushkin, *Non-standard Problems in Basin Modelling*,
DOI 10.1007/978-3-319-33882-8_9

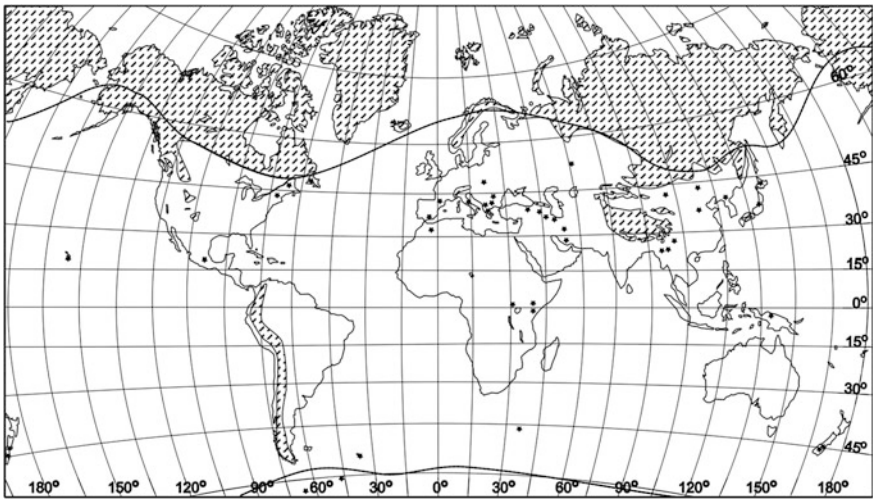

Fig. 9.1 Permafrost occurrence on the Earth surface (according [3]). For better view Antarctic, which is entirely affected by permafrost, is not included in the used cartographical projection. Stars indicate places with local permafrost occurrence not to the scale

The area of distribution of permafrost is extensive and covers many known oil and gas basins of the world (Fig. 9.1). Initiation and development of permafrost have a strong influence on thermal state of the sedimentary cover in the areas of exploration of oil and gas fields (Fig 9.1).

Due to the low thermal diffusivity and conductivity of rock the climatically driven thermal disturbances propagate very slowly in the geological medium and keep the subsurface in a transient thermal condition for geologically relevant times. So, the climate variations in the Pliocene and Quaternary led to non steady thermal regime of sediments up to depth of 3–5 km. It is especially important for high and middle-latitude sedimentary basins. Formation and degradation of permafrost took place repeatedly in the Quaternary. Evolution of permafrost in the Pleistocene-Holocene was studied in many papers (e.g., [5–13]. A two-dimensional analysis of evolution of permafrost zone in the East Arctic shelf in [14–16] can be also mentioned among these papers. However, complexity of the problems forced the authors of the cited papers to limit by approximate models of thermal evolution of one- or two-layer domain. But the numerical analysis of formation of permafrost and temperature field in crustal rocks during major climate changes of the Pliocene-Holocene shows a substantial dependence of the process on variation in lithological composition of rocks with depth, because the latter affects straightly on corresponding variations in petrophysical parameters of frozen and thawing rocks [17, 18].

Consideration of changes in the content of clay and sand fractions in the rock of the basin with depth leads to a change in the estimates of permafrost depth of 100 m or more. Analysis of such problems in the homogeneous one- and two-layers models would lead to considerable errors in estimations of time history and

thickness of permafrost. The need to address the problem of permafrost formation in the basin modeling is related to the fact that reliability of the model increases when the temperatures measured in the present-day section of the basin are close to the values calculated in the model [19]. But the latter can be correctly obtained only if the model considers the changes in rock temperature due to several cooling periods in the Pliocene-Holocene.

The permafrost problem was analyzed on an example of the Urengoy area in paper [17] and for the South Urals area in [18]. The first paper described main principles of numerical reconstruction of permafrost evolution in the frame of the GALO basin modeling system. Second paper considered a special problem of distortion of surface heat flow in the regions where permafrost was in the past but completely degraded by now. The two papers are considered in the book [20]. In present chapter, the previous model of permafrost evolution in the Urengoy area is refined taking into consideration more accurate new data of paleoclimate evolution published in [21–23] and the changes in shape of the unfrozen water curve, $W(T)$, depending upon lithological composition of sedimentary rocks. In next section of the chapter we consider the main principles and specific features of the modeling of permafrost evolution, which will be applied in Chap. 10 to sedimentary basins of the inland and offshore areas.

Determination of the zones of gas-hydrate stability in the sedimentary cover of the basins closely relates to the above problem of formation of non-steady temperature distribution in sedimentary rocks due to sharp changing of climate during the last 2–4 My. The calculations demonstrate that the processes of formation and degradation of the zones of stable existence of gas hydrates in the Pliocene-Holocene time were in close correlation with the events of formation and degradation of permafrost layers and was repeated many times in the past three million years (Chap. 10). Section 9.3 devotes to the principles of such determination and conditions of existence of gas hydrates in the land and marine environments.

9.2 Analysis a Thermal Evolution of the Regions with Permafrost Formation Using of Basin Modeling System

9.2.1 Formation of Initial Distribution of Temperature and Petrophysical Parameters of Sedimentary Rocks in the FROST Program

Reconstruction of thermal history of the basin including evolution of permafrost are carried out with using of the FROST-computer program, which is constructed as a part of general program package GALO for basin modeling (see Chap. 1; [17–20]).

The permafrost modeling requires an initial temperature distribution and knowledge of detailed change in thermophysical parameters of sedimentary rocks with depth. For this reason, the permafrost modeling consists of two steps. The first is general modeling since the basin initiation to the time when the annual temperature at the basin surface has reached 0 °C (about 3.4 My ago in the Urengoy area of the West Siberia Basin). This time is adopted as initial time for permafrost modeling (second step of the modeling) that embraces the time interval from 3.4 My to present day. The main objective of the first step of the modeling (general modeling) is to obtain a temperature distribution T(z) for the time t = 3.4 Ma that is used as initial distribution for subsequent modeling in second step of the modeling. In addition, a detailed distribution of the rock porosity and lithology with depth in present-day section of the basin, corresponding to complex geological history of the basin with repeated events of intensive erosion (as in the example of the Kuyumba section in the Siberian Platform in Chaps. 6 and 10) are computed during the first step (general modeling). Results of the general basin modeling for the Kuyumbinskaya well are shown and discussed in Chap. 6. The temperatures (Chap. 10) and vitrinite reflectance (Fig. 6.7a) measured in the present-day sedimentary section of the basin, as well as an analysis of tectonic subsidence of the basin (Figs. 6.6a), were the main factors to control a validity of the modeling in the Kuyumba area (Sects. 1.1 and 1.2).

The porosity distribution with depth computed in the general modeling for the present time (t = 0) and present-day lithology composition of sedimentary rocks are used in the second step of the modeling to calculate distributions of thermal parameters of sedimentary rocks (heat conductivity, KT(z, t), heat capacity, Cv(z, t), heat generation, A(z, t)) with depth and time during permafrost evolution. These parameters are determined by lithological composition of rocks, porosity and rock temperature, which is calculated in the permafrost modeling. Then, the initial temperature distribution, available variations in the mean annual surface temperature and distributions of porosity and lithological composition of rocks with depth are used in the second step of modeling to reconstruct in detail the temperature evolution of the sedimentary section with help of the FROST computer package with taking into account the repeated processes of formation and degradation of permafrost.

Temperature distribution in sedimentary column is determined in the FROST program by solution of the non steady one-dimensional heat transfer Eq. (1.1) without convective member. Physical parameters in Eq. (1.1) are a function of porosity, $\phi(z)$. Change in porosity versus depth due to consolidation of clay, sand, siltstone, limestones, dolomites were calculated in according with usual algorithm of basin modeling described for example in [17–20].

9.2.2 Heat Conductivity of Frozen and Thawed Rocks

Referring to calculation of thermal-physical parameters of rocks, we emphasize once again that only the distribution of porosity and rock lithology with depth

remain constant during the simulation of the permafrost evolution. They correspond to the values in a modern sedimentary basin. At the same time, thermal conductivity and heat capacity of the frozen and thawed rocks depend on the temperature, ice and water content in the rock pores, and hence will vary with time and depth during permafrost evolution. Thermal conductivity of rock, *KT*, was calculated by the geometric averaging of the values for matrix (*Km*), water (*Kw*) and ice (*Ki*) [5, 17]:

$$KT = K_m^{(1-\phi(z))} \cdot K_w^{\phi(z)} \quad \text{for } T > TL \tag{9.1}$$

$$KT = K_m^{(1-\phi(z))} \cdot K_w^{\phi(z)\cdot W(T)} \cdot K_i^{\phi(z)\cdot(1-W(T))} \quad \text{for } T < TL \tag{9.2}$$

Here *TL* is the ice liquidus temperature (thawed rocks—at $T > TL$; frozen rocks—at $T < TL$) and W(*T*) is a fraction of porosity water, that remains unfrozen at negative temperatures (see below). The matrix thermal conductivity decreases with temperature [5, 24]:

$$K_m = K_m \cdot (T = 20\ ^\circ\text{C})/[1 + \alpha \cdot (T - 20\ ^\circ\text{C})] \tag{9.3}$$

where α is the temperature coefficient, which is maximal (0.003–0.005 $^\circ\text{C}^{-1}$) for sandstone and salt and moderate for clay, limestone and marl [20, 24]. In Eq. (9.2), the thermal conductivity of ice is 2.26 W/m °K. The thermal conductivity of water changes with temperature [24]:

$$K_w = 0.6 \quad for\ T < 50\ ^\circ\text{C}$$

$$K_w = 0.565 + 0.00188 \cdot T - 0.00000723 \cdot T^2 \quad for\ 50\ ^\circ\text{C} < T < 137\ ^\circ\text{C} \tag{9.4}$$

$$K_w = 0.602 + 0.00131 \cdot T - 0.00000514 \cdot T^2 \quad for\ 137\ ^\circ\text{C} < T < 300\ ^\circ\text{C}$$

where K_w is in W/m °K. Calculated distribution of heat conductivity with depth in the present day section of the basins can be seen in Figs. 9.2 and 9.3 on the example upper 500 m of sedimentary sections of the Kuyumba and Urengoy fields (see also Chaps. 6 and 10).

9.2.3 Heat Capacity of Frozen and Thawed Rocks

In permafrost modeling, the volumetric heat capacity of rocks affects strongly solutions of the non steady heat transfer Eq. (1.1). For thawed rocks, heat capacity is [17, 19, 24]:

$$C_v = C_{vm} \cdot [1 - \phi(z)] + C_{vw} \cdot \phi(z) \quad \text{for } T > T_L \tag{9.5}$$

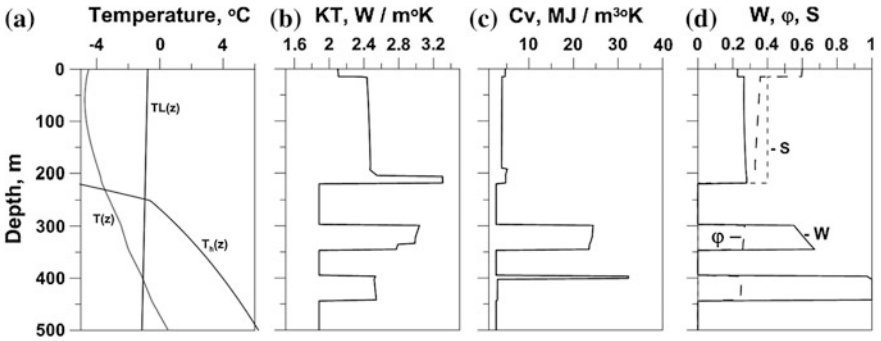

Fig. 9.2 Calculated variations in thermophysical parameters of rocks versus depth in upper 500 m of the present-day sedimentary sections in well 212 in the Kuyumba field ([17], see Chap. 6). **a** T (z)-temperature distribution, TL(z) ice liquidus (Eq. 9.7), $T_h(z)$—the curve of methane gas-hydrate stability (Eq. 9.8). **b** KT-thermal conductivity (Eqs. 9.1, 9.2). **c** *Cv* apparent heat capacity per unit volume (Eqs. 9.5, 9.6). **d** *W* unfrozen water content in the rocks, φ porosity and *S* relative content of coarse grained fraction in the rocks. The salt content is suggested to equal 12 g/l in the Kuyumbinskaya section. Specific feature of the Kuyumbinskaya section is a presence of intrusive sills at the depth 218–298, 347–395 and 442–520 m (Table 6.2; Fig. 6.7) with following characteristics of dolerite rocks: KT = 1.90 W/m °K, Cv = 2.61 MJ/m^3 °K, A = 0.63 mk W/m^3, φ = 0, and W = 0 (formally)

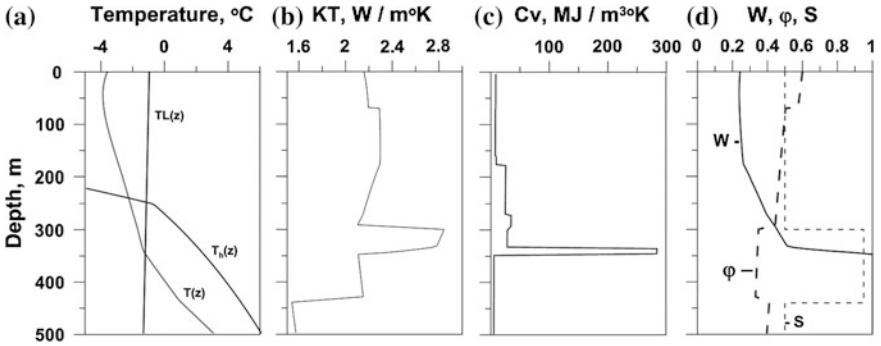

Fig. 9.3 Calculated variations in thermophysical parameters of rocks versus depth in upper 500 m of the present-day sedimentary sections in well 411 the Urengoy field ([17] (see Chap. 10). See caption of Fig. 9.2. The salt content is suggested to equal 15 g/l in the Urengoy-411 section

where C_{vm} is the matrix heat capacity (Chap. 10), C_{vw} = 4187 MJ/m^3 K is the water heat capacity. Terms for ice heat capacity and latent heat of the ice-water phase transition must be added for frozen rocks. Then, an apparent volumetric heat capacity of frozen sedimentary rock is [5, 17, 19]:

$$C_v = C_{vm} \cdot [1 - \phi(z)] + C_{vw} \cdot \phi(z) \cdot W(T) + C_{vi} \cdot \phi(z) \cdot [1 - W(T)] + \phi(z) \cdot \rho L \cdot (dW(T)/dT) \quad \text{for } T < T_L \tag{9.6}$$

Here C_{vi} = 1.926 MJ/m^3 K is the volumetric heat capacity of ice, ρL = 335 MJ/m^3 is the latent heat of ice fusion per unit volume. The last term in (9.6) describes the latent heat effect in the enthalpy approach (Sect. 1.1.3). It can increase the apparent heat capacity of frozen rocks at the temperatures $T < T_L$ by one-two order (Figs. 9.2c and 9.3c), in depending on the form of unfrozen water curve $W(T)$. In enthalpy approach, the temperature for the ice-water phase transition together with a latent heat effect is spread over some temperature range, determined by the shape of the $W(T)$ function [25–30]. Such approach reflects real situation of ice fusion more correctly than the classic Stefan's solution of permafrost problem. The latter suggests a single temperature for the phase transition of ice to water. Close situation is reflected by solid line 1 in Fig. 9.4 which corresponds to the $W(T)$ curve with little content of unfrozen water in pores. It corresponds to coarse grained rocks (sandy or very fractured rocks). Such $W(T)$ curve leads to a very narrow temperature interval of the "water–ice" phase transition and correspondingly to narrow interval of release of latent heat of ice fusion (like to interval ~340–350 m in Fig. 9.3c for Urengoy field). For this reason, result of calculation of permafrost thickness with such $W(T)$ curve must be close to the one in the Stefan's solution. It is supported in paper [17] by comparison between the results of our calculations with the $W(T)$ curve 1 in Fig. 9.4 and the analysis of the problem in papers [10, 11], used the classic Stefan's method. In relation to this problem, it is necessary to note that results of modeling, using the enthalpy method, will differ significantly from the ones of the Stefan's method at considerable content of clay, limestone and other fine grained rocks [17, 19] because in this case the phase transition "water/ice" spread over wide depth-interval (see for example interval ~300–350 m in Fig. 9.2c for the Kuyumbinskaya area).

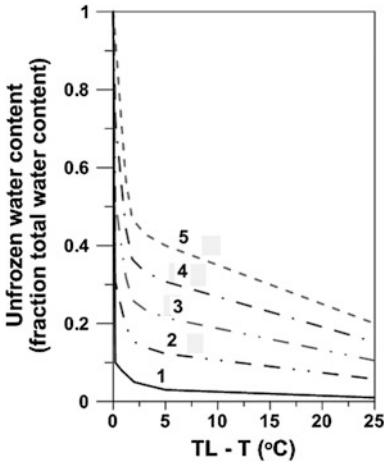

Fig. 9.4 Unfrozen water content in the rock, W, versus difference of the ice liquidus and the rock temperature, (TL-T) [19]. *Line 1* W, typical for coarse grained rock (sandy, fractured rocks); *Line 5* is typical for the fine grained rocks (clayey rocks, limestones) [26, 28]. *Lines 2*, *3*, *4* were constructed from the *curves 1* and *5* for content of coarse grained fraction in the rock equaled to 75, 50 and 25 % correspondingly

9.2.4 Change in Ice Liquidus and Thickness of Permafrost Due to Salt Content in Porous Water

In the FROST program, the base of permafrost zone is determined by intersection of current geotherm with liquidus of ice, TL (i.e. temperature of initiation of water freezing; Figs. 9.2a and 9.3a). But the ice liquidus temperature *TL* depend on pressure and salt content in the pore water [26, 28, 31]:

$$TL = 0\ ^{\circ}\mathrm{C} - 0.073 \cdot P - 0.064 \cdot Cs \tag{9.7}$$

Here *P* is pressure in MPa, which is assumed to be hydrostatic; *Cs* is the *NaCl* and *KCl* concentration in g/L. According (9.7), increase in salt content leads to depression of liquidus temperature, *TL*. The salt content of 15 mg/L decreases TL by 0.96 °C (compared with fresh water) and reduces the predicted present-day depth of permafrost bottom of about 40 m [19]. This effect is illustrated in Fig. 9.5, where an influence of variation in salt content on temperature and solidus distribution with depth is considered. All of the curves in Fig. 9.5 were computed for the sandy type curve *W*(*T*) (curve 1 in Fig. 9.4). These calculations demonstrated, that the depth of permafrost base decreases from 486 to 443 and then to 388 m, if the salt content, *Csalt*, increases from 1 to 15 and to 30 g/l, correspondingly. Of course, a use of single curve W(T) of sandy type for estimation of unfrozen water content in rock pores and micropores in all of variants in Fig. 9.5 is not entirely correct because the W(T) curve depends also on salt concentration (see next section).

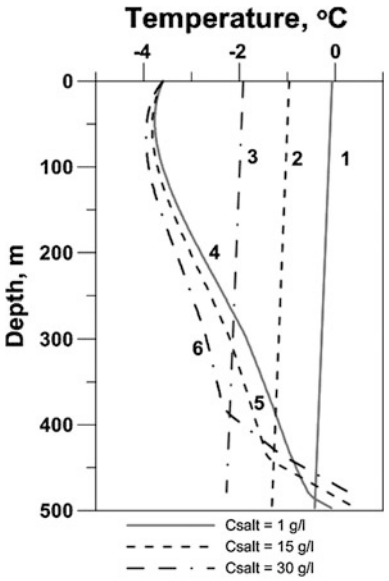

Fig. 9.5 Effect of salt content in porous water on the present-day distribution of temperature T(z) (*curves 4*, *5*, *6*) and liquids TL(z) (*curves 1*, *2*, *3*) with depth [19]. Three pairs of *curves 1*, *4*; *2*, *5*; and *3*, *6* correspond to the values of Csalt = 1, 15 and 30 g/l, correspondingly. All curves were computed for the sandy type curve W(T) (curve 1 in Fig. 9.4) and sedimentary section of the Urengoy-411 (see Chap. 10). According to the calculations, the base of permafrost locates at the depth of 486, 443 and 388 m for salt content Csalt = 1, 15 and 30 g/l, correspondingly

Unfortunately, exact dependence of salinity on depth in the upper 500 m of sedimentary sections of Figs. 9.2 and 9.3 is unknown us. We know only that the salinity of pore water in the Urengoy area increases nearly from zero near the surface up to 30 ppm at a depth of 3 km. That is why, we taken in our modeling steady values Csalt = 15 and 12 % in porous water at all depth of the Urengoy and Kuyumbinskaya areas. Dependence liquidus temperature TL on Csalt is taken into account in our computations in accordance with Eq. (9.7).

9.2.5 *Unfrozen Water Content in Porous Space at Negative Temperatures and Its Influence on Permafrost Evolution*

Estimation of unfrozen water content in frozen rocks is very complex problem of geocryology [26, 32–34]. Numerous investigations in the West Siberia Basin has shown that rocks, located within permafrost and below it, are saturated by ice or water [9]. In the paper [17], the $W(T)$-curve, which determines the unfrozen water content in rock pores at negative temperatures, was taken as typical of that for coarse-grained rocks with a small content of unfrozen water (solid line 1 on Fig. 9.4). According to this curve, about 90 % of pore water is transformed to ice within the temperature interval $TL - 0.2\ ^\circ\mathrm{C} \leq T \leq TL$. The use of this curve $W(T)$ was justified by the fact that Paleogenic rocks in the West Siberia Basin are fractured during last erosion event. In present reconstructions, the shape of the $W(T)$ function changes with depth depending on the content of the fine and coarse grained fractions in the rock:

$$W(T) = S(z) \cdot W_1(T) + (1 - S(z)) \cdot W_5(T) \tag{9.8}$$

Here, $S(z)$ is the fraction of coarse-grained lithological units in the rock (sand, fractured shale, limestone, dolomite, marl). It is shown by short dashed line S in Figs. 9.2d and 9.3d. Then, $(1 - S)$—is a fraction of fine-grained facies in the same rock (clay, non-fractured shale, limestone, dolomite, marl). In Eq. (9.8), $W_1(T)$ and $W_5(T)$ are the curves 1 and 5 in Fig. 9.4. The example of computation in paper [18] where the $W(T)$ curve is considered as a function of lithological composition of the rocks shows decrease in estimated maximal depth of permafrost base during the last ice-period by 80 m in comparison with the variant of single sandy $W(T)$ curve for all sedimentary layers of the section.

Comparison of the curve 5 in Fig. 9.5 with the curve $T(z)$ in Fig. 9.3a for the Urengoy field makes it possible to directly estimate the influence of type of the $W(T)$ function on the modeling results. Indeed, the above curves were computed for one value of Csalt = 15, with one climate curve (see Chap. 10) obtained for Urengoy and for one sedimentary section in the modeling. The only difference in the curves is due to shape of function $W(T)$ (unfrozen water content). The curve 5 in Fig. 9.5 used

the sandy curve $W(T)$ (line 1 in Fig. 9.4). The curve $T(z)$ in Fig. 3a used a composite curve of Eq. (9.8) for $W(T)$ taking into account change in content of fine grained rocks with depth according to actual lithological composition of sedimentary section (see Chap. 10; Figs 9.3a, d). As result, the calculated present-day permafrost thickness in variant of curve 5 in Fig. 9.5 using the sandy $W(T)$ is about 443 m whereas it is 350 m for the composite curve W(T).

Lithological composition of rocks in Kuyumba-12 well (Table 6.1) suggests considerable content of sandy fraction only in upper 218 m of sedimentary blanket. The sediments between intrusions at the depth from 298 to 347 and from 395 to 442 m are presented by fine grained rocks (dolomite, halite, anhydrite and shale). Here the content of unfrozen water is rather high (Fig. 9.2d). It determines the fact that the rate of rapid increase in the Cp values near the permafrost base is less in the Kuyumba area than in the Urengoy area (compare Figs. 9.2c and 9.3c).

As mentioned above the W(T) curve described the unfrozen water content in rock pores and micropores depends also on salt concentration [32–34]. For example, transition from 3 % salinity of pore water to 35 % for coarse-grained rocks is accompanied by transition from the W(T) curve typical of these rocks with fresh porous water (curve 1 in Fig. 9.4) to the curve with greater content of unfrozen water (about 40 % at TL − T = 5 °C and 18 % and less at TL − T > 20 °C) that is similar to the curve for fresh-water in fine-grained rocks (curve 3 in Fig. 9.4). But we did not consider changes in functions W(T) due to content of salt because we did not have the appropriate information about change of salt concentration with depth in upper 500 m of sedimentary sections under consideration.

9.2.6 *Some Specific Features of Numerical Scheme in Solution of Heat Transfer Equation in the Permafrost Problem*

In this section, we do not concern with boundary conditions on the upper and lower boundaries of the domain of temperature calculation. They will be discussed in Chap. 10 on the example of actual basins. Numerical solution of the Eq. (1.1) in analysis of permafrost evolution is carried out using the implicit finite-difference scheme, described in [17]: the thermal-physical parameters in the equation depend on porosity, temperature, depth and time. Consequently, it is impossible to estimate analytically the stability of such solution, but it may be made empirically by comparison of solutions obtained for different time and space steps. For the permafrost problems, the validity of the finite-difference scheme was verified by comparison with another numerical solution [17]. In particularly, we used our computation scheme to repeat the numerical analysis of permafrost evolution in the two-layers case, which was carried out in [10] using the classical Stefan's method. We simulated also the numerical analysis of subsea saline permafrost after [28]. In both cases a good agreement with our model was achieved.

There is one specific feature in the choice of steps ΔZ, related with the sharp change in the apparent volumetric heat capacity Cv near base of permafrost (Figs. 9.2c and 9.3c) The depth-interval, within which the main latent heat effect takes place, must include at least 3–4 depth steps, ΔZ, to ensure reasonable accuracy of the numerical results. In our modeling, the number of depth steps was 570, and ΔZ ranged from 0.5 m near surface to 70 m at the base of the Z-domain (Z = 5550 m). In the variant of the Urengoy (Fig. 9.3c) the depth interval of the main latent heat effect had a thickness about 20 m and included about 7 depth steps. In addition, the calculated movement of the freezing front during time Δt must be smaller than the corresponding depth-step ΔZ. In our model, Δt varied from 50 to 0.5 years. In all cases, the calculations with the steps ΔZ and Δt, which were decreased by 2–4 times, must be carried out to control an accuracy of computing scheme.

9.3 Estimations of the Depths of the Gas Hydrate Stability Zone

9.3.1 Gas Hydrates: Occurrence and Mechanism of Origin

Hydrate reservoirs have been considered as a substantial future energy resource [35, 36]. Hydrates occur wherever methane and water are in close proximity at low temperature and elevated pressures. Gas hydrate crystals consist of gas molecules introduced into framework from water molecules. Gas hydrate is an ice-like crystalline substance, consisted of a cage structure of water molecules with trapped methane or other light gases inside [36]. General formule for hydrate is $M \cdot nH_2O$, where M is gas molecule, n = 6–17 depending on gas composition and P-T conditions. 46 water molecules can content up to 8 molecules of methane CH_4 ($CH_4 \cdot 5.75\ H_2O$) or up to 6 isobuthane molecules, C_2H_6 ($C_2H_6 \cdot 7.66\ H_2O$). At total filling of cells by methane ($CH_4 \cdot 5.75\ H_2O$), 1 m^3 of hydrate will contain about 172 m^3 of methane (at standard P-T conditions). But hydrate can be formed even at filling only 33 % of cells. Then 1 m^3 of hydrate will contain about 60 m^3 of methane. Methane influences strongly on mechanical characteristics of rocks. Even a little mixture of gas hydrates can change the physical attributes of rocks. So, thawing of ice containing only 1–2 % gas hydrates differs from melting of usual ice. The first is accompanied by hissing and fracturing of ice sample [36]. The core of ice comets consists of 95–98 % of ice and 2–5 % of methane hydrate. The rock samples in Yamburg (the West Siberia Basin) taken from the depth of 70–120 m discharged 0.22 cm^3 of gas/g rock during their thawing [37]. This gas originated mainly from gas hydrate, because the free gas content in the rocks was very little due to high ice saturation of pores (90–98 %). The heat conductivity of pure methane gas hydrates (0.45–0.51 W/m °K) is by 20 % lower than the one of water (0.565 W/m °K) and by 80 % lower that the ice one (2.35 W/m °K). Other thermal physical attributes of gas hydrates are mainly close to the ones of ice [36].

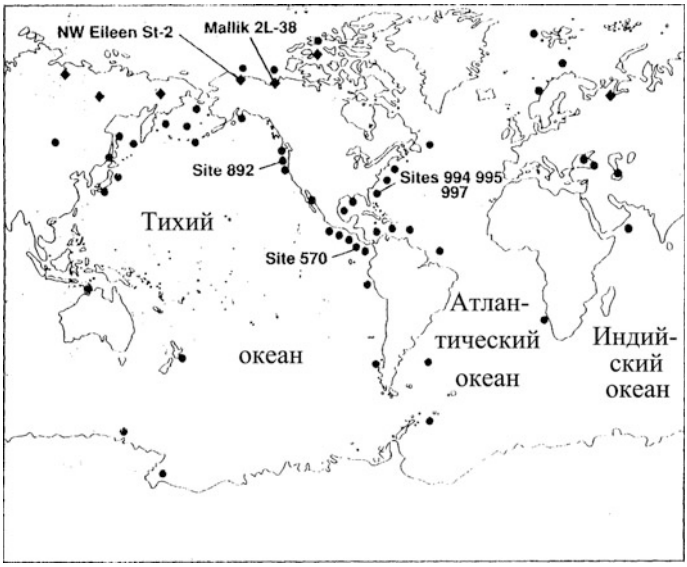

Fig. 9.6 Location of proven and probable (according BSR) gas hydrate accumulations in oceanic depositions of continental passive margins (*black circles*) and in continental permafrost zones (*black rhombs*) (according [39])

A great interest to gas hydrate accumulations is determined by the following reasons: (1) gas hydrate accumulations are considered as a possible important energy source in future [36, 37]; (2) gas hydrates are important in mechanism of underwater landslip [36] and (3) it is suggested that the processes of gas hydrate destruction can contribute considerably to global climate heating is suggested (hotbed effect; [38]).

Gas hydrates spread widely in nature (Fig. 9.6). In the Arctic, gas hydrate accumulations occur at the depth from 130 to 2000 m in the regions with permafrost. But especially great volumes of gas hydrates are expected in the passive margins. Indeed, in the sea regions of passive margins and marginal seas, gas hydrate formation is more frequent than in continental areas, because the weight of the sea water column locates the zone of hydrate stability near the sea bottom in spite of the positive temperatures of bottom water (Fig. 9.7). The volume of gas bounded in hydrates is estimated from 10^{13} to 4×10^{14} m^3 in land and from 3×10^{15} to 4×10^{16} (and even 8×10^{18})—in seas and oceans [39].

The main volume of gas hydrates in nature is formed by the water-filtration mechanism. Decrease of solubility of methane with reduction of water temperature is the main reason of gas hydrate formation within the zone of their stability existence. These gas hydrates are formed from methane contained in the water filtrating from below to the horizons of lower temperatures.

Formation of great gas hydrate accumulations requires a great volume of gas and water. Therefore, a presence of great quantity of HC gases (biogenic or

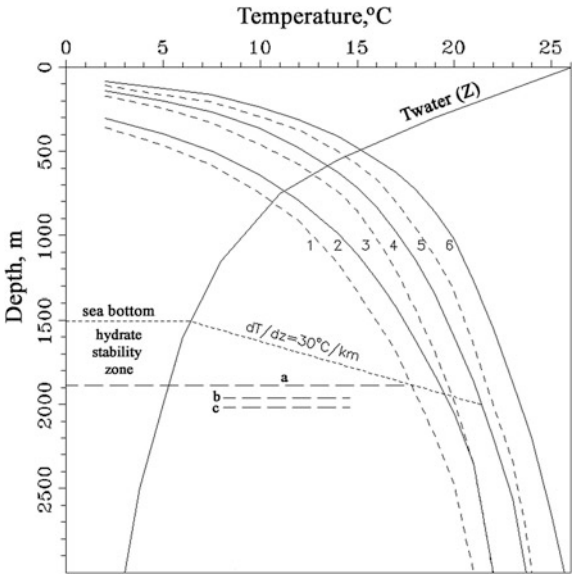

Fig. 9.7 Diagram of gas hydrate stability in sea sediments in coordinates "temperature-depth" at filling of rock pores by sea or fresh water (according to [40] with little changes). The stability curves of pure methane (*1*, *2*), 96 % methane, 3 % ethane and 1 % propane (*3*, *4*) 90 % methane, 7 % ethane and 3 % propane (*5*, *6*) with sea water (*1*, *3*, *5*) and with fresh water (*2*, *4*, *6*). The *lines a*, *b*, *c* are the depths of bottom of the stability zone for *curves 1*, *3* and *5* correspondingly. *Twater* (*Z*) is change of sea water temperature with depth. The line "dT/dz = 30 °C/km" is rock temperature below sea bottom for temperature gradients in sedimentary rocks dT/dz = 30 °C/km

thermogenic) is an important factor to control the formation of gas hydrates and distribution of their accumulations in nature. In majority of gas hydrates, methane has biogenic origin (microbiogenic methane). But in the Mexico Bay, North Alyaska and in the mouth of the MakKenzie river, methane is the gas of thermogenic origin according to isotope and molecular analysis [39].

If there are not effective migration ways, which ensure receiving of water and gas to zone of gas hydrate formation, formation of considerable gas hydrate accumulations is improbable. Thus, permeability of rocks and presence of fractures must be considered as possible factors favorable to formation of migration paths for receiving of hydrate accumulations by gas and water [37, 39]. The presence of traps and porous reservoir rocks is dispensable condition of formation of gas hydrate accumulations. In clay sediments, gas hydrates can formed only in nonconsolidated sediments of the upper 20–100 m of sea deposits. Gas hydrates of continental deposits occur only within the sandy rocks [41]. Migration of gas and water to the sites of active formation of hydrates takes place during gas hydrate formation. Then, presence of clay particles in the sandy rocks hinders water and gas transfer within the rock. That is why that hydrate formation is stopped in consolidated sands at transition from the rocks with 2–5 % of clay particles to the rocks with 5–10 % of clay particles [42].

9.3.2 *Bottom Simulating Reflector and Gas Hydrate Occurence*

In shelf areas, gas hydrate accumulations are discovered by a presence of anomalous seismic reflector (BSR—bottom simulating reflector) at the depth from 100 to 1000 m under sea bottom. This seismic horizon is interpreted often as the base of the gas hydrate zone. Zone of free gas can locate immediately under this seismic boundary BSR [38]. Figure 9.8 demonstrates the examples of the BSR horizons observed along the Blake Ridge in the Atlantic shelf of USA (Fig. 9.8a, [39]), in the Nankai Trough (Fig. 9.8b, [39]) and in sedimentary basins between the islands Sulavezi and Borneo in Idonezia in northern part of the Macassar basin with occurrence of mud volcanoes (Fig. 9.8c–e; [43]). On seismic profiles, the bottom

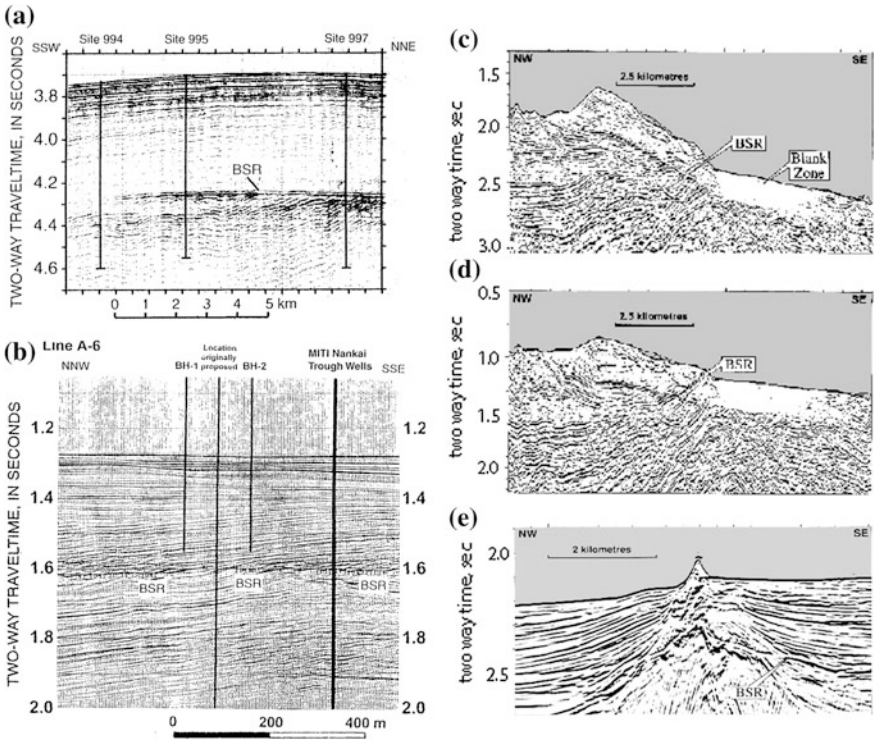

Fig. 9.8 Bottom Simulating Reflectors (BSR) observed in different sea margins of the Earth. **a** Seismic profile along the Blake Ridge (Atlantic shelf of USA) including the wells DSDP 994, 995 and 997 (Fig. 9.6, [39]). **b** Seismic profile in the Nankai Trough [39]. **c**, **d**, **e** The BSR horizons in sedimentary basins between the islands Sulavezi and Borneo in Idonezia (northern part of the Macassar basin) included some mud volcanoes [43]

simulating reflector is shown clearly due to its intensity and intersection of lithological boundaries. Occurrence of the bottom reflector (BSR) relates with sharp change of seismic rates and rock density. Some geologists interpret this seismic horizon as the base of the gas hydrate zone. But there are several probable reasons of contrast in seismic velocity Vp and rock density ρ [37, 40]. At first, the contrast in Vp can be caused by to transition from layer of rocks containing gas hydrates to the rocks with free gas in pores just below these hydrates. At second, it can be contrast between density of rocks with gas hydrates and density of the rocks without hydrocarbons in pores. And, at third, the BSR horizon can be due to contrast of the layer with rather little content of gas hydrates and the free gas pillow just under the above layer. Indeed presence of free gas filling only 1 % of porous space is enough to generate the bottom reflector, BSR. For example, multichannel seismic zonding of the sedimentary section in the north-western Barents sea shelf suggests a presence of sediments containing gas hydrates covered the zone of free gas accumulation [37, 40].

It is believed early that the contrast in densities is caused only by difference of Vp in gas hydrate (Vhydr = 3.3–3.8 km/s [40]) and Vp in the rocks without hydrocarbons (Vrock = 2.4–2.7 km/s). The volume of gas hydrates is estimated often by this contrast in the rates Vp. It led to considerable overestimation of the gas hydrate volume by orders of values [37]. The studies shown, that in majority of cases occurrence of the BSR horizon is caused no by positive anomalies of Vp due to presence of gas hydrates in rocks because a concentration of the latter is very small usually, but by the presence of free gas under the layer, that causes a negative anomalies in Vp [38].

The most often error in estimate of hydrate volumes is consideration of the base of the gas hydrate P-T stability zone as the base of the zone with occurrence of gas hydrates. This fact will be valid if there is the methane flow from below and this flow is enough for formation of hydrate accumulation. In many cases the base of hydrate accumulations locates at more shallow levels than the base of the gas hydrate stability zone. For formation of gas hydrate accumulation it is not enough that the rock occurs in the stability zone. It is necessary, that the methane volume carried from below in water to the rocks of considered horizon, exceeds the methane, that is able to solute in porous water at P-T conditions at the given depth [44]. In many cases, the BSR reflector marks the roof of the free gas zone and then this reflector can locate considerably deeper the base of the gas hydrate stability zone. If free gas is absent, the reflector BSR can be absent too. Thus, we have seen that the presence of the BSR horizon often does not imply the presence of appreciable amounts of gas hydrates, and that the BSR horizon often does not coincide with the base of the stability zone of gas hydrates. Neglect of these facts has led to a strong overestimate of hydrate volume in the research of previous years [39, 45, 46].

9.3.3 *Estimate of Depth of the Zones of Gas Hydrate Stability in the Basin Modeling Procedure*

In the presence of significant gas flow of thermal and biogenic origin in the zone of the hydrate formation, the appreciable volumes of hydrates can be formed within the zones of the stable existence of gas hydrates. Reconstructions of thermal regime of sedimentary cover of the basins including an analysis of temperature distributions during the sharp climate changes of the last millions years in Sect. 9.2 give an opportunity to estimate the depth interval of stability existence of gas hydrates in different time of permafrost evolution. The depths of the top and base of the zones for methane gas hydrate stability will be shown in Chap. 10 on the example of actual areas of sedimentary basins. Here we will consider only algorithm of determination of these depths and their nature. The depths of top and base of the zone are determined by upper and lower intersections of the temperature profiles T(z) predicted in basin modeling (Figs. 9.2a and 9.3a) with the phase-curve for stability of pure methane gas hydrate with fresh water and ice (curves $T_h(z)$ in Figs. 9.2a and 9.3a; [36, 42]):

$$Ln\,P = A - B \cdot T \tag{9.9}$$

Here P is the hydrostatic pressure in MPa, T is the temperature in °K and for temperature intervals $260 < T < 273$ °K, $272 < T < 283$ °K, $282 < T < 291$ °K, $290 < T < 302$ °K parameters $A = 8.968, 29.112, 36.32, 38.569$ and $B = 2196.62, 7694.3, 9735.05, 10378.58$ °K^{-1}, respectively [42]. In Figs. 9.2a and 9.3a, both these intersections are not shown because they are deeper 500 m but they will be shown in Chap. 10. The presence of salt shifts the equilibrium curve "methane—water solution of NaCl" toward the lower temperatures [42]:

$$Ln(P/Po) = (C/T) + D - 128.65 \cdot X + 40.28 \cdot X^2 - 138.49 \cdot Ln(1-X) \tag{9.10}$$

where X—molar fraction of NaCl in solution. For sea water (35 g NaCl in 1000 g H_2O): X = n(NaCl)/n(H_2O) = (35/58.5)/(1000/18) = 0.01077, P—hydrostatic porous pressure in MPa ($P = Po + \rho_w \cdot g \cdot z \approx Po + 10 \cdot z$(km) (MPa)), Po = 0.01013 MPa, parameters C = −8160.43 and D = 55.1103 characterize an equilibrium of methane—gas hydrate—water in absence of NaCl, T—temperature in °K. Difference of the stability curves for fresh and ocean water can be seen in Fig. 9.7. Transition from marine water to the fresh one increases the stability temperature by 1.5–2 °C. The diagrams in Fig. 9.7 demonstrates also that the P-T conditions of gas hydrate stability in the system "gas hydrate—porous water" depend on content of methane, ethane, propane, H_2S and CO_2 in the methane. The mixture of 5–10 % of ethane and propane in methane increases the temperature of gas hydrate stability by 5–10 °C [40, 43, 47–49].

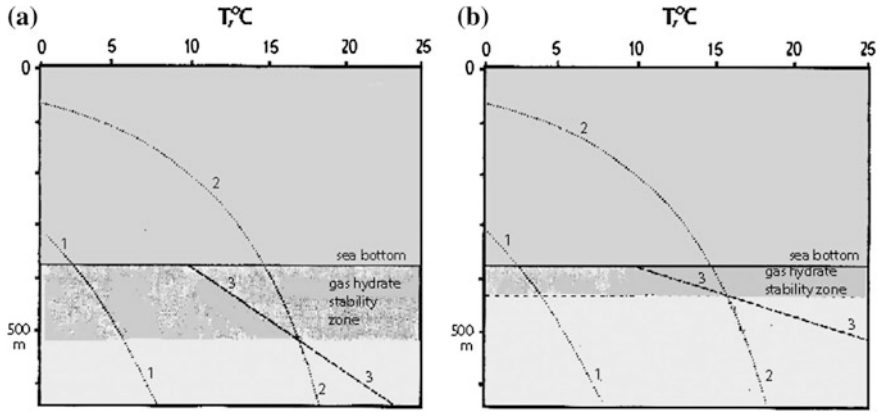

Fig. 9.9 The gas hydrate stability zones under flanks (*a*) and crater (*b*) of mood volcano Mercator in the Morocco shelf (after [49] with little changes). *1* The equilibrium curves for pure methane; *2* the equilibrium curves for methane with 20 % CO_2. *3* temperature distributions in sedimentary blanket (i.e. below sea bottom) corresponding to gradient dT/dz = 60 °C/km under flanks of mood volcano (**a**) and dT/dz = 110 °C/km under the mood volcano (**b**)

The difference between the stability curves for pure methane and methane with admixture of other gas is illustrated also in Fig. 9.9. Here, estimate of depth of base of zone of the gas hydrate stability is used for assessment temperature gradient in the study area. The equilibrium curves for methane with 20 % CO_2 and for pure methane were used for determination of temperature at the base of the gas hydrate stability zone. The following parameters were taken in this assessments: Vp = 1500 m/s—for water, Vp = 1800 m/s—for sedimentary rocks, water density ρ_w = 1030 kg/m^3, density of sedimentary rocks ρ_s = 2300 kg/m^3, density of matrix of the sedimentary rocks ρ_m = 2650 KT/m^3, gas hydrate density ρ_h = 900 kg/m^3. It is supposed that sediments consisted of 20 % of hydrates and 80 % of matrix. Then, the depth and pressure of the base of the gas hydrate stability zone were determined. The pressure increases from 3500 kPa under the volcano crater to 6000 kPa under flanks of volcano in deeper site of the sea. The temperature at the base of the stability zone of gas hydrates was calculated according to curve of P-T equilibrium for the above curves 1 and 2 in Fig. 9.9. Such estimations suggest higher temperature gradient under volcano than under its flanks. In Chap. 10 other examples of determination of top and base of the zone of methane hydrate stability using temperature distributions obtained in the basin modeling procedure.

9.4 Conclusion

In this chapter it was shown that permafrost modeling can be analyzed as a part of procedure of basin modeling. General procedure of basin modeling is used to construct initial temperature distribution for permafrost modeling and calculate also the depth-distribution of thermal physical parameters of frozen and thawed rocks for initial time of permafrost evolution. The use of real lithological composition of sedimentary rocks distinguishes this approach from previous studies of permafrost evolution. The modeling suggests that depth and time variations in thermophysical parameters of rocks (heat conductivity, heat capacity, unfrozen water and salt content, porosity) had a considerable influence on the results of permafrost modeling. The calculations demonstrate that the formation and degradation of the zones of stable existence of gas hydrates in the Pliocene-Holocene time are in close correlation with the events of formation and degradation of permafrost layers in the basins of high latitudes. All of these events were repeated many times during the Quaternary (Chap. 10). The diagrams presented in this chapter demonstrates that the P-T conditions of gas hydrate stability in the system "gas hydrate—porous water" depend strongly on the content of salt, ethane, propane, H_2S and CO_2 in the porous water and methane. This leads to the diversity of conditions of occurrence of gas hydrates in the land and marine environments.

References

1. Gold LW, Lachenbruch AH (1973) Thermal conditions in permafrost—a review of North American literature. In: Second international conference on North American contribution, permafrost, Yakutsk. Nat. Acad. Press, Washington, 13–28 July 1973
2. Brown RJE (1970) Permafrost as an ecological factor in the subarctic. In: Proceedings, conference on ecology of subarctic regions. vol 1966. Helsinki, pp 129–138
3. Dobinski W (2011) Review Permafrost. Earth-Sci Rev 108:158–169
4. Beilman DW, Vitt DH, Halsey LA (2001) Localized permafrost peatlands in western Canada: definition, distributions, and degradation. Arct Antarct Alp Res 33(1):70–77
5. Lachenbruch AH, Sass JH, Marshall BV, Moses TH (1982) Permafrost, heat flow and the geothermal regime at Prudhoe Bay. Alaska J Geophys Res 87:9301–9316
6. Duchkov AD, Lysak SV, Balobaev VT (1987) Thermal field of the Siberian crust. Nauka, Novosibirsk (in Russian)
7. Duchkov AD, Dobretsov NN, Ayunov DE, Sokolova LS (2011) Permafrost-geothermic Atlas of Siberia and Far East. In: Dynamics of physical fields of the Earth. Moscow, Svetoch Plus, pp 207–221
8. Ershov ED (1990) General geocryology. Nedra, Moscow (in Russian)
9. Balobaev VT (1991) Geothermy of permafrost zone in the lithosphere of the northern Asia. Nauka, Novosibirsk (in Russian)
10. Sigunov YA, Fartyshev AI (1991) Study of evolution of cryolitic zone in the Arctica shelf by mathematical modeling. Geologia i Geofisika 8:24–31 (in Russian)
11. Sigunov YA, Fartyshev AI (1995) Freezing and thawing of the East-Arctic shelf in the Late Pleistocene (numerical experiment). Geologiya i geophisika 36(9):24–31 (in Russian)

12. Lebret P, Dupas A, Clet M (1994) Modeling of permafrost thickness during the late glacial stage in France: preliminary results. Canad J Earth Sci 31:959–968
13. Balobaev VT, Tetelbaum AC, Mordovskiy CD (1999) Two-dimensional numerical model of hydrodynamic field below permafrost at permafrost thickness variations. Kriosphera Zemli III (4):48–53 (in Russian)
14. Romanovskii NN, Khubergen XB, Gavrilov AV, Eliseeva AA, Tipenko GS, Kholodov AL, Romanovskii VE (2003) Permafrost and gas hydrate stability zone evolution in the eastern part of the Eurasia Arctic Sea shelf in the Middle Pleistocene-Holocene. Criosphera Zemli VII (4):51–64 (in Russian)
15. Romanovskii NN, Eliseeva AA, Gavrilov AV, Tipenko GS, Khubergen XB (2005) The long-term dynamics of the permafrost and gas hydrate stability zone of rifts of the East Siberian Arctic shelf (report 1). Criosphera Zemli IX(4):42–53 (in Russian)
16. Romanovskii NN, Eliseeva AA, Gavrilov AV, Tipenko GS, Khubergen XB (2006) The long-term dynamics of the permafrost and gas hydrate stability zone of rifts of the East Siberian Arctic shelf (report 2). Criosphera Zemli 1(X):29–38 (in Russian)
17. Galushkin YuI (1997) Numerical simulation of permafrost evolution as a part of basin modeling: permafrost in Pliocene-Holocene climate history of Urengoy field in West Siberian basin. Canad J Earth Sci 34(7):935–948
18. Galushkin YI, Yakovlev GE (2004) Burial and thermal history of the West Bashkirian sedimentary basins. Tectonophysics 379:139–157
19. Galushkin YuI, Sitar KA, Frolov SV (2013) Basin modeling of temperature and heat flow distributions and permafrost evolution, Urengoy and Kuyumbinskaya areas, Siberia. Permafrost Periglac Process 24(4):268–285
20. Makhous M, Galushkin Yu (2005) Basin analysis and modeling of the burial, thermal and maturation histories in sedimentary basins. Editions TECHNIP, Paris
21. Velichko AA (ed) (1999) Change in climate and landscapes during last 65 My (The Cenozoic: from Paleocene to Holocene). GEOS, Moscow (1999) (in Russian)
22. Fotiev SM (2005) Modern conceptions of the evolution of Cryogenic area of West and East Siberia in Pleistocene and Holocene (report 1). Kriosphera Zemli IX(2):3–22 (in Russian)
23. Fotiev SM (2009) Cryogenic methamorphism of rocks and groundwaters (conditions and results). Novosibirsk, Academicheskoe Izdatelstvo “Geo” (in Russian)
24. Deming D, Chapman DS (1989) Thermal histories and hydrocarbon generation: example from Utah-Wyoming thrust belt. AAPG Bull 73(12):1455–1471
25. Jame Y-W, Norum DI (1980) Heat and mass transfer in a freezing unsaturated porous medium. Water Resour Res 16(4):811–819
26. Kudryavzev VA (1981) Permafrost study. Moscow University Press (in Russian)
27. Kudryavzev SA (2003) Numerical investigations of the thermal physical processes in seasonally freezing soils. Kryosphera Zemli VII(4):76–81 (in Russian)
28. Nixon JF (1986) Thermal simulation of subsea saline permafrost. Canad J Earth Sci 23:2039–2046
29. Ershov ED (1990) General geocryology. Nedra, Moscow (in Russian)
30. Cheverev VG, Vidyapin IY, Motenko RG, Kondakov MV (2005) Determination of the content of unfrozen water in ground from sorption-desorption isotherms. Kriosphera Zemli IX (4):29–33 (in Russian)
31. Konrad JM, Seto JTC (1991) Freezing of a clayey silt contaminated within organic solvent. J Contam Hydrol 8(3/4):335–355
32. Hivon E, Sego D (1995) Strength of frozen saline soils. Can Geotech J 32:36–54
33. Arensen LU, Sego DC (2006) The effect of salinity on the freezing of coarse-grained sands. Can Geotech J 43:325–337
34. Nicolsky D, Shakhova N (2010) Modeling sub-sea permafrost in the East Siberian Arctic Shelf: the Dmitry Laptev Strait. Environ Res Lett 5 (January–March) 015006. doi:10.1088/1748–9326/5/1/015006
35. Weaver JS, Stewart JM (1982) In-situ hydrates under the Beaufort Sea shelf. In: 4-th Canadian permafrost conference calgary, pp 312–319

36. Sloan ED Jr (1990) Clathrate hydrates of natural gases. Marcel Dekker Inc, New York
37. Ginsburg GD, Solovjev VA (1994) Submarine gas hydrates. Sanct Peterburg, VNIIOkeanologiya, 1–199
38. Carcione JM, Gei D, Rossi G, Madrussani G (2005) Estimation of gas-hydrate concentration and free-gas saturation at the Norwegian-Svalbard continental margin. Geophys Prospect 53:803–810
39. Collet TS (2002) Energy resource potential of natural gas hydrates. AAPG Bull 86(11):1971–1992
40. Laberg JS, Andreassen K, Knutsen S-M (1998) Inferred gas hydrate on the Barents Sea shelf —a model for its formation and a volume estimate. Geo-Mar Lett 18:26–33
41. Kurchikov AP (1992) Hydrogeological criteria for petroleum potential. Nedra, Moscow
42. Istomin VA, Yakushev VS (1992) Gas hydrates in natural conditions. Nedra, Moscow
43. Jackson BA (2004) Seismic evidence for gas hydrates in the North Makassar Basin Indonesia. Petrol Geosci 10(3):227–238
44. Xu W, Ruppel C (1999) Predicting the occurrence, distribution, and evolution of methane gas hydrate in porous marine sediments. J Geophys Res 104(B3):5081–5095
45. Majorowicz IA, Osadetz KG (2001) Gas hydrate distribution and volume in Canada. AAPG Bull 85(7):1211–1230
46. Mienert J, Posewang J (1999) Evidence of shallow and deep-water gas hydrate destabilizations in North Atlantic polar continental margin sediments. Geo-Mar Lett 19:150–156
47. Hesse R, Harrison WE (1981) Gas hydrates (clathrates) causing pore-water freshening and oxigen isotope fractionation in deep-water sedimentary sections of terrigeneous continental margins. Earth Planet Sci Lett 55:453–462
48. Weaver JS, Stewart JM (1982) In-situ hydrates under the Beaufort Sea shelf. In: 4-th Canadian permafrost conference Calgary, pp 312–319
49. Depreiter D, Poort J, Van Rensbergen P, Henriet JP (2005) Geophysical evidence of gas hydrates in shallow submarine mud volcanoes on the Maroccan margin. J Geophys Res 110 (B10):103–10,102

Chapter 10
Influence of Climate Variations on Rock Temperature and Heat Flow

Abstract This chapter considers application the software package FROST as a part of the GALO system for basin modeling to reconstruction of thermal history and permafrost evolution during the Pliocene-Quaternary in the intra-continental and shelf sedimentary basins. The chapter examines as regions with modern areas of permafrost (Urengoy field in the West Siberian Basin and Kuyumba field in the Siberian Platform) as the basins where permafrost degraded 10–12 thousand years ago (in the South Urals region and Barents and Sakhalin shelf). The calculations confirm the significant role of variations in rock composition with depth in permafrost evolution. Repeated formation and degradation of permafrost in the Pliocene-Holocene results in considerable decrease of rock temperatures within the upper 1500 m of sedimentary section of Siberia. The model allows an estimate of permafrost depth and stability zone of methane gas hydrate in sedimentary section of basin. It is shown that an increase in salt content in porous water and change in shape of the unfrozen water curve, $W(T)$, depending upon lithological composition of sedimentary rocks, can influence considerably the numerical estimations of permafrost depth. The modeling suggests that a changes in heat flow or temperature gradient at depths of less than 2–2.5 km in sedimentary sections of basins can be considerable even in the regions where permafrost has degraded. The modeling in the Barents Sea shelf suggests rather rigorous climate of the last 70–50 thousand years while in the North-East Sakhalin shelf it assumes that the sea smoothed over the climatic jumps of the mean annual temperature during the greater part of the last 2.5 My and here the influence of the Pliocene-Holocene climate fluctuations in the depth profile of temperature is limited.

Keywords Permafrost · Paleoclimate · Basin modeling · West Siberian Basin · Siberian Platform · East Barents Sea · North Sakhalin shelf

Y. Galushkin, *Non-standard Problems in Basin Modelling*,
DOI 10.1007/978-3-319-33882-8_10

10.1 Problem Statement and Initial Data for Modelling the Evolution of Permafrost

According Chap. 9, the low thermal diffusivity and conductivity of sedimentary rocks lead to very slow propagation of the climatically driven thermal disturbances in the geological medium and to keeping the subsurface in a transient thermal condition for geologically relevant times. Formation and degradation of permafrost took place repeatedly in the Quaternary and resulted in noticeable lowering of the temperature in upper 1–3 km of present-day sedimentary section of the basin. Although evolution of permafrost in the Pleistocene-Holocene was studied in many papers (e.g. [1–7]), the numerical analysis of this problem in the frame of the basin modeling system has the advantage that it enables to analyze the processes of formation and degradation of permafrost taking into account the variations in lithological composition of rocks with depth (Chap. 9). The latter affect straightly on corresponding variations in petrophysical parameters of frozen and thawing rocks [8–10].

Evolution of permafrost in the Urengoy area has already been considered in paper [8] where the main principles of numerical reconstruction of permafrost evolution in the frame of the GALO basin modeling system were described (see also Chap. 9). In the present chapter, analysis of permafrost evolution in the Urengoy and Kuyumba areas (Fig. 10.1) is carried out using recent studies on

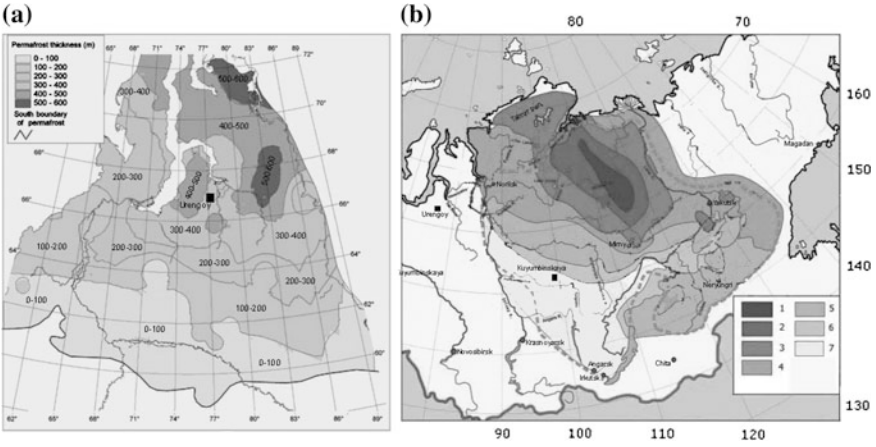

Fig. 10.1 Generalized map of permafrost thickness in the West Siberia (after [14] with few changes) and the Siberian Platform (after [15] with few changes). Numbers in legend of map **a** are the permafrost thickness (in m). Numbers in legend of map **b** correspond to following parameters: *1* continuous permafrost of thickness over 1000 m; *2* continuous permafrost of thickness 800–1000 m; *3* continuous permafrost of thickness 500–800 m; *4* continuous permafrost of thickness 300–500 m; *5* continuous permafrost of thickness 100–300 m; *6* discontinuous permafrost of thickness up to 200 m; *7* discontinuous and sporadic permafrost of thickness up to 100 m. *Dashed gray line* is boundary of the Siberian Platform. Locations of the Kuyumba and Urengoy fields are shown by *black squares* (see also Fig. 6.1)

climate variations [11–13] and taking into consideration the changes in shape of the unfrozen water curve, $W(T)$, depending upon lithological composition of sedimentary rocks (Sect. 9.2.5). It allows a correcting the previous numerical estimations for the Urengoy area and obtaining new results for the Kuyumba area.

This chapter analyzes the permafrost evolution in two different sedimentary sections of the Siberia. The first of them is a section of: the 411-well located in northern part of the West Siberian Basin close to the Urengoy-Koltogor Graben of the Triassic age (Fig. 10.1a). The thickness of sedimentary cover exceeds here 5 km [16]. Permafrost is formed here within sandy-clay and sandy rocks (Table 10.1). The present thickness of permafrost estimated from drilling data and subsequent geothermal research is here about 350 m [2, 3, 17]. The area is a part of the wide region with present-day thickness of permafrost of about 300–400 m (Fig. 10.1a). The second sedimentary section under modeling is a section of the Kuyumba area located to North–West from the Baikal Lake in the Kamov arch of

Table 10.1 Main stages of the West Siberian basin evolution in the Urengoy field, well 411

N	Type	t, My	Z, m	Shale	Sandstone	Siltstone	Volcanite	Coal
1	sedim	208–230	5280–5500	0.20	0.400	0.200	0.200	0.000
2	sedim	203.5–208	4635–5280	0.700	0.095	0.150	0.000	0.055
3	sedim	194.5–203.5	4299–4635	0.700	0.095	0.150	0.000	0.055
4	sedim	187–194.5	4070–4299	0.700	0.095	0.150	0.000	0.055
5	sedim	178–187	4020–4070	0.700	0.095	0.150	0.000	0.055
6	sedim	166–178	3810–4020	0.700	0.095	0.150	0.000	0.055
7	sedim	157–166	3726–3810	0.700	0.150	0.150	0.000	0.000
8	interrup.	152–157	3726–3726	–	–	–	–	–
9	sedim	145.6–152	3694–3726	0.745	0.000	0.000	0.000	0.255
10	sedim	131.8–145.6	2885–3694	0.600	0.200	0.200	0.000	0.000
11	sedim	124.5–131.8	2478–2885	0.500	0.190	0.300	0.000	0.010
12	sedim	119–124.5	2198–2478	0.500	0.190	0.300	0.000	0.010
13	sedim	112–119	1695–2198	0.600	0.184	0.200	0.000	0.016
14	sedim	97–112	1468–1695	0.600	0.184	0.200	0.000	0.016
15	sedim	90.4–97	1243–1468	0.300	0.284	0.400	0.000	0.016
16	sedim	88.5–90.4	1177–1243	0.900	0.050	0.050	0.000	0.000
17	sedim	65–88.5	633–1177	0.900	0.050	0.050	0.000	0.000
18	sedim	56.5–65	539–633	0.150	0.850	0.000	0.000	0.000
19	sedim	50–56.5	440–539	0.500	0.500	0.000	0.000	0.000
20	sedim	42.1–50	300–440	0.050	0.950	0.000	0.000	0.000
21	sedim	30–42.1	70–300	0.500	0.500	0.000	0.000	0.000
22	erosion	6–30	300	–	–	–	–	–
23	interrup.	2–6	70–70	–	–	–	–	–
24	sedim.	0–2	0–70	0.500	0.500	0.000	0.000	0.000

Remarks N is the number of stage of the Basin development, starting with its initiation; *type* type of the stage (*sedim.* sedimentation, *interrup* interruption, erosion). *t* is the start and finish time of the stage in My, *Z* is the depth of top and base of sedmentary layer in the present-day section or thickness of eroded sediments [16]. The column "coal" shows content of organic matter in sedimentary rock of current layer

the East Siberian Platform (Figs. 6.1 and 10.1b). This section of the Riphean age is considerably older than the first. Specific feature of second section is a presence of six intrusive sills of the Lower Triassic age which influence strongly on distribution of heat conductivity and capacity with depth (Fig. 6.4) and largely determine the permafrost thickness (see below). Permafrost was formed here within sandy clay and dolomite rocks with little mixture of halite (Table 6.1 in Sect. 6.1). Paleoclimate studies in the West Siberia and Siberian Platform [11–13] show that climate changes in the Urengoy and Kuyumba areas were largely synchronous, but temperatures in the first area were slightly lower than in the second (see below). However, the present thickness of permafrost determined from drilling in the Kuyumba field is about 400 m (Fig. 10.1b; [17, 18]) that exceeds the value in the Urengoy field. It can be noted, that the Kuyumbinskaya area locates within the region of considerable change in permafrost thickness (Fig. 10.1b). Probably for this reason, the local permafrost thickness (400 m) defined by the drilling data are markedly different from the values estimated by the generalized map in Fig. 10.1b.

The primary goal of this chapter is to investigate the main factors affecting the formation of permafrost and temperature distribution with depth in two different regions of Siberia. On the example of detailed numerical reconstruction of the above sedimentary section, it will be shown that variation in composition of sedimentary rocks with depth together with climate variations and regional heat flow determinate permafrost evolution and its thickness. According to Chap. 9, basin modeling presents a good opportunity to analyze the problem of permafrost evolution taking into consideration an actual lithology of sedimentary section. Of course, the thermal effects of the Triassic rifting in Urengoy or trap activity in the Lower Triassic in Kuyumba area on temperature distribution in the Pliocene-Quaternary are negligible. But basin modeling is a convenient way to construct present-day sedimentary section with detailed distribution of porosity and petrophysical attributes of rocks with depth that take into consideration the changes in rock lithology and decrease of pore volume due to sedimentary load removed during past events of intensive repeated erosion (Tables 6.1 and 10.1).

We apply a non-steady one-dimensional model (flat basin approach) for the problem analysis. Application of the model of a flat basin is justified for basin modeling in considered areas, because thickness of sedimentary blanket and thickness of single layers do not change considerable on the distance of 10–30 km [16, 19, 20]. There are not any disturbing factors like to rivers or lakes in vicinity of the wells under study. Then permafrost modeling can also be considered in the frame of the flat model neglecting lateral heat transfer in comparison with the vertical one. Calculations are carried out with using of the FROST-computer program, which was constructed as a part of general program package GALO for basin modeling and was described in Chap. 9.

According to Chap. 9, an initial temperature distribution and detailed change of thermophysical parameters of rock with depth that are required in permafrost modeling, are obtained in the general basin modeling procedure (Sects. 9.1 and 9.2).

Consequently, the procedure of permafrost modeling consists of two steps, the first of which is general modeling and the second is permafrost modeling. The main objective of general modeling is to obtain a temperature distribution T(z) for the time t = 3.4 My ago which served as initial distribution for subsequent permafrost modeling. Simultaneously, a detailed distribution of rock porosity with depth in present-day section of the basin, corresponding to complex geological history of the basin including repeated events of intensive erosion (Tables 6.1 and 10.1; Fig. 10.1) and lithology composition of its rocks in present-day section of the basin are computed in the general modeling. The Tables 6.1 and 10.1 show the main stages of the basins development together with the present-day sedimentary sections of these basins and lithological composition of their rocks.

It may be noted that geological history of the Kuyumba area includes several stages of erosion resulted in total removing of some layers from present-day section (layers 18, 19, 20 in Table 6.1; Fig. 10.2d). Tables 10.2 and 10.3 show the values of petrophysical parameters for rock matrix that take a part in general and permafrost modeling. These parameters were computed for the rock mixtures with lithological composition pointed in Tables 10.1 and 6.1 using the world-average data for the main lithological units [21, 22]. The main part of modeling consists of reconstruction of burial history of the basin by "backstripping" method and solution of the non-steady heat transfer equation in the domain included in general modeling also the basement up to depth 100 and more km (Sect. 6.2; [10, 20]). Thermal

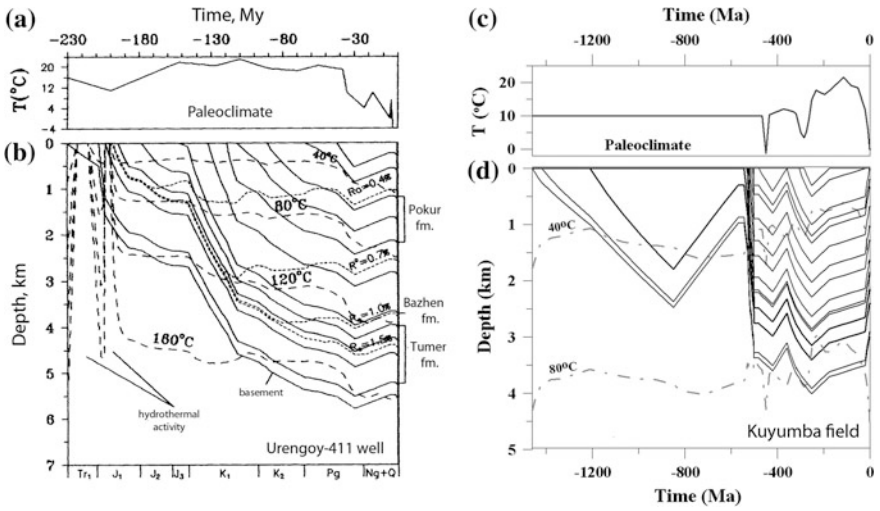

Fig. 10.2 Paleoclimate curves (**a**, **c**) and burial and thermal histories (**b**, **d**) of the Siberia Platform (well Kuyumba-212, Kamov swell; Figs. 6.1 and 10.1; [20]) and the West Siberia Basin (Urengoy field, well 411; Fig. 10.1; [10, 20]). In Figs. **b** and **d**: *solid lines* base of the sedimentary layers; *dashed lines* isotherms; *dotted lines* isolines of vitrinite reflectance (Ro%)

Table 10.2 Petrophysical parameters of sedimentary rocks for basin and permafrost modeling in section of well 411 in the Urengoy field

N	$\phi(0)$	B m	K_m W/m °K	α $°K^{-1}$	C_{vm} MJ/m^3 °K	ρ_m kg/m^3	A mW/m^3
1	0.539	2520	3.019	0.0017	2.642	2670	1.02
2	0.653	1900	2.198	0.0009	2.314	2620	1.73
3	0.653	1890	2.198	0.0009	2.314	2620	1.73
4	0.653	1880	2.198	0.0009	2.314	2620	
5	0.653	1880	2.198	0.0009	2.314	2620	1.73
6	0.653	1880	2.198	0.0009	2.314	2620	1.73
7	0.656	1930	2.495	0.0011	2.420	2690	1.77
8	–	–	–	–	–	–	–
9	0.639	1680	1.390	0.0004	1.939	2370	1.56
10	0.639	1970	2.646	0.0013	2.470	2680	1.67
11	0.622	1980	2.717	0.0014	2.493	2670	1.57
12	0.622	1960	2.717	0.0014	2.493	2670	1.57
13	0.638	1900	2.554	0.0012	2.440	2660	1.65
14	0.638	1880	2.554	0.0012	2.440	2660	1.65
15	0.576	2010	3.014	0.0018	2.587	2650	1.35
16	0.687	1810	2.219	0.0007	2.315	2690	1.98
17	0.687	1800	2.219	0.0007	2.315	2690	1.98
18	0.478	2140	3.772	0.0026	2.797	2660	1.03
19	0.600	1760	2.960	0.0017	2.575	2670	1.47
20	0.429	2520	4.044	0.0029	2.860	2650	0.90
21	0.600	1700	2.960	0.0017	2.575	2670	1.47
22	–	–	–	–	–	–	–
23	–	–	–	–	–	–	–
24	0.600	1620	2.960	0.0017	2.575	2670	1.47

Remarks N just in Table 10.1, $\phi(0)$ rock porosity at the surface (average porosity of the rock at the depth from 0 to 200 m), *B* depth parameter in the law: $\phi(z) = \phi(0)\cdot EXP(-Z/B)$, K_m the thermal conductivity of the rock matrix at the temperature T = 20 °C, α-temperature coefficient for matrix thermal conductivity: $K_m(T) = K_m(20\ °C)/(1. + \alpha\cdot T\ °C)$, C_{vm} volumetric heat capacity of matrix rocks, ρ_m density of matrix rocks, A-heat generation per volume unit in the rock matrix. The values of petrophysical parameters in this Table were calculated for mixtures of rocks pointed in Table 10.1 by an averaging procedure [21] of the world average values for the lithological units presented for example in [22]

parameters of the basement rocks are given in Table 1.1. The duration and amplitude of events of thermal activation or stretching of the lithosphere in the evolution of two basins were determined due to analysis of tectonic subsidence (Sect. 1.2). They are discussed in Sect. 6.2 for the Kuyumba area (see Fig. 6.6 and [10]) and in paper [20] for the Urengoy area.

Table 10.3 Petrophysical parameters of sedimentary rocks for basin and permafrost modeling in section of well 12 in the Kuyumba field

N	$\phi(0)$	B m	K_m W/m °K	α $°K^{-1}$	C_{vm} MJ/m^3 °K	ρ_m kg/m^3	A mW/m^3
1	0.700	1800	2.09	0.0005	2.26	2700	2.09
2	0.559	1910	3.94	0.0017	2.61	2740	0.71
3	0.514	1980	4.44	0.0019	2.68	2750	0.44
4	–	–	–	–	–	–	–
5	–	–	–	–	–	–	–
6	0.508	1890	4.47	0.0022	2.60	2710	0.43
7	0.545	1920	4.09	0.0018	2.63	2740	0.62
8	0.400	1740	4.88	0.0030	2.35	2510	0.30
9	0.527	1860	4.18	0.0020	2.56	2690	0.59
10	0.397	1720	4.89	0.0031	2.32	2590	0.30
11	0.528	1870	4.25	0.0020	2.59	2710	0.54
12	0.534	1830	4.05	0.0020	2.51	2670	0.66
13	0.516	1970	4.42	0.0019	2.68	2750	0.45
14	0.600	1970	3.09	0.0013	2.61	2700	1.12
15	–	–	–	–	–	–	–
16	0.600	2060	2.96	0.0017	2.57	2670	1.47
17	–	–	–	–	–	–	–
18	0.600	2060	2.96	0.0017	2.57	2670	1.47
19	0.600	2060	2.96	0.0017	2.57	2670	1.47
20	0.600	2060	2.96	0.0017	2.57	2670	1.47
21	–	–	–	–	–	–	–
22	–	–	–	–	–	–	–
23	–	–	–	–	–	–	–
24	0.600	2060	2.96	0.0017	2.55	2670	1.47

Remarks N just in Table 6.1, $\phi(0)$ rock porosity at the surface (average porosity of the rock at the depth from 0 to 200 m), *B* depth parameter in the law: $\phi(z) = \phi(0)\cdot EXP(-Z/B)$, K_m the thermal conductivity of the rock matrix at the temperature T = 20 °C, α-temperature coefficient for matrix thermal conductivity: $K_m(T) = K_m(20\ °C)/(1. + \alpha\cdot T\ °C)$, C_{vm} volumetric heat capacity of matrix rocks, ρ_m density of matrix rocks, A-heat generation per volume unit in the rock matrix. The values of petrophysical parameters in this Table were calculated for mixtures of rocks pointed in Table 6.1 by an averaging procedure [21] of the world average values for the lithological units presented for example in [22]

Results of the general basin modeling for the Kuyumba-212 and Urengoy-411 wells are shown in Fig. 10.2a, b. The temperatures (Fig. 10.3) and vitrinite reflectance (Fig. 10.4a, b) measured in the present-day sedimentary section of the basin, as well as an analysis of tectonic subsidence of the basin (Fig. 6.6; Sect. 6.2; [10, 20]), were the main factors to control a validity of the modeling.

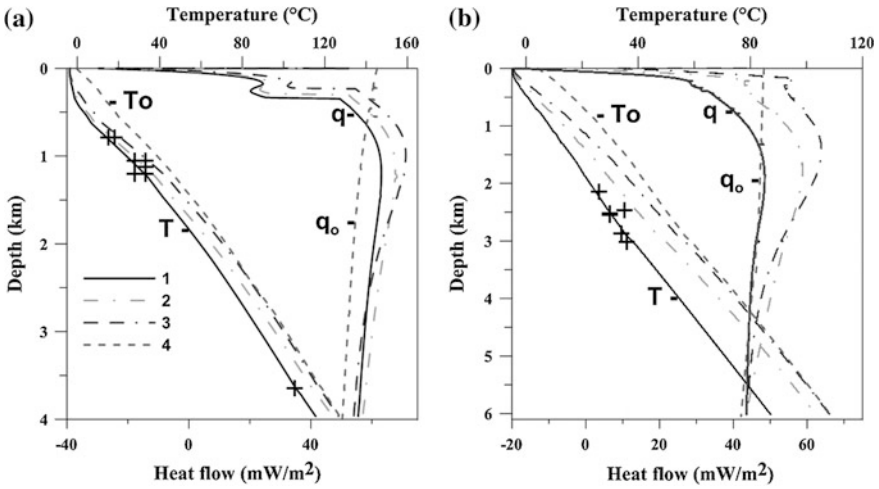

Fig. 10.3 Present-day distributions of temperature (T) and heat flow (q) with depth in the Urengoy (**a**) and Kuyumba (**b**) areas [10]. *1* the distributions, calculated with climate variations during the last 3.4 My; *2* and *3* the distributions, calculated with climate variations during the last 200,000 and 50,000 years for the Kuyumba and Urengoy areas; *4* temperature (To) and heat flow (q_o) distributions with depth for the time 3.4 My ago (initial distribution for permafrost modeling)

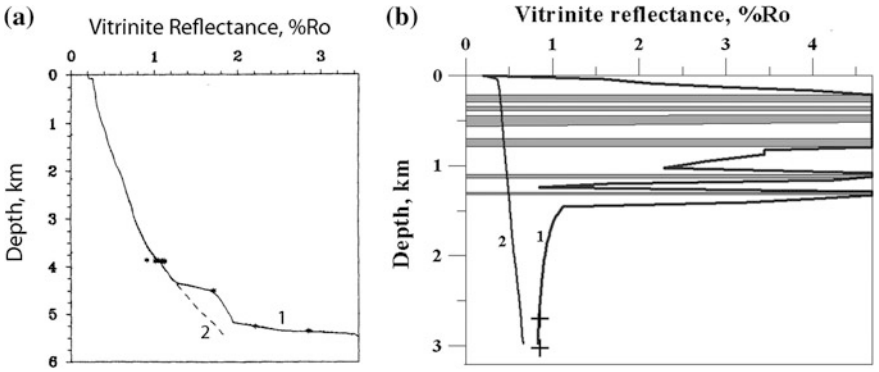

Fig. 10.4 **C**omparison between measured (*symbols*) and computed (*lines*) values of vitrinite reflectance in the Urengoy (**a**) and Kuyumba (**b**) areas [10, 20]. **a** *1* computations with consideration of hydrothermal heat transfer in the Upper Triassic (Fig. 10.2a, [20]), *2* calculations without the latter effect. **b** *1* computations with consideration of intrusions heat, *2* without the latter effect; *gray horizontal strips* intrusions into sedimentary blanket (see Fig. 6.7 and Sect. 6.3.1)

10.2 Change of Temperature and Heat Flow with Depth in Permafrost Zones

The porosity distribution with depth computed by the general modeling for the present time (t = 0) is used in the second step of the modeling for calculation of distributions of thermal parameters of the rocks (heat conductivity, KT(z,t), heat capacity, Cv(z,t), heat generation, A(z,t)) with depth and time of permafrost evolution. In addition to the porosity, these parameters are determined by lithological composition of rocks and their temperature calculated in the permafrost modeling (Sect. 9.2). Consequently, the initial temperature distribution, available variations in the mean annual surface temperature and distributions of porosity and lithological composition of rocks with depth are used in the second step of modeling to reconstruct in detail the temperature evolution of the sedimentary section with help of the FROST computer package that takes into account the repeated processes of formation and degradation of permafrost.

One of the problems in our modeling is the use of steady distribution of rock porosity and lithology with depth during 3.4 million years of permafrost evolution. Initial temperature distribution T(z) for permafrost modeling was obtained in the first step of the modeling (general modeling) for the time t = 3.4 My ago and then it is rewritten on this steady sedimentary section. This porosity and lithology distributions with depth correspond to the ones computed in the first general modeling stage for present time and include the layer of Quaternary sediments. Of course, it is approximate approach, because the Quaternary sedimentation took place during permafrost formation and degradation. For the Kuyumbinskaya area, the time interval of permafrost modeling (the last 3.4 million years) included the erosion of approximately 44 m of sediments (from 3.4 to 1.8 My) and deposition 15 m sandy clays during the last 1.8 My (Table 6.1). At the same time in the Urengoy area, it included deposition of 70 m of the same rocks during the Quaternary (Table 10.1). Of course, an accurate estimate of influence of erosion and sedimentation during the last 3.4 My on permafrost formation requires a special study that must be done in future research. But here we believe that approximation of sedimentary section during last 3.4 My by present-day section (in porosity, rock lithology and depths of sedimentary layers) should not lead to significant deviations from the results of our modeling. In fact, we are talking only about the deposition of 7 m of sediments during the last 200 thousand years that is much lesser than thickness of the present-day permafrost zone. In addition, the heat wave from the earlier events penetrates to a depth much greater than the thickness of the Quaternary sediments and erosion amplitude.

It was stated above, that only the distribution of porosity and rock lithology with depth remain constant during the simulation of the permafrost evolution. They correspond to the values in a modern sedimentary basin. At the same time, thermal conductivity and heat capacity of the frozen and thawed rocks depend on the temperature, ice and water content in the rock pores. Therefore they vary with time and depth during permafrost evolution (Sect. 9.2). The thermal conductivity of

frozen rock depend strongly on the unfrozen water content, $W(T)$, because thermal conductivity of ice exceeds the water conductivity about by 4 times (Sect. 9.2). Indeed, a considerable decrease in heat conductivity, KT, just under permafrost zone in Figs. 9.2b and 9.3b is related to transition from ice above the permafrost base to thawed water under the base. It may be noted also that a sharp break in the measured temperature gradients, related with sharp decrease of heat conductivity near the permafrost base (Figs. 9.2a, b, 9.3a, b and 9.5) is observed practically in all areas of the West Siberia with the present-day permafrost [3]: and also in Alaska [1] and northern Canada. This break in temperature gradient and heat flow is often interpreted as the base of ice-bonded permafrost, lying usually somewhat shallower than the base of 0 °C due to the character of the unfrozen water content curve and in situ salinity (Figs. 9.2a, 9.3a and 9.5).

Figures 9.2b, d and 9.3b, d illustrate a computed change in parameters KT and $W(T)$, versus depth in the present-day sedimentary section of the Kuyumba and Urengoy fields in response to variations in rock composition and porosity. Increase in heat conductivity in Figs. 9.2b is due to increase of sandy fraction in rock composition (Fig. 9.2d). A jump-like increase in thermal conductivity in Fig. 9.3b at depths from 300 to 325 m in the Urengoy-411 well is partly due to increase of sandy fraction up to 95 % in this horizon and partly to the sharp change in unfrozen water content, W, associated with the sand at these depths (see solid line W on Fig. 9.3d). Note that W = 1 at the depth below the permafrost base where all rocks are thawed.

Specific feature of the Kuyumba section is a presence of intrusive sills at the depth 218–298, 347–395 and 442–520 m with porosity $\varphi = 0$ and relatively low heat conductivity KT = 1.90 W/m °K (Figs. 6.4 and 6.7f). As whole, the presence of intrusions reduces significantly the average thermal conductivity of sedimentary rocks because sedimentary rocks even with moderate content of sandy fraction would have higher heat conductivity (see for example Figs. 9.2b). Thus, replacing intrusions in sedimentary cover by sedimentary host rocks in conformity with sedimentary section of Table 6.1 leads to increase of permafrost thickness up to 563 m (instead 400 m). The boundaries of the roof and base of the zone of gas-hydrate stability become 227 and 1932 m instead 240 and 1590 m in previous variant. It is necessary to note that in the Kuyumba area the effect of reducing of the average effective heat conductivity of the sedimentary blanket due to intrusions is compensated partly by the proximity of the basement rocks of the relatively high heat conductivity to the basin surface.

According to Eq. (9.7) in Sect. 9.2.4, the ice liquidus temperature TL depend on pressure and salt content in the pore water. Exact profiles of salt content versus depth in the areas under consideration are unknown and we took steady salt content with depth throughout our calculations: Cs = 15 g/L for the Urengoy-411 section and Cs = 12 g/L for the Kuyumba-212 well. Influence of salt content on modeling results will discussed below. Distributions $TL(z)$, used in our calculations for two areas, are shown in Figs. 9.2a and 9.3a.

The temperature profile for the time t = 3.4 Ma ago (To(z)) computed in general modeling serves as initial temperature distribution in solution of Eq. (1.1) (without

convective member) for the subsequent reconstruction of the thermal regime of the sedimentary sections of the Basins in the Late Pliocene and Quaternary. These profiles To(z) for both areas can be seen in Fig. 10.3. The mean-annual temperatures histories since 3.4 Ma are applied at the upper boundary of the domain of computation and are discussed below. The base of the sedimentary section is at about 5550 m in the Urengoy field near well 411 (Fig. 10.2a; Table 10.1) and at about 3020 m in the Kuyumba area (Fig. 10.2b; Table 6.1). For Urengoy field, the lower boundary of z-domain for temperature computations, ZM, coincides with the base of sedimentary section (ZM = 5550 m). At this boundary, a steady heat flow QM = 52 mW/m^2 is maintained during the permafrost modeling. In the Kuyumba field, a thickness of sedimentary blanket is lesser (3020 m) and two variants with different ZM were considered here to test the sensitivity of the model to the lower boundary conditions. The first variant suggests that lower boundary of z-domain of computation is in the basement at the depth ZM = 6 km. This variant is considered as the main one and the Figs. 10.3b and 10.4b show the results of modeling according to this variant. The second variant of modeling suggests that the lower boundary of z-domain of permafrost computation is at the base of sedimentary blanket, i.e. at the depth ZM = 3.01 km. This variant was considered only for comparison with the first one. The heat flows QM = 43.5 mW/m^2 and QM = 45.2 mW/m^2 were maintained at the depth ZM during the permafrost modeling in the first and second variants correspondingly. These flows QM were matched to the values of heat flows obtained in general basin modeling for the Kuyumba field at the depth z = ZM for the time 3.4 Ma ago (see curves q_o in Fig. 10.3b). In addition, deviation of Q from QM no more than 2 mW/m^2 is permitted to provide an exact match of the measured and calculated thickness of permafrost. It may be noted that increase in heat flow QM in the second variant is due to the contribution of radiogenic heat of the upper layer of the basement (from 3 to 6 km in the basement). Our computations shown that a choice of ZM = 3.02 km as lower boundary of the domain for the Kuyumba area instead ZM = 6 km does not lead to considerable change in the modeling results. Indeed, the present-day distributions T(z) and q(z) calculated in two variants are almost the same with maximum deviations at lower boundary of comparison (Z = 3.02 km) that were: T = 38.15 and 37.97 °C and q = 46.13 and 45.95 mW/m^2 in the first and second variants respectively.

The Fig. 10.3 demonstrates the considerable change in the thermal regime of both sedimentary basins caused by the Pliocene and Quaternary variations in climate. It is confirmed also by measurements of deep temperatures and heat flow in the region [3, 12, 13, 17, 23, 24]. According to the modeling, a cooling of climate during the last 3.4 My led to a reduction of temperatures by 15–20 °C in the upper 2–3 km of the sedimentary section (Fig. 10.3). Geothermal measurements in the West Siberia have shown that the present-day heat flow, measured at depths from 1000 to 1500 m, can exceed the values measured at depths 0–200 m, by 2 times and more [2, 25]. This fact is also confirmed by computed results on Figs. 10.3, which show that the heat flow is unsteady and changes sharply within the permafrost zone, especially near to its lower boundary. Therefore, terrestrial heat flow is influenced by recent changes in surface temperature and the latent heat effect at

the base of both aggrading and degrading permafrost, i.e., non-equilibrium permafrost [8, 23, 26]. The present-day heat flow can be lesser the regional one by 30–50 mW/m^2 within the permafrost, but the deviations from the regional heat flow decrease at greater depths (Fig. 10.3). Therefore, the flow measurements at the depths lesser than 1000 m can give an incorrect estimation of the deep ("undisturbed") heat flow in permafrost areas, if climate factor is not considered.

10.3 Permafrost Thickness and Zone of Gas-Hydrate Stability

The boundaries of permafrost zone were determined by intersection of calculated current temperature profile T(z,t) with the temperature of ice liquidus (Sect. 9.2), TL, depended on depth (Eq. (9.7); Figs. 9.2a and 9.3a). Calculated variations in depths of permafrost for the last 3400, 150 and 50 thousand years are shown in Figs. 10.5 for the Kuyumba (1–3) and Urengoy (4–6) areas. As a result of the last ice age (23–15 Ka), maximal penetration of permafrost took place about 13 thousand years ago and amounted to about 625 m in Kuyumba well and 480 m in the Urengoy 411 well (Fig. 10.5(3b), (6b)). The permafrost zone degraded then in response to increasing surface temperatures (Fig. 10.5(3a), (6a)). According to the modeling, the base of permafrost zone at present time occurs at the depth about of 400 m in the Kuyumba and 350 m in the Urengoy wells in an agreement with observed data in these areas [3, 12, 13, 17]. The calculations suggest that the permafrost zone in the Kuyumba area continues to degrade at present time with a rate of about 18 m/1000 years, whereas the permafrost thickness in the Urengoy area decreases at rate of about 14 m/1000 years. Figure 9.5 in Sect. 9.2.4 shows the sensitivity of the depth to the permafrost base to salinity on the example of the Urengoy area.

The depths of the top and base of the zones of the methane gas hydrate stability shown in Fig. 10.5b are determined by intersection of the predicted temperature profiles with the phase-curve for stability of pure methane gas hydrate with water and ice (Eq. (9.9) in Sect. 9.3.3; curves $T_h(z)$ in Figs. 9.2a and 9.3a). Figure 10.5 demonstrate that formation and degradation of the zones favorable for the methane gas hydrates stability correlate closely (with a small time delay) with dynamics of permafrost zones. The present-day zone for stability of methane gas hydrate is predicted at the depth from 230 to 1515 m in the Kuyumba area (Fig. 10.5(1b)–(3b)) and from 240 to 680 m in the sedimentary section of the Urengoy-411 well (Fig. 10.5 (4b)–(6b)). A greater depth of the zone corresponds to more cold thermal history of the sedimentary blanket in the Kuyumba area despite its warmer climate (Tables 10.4 and 10.5). More intensive cooling of rocks here is attributed to lower regional heat flow in Siberia Platformis (Sect. 10.2), the higher position of the basement with high conductivity of the rocks and also to more high effective heat conductivity of sedimentary rocks in the Kuyumba area (Tables 10.2 and 10.3; Fig. 6.4). The latter is caused by presence dolomites, anhydrites and halite in sedimentary cover (Table 6.1)

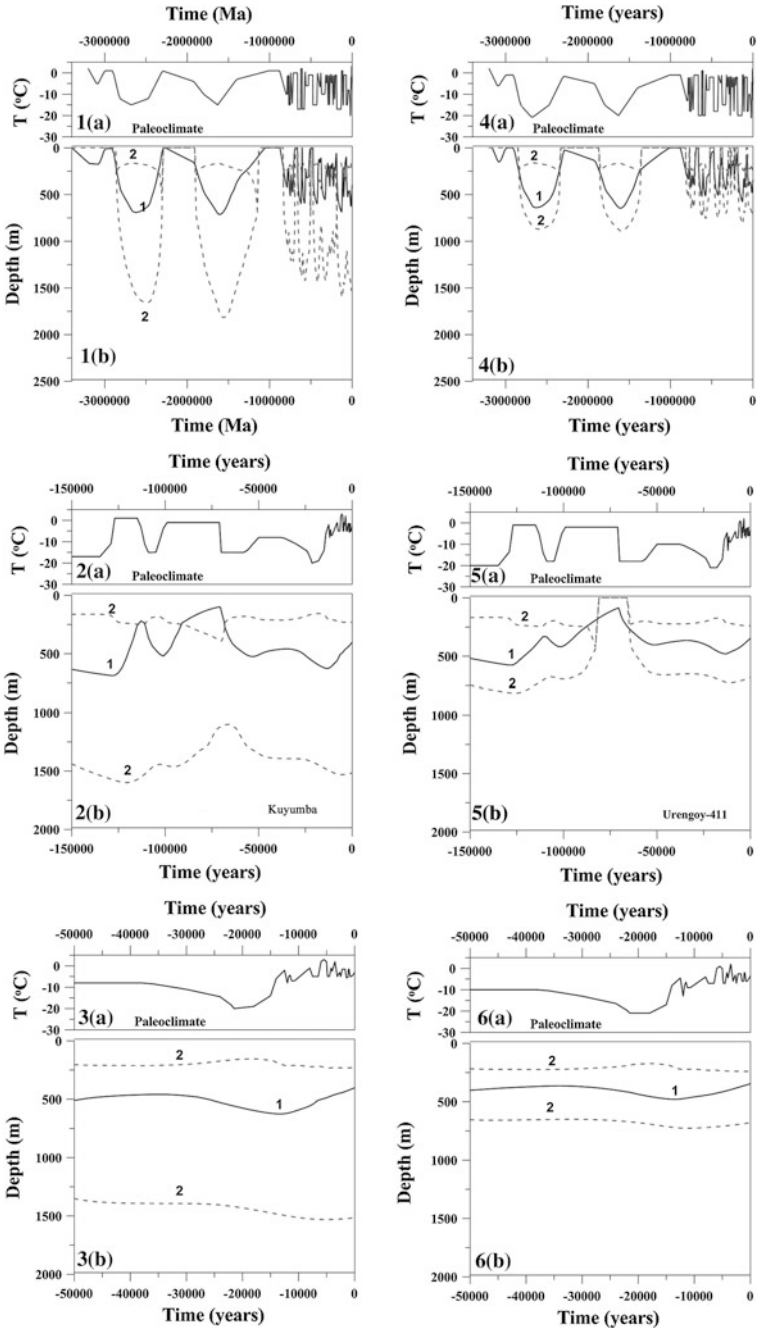
Time (Ma)
T (°C)
1(a)
Paleoclimate
Depth (m)
1(b)
Time (Ma)
Time (years)
4(a)
Paleoclimate
4(b)
Time (years)
2(a)
Paleoclimate
2(b)
Kuyumba
Time (years)
5(a)
Paleoclimate
5(b)
Urengoy-411
Time (years)
3(a)
Paleoclimate
3(b)
Time (years)
6(a)
Paleoclimate
6(b)
Time (years)

◀ **Fig. 10.5** Variations in the depth of the base of permafrost (*curve 1* in Figs. b) and the depths of the roof and base of the zone of methane gas hydrate stability (*curves 2* in Figs. b) computed for Kuyumba (1–3) and Urengoy (4–6) areas with consideration of climate variations during the last 3.4 My. Results are presented for the last 3.4 My (Figs. 1 and 4) and more detailed for the last 150 (Figs. 2, 5) and 50 (Figs. 3, 6) thousand years

and partly due to decrease in porous volume as a result of additional sedimentation removed by intensive erosion (Table 6.1). It is interesting to note that presence of intrusions in sedimentary section of the Kuyumba well (Table 6.4) gives an opposite effect—the sills decrease effective heat conductivity of sedimentary cover (see Sects. 6.2 and 10.2).

The role of changes in the shape of the curve of unfrozen water content in the pores of sedimentary rocks W(T) depending on the lithology of the rocks is discussed in Sect. 9.2.5 including for the Kuyumba and Urengoy areas. In present reconstructions, the shape of the $W(T)$ function changes with depth depending on the content of the fine and coarse grained fractions in the rock (Eq. 9.8). It was noted in Sect. 9.2.5 that neglecting the changes in the W(T) curves depending on lithology can lead to errors in assessment of the thickness of permafrost at 100 m and more.

10.4 Contribution of Different Time-Periods of Climate Variations to Formation of Permafrost

This section considers the role of climate factor in the permafrost modeling. The paleoclimate data used in the permafrost modeling of the Urengoy and Kuyumba areas are presented in Tables 10.4, 10.5 and Figs. 10.5a. These data are based on numerous papers devoted to evolution of paleoclimate in the Siberia [11–13, 27–36]. The temperatures of the "neutral" layer must be used at the upper boundary of domain of computation. This layer locates at the depth where an influence of the annual variations in surface temperature disappears [3, 23]. Variations in paleoclimate presented in Tables 10.4, 10.5 and Fig. 10.5a assume that temperatures at the depth of "neutral" layer exceeded the mean-annual air temperatures by 3–5 °C [37, 38], if the climate in the region was similar to the present-day one or milder than it and snow and vegetation covers were considerable. But these temperatures exceeded the mean-annual values in air only by 1–2 °C for a more rigorous climate when thinner vegetation and snow covers occurred in the region (as in Kuyumba area; [39]). However, we must recognize that this issue requires further study and there are notable uncertainties in determination of these temperatures. By this reason we found it useful to show the temperatures used in the modeling in the Tables 10.4 and 10.5. It may be noted that the time-periods of relative cool and warm climate in the Urengoy area are close to the ones in the Kamov swell of the Siberia Platform. But the climate of the Kamov swell is more continental but slightly warmer (by 1–2 °C), than the climate in the Urengoy area due to more southern location of the Kuyumba

Table 10.4 The mean-annual surface temperatures used for modeling of permafrost evolution in the Pliocene-Holocene climate history of the Kuyumba field

t (Ka)	T (°C)	t (Ka)	T (°C)	t (Ka)	T (°C)	t (Ka)	T (°C)
3400	2	555	−13	100	−13	6	0
3250	−4	550	−3	80	−13	5.5	1
3100	−4	510	−3	75	−5	5	0
2900	−1	505	−13	68	−5	4.87	−7
2600	−1	380	−13	65	−13	4.5	−7
2500	−21	360	−2	50	−13	4.2	−2
2100	−1.5	320	1	45	−6	4	−4.5
1900	−1.5	300	−4	25	−6	3.5	2
1800	−13	280	−2	23	−17	3.1	−6
1650	−1	260	−4	19	−21	2.7	−3
1450	−18	255	−16	15	−17	2.5	−7
1350	−1	230	−16	14	−8	2.2	−2.5
950	−1	225	−4	13	−5	1.7	−2.5
870	−21	205	−4	12.5	−4.5	1.5	−6
800	−2	200	−13	12	−13	1.2	−6
745	−2	190	−13	11.6	−5	1.1	−2
740	−13	185	−2	11.3	−9	1	−2
635	−13	175	−13	9.5	−9	0.8	−6
630	0	140	−13	8	−4	0.6	−6
600	0	130	2	7.5	−7	0.2	−4.5
595	−13	110	2	6.5	−7	0	−3.6

Remark t is the time before Present, *T* is the mean annual surface temperature. Temperatures are assumed to change linearly between neighboring values (Fig. 10.5(1a)–(3a)). The above values of time and temperature were selected based on published papers, cited in text

well (Figs. 10.1 and 10.5a; Tables 10.4 and 10.5). However, the more intensive cooling of sedimentary blanket in the Kuyumbinskaya area is attributed to lower regional heat flow, the higher position of the basement, presence dolomites, anhydrites and halite in sedimentary cover and partly due to decrease in porous volume as a result of intensive erosion (Sects. 9.2 and 10.2).

According to paleoclimate studies, permafrost on the Siberia platform started its formation about 3.25 My ago. The first cooling period was most short (3.25–3.1 My ago) and least cool [11–13, 33]. The climate during next cooling period (from 2.82 to 2.47 My ago) was more rigorous—permafrost lasted continually during about 300 thousand years. Suibsequently, a formation and degradation of permafrost zones occured repeatedly. During Early and Middle Pleistocene, from 1.806 to 0.126 My ago there were 11 periods with formation of permafrost zone (cryochrones), when a mean annual temperature was by 8–12 °C lesser (like to the Sartanian time) than the present-day one. In the same time interval, there were 7

Table 10.5 The mean-annual surface temperatures used for modeling of permafrost evolution in the Pliocene-Holocene climate history of the Urengoy field

t (Ka)	T (°C)	t (Ka)	T (°C)	t (Ka)	T (°C)	t (Ka)	T (°C)
3400	2	555	−13	100	−13	6	0
3250	−4	550	−3	80	−13	5.5	1
3100	−4	510	−3	75	−5	5	0
2900	−1	505	−13	68	−5	4.87	−7
2600	−1	380	−13	65	−13	4.5	−7
2500	−21	360	−2	50	−13	4.2	−2
2100	−1.5	320	1	45	−6	4	−4.5
1900	−1.5	300	−4	25	−6	3.5	2
1800	−13	280	−2	23	−17	3.1	−6
1650	−1	260	−4	19	−21	2.7	−3
1450	−18	255	−16	15	−17	2.5	−7
1350	−1	230	−16	14	−8	2.2	−2.5
950	−1	225	−4	13	−5	1.7	−2.5
870	−21	205	−4	12.5	−4.5	1.5	−6
800	−2	200	−13	12	−13	1.2	−6
745	−2	190	−13	11.6	−5	1.1	−2
740	−13	185	−2	11.3	−9	1	−2
635	−13	175	−13	9.5	−9	0.8	−6
630	0	140	−13	8	−4	0.6	−6
600	0	130	2	7.5	−7	0.2	−4.5
595	−13	110	2	6.5	−7	0	−3.6

Remark t is the time before Present, *T* is the mean annual surface temperature. Temperatures are assumed to change linearly between neighboring values (Fig. 10.5(4a)–(6a)). The above values of time and temperature were selected based on published papers, cited in text

thermochrones, when a mean annual temperature was by 2–4 °C higher (like to the Kazanzev time) than the present-day one (Fig. 10.5a; Tables 10.4 and 10.5).

Figure 10.3 gives an opportunity to estimate a contribution of different time interval from the last 3.4 My to permafrost formation. It shows the present-day temperature and heat flow distributions with depth $T(z)$ and $q(z)$, computed with consideration of climate variations during the last 3.4 My, 200 and 50 thousand years, correspondingly, and with the same initial temperature profile (3.4 My). It can be seen that use of climate variations of the last 200,000 years leads to the T(z) and q(z) distributions which are relatively close to the ones computed with climate variations of the last 3.4 My. Deviations observed at depth more than 2–3 km, are reduced because the distance a heat wave penetration increases with time proportional to $\sqrt{\kappa \cdot t}$. At the same time, calculations with climate variations restricted to the last 50,000 years differ considerable from the models using a climate history of the last 200,000 years and 3.4 My (Fig. 10.3). It is interesting to note that the computations with climate variations during the last 3.4 My, 200,000 years and

50,000 years and with the same initial temperature profile (3.4 My) give a depth of base of present-day permafrost zone 400, 352 and 161 m in the Kuyumba area and 346, 300 and 233 m in the Urengoy-411 well, correspondingly. Differences in the estimation of depth are rather considerable.

10.5 Influence of Climate Variations on the Temperature and Heat Flow Distributions with Depth in the Regions of Total Degradation of Permafrost

In this section, we consider briefly special problem of distortion of surface heat flow and temperature-depth distribution due to paleoclimate variations in the regions where permafrost was in the past but completely degraded by now. The problem is illustrated on the example of three wells in the South Urals area (Fig. 10.6; [9, 42]). Figure 10.7c shows the example of the permafrost evolution during the last 500,000 years in Yugomashskaya area in the West Bashkirian. The modeling uses the climate history of the region constructed by the data from papers [11, 41] with detailed analysis the Cenozoic climate variations for the last 5 My. In our modeling, a number of depth-steps reached 800, the steps of Δz ranged from 0.5 m near the basin surface to 70 m in the base of sedimentary column. The time-steps, Δt, varied

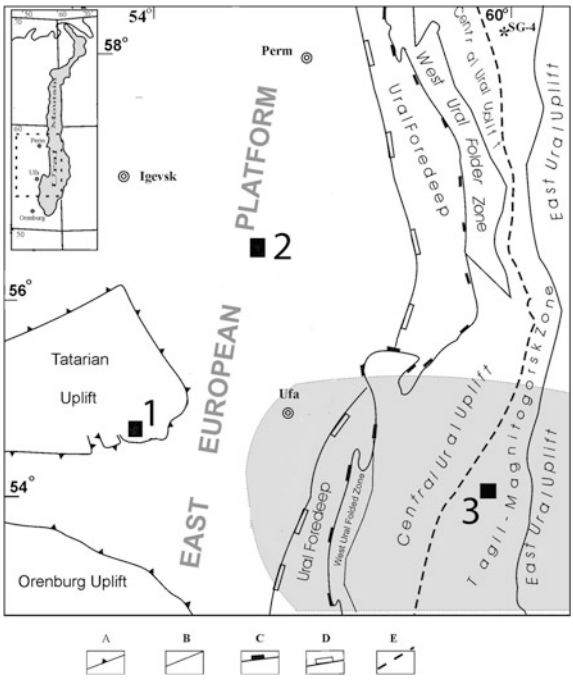

Fig. 10.6 Generalized location map and main tectonic structures of the South Urals region, showing modeled wells in the West Bashkirian (after [9, 42] with a few changes) *A* main tectonic structure of the West Bashkirian, *B* boundaries of the West Ural Folded Zone and the East Ural Uplift, *C* and *D* western and eastern boundaries of the Ural Foredeep, *E* the Main Ural Fault. *Shaded area* shows approximately the region of low heat flow after [40]. The numbers correspond the following wells:
1 Morozovskaya,
2 Yugomashskaya,
3 Magnitogorskaya

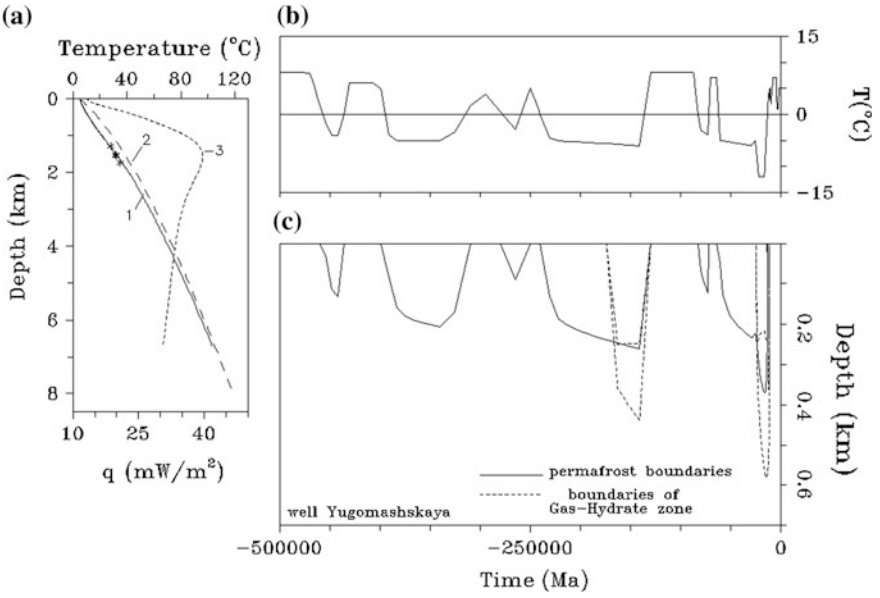

Fig. 10.7 Variation in thermal regime of sedimentary blanket in the Yugomashskaya field during last 500,000 years [9, 42]. **a** *1* present-day temperature distribution; *2* the distribution of temperature 4 My ago; *3* present-day distribution of heat flow with depth (*lower axis*). *Symbols* temperatures measured in present-day section of the area. **b** Paleoclimate history of the region for last 500,000 years after [11, 41]. **c** Calculated variations in depth of the permafrost base and boundaries of the zone for gas hydrate stability during last 500,000 years

from 50 to 0.1 years. In this modeling, the shape of the W(T) function changes in the model with the depth depending on the content of fine and coarse grained fractions in the rock (Eq. (9.8) in Sect. 9.2.5). Although the corrections in computed present-day temperatures due to fractions effect did not exceed 1.5 °C, difference in maximal depth of permafrost computed with W(T) of different fractions could reach 80 m for the last ice-age [11, 41]. Curve 2 in Fig. 10.7a describes the initial temperature profile computed in general basin modeling for the age of 4 Ma [11, 41]. The curve 1 in Fig. 10.7a is the present-day temperature distribution computed with consideration of the detail climate variations for last 4 My, the part of which is shown in Fig. 10.7b. According to the modeling, the temperature reduction due to climate factor at the upper 2–4 km of the sedimentary section can reach 10 °C (Fig. 10.7a). Calculated variations in the present-day heat flow with depth typical for all the considered wells of the region are shown by the curve 3 in Fig. 10.7a. As a result of climatic factor, the heat flow increases quickly in the upper 1–1.2 km, reaches a maximum at depth of 1.5–1.8 km and then decreases gradually to its value at the basement surface. The measurements in wells confirm such behavior of the heat flow [43]. Therefore, it is necessary to take care in the modeling based on the measurements of heat flow or temperature gradient at the

depths less than 2–2.5 km. Figure 10.7c shows the calculated variations in the depth of boundaries of the permafrost zone and the zone for methane gas-hydrate stability for last 500 thousand years. The calculation suggests that permafrost can reach the depth of 375 m during the last glacial age. The subsequent warming which started around 16 thousand years ago (Fig. 10.7b) led to its fast degradation (Fig. 10.7c).

Figure 10.8 is the last illustration of temperature and heat flow distributions with depth in the region of the South Urals with the lack of modern permafrost zone. Figure 10.8a presents the result of permafrost modeling on the example of the Morozovskaya area with a small thickness of the sedimentary cover (about 2.5 km). Curve 1 in this Figure shows initial temperature profile computed in the general basin modeling for the age of 4 Ma ago. The curve 3 here is the present-day temperature distribution computed with consideration of the detail climate variations for last 4 My [9, 42]. The calculations confirm the conclusions made above in discussion of Fig. 10.7a. According to the modeling, the climate variations influence again on modern distributions of temperature and heat flow distributions despite the degradation of the permafrost 10–12 thousand years ago. The curve 4 in

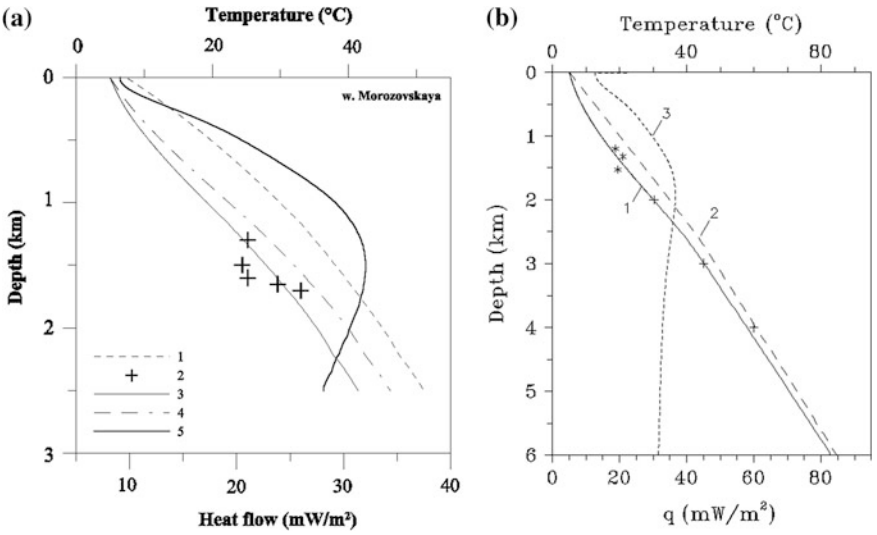

Fig. 10.8 Temperature and heat flow profiles calculated for sedimentary sections of the Morozovskaya well (**a**) and back-arc sedimentary complex of the Magnitogorsk well (**b**) in the Tagil-Magnitogorsk Zone of the South Urals [9, 42]. **a** *1* temperature profile for the time of 4 My ago (initial profile for permafrost modeling), *2* temperatures measured in the present-day section of the area, *3* the present-day temperatures computed with climate factor of the last 4 My, *4* the present-day temperatures, calculated with climate factor of the last 100,000 years, *5* calculated present-day heat flow profile. **b** the calculated present-day temperature (*1*) and heat flow (*3*) distributions with depth within the sedimentary section of the Magnitogorsk well; *2* temperature profile for the time of 4 My ago. *Symbols* temperatures measured in present-day section of the area (see [9, 42])

Fig. 10.8a illustrates the present-day temperatures, computed with climate factor of the last 100,000 years. Comparison between the curves 3 and 4 demonstrates the contribution of the climate factor before 100,000 years to formation of the present-day temperature profile (see Fig. 10.3 and Sect. 10.4). It can reach 5 °C at depths of more than 1.5–2 km. The difference in heat flow is less considerable, and estimated maximal depth of permafrost for the last glacial age increases approximately by 30 m (375 instead 346 m) due to consideration of the climate history before 100,000 years ago.

Calculated variations in the present-day heat flow with depth are typical for all the considered wells in the region and similar to the ones in Fig. 10.3. As a result of climatic variations, the heat flow increases quickly in the upper 1–1.2 km, reaches a maximum at depth of 1.5–1.8 km and then decreases gradually to its value at the basement surface. The measurements in the wells of the region confirm such behavior of the heat flow [43] (Kukkonen et al. 1997).

Figure 10.8b show present-day temperature and heat flow distribution computed for the back-arc sedimentary complex of the Magnitogorsk well in the Tagil-Magnitogorsk Zone of the South Urals. The deviation between lines 1 and 2 in Fig. 10.8b is due to the climate variations in the Pliocene-Holocene. As result of these variations, present-day heat flow changes from 14.1 mW/m^2 near the surface to maximal value of 36.6 mW/m^2 at depth of about 2,100 m and then decreases slowly to 30.4 mW/m^2 at depth of 10,000 m (line 3 in Fig. 10.8b).

Therefore, the information presented in this section demonstrates that it is necessary to be careful in the modeling based on the measurements of heat flow or temperature gradient at depths of less than 2–2.5 km even in the regions where permafrost has degraded.

10.6 Formation the Present-Day Temperature Distribution with Depth in the Arctic Field of the East Barents Basin

One of the problems in modeling of thermal regime of the lithosphere in the East Barents Basin is a considerable contradiction between high values of heat flow measured in the region (Fig. 3.4) and relatively low values of deep temperatures and degree of organic matter maturation, measured in wells (Fig. 3.7, right Fig. 3.11). Indeed, measured heat flow is about 70 mW/m^2 in the Ledovaya, Shtockman and Arctic areas and about 90 mW/m^2 in the Admiralteyskaya area (Fig. 3.4). The values of surface heat flow calculated in our model (without correction on Quaternary climate variations) are equaled to 53.4, 56.2, 58.1 mW/m^2 in the Ledovaya, Shtockman and Arctic areas and 71 mW/m^2 in the Admiralteyskaya area. They are smaller than the measured values by 15–20 mW/m^2. The corrections on the Quaternary climate variations could decrease more these flows. But the paradox is that the deep temperatures calculated in the model with consideration of Quaternary

climate variations are in rather good agreement with the reliable measured temperatures (Figs. 3.7 and 3.8). For example, in the Arctic area calculated temperatures at the depth z = 2600 and 4050 m are 88 and 119 °C, whereas the measured values of T are 90 and 122 °C, correspondingly (Fig. 3.7). These values would be equal to 115 and 159 °C if we took heat flow to be equal to 69 mW/m^2 (in this case the heat flow through the basement surface is 48.5 mW/m^2). Similar situation takes place with vitrinite reflectance: the value of Ro, calculated for q = 69 mW/m^2 at the depth z = 4050 m would be about 2.02 %, whereas measured value Ro = 0.90 % (Fig. 3.11). Our calculations shown that a using of surface heat flow q = 70 mW/m^2 in the Ledovaya, Shtockman and Arctic areas led to overestimation of rock temperatures by 30–40 °C and to considerable overstating in the %Ro values. Corrections on the Quaternary climate variations must only enhance the above contradiction. It can be noted also, that the heat conductivities measured in the aleurolite and sandstone samples from the depth of 1440 and 3100 m in the Shtockman area are in agreement with the values computed in our basin model with an accuracy of 10–20 %. Similar challenges faced the authors of the work [44] in modeling of temperature-depth distribution along the profile across the East Barents Basin. The surface heat flow computed in the paper was also lesser by 15–20 mW/m^2 than the measured here (65–75 mW/m^2). The authors believe that the above contradiction is related to the hardness of heat flow measurements in the shelf, because numerous distortions of heat flow by exogenic and relief factors that lead to considerable scatter in the measured values of heat flow. They believe that the reliable method of heat flow measurement is only its measurement in deep wells.

The results of general modeling of sedimentary section of the East Barents Basin in the Arctic area are discussed in Sect. 3.2.1. Figure 3.5 in this section demonstrates the burial, thermal and maturation histories of the Basin, while Fig. 3.7 shows the present-day temperature profile in sedimentary section of the Arctic area in the Basin. Below in this section of the chapter, we will concentrate on the problem of determining this profile. The temperature distribution presented by line 2 in Fig. 3.7 differ from the one of line 1 due to taking into consideration the climate variations during last 3.5 My. The climate of Arctic in the Barents Sea region was studied in many works [3, 11, 17, 30, 32, 33, 41, 45–50]. Table 10.6 is a compilation of cited works to change in mean-annual air temperature in the Arctic well region for the entire Cenozoic.

For areas with a sea depth z > 150 m. and positive temperatures we adopt the data of this table suggesting that a positive mean annual air temperature is transferred by convection on the shallow sea bottom (z < 300–500 m) is almost unchanged. At the same time, we taken T = −1.7 °C for negative air temperatures T < −2 °C if the sea was in the study area. In this case negative air temperatures are transmitted to bottom in accordance with a temperature gradient dT/dz in sea water typical for the Arctic seas. According to this gradient, at the negative air temperature in the Sea surface, the temperature of sea water increases to 0 °C at a depth of 2 m, then increases slightly above 0 °C, decreases again up to 0 °C at z = 7–8 m and continues to drop, reaching temperature −1.7 to −1.8 °C at depth z = 35–40 m. Further to a depth of 150–200 m water remains at this temperature and not subjected to seasonal

temperature fluctuations. At a depth z > 150–200 m the temperature increases, reaching a value of −0.8 °C at a depth z = 500 m [45]. Such temperature profile is typical for the Arctic seas. But in the bottom sedimentary layer in the first 12 m the porous water salinity decreases with depth from 35 ‰ at the bottom to 24 ‰ at z = 12 m. Increase in salinity results in increase in the onset temperature of freezing water. So in the bottom layers of sediments, the formation of a small capacity of up to 10 m layer of frozen rocks, due to excess of the liquidus temperature of the pore water above the temperature of the bottom water and sediments [45].

It should be noted that the epoch of maximum of the last glaciation (20–18 thousand years ago) was a major climatic boundary Pleistocene. It was characterized by a very strong fall of temperature and the lowest (120 m) glacioeustatic the decrease in the ocean level. In the glacial epoch, the surface of the open part of the North Atlantic has experienced particularly strong cooling and the Northern hemisphere were generally colder than the South. The reason for such drastic environmental changes is believed to be a massive glaciation of the ocean in temperate and polar latitudes as a consequence of continental glaciations [50]. According to the above, for seabed with modern depth z < 120–150 m it is necessary to consider their landfall and freezing in the Late Valdai epoch (20–14 thousand years ago) when the sea retried to the depth contour of 110–130 m.

Figure 10.9 presents temperature profiles in present-day sedimentary section of the Arctic area in the East Barents sea computed for different histories of temperature

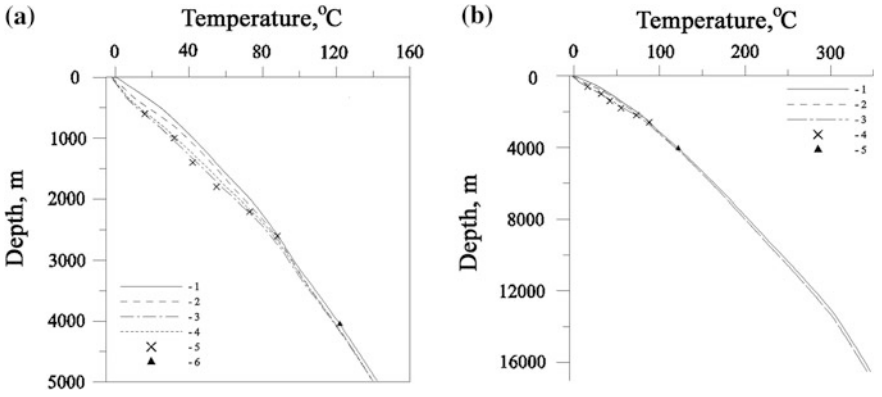

Fig. 10.9 Comparison of measured temperatures with the temperatures computed for different histories of temperature at the sea bottom in the Arctic area in the East Barents Sea. *1* calculations in the frame of general basin modeling without consideration of detailed climate variations during last 5 My (Sect. 3.2.1, lines 1 in Fig. 3.7). *2–4* calculations with detailed climate variations during last 5 My (Table 10.6) with corrections: *2* minimal temperatures in the cold periods (T < 0 °C) were assumed to be equal to −1.7 °C that is assumption of unfrozen sea during all of the cold periods. 3 minimal temperatures in the cold periods (T < 0 °C) were again assumed to be equal to −1.7 °C but T = −15 °C in the interval 80,000 < t < −15,000 years ago (that is assumption that in this interval of time the sea froze). *4* the variant 3 but T = −15 °C in the interval of time 50,000 < t < −15,000 years ago. *5* measured temperatures from [51, 52]. *6* reservoir temperature (private message). The salt content in porous water was taken 15 g/l in the above computations

at the sea bottom. In all variants steady heat flow, equal to 30.2 mW/m^2, was maintained at the base of the sedimentary section, i.e. at a depth of 16.5 km (Table 3.1; Fig. 3.5). Such flow is an average heat flow through the basement surface during last 3.5 My (Fig. 3.9a). The variant of line 1 in Fig. 10.9 corresponds to the calculations in the frame of general basin modeling considered in Sect. 3.2.1. This variant uses the climate history of Table 10.6 and earlier that is shown by upper Fig. 3.5. but without consideration of detailed climate variations during last 5 My (lines 1 in Fig. 3.7, see also Lower Figs. 3.5 for present time, t = 0.). Lines 2–4 present the calculations carried out with consideration of detailed climate variations during last 5 My (Table 10.6) but with some corrections to the data of the table. In particularly, line 2 present calculation with climate history of Table 10.6 but under

Table 10.6 Mean-annual air temperature in Barents Sea constructed by compilation of the works [3, 11, 17, 30, 32, 33, 41, 45–50]

N	t in 1,000 years	T °C	N	t in 1,000 years	T °C	N	t in 1,000 years	T °C
1	65000	+18	26	2300	+2	51	110	+2
2	45000	+18	27	1900	−5	52	85	+1
3	43000	+14	28	1700	−5	53	80	−6
4	34000	+14	29	1400	+3	54	50	−6
5	32000	+12	30	1300	−4	55	45	−3
6	22000	+12	31	1100	+3	56	22	−4
7	16000	+9	32	1000	−4	57	20	–17
8	13000	+6	33	900	+1	58	18	−17
9	10000	+6	34	750	+1	59	14	−7
10	8700	+2	35	700	+3	60	13.5	+0
11	8000	+2	36	630	−5	61	12.9	−7
12	6800	+6	37	590	+2	62	12.7	+1
13	6400	+6	38	500	+2	63	12.3	−6
14	5800	+1.5	39	460	−6	64	12.0	+1
15	5400	+1.5	40	450	+1	65	11.7	−6
16	5000	+6	41	380	+1	66	10.5	+1.5
17	4700	+6	42	340	−6	67	8.0	+3
18	4250	+1.5	43	320	+3	68	5.1	+3
19	4000	+1.5	44	280	+3	69	4.0	+0
20	3850	+5	45	260	−5	70	3.9	−2
21	3600	+5	46	250	+3	71	2.0	−2
22	3500	+1	47	220	+3	72	1.9	+0
23	3300	+1	48	170	−10	73	0.0	+0
24	3100	+3	49	140	−10			
25	2600	−3	50	130	+6			

Remarks N number of data, *t* time in thousand years, *T* is mean-annual air temperature in °C. For time 0 < t < 3 million years ago, Table 10.6 gives the deviation of the air paleo-temperatures from the modern mean-annual air temperatures

condition when minimal temperatures in the cold periods (T < 0 °C) were replaced by the value of −1.7 °C. By other words, this variant considers the assumption about unfrozen sea during all of the cold periods. We see that the temperatures computed with this variant of climate history are significantly less than that observed in the sedimentary section. The variant of line 3 assumes that minimal temperatures in the cold periods (T < 0 °C) are again equaled to −1.7 °C but these temperatures T = −15 °C in the time-interval 80,000 < t < −15,000 years ago (that is assumption that in this time-interval the sea froze). This variant is in agreement with the observed data better than the other. Decrease this time-interval to 50,000 < t < −15,000 years ago leads to a deterioration in the agreement between the computed and measured temperatures. Thus, the modeling suggests a relatively rigorous climate for the time interval from 80 to 15 thousand years ago. It is essential, that all calculations took into account the lithological composition of rocks in the sedimentary section of the Arctic area, presented in Table 3.1.

10.7 Paleoclimate and Depth-Variations in Rock Temperatures in the North-East Sakhalin Shelf

The climatic curve that took a part in general basin modeling of Fig. 5.6b, c is presented in Fig. 5.6a. It was constructed on the base of data from papers [11, 53, 54]. The temperature distribution (T) shown in Fig. 5.5a is the present-day distribution computed with consideration of variations in the climate of the last 2.5 My. These variations are presented in Table 10.7 that used the data from the works [11, 53]. Table 10.7 includes the corrections to the climate temperatures due to sea regressions and transgressions in the study region. Data presented in the T1 rows (temperatures on sea bottom) were used in calculations of the temperature and heat flow distributions in Fig. 5.5a. Among others periods, these data include two periods (about 55,000 years ago and from 20 to 18 thousand years ago), when a mean-annual temperature at the surface of sedimentary cover decreased up to −10 and −12 °C, correspondingly. Sea regression reached 110–130 m in the two periods and sea froze to the bottom in study area of the basin [11]. The data of Table 10.7 suggests that the sea smoothed over the climatic jumps of the mean annual temperature during the greater part of the last 2.5 My. The climatic temperature jumps were significant only at the times of freezing and regression of the sea. For this reason, the present-day temperature distribution, calculated with consideration of detailed climate variations of the last 2.5 My and presented by T-line in Fig. 5.5a, is close to the one calculated in the frame of general modeling with the climate variations of Fig. 5.6a. The modeling shows that a maximal depth of permafrost zone in sedimentary blanket of the well 1 about of 177 m was reached about 15,000 years ago, that is about two thousand years after the last icing period lasted from 21 to 17 thousand years ago (see Table 10.7). This zone was degraded totally about 6,500 years ago as result from rise of the mean-annual temperature (Table 10.7). The climate variations during the last

Table 10.7 A change in the mean-annual temperature at the basin surface during the last 2.5 My (the north-eastern shelf of the Sakhalin, the Sakhalin-5 area)

t (Ma)	2.5	2.0	1.2	0.95	0.80	0.60	0.45	0.35	0.18	0.13
T1 (°C)	0	3	3	−1	3	2	−1	2	−1.4	2
T2 (°C)	−1	3	3	−9	3	2	−9	2	−11	2
t (Ma)	0.11	0.08	0.06	0.055	0.050	0.033	0.027	0.024	0.021	0.020
T1 (°C)	0	−1.4	−1.5	−10.0	−1.5	0	−1.0	−0.5	−1.5	−12.0
T2 (°C)	−6	−9	−11	−11	−9	1	−6	−5	−9	−15
t (Ma)	0.018	0.012	0.010	0.008	0.0075	0.006	0.005	0.004	0.0035	0.001
T1 (°C)	−12.0	−1.5	0	0	2.5	1.5	2.5	−1.5	−0.0	−0.5
T2 (°C)	−15	−9	−7	−7	3.5	2.5	3.5	−3	−2	−1
t (Ma)	0.000									
T1 (°C)	−1.0									
T2 (°C)	−2									

Comment t the time in My; *T1* the sea bottom temperature; *T2* the land temperature

100,000 years had more considerable effect on the modern heat flow distribution with depth (Q-line in Fig. 5.5a). The minimum and maximum in the heat flow distribution in the q-line are the memory about the last periods of warming and cooling of the climate (Table 10.7).

The rows T2 (the land temperature) in Table 10.7 show the mean-annual temperatures of air in the Sakhalin-5 area evaluated under the condition that the sea was absent in the study area during all 2.5 million years. These air temperatures for this rigorous climate were assessed on the basis of paleoclimatic information in papers [11, 53]. The modeling carried out for this case results in decrease of rock temperatures in upper 2 km of the sedimentary cover by 5–10 °C in comparison with the T-curve in Fig. 5.5a. In this case, the permafrost zone reached the maximal depth of about 290 m around 11,000 years ago, while its modern thickness could be equal to 190 m.

10.8 Conclusion

A strong dependence of a numerical solution on the petrophysical parameters of frozen and unfrozen rocks suggests a significant role of lithological composition of rocks and its variation with depth in permafrost modeling, especially, in the upper 1000 m of sedimentary section. The modeling shows that the climate variations in Siberia during the Late Pliocene–Holocene led to reduction of rock temperatures by 15–20 °C in the upper 1500 m of the sedimentary section and by 8–10 °C in the deeper layers of the section. This effect is more considerable in the Kuyumba area, than in the more northern Urengoy area despite the warmer climate in the first area. The main reason of this is the thinner sedimentary cover in the Kuyumba area. The model suggests that a present-day permafrost base is at depth of about 350 m in the

Urengoy area and 405 m in the Kuyumbinskaya area, that is in reasonable agreement with observed data. According to our assessments, the present-day zone of methane gas hydrate stability locates at the depth from 250 to 700 m in the Urengoy area and from 240 to 1590 m in the Kuyumba area. Variations in such parameters as salt concentration or type of function of unfrozen water content (in depending on the fraction of fine grained rocks) affect considerably the temperature and heat flow distributions with depth and permafrost thickness. The modeling shows that limitation by time-interval of the last 50,000–100,000 years can lead to errors in estimations of permafrost thickness up to 50–100 m. Our numerical reconstructions indicate that it is necessary to be careful in the modeling based on the measurements of heat flow or temperature gradient at depths of less than 2–2.5 km even in the regions where permafrost has degraded. The modeling in the Barents Sea shelf suggests rather rigorous climate of the last 70–50 thousand years while in the North-East Sakhalin shelf it assumes that the sea smoothed over the climatic jumps of the mean annual temperature during the greater part of the last 2.5 My and here the influence of the Pliocene-Holocene climate fluctuations in the depth profile of temperature is limited.

References

1. Lachenbruch AH, Sass JH, Marshall BV, Moses TH (1982) Permafrost, heat flow and the geothermal regime at Prudhoe Bay Alaska. J Geophys Res 87:9301–9316
2. Duchkov AD, Lysak SV, Balobaev VT (1987) Thermal field of the Siberian crust. Nauka, Novosibirsk (in Russian)
3. Balobaev VT (1991) Geothermy of permafrost zone in the lithosphere of the northern Asia. Nauka, Novosibirsk (in Russian)
4. Sigunov YuA, Fartyshev AI (1991) Study of evolution of cryolitic zone in the Arctica shelf by mathematical modeling. Geologia i Geofisika 8:24–31 (in Russian)
5. Sigunov YuA, Fartyshev AI (1995) Freezing and thawing of the East-Arctic shelf in the Late Pleistocene (numerical experiment). Geologiya i geophisika 36(9):24–31 (in Russian)
6. Lebret P, Dupas A, Clet M (1994) Modeling of permafrost thickness during the late glacial stage in France: preliminary results. Canad J Earth Science 31:959–968
7. Balobaev VT, Tetelbaum AC, Mordovskiy CD (1999) Two-dimensional numerical model of hydrodynamic field below permafrost at permafrost thickness variations. Kriosphera Zemli, III (4):48–53 (in Russian)
8. Galushkin YuI (1997) Numerical simulation of permafrost evolution as a part of basin modeling: permafrost in Pliocene-Holocene climate history of Urengoy field in West Siberian basin. Canad J Earth Sci 34(7):935–948
9. Galushkin YuI, Yakovlev GE (2004) Burial and thermal history of the West Bashkirian sedimentary basins. Tectonophysics 379:139–157
10. Galushkin YuI, Sitar KA, Frolov SV (2013) Basin modeling of temperature and heat flow distributions and permafrost evolution, Urengoy and Kuyumbinskaya areas Siberia. Permafrost Periglacial Processes 24(4):268–285
11. Velichko AA (ed) (1999) Change in climate and landscapes during last 65 My (The Cenozoic: from Paleocene to Holocene). Moscow, GEOS (in Russian)

12. Fotiev SM (2005) Modern conceptions of the evolution of Cryogenic area of West and East Siberia in Pleistocene and Holocene (report 1). Kriosphera Zemli, IX 2:3–22 (in Russian)
13. Fotiev SM (2009) Cryogenic methamorphism of rocks and groundwaters (conditions and results). Novosibirsk, Academicheskoe Izdatelstvo "Geo" (in Russian)
14. Duchkov AD, Dobretsov NN, Ayunov DE, Sokolova LS (2011) Permafrost-geothermic Atlas of Siberia and Far East. In: Dynamics of physical fields of the Earth. Svetoch Plus, Moscow, pp 207–221
15. Zheleznyak M (2006) The Siberian platform geocryological database (Melnikov Permafrost Institute, Russia). In: Proceedings of 1st Asia CliC symposium "The state and fate of Asian Cryosphere", April 20 to 22, 2006, Yokohama Institute for Earth Science, JAMSTEC, Yokohama, Japan
16. Kontorovich AE, Nesterov II, Salmanov FK, Surkov VS, Trofimuk AA, Ervje YuG (1975) Geology of oil and gas in West Siberia. Nedra, Moscow (in Russian)
17. Ershov ED (1990) General geocryology. Nedra, Moscow (in Russian)
18. Gromovykh SA (2005) Research and development of well construction technology at the formation of hydrates dissertation of the candidate of technical sciences. Tyumen (in Russian)
19. Kontorovich AE, Surkov VS, Trofimuk AA (1981) Geology of oil and gas in Siberian Platform. Nedra, Moscow (in Russian)
20. Galushkin YuI, Simonenkova OI, Lopatin NV (1999) Thermal and maturity maturation modeling of the Urengoy field, West Siberian basin: some special considerations in basin modeling. AAPG Bull. 83(12):1965–1979
21. Deming D, Chapman DS (1989) Thermal histories and hydrocarbon generation: example from Utah-Wyoming thrust belt. AAPG Bull 73(12):1455–1471
22. Makhous M, Galushkin Y (2005) Basin analysis and modeling of the burial, thermal and maturation histories in sedimentary basins. Editions TECHNIP, Paris
23. Kudryavzev VA (1981) Permafrost study. Moscow University Press (in Russian)
24. Devyatkin VN (1993) Heat flow in cryolitic zone of the Siberia (methods and results of study). Nauka, Novosibirsk (in Russian)
25. Kurchikov AP (1992) Hydrogeological criteria for petroleum potential. Nedra, Moscow (in Russian)
26. Majorowicz JA, Osadetz KG, Safanda J (2008) Modeling temperature profiles considering the latent heat of physical-chemical reactions in permafrost and gas hydrates—the Mackenzie Delta terrestrial case. In: Kane DL, Hinkel KM (eds) Proceedings of the ninth international conference on permafrost. University of Alaska Fairbanks, Institute of Northern Engineering, 2, pp 1113–1118
27. Volkova VC (1991) Climate variations in the West Siberia during the Late Pliocene and Quaternary. In: Zacharov VA (ed) Evolution of climate in Late Cenozoic of Siberia, pp 17–30 (in Russian)
28. Volkova VC (1994) Dynamics of natural zones and climate of Kazantsev interglacial period in the West Siberia. In Yanshin AL (ed) Study of quaternary period. Moscow, pp 58–67 (In Russian)
29. Zubakov VA (1990) Global climatic events of Neogenic. Gidrometeoizdat, Leningrad (in Russian)
30. Velichko AA (ed) The West Siberia. Development of landscapes and climate in the North Eurasia. In: The Late Pleistocene-Holocene. Moscow, Nauka 1, pp 27–46 (1993) (in Russian)
31. Votah MP, Klimanov VA (1994) Vegetation and climate of the Tomian-Ob area in the Holocene. Geologia i Geofisika 10:25–31 (in Russian)
32. Klimanov VA, Klimenko VV (1995)Temperature variations in climatic optimums of Holocene and Pleistocene. DAN Russia 342(2):242–245 (in Russian)
33. Konischev VN (1999) Evolution of ground temperature of Russian Arctic zone in Upper Cenozoic. Cryosphera Zemly III 4:39–47 (in Russian)

34. Romanovskii NN, Khubergen XB, Gavrilov AV, Eliseeva AA, Tipenko GS, Kholodov AL, Romanovskii VE (2003) Permafrost and gas hydrate stability zone evolution in the eastern part of the Eurasia Arctic Sea shelf in the Middle Pleistocene-Holocene. Criosphera Zemli, VII 4:51–64 (in Russian)
35. Romanovskii NN, Eliseeva AA, Gavrilov AV, Tipenko GS, Khubergen XB (2005) The long-term dynamics of the permafrost and gas hydrate stability zone of rifts of the East Siberian Arctic shelf (report 1). Criosphera Zemli, IX 4:42–53 (in Russian)
36. Romanovskii NN, Eliseeva AA, Gavrilov AV, Tipenko GS, Khubergen XB (2006) The long-term dynamics of the permafrost and gas hydrate stability zone of rifts of the East Siberian Arctic shelf (report 2). Criosphera Zemli, X 1:29–38 (in Russian)
37. Judge AS (1975) Geothermal studies in the Mackenzie valley by the Earth physics branch. Energy. Mines and Resources Canada, K1A 0E4, Ottawa
38. Goralchuk MI, Krizuk LM (1980) Some specific features of soil temperature distribution in the left riverside of Pur (between the rivers Evo-Yacha and Yagenetta). Geokriologicheskie issledovaniya, Trudy VSEGINGEO, Moscow 138:22–34 (in Russian)
39. Goodrich LE (1982) The influence of snow cover on the ground thermal regime. Canad. Geotech. J. 19:421–432
40. Smirnov YaB (1980) Heat flow in USSR: remarks to the heat flow and deep temperatures maps in the scale 1:10,000,000. GUGK, Moscow (in Russian)
41. Velichko AA (1987) Climatic variations in Meso-Cenozoic by the data for East Europe. *In* Climates of the Earth in geological history. Moscow. Nauka, 5–43 (in Russian)
42. Galushkin YuI, Yakovlev GE (2003) Thermal evolution of the lithosphere in the West Bashkirian basins and comparison with present-day temperature field of the Tagil-Magnitogorsk zone. Geotectonica 6:28–42 (in Russian)
43. Kukkonen IT, Golovanova IV, Khachay YuV, Druzhinin VS, Kosarev AM, Schapov VA (1997) Low geothermal heat flow of the Urals fold belt-implication of low heat production, fluid circulation or paleoclimate? Tectonophysics 276:63–85
44. Podgorny LV, Khutorskoy MD (1998) Thermal evolution of the lithosphere in the zone of joint of the Baltic shield and the Barents Sea plate. Phizika Zemli 4:3–9 (in Russian)
45. Rozenbaum GE, Shpolyanskaya NA (2000) Late Cenozoic history of Arctic permafrost and trend of its development in future. Moscow, Nauchny Mir (in Russian)
46. Arkhipov SA (1989) Chronostratigraphy of pleistocene in the North Siberia. Geologia i Geophysika 6:13–33 (in Russian)
47. Ershov ED (ed) (1988) Geocryology of USSR. Europian part of USSR. Nedra, Moscow (in Russian)
48. Klimanov VA (1994) Specific features of climate variations in the North Euroasia in the Late Glaciation and Holocene. Bulletin MOIP, 69, (1), 58–63 (in Russian)
49. Markova AK (1994) The Pleistocene landscapes of the Russian Plain according to the fauna of small mammals. Bulletin MOIP 69(1):64–69 (in Russian)
50. Matishov GG (1984) Ocean bottom in Ice Age. Nauka, Moscow (in Russian)
51. Tsybulya LA, Levashkevich VG (1992) Heat flow in the Barents Sea region. Appatite (in Russian)
52. Tsybulya LA (1993) Geothermal conditions in the Barents-Karsky region and their influence on formation of oil and gas accumulations. In: Gavrilov VP (ed) Geodynamics and oil and gas bearing in Arctic. Nedra, Moscow, pp 146–159 (in Russian)
53. Gladenkov YuB, Bazhenova,OK, Grechin VI et al (2002) Cenozoic of sakhalin and its oil and gas potential GEOS, Moscow (in Russian)
54. Frakes LA (1979) Climates throughout geological time. Elsevier, Amsterdam

Conclusions

In the book, the GALO system for basin modeling is applied to the study of some nonstandard problems of Geology. An analysis of variations in the basin tectonic subsidence calculated by removal of the water and sediment load from the basement surface, and by computing variations in density distribution of the basement rocks with depth and time provides an ability to estimate the amplitude and duration of the thermal and stretching events in the basin lithosphere. The method is applied to the basins with different amplitudes of lithosphere stretching including both continental rift basins and basins of continental passive margins. Our investigations show that the only tectonic analysis does not give the desirable assessment of amplitude and duration of the extension and heating events in the basin lithosphere. However, combination of the tectonic method with the control by temperatures measured in boreholes and by measured vitrinite reflectance decreases the uncertainties in modeling procedure and reduces the number of appropriate variants suggested by modeling for the basin evolution.

The analysis of tectonic subsidence used in the modeling suggests local-isostasy response of the lithosphere on load. The state of isostasy closely linked to the strength of the lithosphere. Modeling the distribution of stress with depth in the lithosphere suggests a considerable weakening of the continental crust due to deposition of thick sedimentary cover. In any case, the modeling results suggest that the rheological thickness of the lithosphere is considerably lesser than its thermal thickness.

An application of analysis of the basin tectonic subsidence to evolution of sedimentary basins in passive continental margin of India in the Bay of Bengal suggests that the amplitude of the lithosphere stretching increases from $\beta = 1.03–1.3$ in shallow-water offshore to $\beta = 1.7–2.9$ in the deep-water offshore. As a result of this extension, the crustal thickness in the deep-water area reduced from initial value of 40 km to 25–29 km at present time (including rather thick sedimentary cover). At the same time, the sea depth increased from 50–100 m to 2–3 km. The degree of the lithosphere stretching and the distance of the studied area from the fan of Gang River are the main factors caused the difference in burial, thermal and maturation histories of sedimentary sections in the shallow and deep-water offshore of the Bay of Bengal.

Y. Galushkin, *Non-standard Problems in Basin Modelling*,
DOI 10.1007/978-3-319-33882-8

The reconstructions of burial, thermal and maturation histories of the East Barents Basin suggests two main stage of the lithosphere extension. The first stage with extension amplitude $\beta = 1.15–1.17$ lasted during all Devonian in the Arctic area and during the Upper Devonian in the Admiralteyskaya area. After the first period, the second stage of the lithosphere extension with amplitude $\beta = 1.20$ occurred in the Upper Permian-Lower Triassic in both considered areas of the East Barents Basin. The modeling suggests more intensive thermal activation of the lithosphere in the northern areas of the Basin than in the southern ones. According to the modeling, sufficient part of the Permian-Triassic deposits in the South Barents Depression occurs within the gas generation zone. Liquid hydrocarbons generated by the Ordovician, Silurian and Devonian deposits in the Admiralteyskoe Rise and by Devonian, Permian and considerable part of Triassic rocks in the South Barents Depression were completely or partially destroyed due to the secondary cracking.

In the Sirte Basin, analysis of tectonic subsidence suggests that thermal activations of the lithosphere in the Albian–Cenomanian and Oligocene–Pleistocene are common for all tectonic structures of the Sirte Basin and the Cyrenaica Platform. A relatively high temperature regime caused mainly by the thermal activation of the lithosphere during the last 10 Ma is also typical for modern state of these structures. The analysis of variations in the basin tectonic subsidence suggests that two intervals of significant extension of the lithosphere in the Upper Cretaceous and Paleocene are also common for all areas within the Basin. The total amplitude of the crustal extension attains 1.5 in the central part of the Sirte Basin (the Ajdabiya and Maradah troughs and Zelten and Dahra platforms). It is equal to 1.3 in the Hameimat and Zallah troughs, and it is minimal (1.11–1.17) in the periphery of the basin (within the Hun Graben and Cyrenaica Platform).

The location of considered area in the eastern part of the North Sakhalin shelf near to the East Sakhalin accretion complex has led to the need to consider two variants of the Basin evolution. In the first variant the local isostatic response of the basin's lithosphere on internal and external load are assumed to be during entire history of the Basin. In the second variant, such response is suggested only for the time beginning with the Kuril Island Arc's formation that is from about 34 Ma BP up to now. The computations demonstrate a weak dependency of the lithosphere thermal regime and organic matter maturation in the Cenozoic section on the choice of the variants of the basin evolution. The modeling implies a rather high thermal regime of the Basin with modern temperatures of 100 and 200 °C at depths of 3 and 6.7 km, respectively, in spite of intensive sedimentation during the recent 10 Ma. The analysis of maturation and generation history of the probable source rocks in the area Sakhalin-5 of the North-East shelf of Sakhalin suggests that the rocks of the Upper Cretaceous, Eocene, Machigar (34–28.5 Ma), Daekhurin (28.5–25 Ma), and Lower Uynin (23.8–20.5 Ma) complexes can be considered as perspective oil bearing rocks.

The modeling of thermal regime and maturation history of sedimentary basin of the Siberian Platform conducted on the examples of two sedimentary sections with six and eight intrusive bodies of the Lower Triassic age demonstrates that the

thermal influence of the intrusive complex on the maturation and generation histories of the host rocks can be both significant and negligible depending on the size of the intrusion and the distance of the host rocks to the surface of the intrusive body. However, an estimation of the thermal effect of intrusions was carried out in the framework of a model of instantaneous intrusions and therefore can be considered as the evaluation of such effect to the maximum.

The study shows that a size of maturity aureoles of the single intrusions and trap complex decreases considerably with increase of duration of the complexes formation. A maturation level of organic matter in sedimentary rocks under trap and within the host rocks of single intrusions can be rather moderate if the time span of formation of these structures (or formation of their single layers) was enough long. The size of maturity aureole of the trap complex formed during several stages can be close to the aureole of single trap layer with maximal thickness. Comparison of computed and measured values of vitrinite reflectance within the thermal aureole of some well-dated intrusions shows that traditional calculations in the frame of the model of instantaneous intrusion considerably over-estimate temperatures and maturation of organic matter in the host rocks. Models which consider formation of the intrusive body over time (as distinct from instantaneous intrusion) and especially models of emplacement of the intrusive body in the shell of relatively cool magmatic rocks show better agreement between computed and observed data.

The modeling shown that the rocks of sub-trappean complex in the Deccan Plateau and the western passive margin of India can be as oil prone and gas prone depending on the thickness of the Trap and duration of its formation. Uncertainty in the thickness of the layers and the time of the trap formation has noticeable affect results of the modeling. Therefore, further refinement of these parameters can be adjusted results obtained above. Nevertheless, the reconstructions presented in Chap. 8 can help in estimations of hydrocarbon perspective of the rocks in sub-trappean complex of the Deccan Plateau and western passive margin of India.

In the third part of the book, it was shown that permafrost formation and degradation can be analyzed as a part of procedure of basin modeling. General procedure of basin modeling is used to construct initial temperature distribution for permafrost modeling and calculate also the depth-distribution of thermal physical parameters of frozen and thawed rocks for initial time of permafrost evolution. The use of real lithological composition of sedimentary rocks distinguishes this approach from previous studies of permafrost evolution. The modeling suggests that depth and time variations in thermophysical parameters of rocks (heat conductivity, heat capacity, unfrozen water and salt content, porosity) had a considerable influence on the results of permafrost modeling. The calculations demonstrate that the formation and degradation of the zones of stable existence of gas hydrates in the Pliocene-Holocene time are in close correlation with the events of formation and degradation of permafrost layers in the basins of high latitudes. All of these events were repeated many times during the Quaternary. It is known that the gas hydrate stability in the system “gas hydrate—porous water” depend strongly on the content of salt, ethane, propane, H_2S and CO_2 in the porous water and methane. This leads to the diversity of conditions of occurrence of gas hydrates in the land and marine

environments. The modeling shows that the climate variations in Siberia during the Late Pliocene-Holocene led to reduction of rock temperatures by 15–20 °C in the upper 1500 m of the sedimentary section and by 8–10 °C in the deeper layers of the section. This effect is more considerable in the Kuyumba area, than in the more northern Urengoy area despite the warmer climate of the first. The main reason of this is the thinner sedimentary cover in the Kuyumba area. The model suggests that a present-day permafrost base is at depth of about 350 m in the Urengoy area and 405 m in the Kuyumbinskaya area, that is in reasonable agreement with observed data in the studied areas. According to our assessments, the present-day zone of methane gas hydrate stability locates at the depth from 250 to 700 m in the Urengoy area and from 240 to 1590 m in the Kuyumba area. Variations in such parameters as salt concentration or type of function of unfrozen water content (in depending on the fraction of fine grained rocks) affect considerably the temperature and heat flow distributions with depth and permafrost thickness. The modeling shows that limitation by time-interval of the last 50,000–100,000 years can lead to errors in estimations of permafrost thickness up to 50–100 m. Our numerical reconstructions indicate that it is necessary to be careful in the modeling based on the measurements of heat flow or temperature gradient at depths of less than 2–2.5 km even in the regions where permafrost has degraded about 10–12 thousand years ago. The modeling in the Barents Sea shelf suggests rather rigorous climate of the last 70–50 thousand years while in the North-East Sakhalin shelf it assumes that the sea smoothed over the climatic jumps of the mean annual temperature during the greater part of the last 2.5 My and here the influence of the Pliocene-Holocene climate fluctuations on the depth profile of temperature is limited.

In general, the modeling examples presented in three parts of the book, confirm an expedience of using of the GALO system for basin modeling in the analysis of some nonstandard problems in Geology of the oil and gas-bearing provinces discussed in the book.